METASTABLE PHASES IN THE ALUMINUM-GERMANIUM ALLOY SYSTEM.
SYNTHESIS BY MECHANICAL ALLOYING AND PRESSURE INDUCED TRANSFORMATIONS.

Thesis by
Pascal Yvon
In Partial Fulfillment of the Requirements
for the Degree of
Doctor of Philosophy

California Institute of Technology
Pasadena, California

1994
(Submitted June 9, 1993)

To my parents

ACKNOWLEDGMENTS

First and foremost, I would like to thank my advisor at Los Alamos, Dr. Ricardo B. Schwarz, for his guidance, encouragement, sharing his knowledge, and his patience. This work would not have been accomplished if not for his constant support. These acknowledgments would not be complete without an inclusion of Fanny Schwarz for her kindness and caring.

I also would like to thank Prof. William L. Johnson, my academic advisor at Caltech, for his help throughout this project, especially for his vision and originality in defining the goals of this research.

I would like to acknowledge the Center for Materials Science, namely Drs. D. M. Parkin and A. M. Boring, for its financial support over the course of the last five years.

The guidance of Dr. Dave Schiferl in the design and performance of the high pressure experiments is acknowledged. Nothing would have been accomplished without the help of "Cowboy" Robert L. Martinez who corrected , improved, and made my designs work, in addition to teaching me the value of donuts in the fast processing of parts in the machine shop.

I would like to acknowledge the use of the TEM facilities at the University of New Mexico, and especially the kindness and efforts of Stacy Kasser.

The interaction with the various members of Ricardo Schwarz's research group has proved to be invaluable, and I would like to extend special thanks to soon-to-be Dr. Paul Desch, Dr. Dan J. Thoma (and family), Dr. S. Srinivasan, Dr. Jim Rubin, Jim Hannigan, Windy Jaeger, and Andy Clarke. I cannot express enough my appreciation for Don Nye's resourcefulness and constant efforts in maintaining and repairing the equipment.

I also had fruitful discussions with members of Bill Johnson's research group, and most particularly Dr. P. Askenazy, Dr. Jorge Kittl, Dr. David Lee, Dr. Carl E. Krill, III, Prof. Hans Fecht, Prof. Pierre Desré, Prof. Konrad Samwer, Dr. Egon Hellstern, Dr. Steve Anlage, and Dr. Y.T. Cheng. The help of Doug Pearson in preparing samples is gratefully acknowledged. Finally, the friendship of Andy Mutz, as well as his scientific input, was very precious.

Many people made my stay at Caltech infinitely more enjoyable, and I would like to thank Angie and Mario Bressan for their friendship, Coach Lin Parker for teaching me the subtleties of football, trainer Jaye Tashima for patching me up, Dr. Don Caldwell and the Caltech Glee Club, Rosy Meiron, Marc Schuyler, Olivier Cojot, and Dr. Tony Skjellum, Coach K. Takarabe and the Pasadena Rugby Club.

Special thoughts go to Dr. Susanna W. Johnson whose self motivation while obtaining her degree, as well as her determination while fighting her terrible illness, was a source of inspiration. I hope for her full recovery.

It would be impossible to mention all the persons at Los Alamos National Laboratory who contributed to the success of this work, but I would like to thank Roy Rockage, Tim Pierce, Chris Espinoza, Jim Smith, Dr. Terry Mitchell, Dr. Kurt Sickafus, Dr. Bob Margevicius and Kristen, Dr. David Wu, Dr Joe Thompson, Dr. Dermot Coffey, Dr. Jun Koike, Almost Drs. Stuart Maloy, Ken Mc Clellan, Cory Czarnik, Florian Heidelbach, Kristin Bennett, Dr. Ozer Unal, Dr. Francois Rossi, Tim Burke, Deirdre Ragan, Tim Culler, Karen Schwarz, Bill Carter, Darrell Gonzales, Dr. Nicole Bordes, Bertrand Meltz, Gretchen Skofronick, Dr. Ivar Reimanis, Dr. Harriet Kung, Padma Kodali, Dr. Chris Aumann, Carl Necker, Stella Taylor, Melissa Ortiz, Bettye Mc Culla, Laurie Lauer, Brenda Romera, Betty Northrup, Tara Martinez, Eric Ahrens, Dr. Dean Taylor, Prof Dennis Bennett, Prof. Alain Bulou, Sabina Johnson, Heike Vollath. Very special thanks go to very special Dr. Diane Albert who took an active part in the completion of this work and made everything, but leaving Los Alamos, easy.

Many people made this stay in New Mexico an unforgettable experience, and I particularly would like to thank Karyn Abeyta-Canfield, Lila and Trish from Montoya's, all members of Los Alamos High School Rugby Club, Trish and Michel Guerin. Memorable times were spent with the Santa Fe Rugby Club, and the list is too long to be complete, but Dave Wheelock, Richard Morris, Shannon Robinson, Derek and Andrea Gordon, Dr. Jeff Knauf, Coach Larry Smith, Coach Herb Howell, Coach Rob Thomson, Todd Fabec, just to name a few, will always be remembered.

Finally, my thoughts turn to Concetto Geremia and Barry Krueger whose untimely passing brought deep sadness and whose memory will always remain bright.

ABSTRACT

Amorphous alloys have been prepared by a variety of techniques from rapid solidification to solid state crystal-to-glass transformations. In this work we report the use of pressure to obtain amorphous alloys in the aluminum-germanium alloy system. Aluminum and germanium form a simple equilibrium eutectic with limited mutual solubility and no intermetallic intermediate phases. We used a regular solution approach to model the effects of pressure on the Al-Ge binary phase diagram. The main effects of pressure are to extend the solubility of germanium in aluminum, to displace the eutectic composition towards the germanium-rich side, and to slightly decrease the eutectic temperature. Using this modeled phase diagram, we designed thermobaric treatments to induce crystal-to-glass transformations in fine grain mixtures of aluminum and germanium.

We used Merrill-Bassett diamond anvil cells to perform experiments at high pressures. We designed and built an x-ray apparatus to enable us to determine the structure of the alloys at pressure and from cryogenic temperatures to 400^{o}C. Two-phase Al-Ge samples with fine microstructures were prepared by splat-quenching and mechanical alloying. We observed a crystal-to-glass transformation at about 80 kbar. The amorphous phase formed was metastable at ambient temperature after the pressure was released. This result was confirmed by transmission electron microscopy (TEM) studies. The amorphous phase obtained by pressurization was found to have a liquid-like structure and was metallic. This is the first time such an amorphous phase is reported in the aluminum-germanium alloy system. In the TEM samples we also observed the presence of a second amorphous phase that was formed upon release of the pressure. This second phase had a tetrahedrally-bonded continuous random network structure, similar to that of semi-conducting amorphous germanium.

TABLE OF CONTENTS

APPENDICES

List of Figures

Chapter 1

Chapter 2

Chapter 3

Chapter 4

CHAPTER 5

List of Tables

Chapter 1

Chapter 2

Chapter 4

1. INTRODUCTION

1. 1. Thermodynamics of Phase Transitions

There are three states of matter: solid, liquid, and gas. In this dissertation, we shall consider only the solid and liquid states, as well as the transitions between these two states. The solid state can be either crystalline or amorphous and experience has shown that in thermodynamic equilibrium the solid state is crystalline. A crystalline solid is a regular array of atoms, with periodicity and a high degree of long-range order. If a liquid is cooled fast enough to prevent the nucleation and growth of the crystalline phase, an amorphous solid can be obtained, which may be thus visualized as a high-viscosity state of the liquid. Amorphous solids have no long-range atomic order or periodicity, but may have appreciable short range order. The transition between the liquid and amorphous states occurs at the glass-transition temperature, T_g. Strictly speaking, T_g cannot be considered a thermodynamic quantity, as this transition depends on the cooling rate, and there is no sharply defined glass-transition temperature [1]. This transition is due to the abrupt freezing-in of degrees of freedom in the liquid. This freezing-in is a kinetic phenomenon arising from the slowness with which molecules or atoms change positions below a certain temperature. It is customary to define T_g as the temperature at which the undercooled liquid reaches a viscosity in the 10^{13} poise range.

A thermodynamic state is described by a number of variables such as temperature (T), pressure (P), volume (V), partial molar fractions (x_i) in multicomponent alloys, etc. These variables are not independent from each other, as the number of degrees of freedom (n) from the set [T, P, $x_1, x_2 \ldots x_N$] is given by Gibbs phase rule:

$$n = N - \varphi + 2 \qquad (1.1)$$

where N is the number of constituents, and φ the number of phases coexisting in thermodynamic equilibrium.

For instance, for a one-component system with one phase, there are only two independent variables, which can be chosen to be P and T. Liquid, solid, and gas occupy regions in the P-T phase diagram as shown in Figure 1.1. If two phases coexist, then the number of degrees of freedom is reduced to 1, and the P-T region is reduced to the boundary between the two phases. If three phases coexist there is no degree of freedom, and the coexistence can only occur at points in the P-T diagram called triple points. Also, the boundary between liquid and gas ends at a point called the critical point. Past this point, it is possible to go continuously from liquid to gas and from gas to liquid.

Thermodynamic functions are used to describe the state of the system and explain the phase transitions. The internal energy of the system is represented by E. Another important thermodynamic function is the entropy (S), which is a measure of the number of possible equivalent configurations for the system. It is a measure of the order of the system. This is an extensive variable and is always maximized for a closed system in equilibrium. We can write [2]:

$$E = T\,dS - P\,dV \qquad (1.2)$$

for systems at fixed composition and constant pressure.

Finally, we also use the Gibb's free energy (G), which is defined as

$$G = E + P\,V - T\,S \qquad (1.3)$$

We will use P and T as independent variables to describe thermodynamic states, because the experimental setup used allows us to directly modify and measure accurately these two variables. Therefore, G is important as it is minimum when the system is in equilibrium. For instance, if we plot in a G-T diagram the Gibbs free energies of the solid phase (G_x) and the liquid phase (G_l), we see that these curves intersect at $T = T_m$ (Fig. 1.2). Above T_m, the free energy of the liquid is lower than that of the solid, and therefore the liquid phase is more stable than the solid phase, under the same conditions of pressure and temperature. Also, the difference in free energy between two phases is the thermodynamic "driving force" for a transition to occur from the higher free energy state to the lower one.

In principle, all these thermodynamic functions are defined for equilibrium states. However, we can define thermodynamic state functions for non-equilibrium phases, as long as the time scale for the transition to the equilibrium phase is long enough to allow the metastable phase to behave ergodically. Therefore, it is possible for us to construct metastable phase diagrams and explain through thermodynamics phase transitions involving metastable phases.

1. 2. Retention of Amorphous Structures by the Rapid Quenching of Melts

Metallic compounds usually have a crystalline structure. In the 1950's, Buckel and Hilsch [3,4] obtained non-crystalline metallic solids during an investigation of the influence of lattice defects on superconductivity. By quenching vapors of elemental metals (Zn, Ga, Bi) or mixtures of elemental metals (Zn-Cu) on a substrate maintained at cryogenic temperatures, they produced thin films of metallic glasses or amorphous metals. Like the more conventional oxide glasses, metallic glasses have a glass-transition temperature [5,6], T_g, which represents the temperature boundary between liquid and glass. The amorphous phases obtained by Buckel and Hilsch were metastable at cryogenic temperature only, and were found to crystallize as the temperature was raised to allow nucleation of the equilibrium crystalline phase. The temperature at which this occurs is called the crystallization temperature, T_x. For metallic glasses, T_x is usually rather close to T_g.

Another advance in amorphization was made by Duwez and coworkers [7,8] who in 1960 obtained an amorphous alloy by rapidly quenching a metallic melt of gold-silicon to room temperature. This was an accidental discovery, as the purpose of the experiments was to produce extended solid solutions of silicon in gold. By using quenching rates on the order of 10^6 K s^{-1}, the nucleation and growth of equilibrium crystalline phases were bypassed as the melt undercooled to obtain a frozen liquid. Following this discovery, a wide variety of techniques and equipment were developed to produce amorphous phases in many alloy systems. These rapid-quenching techniques have a drawback, however, as the required high cooling rates needed to bypass crystallization impose size restrictions on the dimensions of the metallic glasses that can be produced (ribbons, thin films, or powders).

1. 3. Crystal-to-Amorphous Transformations in the Solid State

Instead of starting from vapors or melts, mechanisms have been devised to achieve crystal-to-glass transformations through solid-state isothermal reactions. Extensive reviews on this subject have been published [9,10,11]. As discussed previously, melting occurs at the temperature T_m at which the free energy of the crystal (G_x) equals the free energy of the liquid (G_l) (Fig. 1.2). If the free energy of the solid phase is raised (by introducing defects in the crystal, for instance), the melting temperature can decrease (Figure 1.3). If T_m were lowered to T_g, then the crystal would have the tendency to "melt" in the solid state, thus transforming to a glass.

Another example of solid-state amorphization involves particle irradiation of intermetallic compounds. The particle irradiation introduces chemical disorder and point defects, which raise the free energy of the crystal. This excess free energy is the thermodynamic driving force for amorphization since the free energy of the irradiated crystal may become higher than that of the liquid phase (Figure 1.3). Amorphization by irradiation was first achieved by Bloch [12] who used neutron irradiation to amorphize U_6Fe at room temperature. Later Carpenter and Schulson [13] discovered that it was possible to amorphize alloys using electron irradiation. They irradiated Zr_3Al, which is a $L1_2$ ordered intermetallic compound, and obtained an amorphous phase at temperatures between 130 and 375 K. Later, Brimhall et al. reported ion irradiation-induced amorphization in several binary systems [14]. They irradiated Ti-Ni, Ni-Al, Fe-Ti, Mo-Ni, and Re-Ta with 2.5 MeV Ni^+ ions to obtain amorphous alloy phases.

Cullis et al. [15] reported that it was possible to obtain amorphous alloys by ion implantation . Injecting a beam of W^+ ions into a thin film of copper produced a supersaturated solid solution of tungsten in copper. When additional W^+ ions were implanted, the crystalline structure transformed to a glass. This amorphization method has been found to occur in a number of alloys and is especially well suited for obtaining a thin amorphous film at the surface of a bulk sample.

Another way to produce amorphous thin layers is by ion mixing. In this method, bilayers or multilayers of two pure elements having a large negative heat of mixing in the liquid state are irradiated by high-energy inert gas ions at low or ambient temperature [16]. The penetrating ions create cascades and atoms of the two constituents intermix. When the ambient temperature is high, the radiation also enhances the interdiffusion of the species. However, if the substrate temperature is chosen sufficiently low to avoid thermally-activated long-range atomic rearrangements, thus preventing the formation of a crystalline intermetallic equilibrium phase, then the final product can be a metastable amorphous phase.

An amorphization mechanism that presents similarities with particle irradiation is based on the hydrogenation of metallic alloys. First Malik and Wallace [17], then Yeh et al. [18], found that introducing hydrogen into certain intermetallic compounds induces a crystal-to-glass transformation. Yeh et al. annealed $Zr_{0.75}Rh_{0.25}$, which had a metastable $L1_2$ crystalline structure, in a hydrogen atmosphere between 150 and 225 ^{o}C and obtained an amorphous metallic hydride, $Zr_3RhH_{5.5}$. There is no coherent hydride of $L1_2$ phase in the ternary Zr-Rh-H system, and the equilibrium state should be a two-phase mixture of ZrH (or ZrH_2) and a Rh-rich crystalline phase. However, at the anneal temperature there is not enough mobility of Zr and Rh to allow these phases to form. On the other hand, the glassy hydride is a metastable alternative that does not require interdiffusion of Zr and Rh. The amorphization is a polymorphous process whereas the formation of the crystalline equilibrium phases require chemical segregation.

Amorphous alloys can also be produced in the solid state. Hauser [19], and later Herd et al. [20,21], reported that certain metals can diffuse at low temperature into amorphous semiconductors such as tellurium, silicon, and selenium without causing the amorphous semiconductor to crystallize. The first example of amorphization by interdiffusion between two crystalline solids was reported by Schwarz and Johnson [22]. In this study, a single-phase amorphous alloy was obtained by annealing thin film crystalline multilayers of lanthanum and gold. Figure 1.4 (a) (from [23]) is a schematic phase diagram for a binary alloy AB having a negative heat of mixing in the liquid state. Figure 1.4 (b) shows the free energy curves for the various phases at the temperature T_r. Phases α and β are crystalline primary solid solutions, and γ is a crystalline intermetallic. As illustrated in Figure 1.4 (b), the free energy of the mixture of A and B (dotted line) is much higher than that of the amorphous phase or the equilibrium crystalline intermetallic

γ. This difference provides the thermodynamic driving force for the amorphization reaction. At room temperature, there is not enough interdiffusion to allow a reaction to occur. However, if an anneal is performed (70°C for 6 hours for Au-La), then the two pure elements react to form a single-phase amorphous alloy or an amorphous phase in equilibrium with one of the crystalline pure elements, depending upon the initial thicknesses of the films. The glass forming range for solid state amorphization is shown at the bottom of the figure. For $x_2 < x < x_3$, a single-phase amorphous alloy is obtained, whereas for $x_1 < x < x_2$ or $x_3 < x < x_4$, a two-phase mixture is obtained. This glass forming range is to be compared with that of rapid solidification: the homogeneity range of amorphous alloys prepared by rapid solidification is usually divided into relatively narrow regimes located near deep eutectics in the liquidus [24], as shown by the black bars in Figure 1.4. At this temperature there is enough atomic mobility to allow the formation of an amorphous phase, but not enough to enable the formation of crystalline intermetallic equilibrium phases. If the anneal takes place at a higher temperature (125 °C for Au-La), then intermetallic phases form instead. This behavior has been observed in a number of binary alloy systems [10], and the conditions required are a negative heat of mixing in the amorphous state and anomalous diffusion of one element into the other. These two criteria have been proposed by Schwarz, Johnson and coworkers [22,25] and have been experimentally verified. The first criterion is thermodynamic, as the negative heat of mixing provides the driving force for the solid state amorphization. The second criterion is kinetic, and it ensures that there is a range of temperatures for which one element (solute) can diffuse into the other (solvent), while the solvent is stationary. This mechanism allows the two elements to mix, but the crystalline intermetallic equilibrium phases cannot form, as this would require mobility of both elements.

Yet another way to produce an amorphous alloy is to alloy elemental mixtures of the metal powders in a high energy ball mill [26-29]. This is called mechanical alloying.

This amorphization is somewhat analogous to the one described in the previous paragraph, as the amorphous alloy forms through interdiffusion of the two pure metals. The ball milling provides a large density of clean A/B interfaces where the reactions may occur. The diffusion is enhanced by the large number of defects introduced by the milling.

Another amorphization through mechanical attrition was discovered by Schwarz and Koch [30] when an amorphous phase was obtained by mechanical attrition of the equilibrium intermetallic compound $NiTi_2$. In this case, the amorphization process is similar to irradiation, as the ball milling introduces defects in the lattice that lead to the collapse of the crystalline structure. Certainly, the rate at which these defects are created must exceed the rate of recovery.

In related experiments, it has been possible to achieve amorphization by slow co-deformation of two elemental metals [31,32]. Schultz [31] started with 25 μm foils of elemental nickel and zirconium for an overall composition of $Ni_{0.68}Zr_{0.32}$. The composite material was rolled in a steel jacket until a layer thickness between 0.1 and 1 μ m was obtained. On a subsequent anneal at 300 ^{o}C, the mixture of crystalline nickel and zirconium became amorphous. Atzmon et al. [32] obtained similar results with the same method in the copper-zirconium system at the composition $Cu_{0.60}Zr_{0.40}$.

A controversial way to produce bulk amorphous alloys has been reported by Blatter and coworkers [33,34]. A metastable b.c.c. solution of $Ti_{0.60}Cr_{0.40}$ was prepared by quenching from 1100^{o}C. This metastable phase was subsequently annealed at 600^{o}C for 30 hours and the production of an amorphous phase was reported. Blatter and coworkers explained this discovery in terms of a proposed Gibbs free energy diagram for the Cr-Ti system at 600^{o}C shown in figure 1.5 [34]. The driving force for the amorphization is the free-energy difference between the metastable b.c.c. phase and the amorphous phase. The equilibrium phase of lowest free energy, a mixture of α-titanium and the $TiCr_2$ Laves phase, cannot be produced since the formation of the Laves phase requires long-range atomic rearrangements which cannot occur at the annealing temperature of 600^oC. This method, called spontaneous vitrification, is intriguing in its implication that the free energy curves of the liquid phase and the b.c.c. phase have two crossings, one at 1400^oC, when the b.c.c. phase melts, and another one below 600^oC. These results and interpretations are, however, still controversial: the observations have been reproduced by Kim and Lee [35], but have not been reproduced by other researchers [36,37], including the author. Researchers [38,39] modeled the free energy difference between the b.c.c. phase and the liquid, and showed that spontaneous vitrification was not feasible for an undistorted b.c.c. phase, but could happen if there were excess free energy in the form of defects in the b.c.c. phase. Recently, Bormann et al. [40] have reported a solid-state amorphization reaction by annealing at 650^oC a metastable b.c.c. phase of Ti-55 at.%Cr prepared by mechanical alloying.

Finally, pressure can be use to induce crystal-to-glass transformations in certain systems. This transformation is the subject of the dissertation and thus the use of pressure to obtain amorphous phases will be explained in detail in the next section.

1. 4. Pressure-Driven Crystal-to-Amorphous Transformations

The effect of pressure on phase transitions in pure elements and in compounds has been investigated since the 1700's [41]. The experimental work can be classified according to the techniques used. The most important are shock compression tests, isobaric heating tests, and static high pressure tests. The pressure-temperature-time paths of these three methods are shown in Figure 1.6.

Shock compression has been used since the 1940's [42]. A shock wave is a sharp elastic disturbance which propagates at supersonic speed in the medium. The state of the system is determined by the Rankine-Hugoniot equations, which express the conservation of mass, momentum, and energy across the shock front. The advantage of this technique is that very high pressures can be obtained [43,44]. However, the duration of the shock state is very short (about 1 μs), and the temperature may increase sharply behind the shock front.

Isobaric heating is usually employed at low pressures, up to 500 MPa, but high temperatures. This technique is used to study structure changes and thermodynamic functions as a function of temperature. In some apparatus, temperatures up to 8000 K have been obtained [45].

The third method, static compression, is the focus of this study. The first static high-pressure apparatus used an external source of compressed gas and attained pressures up to 2 GPa. Then piston-cylinder devices were developed in the beginning of the 20th century, mostly by Bridgman and coworkers, and reached pressures up to 10 GPa. In these devices, a piston is driven in a hollow cylinder containing the sample (Figure 1.7 (from 45)). More recently, diamond-anvil cells (DAC) have been developed, and will be described in detail in the experimental section of this thesis. These devices have produced pressures up to 500 GPa.

Pressure-temperature phase diagrams have been experimentally established for most of the elements [45,46,47]. At the same time, with the help of computers, theoretical methods have been developed to model the behavior of materials under high-pressure and predict the influence of pressure on phase transformations. One point of interest is the influence of pressure on melting temperature. The slope of the $T_m(P)$ curve is given by the Clausius-Clapeyron equation (x refers to the crystalline phase, and l refers to the liquid phase):

$$dG_x = V_x dP - S_x dT \qquad (1.4)$$

$$dG_l = V_l dP - S_l dT \tag{1.5}$$

On the melting curve $dG_x = dG_l$. This yields:

$$\frac{dP}{dT} = \frac{(S_l - S_x)}{(V_l - V_x)} \tag{1.6}$$

According to the second law of thermodynamics, $S_l > S_x$ at the melting temperature, as melting has to be endothermic. Therefore, the sign of the slope is the sign of $(V_l - V_x)$. There is one exception to this rule: Helium is the only element to be liquid at 0 K and ambient pressure. For all other elements, the entropy of the liquid state is higher than that of the crystalline solid at the same temperature and pressure. For most elements or compounds, the specific volume of the liquid phase exceeds that of the solid phase at atmospheric pressure, which results in a positive dP/dT value. This causes the melting temperature to increase with increasing pressure. There are several exceptions to this behavior (Ge, Si, H_2O,...), where $dP/dT < 0$ at $P = 1$ bar.

The shape of the $T_m(P)$ curve has been a subject of speculation for a long time. Experimentally, all known melting curves are concave downward. Kawai [48] claimed that $\frac{d^2P}{dT^2} \leq 0$ for all elements and alloys, but did not present a proof to substantiate his claim. This seems to be intuitively true, as the compressibility of the liquid is usually higher that than of the crystal, causing therefore $V_l - V_x$ to decrease with increasing pressure. However, the change of $S_l - S_x$ with pressure also has to be taken into account. In Appendix A we discuss the curvature of the melting curve; we conclude that in most cases, the curvature of the melting curve is indeed negative, but cannot draw absolute conclusions since the changes of some thermodynamic quantities with pressure are not known. Researchers also speculated that the $T_m(P)$ curve might end in a critical point, similarly to the liquid-gas transition (Figure 1.1). This would have made it possible, beyond certain pressures, to go continuously from the solid state to the liquid state.

According to Kirzhnits [49], who considered the states of matter at extreme values of pressures and temperature, (a) there is no such critical point in the $T_m(P)$ curve and (b) the melting temperature reaches a maximum with increasing pressure before decreasing.

1. 4. 1. Serendipity in Pressure-Induced Amorphizations

There are several reports in the literature of researchers obtaining amorphous phases when their primary focus was to study the effects of pressure on crystalline/crystalline phase transitions. First, Mc Donald et al. [50] reported the formation of an amorphous phase when applying pressure to Ga-50 at.% Sb alloy. The purpose of the study was to obtain a metallic phase of GaSb by applying 120 kbar (12 GPa) at 200^oC, then quenching to 77 K before releasing the pressure. Instead they observed the formation of a mixture of a white-tin structured phase (identified as GaSb) and an amorphous phase. The two diffraction halos of the amorphous phase disappeared after an anneal at 200^oC.

Brixner [51] obtained an amorphous Gd-Mo-O phase by applying pressure to the tetragonal-β phase of $Gd_2(MoO_4)_3$. He was trying to reproduce the β to monoclinic-α phase transition that had been reported to occur at 30 Kbar (3 GPa) and 555^oC [52]. After applying a pressure of 65 kbar (6.5 GPa) at 400^oC, the β phase transformed into an amorphous phase. This phase crystallized to the α phase when heated between 550 and 590^oC. The explanation for the formation of the amorphous phase was that, in the process of going from β to α, the lattice of the β phase first collapses, but the slow kinetics prevent the formation of the α phase.

Belash and Ponyatovsky [53] observed a pressure-induced amorphization in the Zn-Sb system. In separate experiments, they pressurized the intermetallics ZnSb,

Zn_4Sb_3, and Zn_3Sb_2. The samples were held at 300°C and 90 kbar (9 GPa) for 2 hours, then cooled to room temperature, before releasing the pressure. The x-ray diffraction patterns of Zn_4Sb_3 and Zn_3Sb_2 only showed weak diffraction lines of Zn. The pressed ZnSb sample did not show any diffraction peaks. They concluded that ZnSb formed a single-phase amorphous alloy, whereas for the other two compositions, the amorphous phase was in equilibrium with crystalline Zn.

In these experiments, researchers produced amorphous phases by applying pressure and temperature, but they did not elaborate on the phenomenon, nor did they investigate the mechanisms that led to amorphization.

1. 4. 2. Pressure-Induced Amorphization of Ice

Ice was the first compound for which researchers tried to deliberately drive a crystal-to-amorphous transformation by applying an adequate thermobaric treatment [54]. As mentioned earlier, in most elements and compounds, the melting temperature increases with increasing pressure. However, because at atmospheric pressure H_2O is denser in the liquid phase than in the solid hexagonal ice I phase, the melting curve of H_2O has a negative slope in the P-T phase diagram (see Fig. 1.8). The $T_m(P)$ curve decreases with increasing pressure until it reaches a triple point at which liquid, ice Ih, and ice III coexist. The dashed curve in Fig. 1.8 shows an extrapolation to higher pressures of this melting curve. If the sample is cooled to 77 K and the pressure is increased, ice Ih should transform to rhombohedral ice II at 0.3 kbar (30 MPa). This transformation requires the nucleation and growth of the crystalline ice II phase. If the formation of Ice II is prevented by kinetics, the system will remain in the metastable ice Ih structure. When P is increased to 10 kbar (1 GPa), we cross the extrapolation of the melting curve of ice Ih. At this point the crystal should melt, and since melting does not require nucleation, this transformation is not hindered by slow kinetics. Because the crystal-to-amorphous transformation occurs below the glass-transition temperature of Ice Ih (150 K), the product is not a liquid but an amorphous solid.

1. 4. 3 Pressure-Induced Amorphizations in Carbon, Silicon, and Germanium

Pressure-induced amorphization has been investigated in the group IV elements, as their P-T phase diagrams present some similarities with that of ice. Thus, the mechanism described in section 1. 4. 2. could also be used to produce an amorphous phase. The melting curve of carbon increases with pressure, but reaches a maximum (4000°C, 70 kbar (7 GPa)) as shown in Figure 1.9. The extrapolation of the melting curve to high pressures suggests that the melting temperature should be near room temperature for a pressure in the range 300-400 kbar (30-40 GPa). Goncharov et al. [55,56], using a diamond-anvil cell, observed the amorphization of carbon at 260 kbar (26 GPa) at room temperature. This amorphization is similar to that of ice, and happens when the applied pressure increases beyond the metastable extension of the melting curve.

The $T_m(P)$ curves of silicon and germanium decrease with increasing pressure which makes them likely candidates for this type of pressure-induced amorphization. The metastable extensions of their melting curves in the P-T phase diagram predicts amorphization at room temperature and $P = 170$ kbar (17 GPa) for germanium, and $P = 270$ kbar (27 GPa) for silicon, as shown in Figures 1.10 and 1.11. Clarke and coworkers [57] used a diamond indenter to apply high pressures to germanium and silicon. They obtained a metallic phase upon loading and an amorphous non-metallic phase upon unloading. They propose two mechanisms to explain these results. The first one (and most likely according to Clarke [58]) suggests that amorphization takes place upon increasing pressure as the metastable extension of the melting curve is crossed. This amorphous phase is metallic but transforms to a non-metallic amorphous phase upon release of the pressure. The second one suggests a transformation to a crystalline high-pressure metallic phase (β-white tin for both elements) upon loading, and then a transformation to an amorphous phase upon releasing the pressure.

Imai and coworkers [59] performed high-pressure experiments in a diamond-anvil cell at 80 and 300 K on amorphous $Si_{1-x}Ge_x$ alloys. They found that these amorphous alloys crystallized into a white-tin structure at pressures higher than 50 kbar (5 GPa). In a set of experiments conducted at room temperature, after the pressure was released, the samples transformed back to an amorphous structure. For the samples studied at 80 K, the metastable crystalline phase was retained upon release of the pressure, but they became amorphous on a subsequent annealing at 300 K.

1. 4. 4. Pressure-Induced Amorphizations in Other Systems

Cd-Sb alloys have been found to become amorphous under an specific thermobaric treatment [60,61]. At the composition $Cd_{0.43}Sb_{0.57}$ and a pressure of 50 kbar (5 GPa), the equilibrium orthorhombic phase transforms to a metastable hexagonal γ phase. This phase is retained after releasing the pressure at liquid nitrogen temperature. Under slow heating to room temperature, the γ phase becomes amorphous.

Similar results were found in the Ga-Sb system [62]. A β white-tin structure phase forms at 90 kbar (9 GPa) and 300^oC. This phase is retained after quenching to liquid nitrogen temperature and releasing the pressure. Under slow heating to room temperature, the metastable β phase transforms to an amorphous phase.

Another case of this type of behavior is observed in the Al-Ge system [63,64]. A metastable hexagonal γ phase was obtained by applying a pressure of 90 kbar (9 GPa) at 320^oC at the composition $Al_{0.30}Ge_{0.70}$. To avoid confusion, let us point out here that this γ phase is different from any of the γ_i metastable phases produced by rapid solidification in this alloy system. This phase was retained upon quenching to liquid nitrogen temperature and releasing the pressure. Under slow heating, the γ phase transforms to a β-white tin structure phase at -30°C, which subsequently transforms to an amorphous phase at 20°C.

The purpose of the three aforementioned experiments was to produce metastable high pressure phases by applying adequate thermobaric treatments. It was observed that after retaining this phase at low temperature and releasing the pressure, the alloys transformed to amorphous states. Figure 1.12 shows the path followed in a schematic P-T phase diagram (from [65]). In the first step (a) the pressure is increased at room temperature beyond the boundary (dash-dot line) between the low-pressure crystalline phase A_mB_n and the high-pressure crystalline phase γ (a). Then the sample is annealed (b) at a higher temperature to ensure that the transformation to the γ phase did occur and was not prevented by slow kinetics. The sample is subsequently quenched to liquid nitrogen temperature (c). On releasing the pressure while at low temperature (d), the γ phase cannot transform back to the equilibrium phase, as the nucleation of the A_mB_n crystalline phase is prevented by kinetics. Upon heating (e), the alloy cross the metastable extension of the melting curve of the γ phase, and thus γ melts. If T_g is above room temperature, the amorphous phase would be retained at ambient conditions of temperature and pressure. This is another way to achieve amorphization by using thermobaric treatments to cross a melting line below T_g.

For completeness, we mention a few other examples of pressure-induced amorphization. Durachenko et al. [66] reported amorphization in $Cu_{0.60}Zr_{0.40}$ and Fe-Ni-P-C after pressurizing these alloys to 20 kbar (2 GPa) at 1000 $^{\circ}$C. Dachille and Roy [67] observed amorphization of SiO_2 upon annealing to 650 $^{\circ}$C after releasing a pressure of 40 Kbar (4 GPa). Pressure-induced amorphization was also found to occur in SnI_4 [68], Cu-Sn [69], $LiKSO_4$ [70], Al_6Li_3Cu [71], $C_2(CN)_4$ [72], and Al_5Li_3Cu [73].

1. 5. The Aluminum-Germanium System: Stable and Metastable Phases

Aluminum and germanium form a simple eutectic system with no stable intermetallic phase and limited mutual solubility [74] as shown in figure 1.13 [74].

Metastable crystalline phases of aluminum and germanium have been investigated extensively, because of the similarities between the aluminum-germanium system and the commercially important aluminum-silicon system, and also because of superconducting properties of Al-Ge alloys. Metastable aluminum-germanium phases have been prepared using a variety of processing techniques, including rapid solidification, thin-film physical vapor deposition, submicron powder atomization, droplet undercooling, and high pressures. Five metastable crystalline phases, γ_1, γ_2, γ_3, γ_4, and γ_5 have been produced by rapid solidification [75-88]. These results are summarized in Table 1.1. Although the γ_1 phase has been extensively studied, there are still discrepancies in the literature about its structure and composition. Salli and Kushnereva [77] reported this phase to be cubic with $a = 1.287$ nm. Suryanarayana and Anantharaman [80] found the γ_1 phase to be tetragonal, with lattice constants of $a = 1.291$ nm and $c = 1.2$ nm. Ramachandrao et al. [81] also reported the γ_1 phase to be tetragonal, but with $a = 0.659$ nm and $c = 1.201$ nm. These last two results are practically identical, except for the halving of the lattice parameter a. Suryanarayana et al. [89] report extra diffraction reflections that cannot be explained by the smaller a-lattice. Köster [76] reported the γ_1 phase to be rhombohedral, with $a = 0.767$ nm and $\alpha = 96.55^{o}$. This result was confirmed by Laridjani et al. [80]. More recent publications [86,87] also support Köster's findings. It has been suggested [79] that the disagreement over the structure of the γ_1 phase could be due to a lack of control over the cooling rates, which may vary considerably (several orders of magnitude) from one rapid quenching apparatus to another. However, Laridjani and Cahn [81] repeated the synthesis of the γ_1 phase with different apparatuses with cooling rates varying from 10^4 to 10^9 K s^{-1}. They did not notice any differences between the positions of the diffraction peaks of the metastable phases. Another explanation proposed was difference of resolution between the different x-ray diffraction equipment used. Researchers using the Debye-Scherrer technique [77,80,81] were unable to observe some of the diffraction peaks, especially those almost overlapping stronger reflections. On the other hand, Köster, and later Laridjani, used a Guinier camera, which gave them much better resolution. In addition to this apparent lack of resolution in certain instances, the task of indexing the reflections was difficult, as there were always several phases coexisting. Even though calorimetry was used in some cases to help identify the diffraction reflections, there are some discrepancies between the sets of reflections reported. The composition of the $\gamma 1$ phase is also subject to controversy, as it is reported to be 30-40 at.% Ge [75], 33 at.% Ge [77,80], 37.5 at. % Ge [81], 43-45 at.% Ge[86]. The last reference was the only one to perform an EDX analysis, but the EDX machine was only calibrated to pure aluminum and pure germanium, which can lead to errors. It has been recently found that in the Al-Ge system, the relative intensity of the aluminum and germanium peaks is not a linear function of composition [90,91].

The $\gamma 2$ phase also has been a subject of controversy. Suryanarayana [80,88] reported it to be tetragonal with a = 1.498 nm and c = 1.603 nm. Ramachandrao [81] also reported it to be tetragonal, but with a = 0.625 nm and c = 0.944 nm. Kushnereva [77] reported the $\gamma 2$ phase to be simple cubic with a = 1.3805 nm. Köster [75] reported the $\gamma 2$ phase to be monoclinic with a = 0.6734 nm, b = 0.5818 nm, c = 0.4282 nm, and $\beta = 88.98^{o}$. This was confirmed by Laridjani [83] and Kaufman [86]. There is, however, agreement on the composition of this phase, which is reported to be 50% at. Ge [75,77,80,81,86].

The $\gamma 3$ phase has been found to be hexagonal by all researchers. However, the reported lattice parameters do not agree. Köster [75] found a = 1.35 nm and c = 0.71 nm, Ramachandrao [81] reported a = 0.288 nm and c = 0.458 nm, and Kaufman [84,85] reported a = 1.42 nm and c = 0.74 nm. The composition of this phase was measured by EDX to be between 42 and 45 at. % Ge [86].

The $\gamma 4$ phase has been reported to be tetragonal with a = 0.75 nm and c = 0.58 nm [75]. Kaufman [86] refined the measurements later and found it to be orthorhombic with a = 0.78 nm, b = 0.57 nm, and c = 0.73 nm. The composition measured by EDX was found to be between 41 and 50 at. % Ge [86].

A new metastable crystalline phase in Al-Ge, which we denote γ_5, has been reported recently by Zhukova et al. [88]. They observed this phase in thin films of Al-Ge made by vacuum condensation. This phase has a β white-tin structure with lattice parameters a = 0.566 nm and c = 0.310 nm. The composition of this phase is estimated to be between 46 and 50 at. % Ge.

Amorphous phases in the aluminum-germanium system have been obtained in the germanium-rich end of the phase diagram by several researchers [92-102]. Ramachandrarao et al. [92] obtained a mixture of f.c.c. aluminum and an amorphous phase by quenching $Al_{70}Ge_{30}$. The first two amorphous diffraction halos were located near $k = 19.6\ nm^{-1}$ and $33.1\ nm^{-1}$ [81], where $k = \frac{4\pi \sin\theta}{\lambda}$. Nath et al. [93] prepared amorphous Al_xGe_{1-x} by the simultaneous vapor deposition of aluminum and germanium ($x < 0.3$). Randhawa et al. [94] using the same preparation technique as Nath found that the amorphous diffraction halos of amorphous $Al_{30}Ge_{70}$ and amorphous germanium have approximately the same k-values. Krapp et al. [97] produced amorphous germanium, amorphous $Al_{29}Ge_{71}$, and amorphous $Al_{38}Ge_{62}$. For amorphous germanium, they obtained well defined first and second coordination shells at .245 and .400 nm. The amorphous Ge-Al films were similar to amorphous Ge. The amorphous Al-Ge alloys showed a small broadening of the first coordination shell, and a greater distance of .250 nm. The structure was very similar to amorphous germanium, and presented similar annealing behavior. The coordination number was found to be 3.8. They concluded that Ge-Al form a continuous random network with strong covalent bonding. The Al atoms participate on the Ge sites in the construction of the network.

Catalina et al. [99] studied the aluminum-rich side of the Al-Ge phase diagram. Thin films with 81, 70, and 59 at. % aluminum were prepared by sputtering. They characterized the structure of the alloys by transmission electron microscopy. The $Al_{81}Ge_{19}$ film showed a two-phase structure of an amorphous Al-Ge matrix and aluminum crystals. The volume fraction of crystals decreased as the germanium content was increased, and the films were single-phase amorphous for $Al_{59}Ge_{41}$. The short range order in the amorphous Al-Ge phase was similar to that of amorphous germanium.

Adams et al. [102] obtained a mixture of an amorphous Al-Ge phase and f.c.c. aluminum by coevaporation of aluminum and germanium at the composition $Al_{60}Ge_{40}$. They estimated the amorphous phase to have a composition of 45 at. % germanium.

In these works the amorphous Al-Ge phases have been produced by a rapid quenching process (equivalent cooling rates of 10^{12} K s^{-1})at ambient pressure. In the next paragraphs we discuss the effects of pressure on the aluminum-germanium system.

Aluminum has an f.c.c. structure at ambient pressure. No phase changes have been observed in aluminum under pressures up to 1.5 Mbar (150 GPa). The P-T phase diagram, as determined by Lees and Williamson [103] is shown in figure 1.14. *Ab initio* pseudopotential calculations [104,105] predict that aluminum transforms from f.c.c to h.c.p. to b.c.c. at pressures above 1 Mbar, but this claim has not been supported by experiment.

Germanium has a diamond structure at room pressure. Germanium can also exist in a metastable amorphous form that is retained at ambient pressure. Amorphous germanium has been extensively studied [106-113]. All researchers report the amorphous state non metallic, contrary to metallic amorphous alloys such as Ni-Zr. The structure of amorphous germanium is very different from that of liquid germanium [106]. The coordination number is close to 4 for the amorphous state, compared with 8 for the liquid state. The x-ray diffraction pattern of amorphous germanium shows broad halos at 0.33 nm, 0.183 nm, 0.118 nm, and 0.097 nm [107] . Using d-spacings in the case of amorphous alloys has no physical meaning, therefore we converted these values in k-numbers. The halos were at 19.04, 34.33, 53.25, and 64.78 nm^{-1} . All studies indicate that the short range order of the crystalline diamond phase of germanium is preserved in the amorphous state, and that the randomness of the amorphous phase results from variations in the tetrahedral bond angle and rotations about the bonds. This structure can be modeled by a continuous random network [109].

When pressure is applied to germanium, new phases are formed. The P-T phase diagram in Figure 11 shows a room-temperature phase transformation at 106 kbar to the β white-tin structure [114]. This transition is sensitive to shear stresses (non-hydrostatic pressure) and can occur at lower pressures in the presence of shear. Further compression causes germanium to transform to a simple hexagonal phase at 750 kbar (75 GPa), and to a double hexagonal phase at 1.02 Mbar (102 GPa) [115]. These transformations have been predicted by *ab initio* pseudopotential calculations [116]. Vohra et al. [115] determined the structures of the high-pressure phases by neutron diffraction. There is some controversy about the last two transformations, however, as Nelmes [117], using more powerful structure determination techniques, obtained different results. Furthermore, the transformations reported by Vohra et al. [115] also do not agree with earlier reports of a body-centered-tetragonal phase forming above 30 K at 25 kbar (2.5 GPa), and a b.c.c. phase forming above 110 kbar (11 GPa) [118,119]. After releasing the pressure, the β white-tin structure transforms to a metastable simple tetragonal phase [115]. These phases are summarized in Table 1.2.

The influence of pressure on the eutectic temperature has been studied by Clark and Pistorius [120]. They investigated the composition $Al_{69.7}Ge_{30.3}$ from room pressure to 40 kbar (4 GPa). They found that the melting curve initially rises with pressure to reach a maximum at 13.9 kbar (1.39 GPa), and then decreases. They fitted the melting curve to a parabola:

$$T_m = 415.5 + 0.746 \,.\, P - 0.0268 \,.\, P^2 \tag{1.7}$$

where P is expressed in kbar and T in ^oC. This is an important result as we can expect the melting temperature to be about room temperature at 100 kbar (10 GPa).

Pressure has also been used in the aluminum-germanium system to increase the solubility of germanium in aluminum. At room pressure, there is very little solubility of germanium in aluminum. However, above 100 kbar (10 GPa), germanium becomes metallic, and Hume-Rothery rules [121] predict a potential large solubility of germanium in aluminum as their atomic radii differ by only 5.6 % (1.43 for aluminum in f.c.c. structure, 1.35 for germanium in the β white-tin structure), and their electronegativity is close, as aluminum and germanium belong to adjacent columns in the Periodic Table. An increase in solubility can be obtained also by rapid solidification, but does not exceed a few at.% Ge. The relation between the lattice parameter a and the atomic germanium concentration C_{Ge} is given by [80]:

$$a = 0.40495 + 0.000166.C_{Ge} \tag{1.8}$$

This predicted increase in solubility has been confirmed experimentally [122]. Using a thermobaric treatment of 420 K and 100 kbar (10 GPa), the solubility was found to increase to 18 at. % germanium in aluminum. A high-pressure γ phase was also found in the aluminum-germanium system [63,123]. This γ phase was found to be hexagonal with $a = 0.283$ nm and $c = 0.2622$ nm. As mentioned in a previous section, this phase, retained after quenching to cryogenic temperatures, becomes amorphous after heating to room temperature. The amorphous halos were located at $k = 19.34\ \text{nm}^{-1}$ and $k = 33.46\ \text{nm}^{-1}$. This phase was stable at room temperature and transformed to a mixture of aluminum and germanium at 200°C. These high pressure phases are also included in Table 1.2.

Table 1.1. Summary of metastable phases reported in the aluminum-germanium alloy system

Phase	structure	a (nm)	b (nm)	c (nm)	β	Composition	Reference
γ_1	Cubic	1.287				33 at. % Ge	77
γ_1	Tetragonal	1.291		1.200		33 at. % Ge	80
γ_1	Tetragonal	0.659		1.201		37.5at. % Ge	81
γ_1	Rhombohedral	0.767			96.55	30-40 at. % Ge	75
γ_1	Rhombohedral	0.767			96.55		82
γ_1	Rhombohedral	0.767			96.55	49-51 at. % Ge	86
γ_1	Rhombohedral	0.767			96.55	13-30 at. % Ge	87
γ_2	Cubic	1.3805				50 at. % Ge	77
γ_2	Tetragonal	1.498		1.603		50 at. % Ge	80
γ_2	Tetragonal	0.625		0.944		50 at.% Ge	81
γ_2	Monoclinic	0.6734	0.5818	0.4282	88.98	50 at. % Ge	75
γ_2	Monoclinic	0.6734	0.5818	0.4282	88.98		82
γ_2	Monoclinic	0.6734	0.5818	0.8045	147.85	43-45 at. % Ge	86
γ_2	Monoclinic	0.6734	0.5818	0.8045	147.85	45 at. % Ge	87
γ_3	Hexagonal	0.288		0.458			81
γ_3	Hexagonal	1.35		0.71			75
γ_3	Hexagonal	1.42		0.74		42-45 at. % Ge	86
γ_4	Tetragonal	0.75		0.58			75
γ_4	Orthorhombic	0.78	0.57	0.73		41-50 at. % Ge	86
γ_5	Tetragonal	0.566		0.310		46-50 at.% Ge	88

Table 1.2. Possible high-pressure phases in the aluminum-germanium alloy system

Composition	Structure	a (nm)	c (nm)
Ge	Tetragonal	0.593	0.698
Ge	Tetragonal	0.44884	0.2692
Ge	Tetragonal (B.C.)	0.593	0.698
Ge	B.C.C.	0.694	
Ge	Simple Hexagonal		
Ge	Double Hexagonal		
$Al_{30}Ge_{70}$	Tetragonal	0.508	0.282
$Al_{30}Ge_{70}$	Hexagonal	0.283	0.262

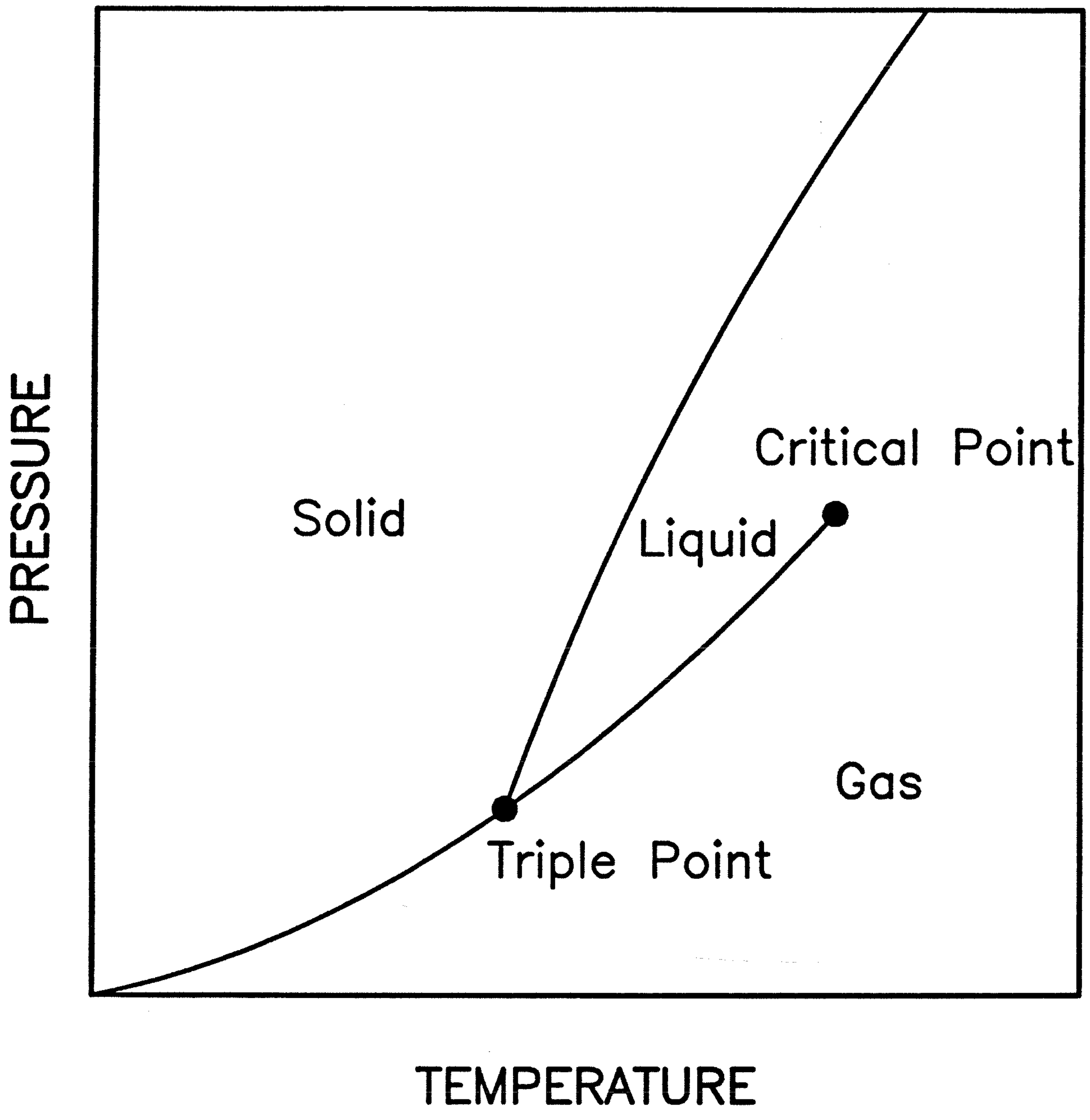

Figure 1.1 Schematic pressure-temperature phase equilibrium diagram.

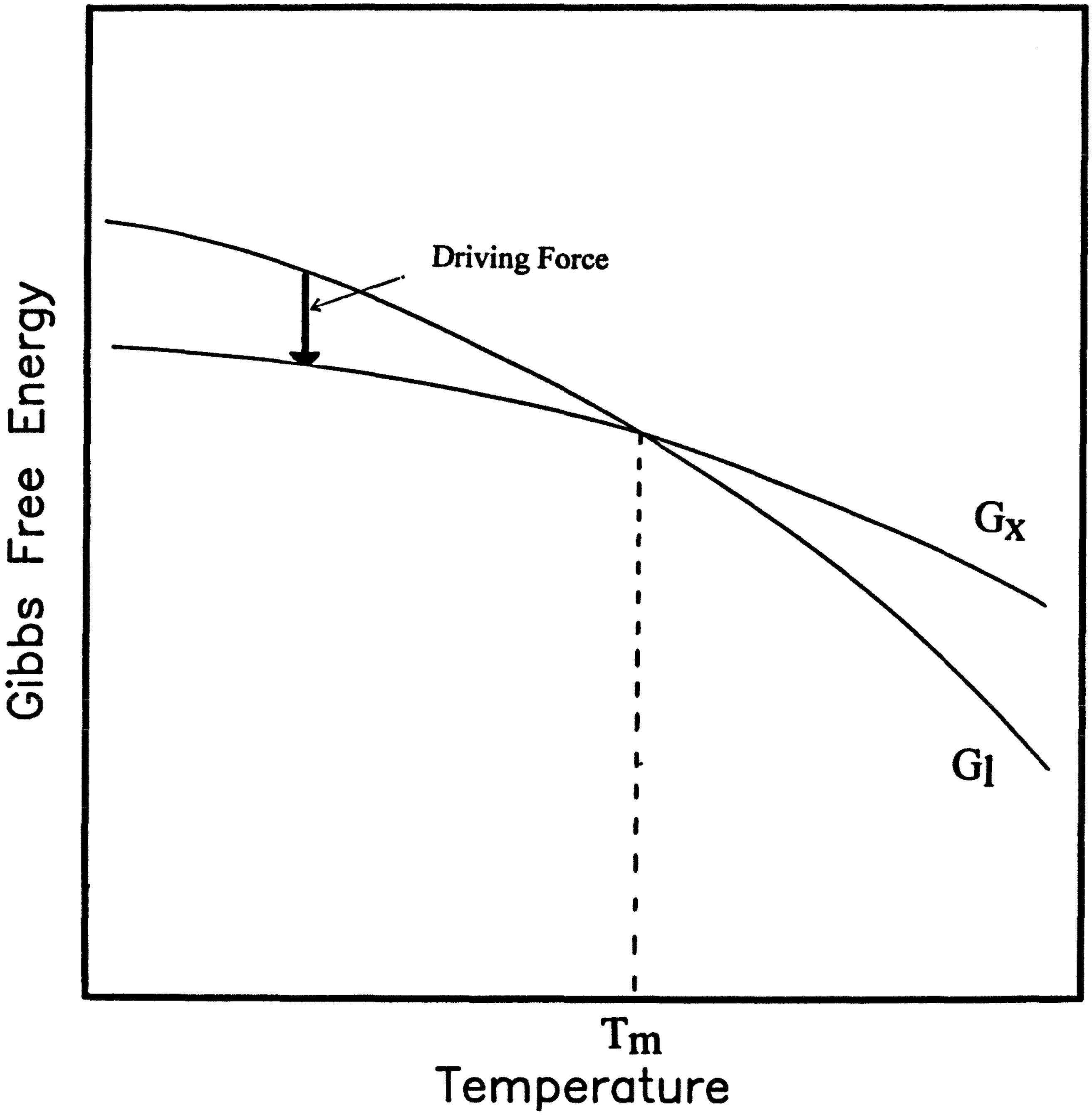

Figure 1.2 Schematic Gibbs free energy-temperature phase diagram. G_x is the Gibbs free energy of the crystalline phase and G_l is the Gibbs free energy of the liquid phase. T_m is the melting temperature.

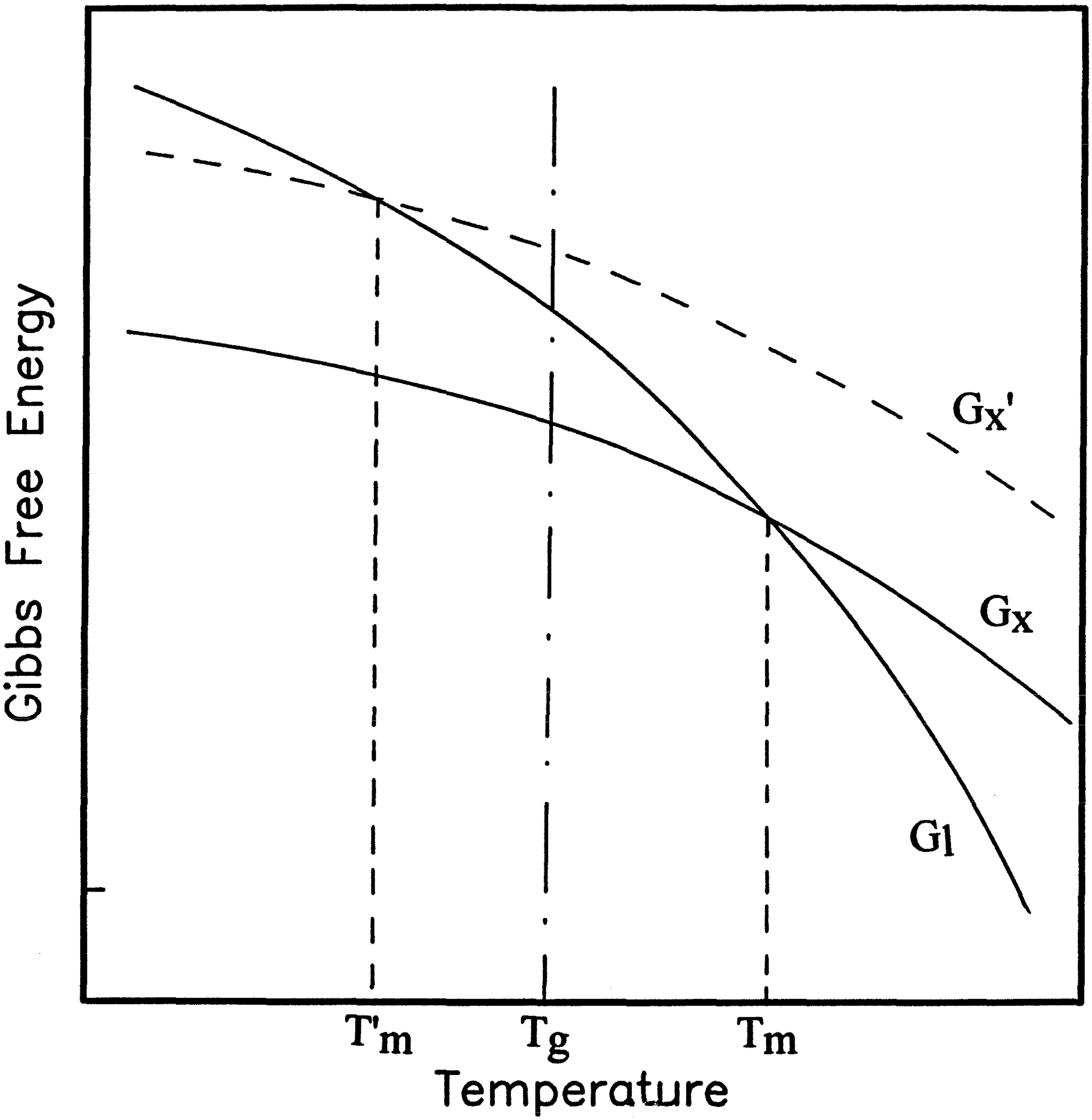

Figure 1.3 Schematic Gibbs free energy-temperature diagram.
The notations are identical to Figure 1.2. $G_{x'}$ is the raised Gibbs free energy of the crystalline phase and T'_m is the melting temperature of this phase. T_g is the glass-transition temperature

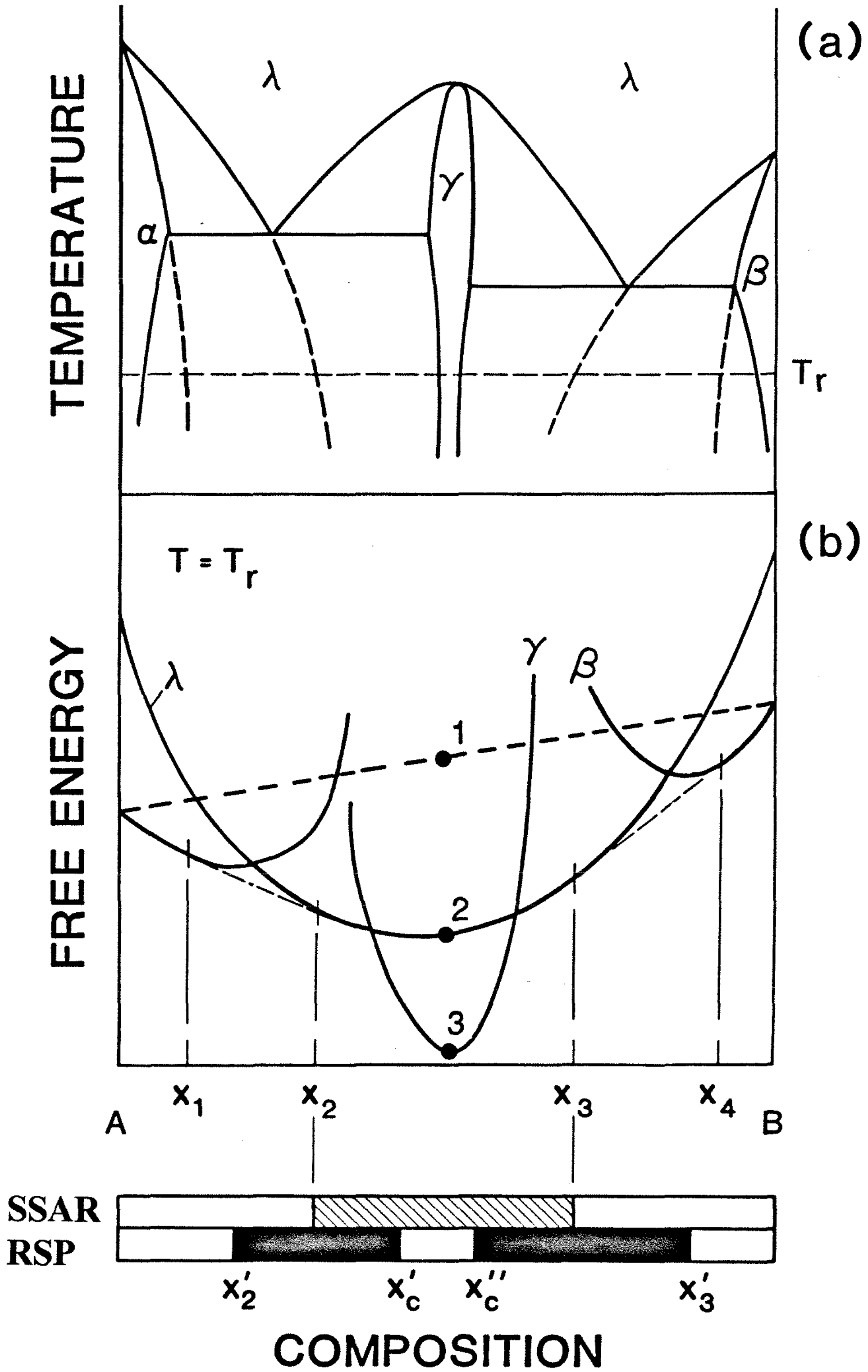

Figure 1.4 Schematic Gibbs free energy-composition and temperature-composition binary phase diagram. The dashed bar at the bottom indicates the glass forming range by solid state reaction, whereas the solid bars indicate it for rapid solidification.

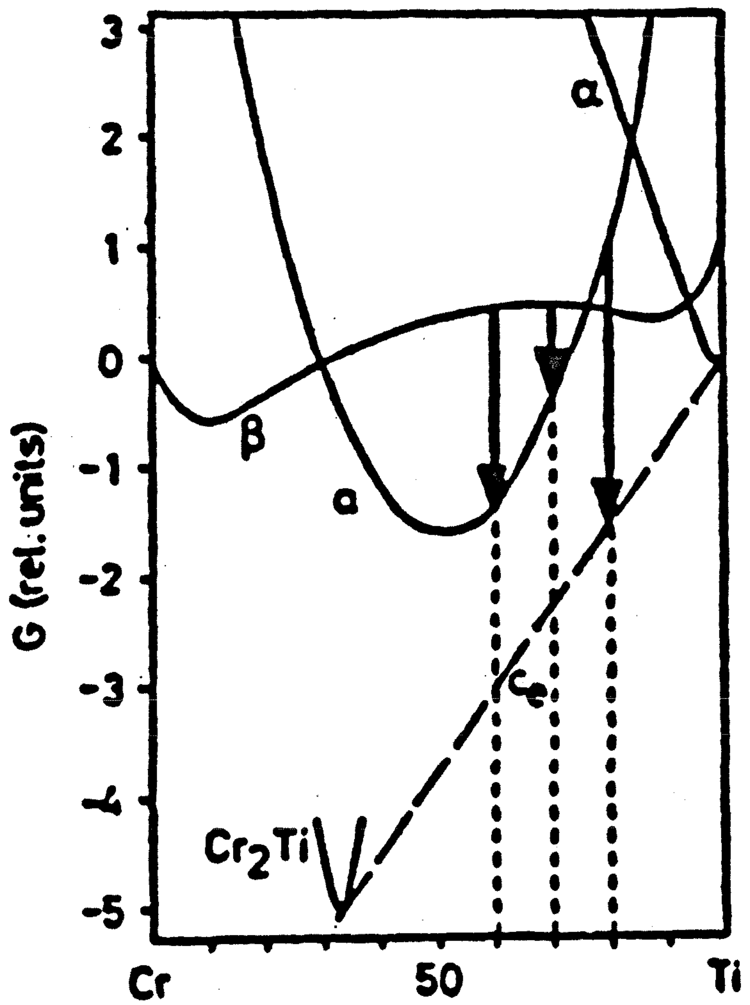

Figure 1.5 Proposed Gibbs free energy-composition phase diagram [34]

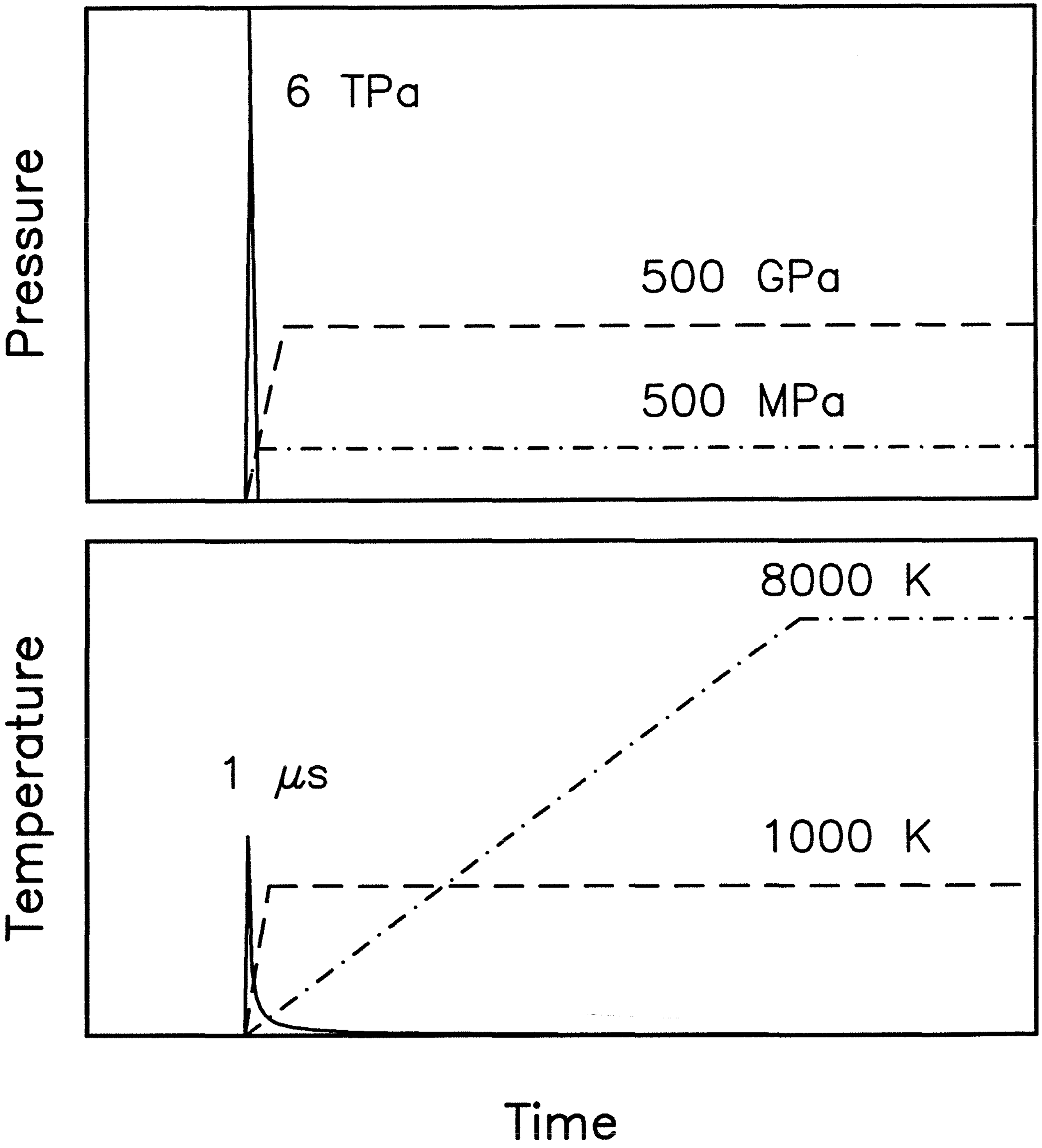

Figure 1.6 Pressure-time and temperature-time paths for the shock wave technique (solid line), the isobaric heating technique (dash-dot line), and the static compression technique (dashed line).

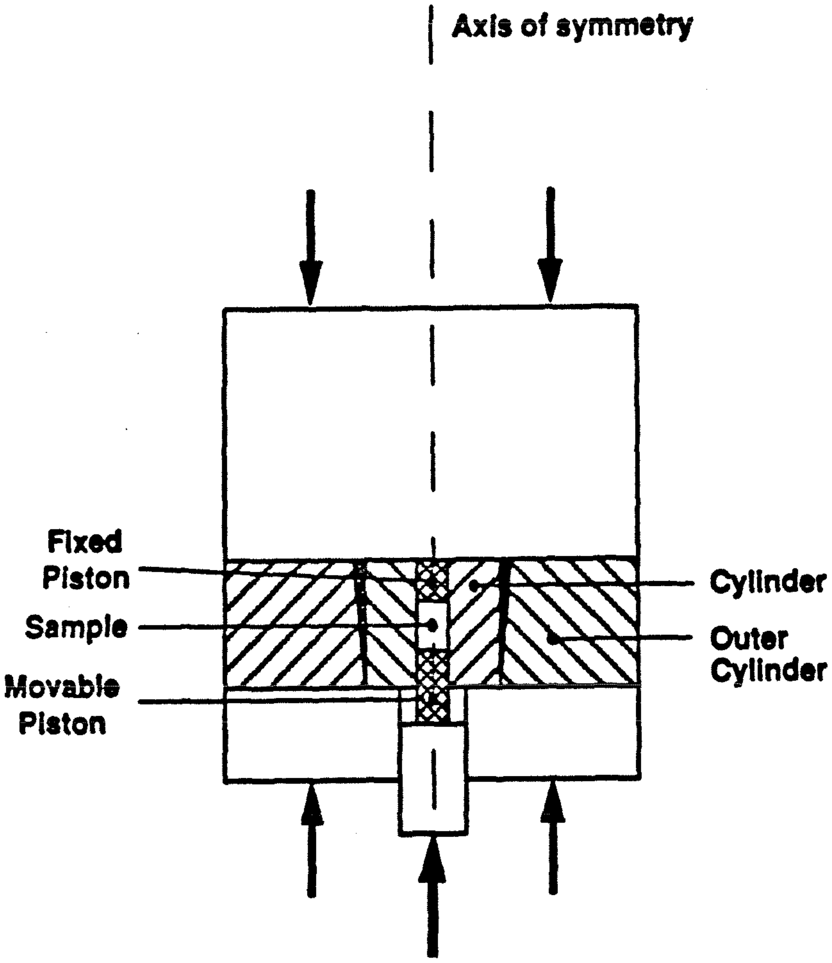

Figure 1.7 Schematic cross-section of a supported piston-cylinder apparatus [45].

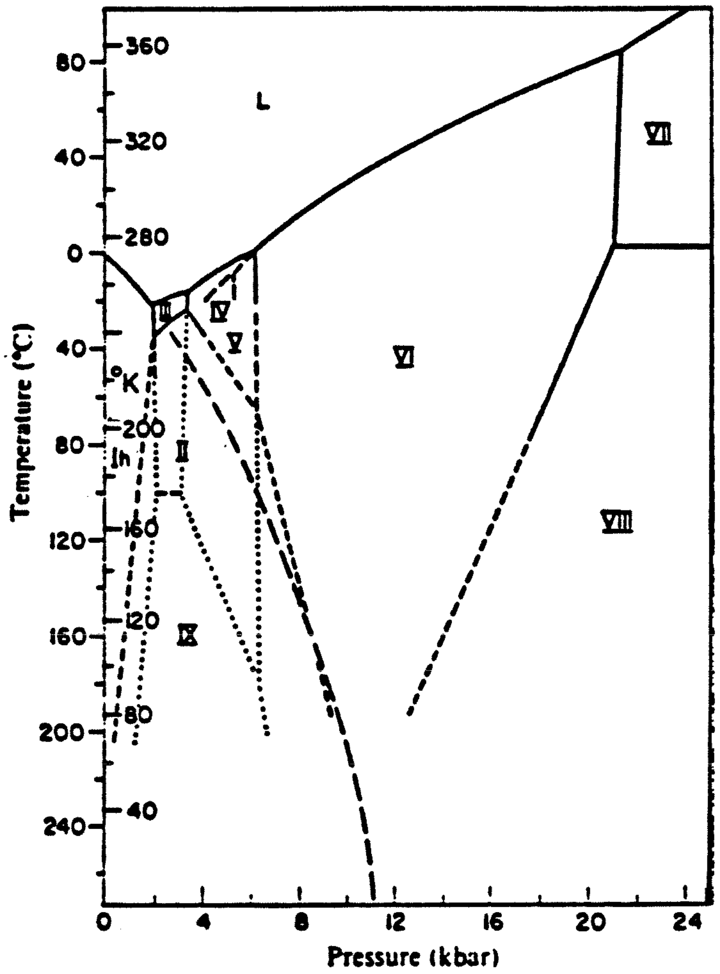

Figure 1.8 The phase diagram of ice in the pressure-temperature plane. The melting line of ice I is extrapolated as a dashed line [54].

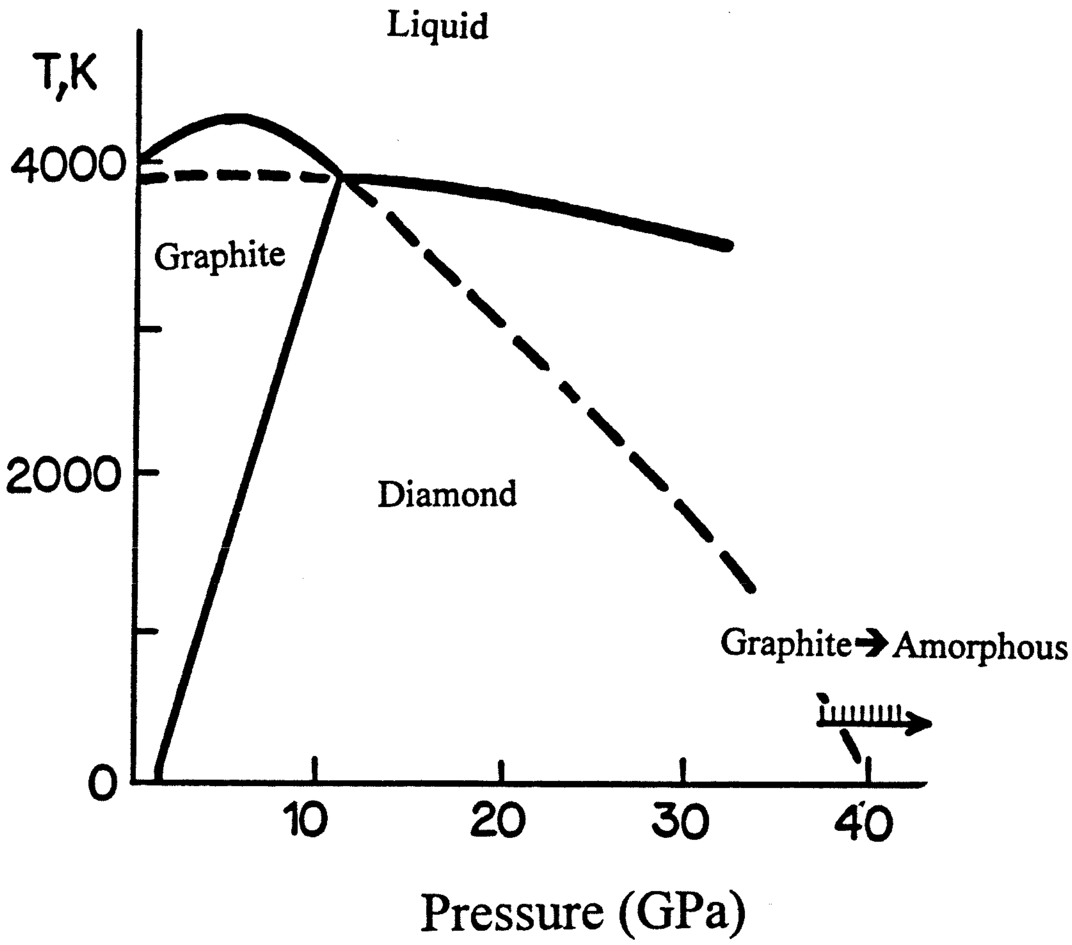

Figure 1.9 Pressure-temperature phase diagram of carbon [65].

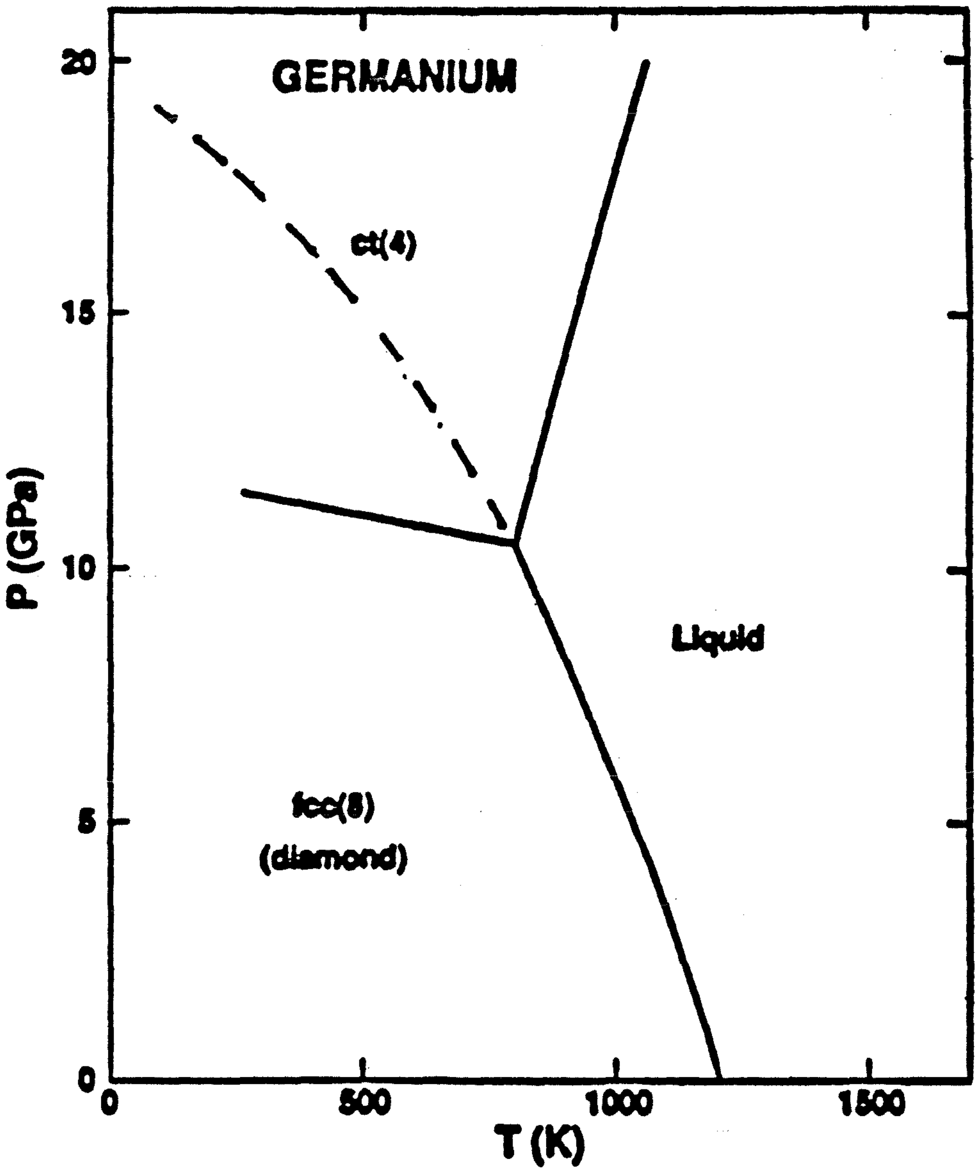

Figure 1.10 Pressure-temperature phase diagram of germanium [45].

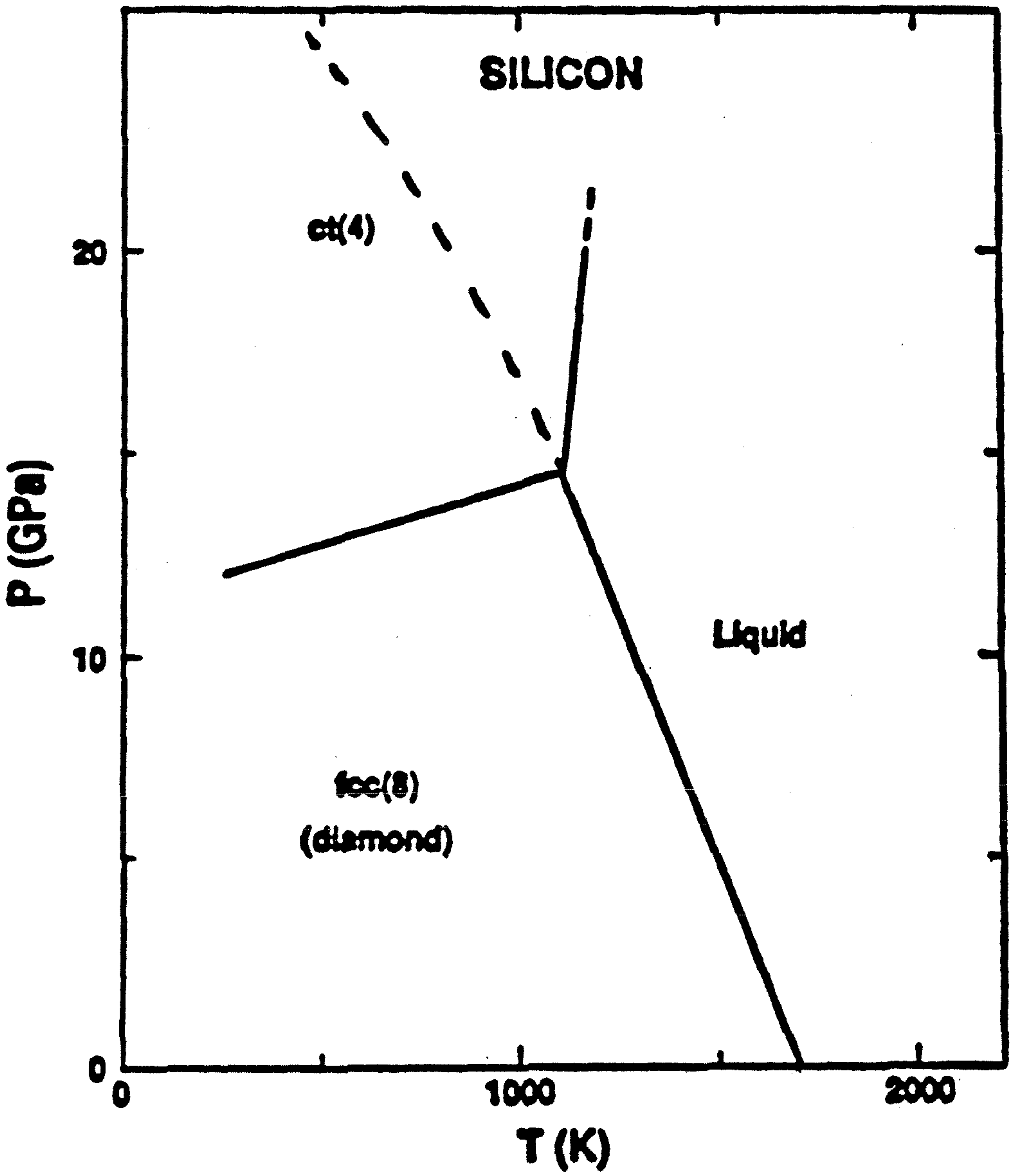

Figure 1.11 Pressure-temperature phase diagram of silicon [45].

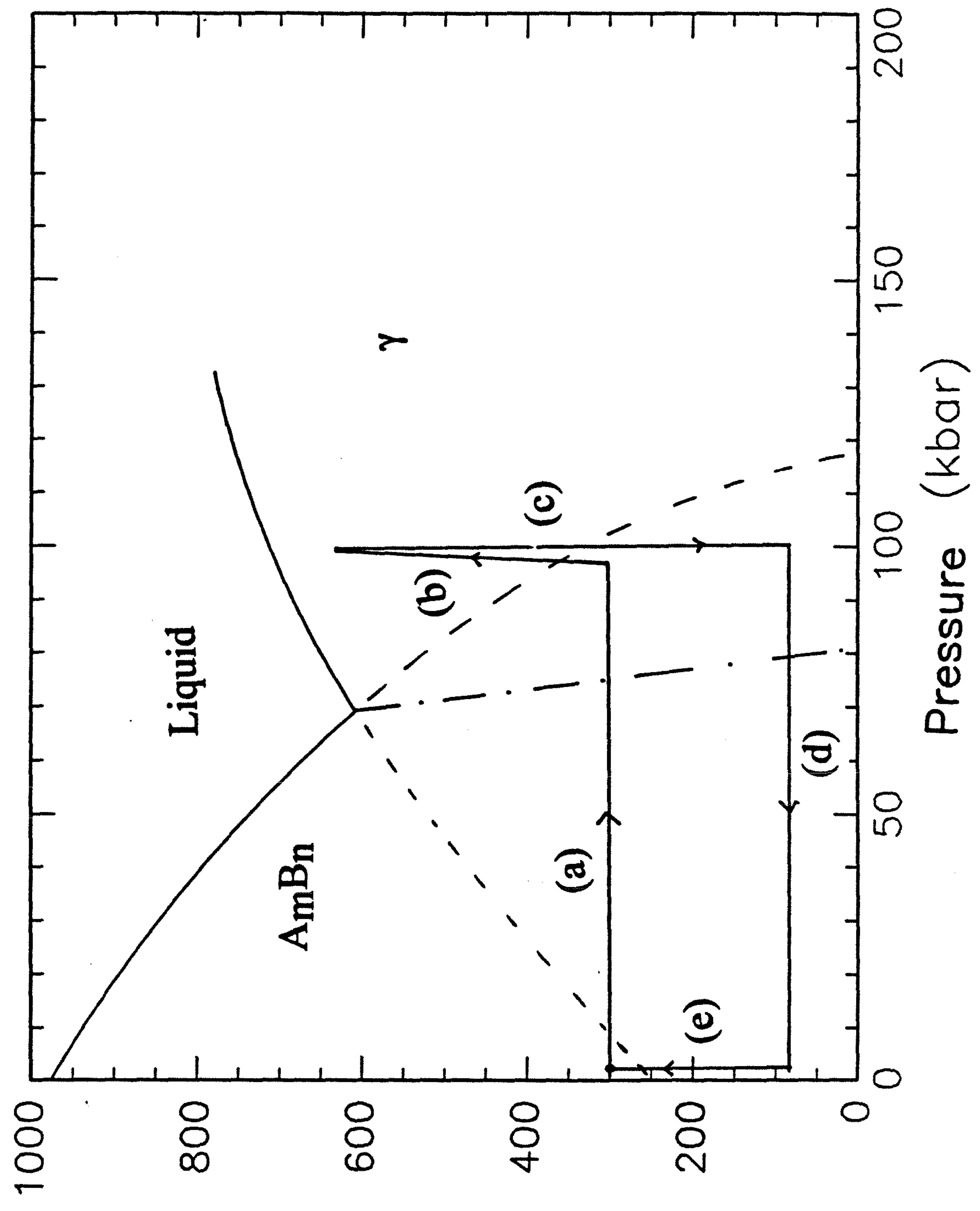

Figure 1.12 Schematic pressure-temperature phase diagram to explain the thermobaric treatment to induce amorphization proposed by Ponyatovsky et al. [65]

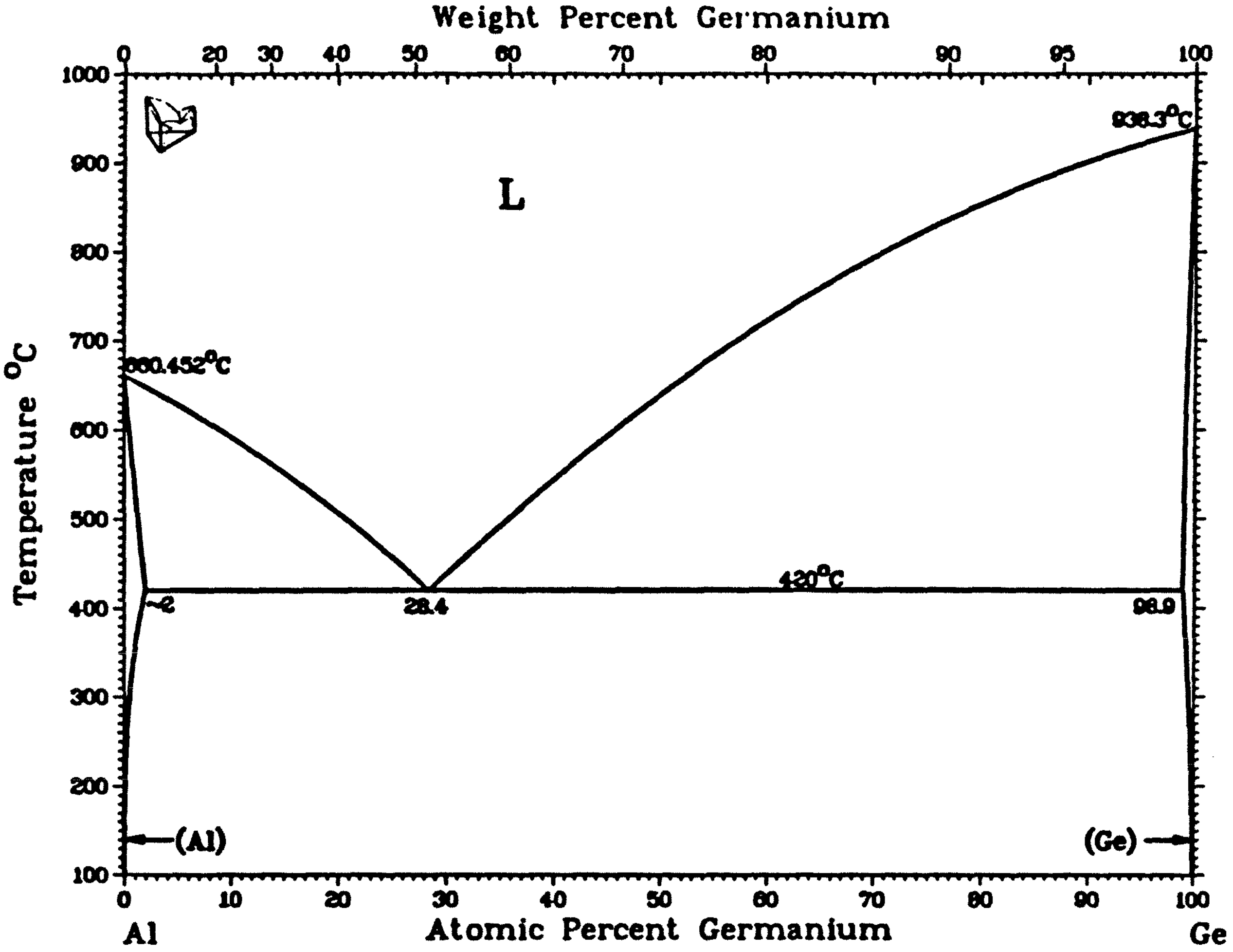

Figure 1.13 Equilibrium binary phase diagram for aluminum-germanium at ambient pressure [74].

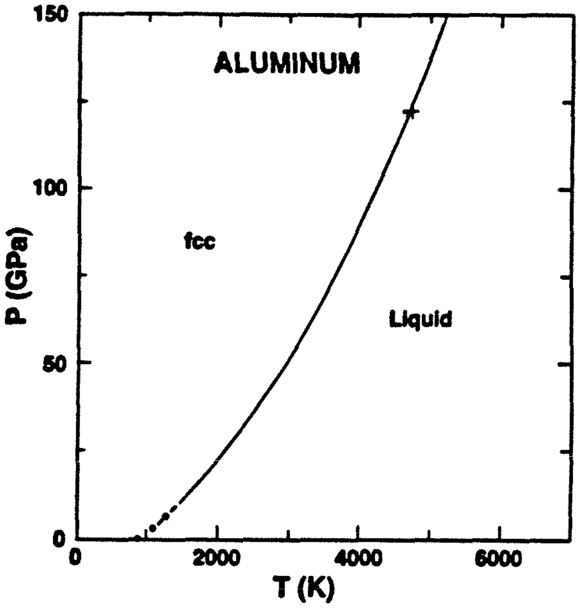

Figure 1.14 The theoretical melting curve of aluminum at high pressure. The points are low-pressure experiments and the cross is the predicted shock-Hugoniot melting point.

---

1. W. Kauzmann, *Chem. Rev.* 43, 219 (1948).
2. H.B. Callen, Thermodynamics and an Introduction to Thermostatistics (John Wiley and sons, New York, 1985).
3. W. Buckel and R. Hilsch, *Z. Physik* 138, 109 (1954).
4. W. Buckel, *Z. Physik* 138, 120 (1954).
5. D. Turnbull, *Trans. AIME* 221, 422 (1961).
6. H. S. Chen and D. Turnbull, *J. Chem. Phys.* 48, 2560 (1968).
7. W. Klement, Jr., R. H. Willens, and P. Duwez, *Nature* 187, 869 (1960).
8. P. Duwez, R. H. Willens, and W. Klement, Jr., *J. Appl. Phys.* 31, 1136 (1960).
9. W. L. Johnson, *Prog. Mater. Sci.* 30, 81 (1986).
10. K. Samwer, *Phys. Rept.* 161, 1 (1988).
11. R. B. Schwarz, J. B. Rubin, and T. J. Tiainen, Science of Advanced Material (H. Weidersich and M. Meshii, ASM International, Materials Park, Ohio), 1 (1988).
12. J. Bloch, *J. Nucl. Mater.* 6, 203 (1962).
13. G. J. C. Carpenter and E. M. Schulson, *J. Nucl. Mater.* 73, 190 (1978).
14. J. L. Brimhall, H. E. Kissinger, and L. A. Charlot, *Rad. Effects* 77, 273 (1983).
15. A. G. Cullis, J. M. Poate, and J. A. Borders, *Appl. Phys. Lett.* 28, 314 (1976).
16. B. Paine and R. Averback, *Nucl. Instrum. and Methods B* 7/8, 666 (1985).
17. S. K. Malik and W. E. Wallace, *Solid State Comm.* 24, 283 (1977).
18. X. L. Yeh, K. Samwer, and W. L. Johnson, *Appl. Phys. Lett.* 42, 242 (1983).
19. J. J. Hauser, *J. Phys. Colloq.* 42, C4-943 (1981).
20. S. R. Herd, K. N. Tu, and K. Y. Ahn, *Appl. Phys. Lett.* 42, 597 (1983).
21. S. R. Herd, K. Y. Ahn, and K. N. Tu, *Thin Solid Films* 104, 197 (1983).
22. R. B. Schwarz and W. L. Johnson, *Phys. Rev. Lett.* 51, 415 (1983).
23. R. B. Schwarz and P. Nash, *J. of Metals* 41, 27 (1989).
24. P. Nash and R. B. Schwarz, *Acta Metall.* 36, 3047 (1988).
25. R. B. Schwarz, K. L. Wong, W. L. Johnson, and B. M. Clemens, *J. Non-Cryst. Solids* 61&62,129 (1984).
26. A. Y. Yermakov, Y. Y. Yurchikov, and V. A. Barinov, *Phys. Met. Metall.* 52, 50 (1981).
27. C. C. Koch, O. B. Cavin, C. G. McKamey, and J. O. Scarbrough, *Appl. Phys. Lett.* 43, 1017 (1983).
28. R. B. Schwarz, R. R. Petrich, and C. K. Saw, *J. Non-Cryst. Sol.* 76, 281 (1985).
29. C. Politis and W. L. Johnson, *J. Appl. Phys.* 60, 1147 (1986).

---

30. R. B. Schwarz and C. C. Koch, *Appl. Phys. Lett.* 49, 146 (1985).
31. L. Schultz, *Proc. 5th Int. Conf. on Rapidly Quenched Metals* (edited by S. Steeb and H. Warlimont, North Holland, Amsterdam), 1585 (1985).
32. M. Atzmon, J. R. Veerhoven, E. R. Gibson, and W. L. Johnson, *Appl. Phys. Lett.* 45, 1052 (1984).
33. A. Blatter and M. von Allmen, *Phys. Rev. Lett.* 54, 2103 (1985).
34. A. Blatter, N. Balzer, and M. von Allmen, *J. Appl. Phys.* 62, 276 (1987).
35. Y. -G. Kim and J. -Y. Lee, *J. Non-Cryst. Solids* 122, 269 (1990).
36. R. Prasad, R. E. Somekh, and A. L. Greer, *Mater. Sci. Eng.* A133, 606 (1991).
37. W. Sinckler and D. E. Luzzi, *Acta Metal.* (submitted, 1993).
38. L. J. Gallego, J. A. Somoza, and J. A. Alonso, *Physica B* 160, 108 (1989).
39. K. Ohsaka, E. H. Trinh, J. C. Holzer, and W. L. Johnson, *Appl. Phys. Lett.* 60, (1992).
40. Z. H. Yan, T. Klassen, C. Michaelsen, M. Oehring, and R. Bormann, *Phys. Rev. B* 47, 8520 (1993).
41. P. W. Bridgman, The Physics of High Pressure (Dover, New York, 1970), chapter 1.
42. R. G. McQueen, S. P. Marsh, J. W. Taylor, J. N. Fritz, and W. J. Carter, High-Velocity Impact Phenomena (Academic, New York, 1970), chapter 7.
43. C. E. Ragan, B. C. Diven, M. Rich, and W. A. Teasdale, Shock Waves in Condensed Matter-83 (J. R. Asay, R. A. Graham, and G. K. Straub (Elsevier, Amsterdam)), 77 (1984).
44. T. J. Ahrens, *Science* 207, 1035 (1980).
45. D. A. Young, Phase Diagrams of the Elements (University of California Press, Berkeley, California, 1991).
46. J. F. Cannon, *J. Phys. Chem. Ref. Data* 3, 781 (1974).
47. C. W. F. T. Pistorius, *Prog. Solid State Chem.* 11, 1 (1976).
48. N. Kawai and Y. Inokuti, *Japan J. Appl. Phys.* 9, 31 (1970).
49. D. A. Kirzhnits, *Usp. Fiz. Nauk* 104, 489 (1971). English translation in *Sov. Phys.-Usp* 14, 512 (1972).
50. T. R McDonald, R. Sard, and E. Gregory, *Science* 147, 1441 (1965).
51. L. H Brixner, *Mater. Res. Bull.* 7, 879 (1972).
52. L. H. Brixner, P. E. Bierstedt, A. W. Sleight, and M. S. Licis, *5th Mater. Res. Soc. Symposium*, NBS Abstracts, 89 (1971).
53. I. T. Belash and E. G. Ponyatovsky, *High Temp. High Press.* 7, 523 (1975).
54. O. Mishima, L. D. Calvert, and E. Whalley, *Nature* 310, 393 (1984).

---

55. A. F. Goncharov, I. N. Makarenko, and S. M. Stishov, *Soviet Phys. JETP* 96, 380 (1989).
56. A. Goncharov, *JETP Letters* 51, 418 (1990).
57. D. R. Clarke, M. C. Kroll, P. D. Kirchner, R. F. Cook, and B. J. Hockey, *Phys. Rev. Lett.* 60, 2156 (1988).
58. D. R. Clarke, University of California Santa Barbara, private communication (1992).
59. M. Imai, T. Mitamura, K. Yaoita, and K. Tsuji, *Proceedings of the International Conference on High Pressure in Semiconductor Physics*, August 11-13, 1990, Greece.
60. E. G. Ponyatovsky, I. T. Belash, and O. I. Barkalov, *J. Non-Cryst. Solids* 117/118, 679 (1990).
61. O. I. Barkalov, I. T. Belash, and A. F. Gurov, *Phys. Stat. Sol.* 115a, K19 (1989).
62. V. F. Degtyareva, I. T. Belash, E. G. Ponyatovsky, and V. I. Rashupkin, *Soviet Phys. Solid State* 32, 834 (1990).
63. O. I. Barkalov, I. T. Belash, V. F. Degtyareva, and E. G. Ponyatovsky, *Soviet Phys. Solid State* 29, 1138 (1987).
64. E. G. Ponyatovsky, *Proceedings of the 5th International Conference on Non-Equilibrium Solid Phases of Metals and Alloys, Suppl. Trans. Japan. Inst. Met.* 29, 111 (1988).
65. E. G. Ponyatovsky and O. I Barkalov, *Mat. Sci. Rept.* 8, 147 (1992).
66. A. M. Durachenko, V. A. Zhorin, and E. Ya. Malinochka, *Metallofizika Kiev* 8, 105 (1986).
67. F. Dachille and R. Roy, *Abstracts of the 4th Annual Meeting of the Geological Society of America*, 34 (1962).
68. Y. Fujii, M. Kowaka, and A. Onadera, *J. Phys. C* 18, 789 (1985).
69. V. V. Braschkin and S. V. Popova, *J. Less-Common Met.* 138, 39 (1988).
70. H. Sankaran, S. K. Sikka, S. M. Sharwa, and R. Chidambaram, *Phys. Rev. B* 38, 170 (1988).
71. Y. Akahama, Y. Mori, M. Kobayashi, H. Kawamura, K. Kimura, and S. Takeuchi, *J. Phys. Soc. Japan* 58, 2231 (1989).
72. S. L. Chaplot and R. Mukhopadhyay, *Phys. Rev.* 33, 5099 (1986).
73. R. R. Winters, and W. S. Hammack, *Science* 260, 202 (1993).
74. A. J. Mc Alister and J. L. Murray, *Bull. Alloy Phase Diag.* 5, 341 (1984).
75. U. Koster, *Z. Metallk.* 63, 472 (1972).
76. U. Koster, *Acta Met.* 20, 1361 (1972).

---

77. I. V. Salli and A. K. Kushnereva, *Akad. Nauk. Ukrain. SSR, Metallofizika* 27, 189 (1970); also *Izv. Akad. Nauk. SSR, Neorg. Materialy* 6, 1867 (1970).
78. P. Ramachandrao, M. Laridjani, and R. W. Cahn, *Z. Metallk.* 63, 43 (1972).
79. M. G. Scott, *Z. Metallk.* 65, 563 (1974).
80. C. Suryanarayana and T. R. Anantharaman, *J. Mater. Sci.* 5, 992 (1970).
81. P. Ramachandrao, M. G. Scott, and G. A. Chadwick, *Phil. Mag.* 25, 961 (1972).
82. M. Laridjani and R. W. Cahn, *Mat. Sci. Eng.* 23, 125 (1976).
83. M. Laridjani, K. D. Krishnanand, and R. W. Cahn, *J. Mater. Sci.* 11, 1643 (1976).
84. M. J. Kaufman and H. L. Fraser, *Mat. Sci. Eng.* 57, L17 (1983).
85. M. J. Kaufman and H. L. Fraser, *Metall. Trans. A* 14, 623 (1983).
86. M. J. Kaufman and H. L. Fraser, *Acta Metall.* 33, 191 (1985).
87. V. T. Swamy, K. Chattopadhyay, and S. Ranganathan, *Mater. Sci. Eng.* A123, 247 (1990).
88. L. A. Zhurova, S. I. Popel, and S. R. Shagapova, *Isv. Akad. Nauk.SSSR Metally* 2, 100 (1991).
89. C. Suryanarayana and T. R. Anantharaman, *Z. Metallkde.* 64, 800 (1973).
90. Eugene P. Bertin, Principles and Practice of X-ray Spectrometric Analysis (Plenum, New York, 1975).
91. P. J. Yvon and R. B. Schwarz, *J. Mater, Res.* 8, 239 (1993).
92. P. Ramachandrao, M. Laridjani, and R. W. Cahn, *Z. Metallkde* 63, 43 (1972).
93. P. Nath, S. K. Barthwal, and K. L. Chopra, *Solid State Comm.* 16, 301 (1975).
94. H. S. Randhawa, P. Nath, L. K. Malhotra, and K. L. Chopra, *Solid State Comm.* 20, 73 (1976).
95. H. S. Randhawa, L. K. Malhotra, and K. L. Chopra, *J. Non-Crystalline Solids* 29, 311 (1978).
96. P. Nath, V. Dutta, and K. L. Chopra, *Thin Film Solids* 64, 65 (1979).
97. M. Krapp, A. Lambrecht, and J. Hasse, *Z. Phys. B* 61, 167 (1985).
98. F. Catalina, C. N. Afonso, E. Rollan, and C. Ortiz, *J. Less-Common Met.* 145, 209 (1988).
99. F. Catalina, C. N. Afonso, and C. Ortiz, *Thin Solids Films* 167, 57 (1988).
100. T. Okabe, S. Endo, and S. Saito, *J. Non-Crystalline Solids* 117/118, 222 (1990).
101. C. N. Afonso, F. Catalina, and J. Solis, *Mater. Sci. Eng.* B7, 169 (1990).
102. C. D. Adams, M. Atzmon, Y-T. Cheng, and D. J. Srolovitz, *J. Mater. Res.* 7, 653 (1992).
103. J. Lees and B. H. J. Williamson, *Nature* 208, 278 (1965).

---

104. A. K. McKahan and J. A. Moriarty, *Phys. Rev. B* 27, 3235 (1983).

105. P. K. Lam and M. L. Cohen, *Phys. Rev. B* 27, 5986 (1983).

106. O. Fürst, R. Glocker, and H. Richter, *Z. Naturforschg.* 4a,540 (1949).

107. H. Richter and O. Fürst, *Z. Naturforschg.* 6A, 38 (1951).

108. H. Richter and G. Breitling, *Z. Naturforschg.* 13a, 988 (1958).

109. D. E. Polk, *J. Non-Crystalline Solids* 5, 365 (1971).

110. N. J. Shevchik and W. Paul, *J. Non-Crystalline Solids* 8-10, 381 (1972).

111. K. L. Chopra, P. Nath, and A. C. Rastogi, *Phys. Stat. Sol.* 27a, 645 (1975).

112. K. L. Chopra, H. S. Randhawa, and L. K. Malhotra, *Thin Solids Films* 47, 203 (1977).

113. G. Etherington, A. C. Wright, J. T. Wenzel, J. C. Dore, J. H. Clarke, and R. N. Sinclair, *J. Non-Crystalline Solids* 48, 265 (1982).

114. C. S. Menoni, J. Z. Hu, and I. L. Spain, *Phys. Rev. B* 34, 362 (1986).

115. Y. K. Vohra, K. E. Brister, S. Desgreniers, A. L. Ruoff, K. J. Chang, and M. L. Cohen, *Phys. Rev. Lett.* 56, 1944 (1986).

116. K. J. Chang and M. L. Cohen, *Phys. Rev. B* 34, 8581 (1986).

117. R. Nelmes, University of Edinburgh, private communication.

118. F. P. Bundy and J. S. Kasper, *Science* 139, 340 (1963).

119. C. H. Bates, F. Dachille, and R. Roy, *Science* 147, 860 (1965).

120. J. B. Clark and C. W. F. T. Pistorius, *J. Less-Common Met.* 34, 233 (1974).

121. W. Hume-Rothery, G. W. Mabbott, and K. M. Channel Evans, *Phil. Trans. Roy. Soc.* 233, 1 (1934).

122. V. F. Degtyareva, G. V. Chipenko, I. T. Belash, O. I. Barkalov, and E. G. Ponyatovskii, *Phys. Stat. Sol. (a)* 89, K127 (1985).

123. V. F. Degtyareva, G. V. Chipenko, E. G. Ponyatovsky, and V. I. Rashchupkin, *Sov. Phys. Solid State* 26, 733 (1984).

2. MODELING OF THE ALUMINUM-GERMANIUM PHASE DIAGRAM UNDER PRESSURE

In this section we discuss the thermodynamic modeling of the aluminum-germanium binary phase diagram. We first model the binary phase diagram at room pressure, and then model the influence of pressure on this phase diagram. Using calculations and experimental data we construct tentative phase diagrams of aluminum-germanium at different pressures. We then use these diagrams to explain the different approaches to amorphization that can be used in this alloy system.

2.1 T_0-Curves in the Aluminum-Germanium Alloy System

The free energies of the phases are described by the Calphad model [1]:

$$\begin{aligned} G^i &= {}^oG^i_{Al}\,(1-x) + {}^oG^i_{Ge}\,x + RT(xLnx + (1-x)Ln(1-x)) \\ &+ x(1-x)[A^i + B^i\,(1-2x) + C^i\,(1-6x-6x^2)] \end{aligned} \tag{2.1}$$

${}^oG^i_{Al}$ and ${}^oG^i_{Ge}$ are the lattice stabilities of the pure elements, x the atomic fraction of germanium, and A^i, B^i, and C^i are temperature-dependent parameters that describe the excess free energy of phase i. The polynomial expansion in the last bracket in Eq. 2.1 is commonly used but any polynomial second order polynomial expansion would give similar results. The lattice stabilities of aluminum and germanium were taken from Ansara et al. [2] and McAlister and Murray [3] and are given in Table 2.1. The computer program used to perform the calculations is found in Appendix B. The modeled phase diagram appears quite accurate as shown in Figure 2.1. We also calculated the T_0-lines (loci of the compositions and temperature at which the free energies of the liquid and of the crystalline phases are equal) and compared our calculations with the T_0-line on the aluminum-rich side calculated by Ishihara and Shingu [4], using a different program and only the thermodynamic data of Ansara [2]. Their T_0-line was shifted to the right, but this is probably due to the fact that the solidus was poorly modeled in their model. The actual T_0-lines are probably closer to the solidus lines than those we calculated, as there is a fairly broad glass forming range by rapid solidification.

2.2. Pressure Effects on the Aluminum-Silicon Binary Phase Diagram: Thermodynamic Modeling

We will construct the phase diagram for aluminum-germanium under pressure following the approach of Shinyaev et al. [5]. Before attempting to do so, we first reproduced their results for the aluminum-silicon system. The approximation of regular solution is used to evaluate thermodynamic functions [6].

$$E^i = (1-x)\,E^i_A + x\,E^i_B + x(1-x)\,E^i_m \tag{2.2}$$

$$S^i = (1-x)\,S^i_A + x\,S^i_B - k[x\mathrm{Ln}x + (1-x)\mathrm{Ln}(1-x)] \tag{2.3}$$

where x is the atomic fraction of component B; E^i_A and E^i_B are the atomic energies of components A and B in phase i; E^i_m, the energy of mixing,; k, the Boltzman's constant; and S^i_A and S^i_B the atomic entropies of components A and B in phase i

The volume V is expressed as

$$V^i = (1-x)\,V^i_A + x\,V^i_B + x(1-x)\,V^i_m \tag{2.4}$$

where V^i_A and V^i_B are the volumes of the components, and V^i_m, the change of volume accompanying mixing of the elements, all in phase i.

The Gibb's free energy function can be written as

$$G = E - T\,S + P\,V \tag{2.5}$$

$$\begin{aligned}G = (1-x)\,E_A + x\,E_B + x(1-x)E_m - T\,[(1-x)\,S_A + x\,S_B \\ -k(x\mathrm{Ln}x + (1-x)\mathrm{Ln}(1-x))] + P\,[(1-x)\,V_A + x\,V_B + x(1-x)\,V_m]\end{aligned} \tag{2.6}$$

We are going to use α and β to denote the two different phases, and x_α and x_β will denote the composition of component B in the two phases. The conditions of thermodynamic equilibrium between the two phases can be written as

$$\left.\frac{\partial G^\alpha}{\partial x}\right|_{x=x_\alpha} = \left.\frac{\partial G^\beta}{\partial x}\right|_{x=x_\beta} \tag{2.7}$$

$$G^\alpha - x_\alpha \left.\frac{\partial G^\alpha}{\partial x}\right|_{x=x_\alpha} = G^\beta - x_\beta \left.\frac{\partial G^\beta}{\partial x}\right|_{x=x_\beta} \tag{2.8}$$

These conditions can be easily deduced with the help of Figure 2.2. Using (2.8) and (2.6), we obtain:

$$T = \frac{x_\alpha{}^2(E_m^\alpha + P\,V_m^\alpha) - x_\beta{}^2(E_m^\beta + P\,V_m^\beta) + (T_A\,\Delta S_A + P\,\Delta V_A)}{\Delta S_A - R\,\mathrm{Ln}(\frac{1-x_\alpha}{1-x_\beta})} \tag{2.9}$$

and using (2.7) and (2.9):

$$T = \frac{(1-x_\alpha)^2(E_m^\alpha + P\,V_m^\alpha) - (1-x_\beta)^2(E_m^\beta + P\,V_m^\beta) + (T_B\,\Delta S_B + P\,\Delta V_B)}{\Delta S_B - R\,\mathrm{Ln}(\frac{x_\alpha}{x_\beta})} \tag{2.10}$$

where T_A and T_B are the transition temperatures from phase α to phase β of the components A and B, ΔV_A and ΔV_B are the change of volume for components A and B at the phase transition, and ΔS_A and ΔS_B are the entropy changes at the phase transition.

For a given pressure, these relations define a simple diagram as schematically shown in Figure 2.3. Here A and B are assumed to have the same structure, and they form a continuous solid solution (Phase II). To obtain the phase diagram of aluminum-silicon (Figure 2.4a), three simple diagrams are used (Figures 2.4b, 2.4c, and 2.4d). To simplify the equations, the solubility of aluminum in silicon is taken to be zero. In this case the equations (2.9) and (2.10) become:

$$T = \frac{(1 - x_\alpha)^2 (E_m^\alpha + P\, V_m^\alpha) + T_B\, \Delta S_B + P\, \Delta V_B}{\Delta S_B - R\, \mathrm{Ln}(x_\alpha)} \tag{2.11}$$

$$x_\beta = 1 \tag{2.12}$$

In this approach, the parameters E_m, ΔV, ΔS, V_m are independent of pressure and temperature. The calculations were also based on the assumption that $V_m^\alpha = V_m^\beta = 0$ [7]. The values used to model this phase diagram are summarized in tables 2.2 and 2.3. First, the parameters E_m, $T_{Si}^{fcc \to liq}$, and $T_{Si}^{fcc \to diam}$ were determined at $P = 0$. The liquid-silicon equilibrium (figure 4b) was first used to obtain E_m^{liq} by using equation (2.11) for the eutectic point. Then, using E_m^{liq} and equation (2.9) for the aluminum-liquid equilibrium (figure 4c), we derived E_m^{Al}. S_A was assumed to be equal to S_B [7,8]. Then, using equation (2.10), $T_{Si}^{fcc \to liq}$is obtained. The lattice stability for fcc silicon [9] was used to determine $T_{Si}^{fcc \to diam}$. Then we used the equilibrium between fcc aluminum and diamond-silicon (figure 2.4d) to determine ΔS_C (entropy of transformation between diamond-silicon and fcc silicon), knowing the solubility at the eutectic temperature. Using more recent values than in Shinyaev 's work, we obtained a good model of the room pressure binary phase diagram of aluminum-silicon, as shown in Figure 2.5.

To obtain the pressure effects on the phase diagram, we need to know the changes of volume at the phase transitions. The changes upon melting for f.c.c. aluminum and diamond-structured silicon are known experimentally [10-15]. Because f.c.c. silicon or diamond-structured aluminum have never been obtained, experimental data were not available for the volume change on melting of these phases. The volume change for the f.c.c. to diamond transformation in silicon is also unknown. We estimated these volume changes using thermal expansion coefficients and atomic radii, and the results are given in Tables 2.2 and 2.3.

We modeled the aluminum-silicon binary phase diagram for different pressures, up to 120 kbar, the pressure at which diamond-silicon transforms to the β white-tin structure. The program used to model these phase diagrams is given in Appendix C. All available data on the aluminum-silicon system under pressure [16,17,18] was compared to our model. The phase diagram for P = 54 kbar (5.4 GPa) is shown in Figure 2.6. The figure also shows experimental data from Mii et al. [17]. The agreement with the liquidus is good, less so with the solidus and serious disagreement with the solvus. The pressure dependence of the solubility of silicon in aluminum deduced from this model is summarized in Table 2.4 together with available data.

2.3. Pressure Effects on the Aluminum-Germanium Binary Phase Diagram: Thermodynamic Modeling

The aluminum-germanium system is more difficult to model than the aluminum-silicon system because aluminum has a non-negligible solubility in germanium and because not many experimental data are available on the behavior of aluminum-germanium under pressure. Four simple equilibrium phase diagrams were combined as shown in Figure 7 to obtain the aluminum-germanium binary phase diagram as shown in Figure 2.8. Once again the first step was to obtain the modeling parameters at room pressure, using the invariant points of the equilibrium phase diagram. The parameter values used for this phase diagram are summarized in Tables 2.2 and 2.5.

The melting temperature of germanium in the f.c.c. structure, $T_{Ge}^{fcc\rightarrow liq}$, was determined using lattice stabilities. Then, the aluminum-liquid equilibrium diagram (figure 2.7b) was used to find E_m for the liquid and the aluminum phase. We used the eutectic point (693 K, x = .289, y = .989) to obtain E_m^{liq} and E_m^{Al} from equations (2.9) and

(2.10). Then E_m^{Ge} and the melting temperature of diamond-aluminum, $T_{Al}^{diam \to liq}$, were obtained using equations (2.9) and (2.10) for the germanium-liquid equilibrium phase diagram (Figure 2.7a). The lattice stability of f.c.c. germanium was used to obtain the transition temperature between diamond-germanium and f.c.c. germanium, $T_{Ge}^{fcc \to diam}$. Then, using equation (2.11) for the aluminum-germanium equilibrium (figure 2.7c), ΔS is obtained for the f.c.c. germanium to diamond-germanium transformation. Finally, using this ΔS and equation (2.11) for the germanium-aluminum equilibrium (figure 2.7d), we obtained the temperature for the f.c.c. aluminum to diamond-aluminum, $T_{Al}^{fcc \to diam}$. The fit to the phase diagram at room pressure is shown in figure 2.8. The dashed lines in Fig 2.8 show the modeled phase diagram. The solid lines in this figure are the assessed experimental phase diagram [3]. The agreement is quite good.

Pressure is introduced into the model by using measured and estimated changes of volume during phase transitions. The volume changes upon melting for f.c.c. aluminum and diamond-germanium have been measured [19,11,14]. As for the aluminum-silicon system, we use lattice stabilities and thermal expansion coefficients to estimate the volume changes at the phase transitions in the aluminum-germanium system. The estimated values are close to the values estimated recently by Minamino et al. [20] from similar considerations. They also used a regular solution model to estimate the solidus of the aluminum-rich side of the binary phase diagram and compare it to experimental solidus points they obtained at 22 and 26 kbar (respectively 2.2 and 2.6 GPa). The computer program we used to model aluminum-germanium under pressure is given in appendix D. The modeled phase diagram at 90 kbar is plotted in figure 2.9. Figure 2.10 compares the pressure dependence of the eutectic temperature predicted by our model and the experimental data from Clarke and Pistorius [21], Banova et al. [22], and Minamino et al. [20] on the behavior of the eutectic temperature under pressure.

Ponyatovsky and coworkers [23] used experimental data on the aluminum-germanium system [18,24] to construct a tentative binary phase diagram at 90 kbar (9 GPa). The data included for this estimate was the melting temperature of the pure elements, their mutual solubility, and the existence and composition of a hexagonal γ phase. On comparing Ponyatovsky's phase diagram (Figure 2.11) with our modeled diagram (2.10), we notice: (a) The solubility predicted by our model is slightly higher and (b) the eutectic temperature predicted by our model is higher. We are going to use the phase diagram we modeled because we believe it is more consistent with the experimental data obtained.

2.4. Proposed Thermobaric Treatments to Induce Crystal-to-Glass Transformations in Aluminum-Germanium Alloys

The aluminum-germanium phase diagram in Figure 2.10 will be used in this section to propose thermobaric treatments that should lead to amorphization. One such treatment seemed to be particularly promising for preparing amorphous alloys.

This thermobaric treatment is described with the help of Figure 2.12. The average composition of the two-phase aluminum-germanium $Al_{1-x}Ge_x$ is outside the T_0-line at room temperature and pressure (Point A). This is to ensure that an f.c.c. Al(Ge) solid solution would be unstable under these conditions. The first step is to bring the sample to a pressure at which the maximum solubility of germanium in aluminum is greater than x (Point B). Then the temperature is raised to obtain a homogeneous solid solution (Point C). Notice that the annealing temperature is close to the eutectic temperature where the solubility is maximum. The sample is then quenched to a cryogenic temperature (Point D), and the solid solution is retained. The pressure is released at low temperature. During the pressure release, the T_0 surface (locus of the compositions, pressures and temperatures at which the free energies of the liquid and crystalline phases are equal) is crossed, and the f.c.c. solid solution becomes unstable. The sample is expected to melt, but since the temperature is below the glass transition temperature, the sample should become amorphous. There is also a large driving force for the sample to transform to the equilibrium mixture of f.c.c. aluminum and diamond-germanium. This transformation, however, requires phase separation and long-range diffusion, which is prevented by kinetics.

Table 2.1. Thermodynamic and Lattice Stability Parameters (J/mol)

${}^{o}G_{Al}^{liq}$	0
${}^{o}G_{Ge}^{liq}$	0
${}^{o}G_{Al}^{Al}$	-10711+11.56 T
${}^{o}G_{Ge}^{Al}$	5021+8.368 T
${}^{o}G_{Al}^{Ge}$	30 T
${}^{o}G_{Ge}^{Ge}$	-36954+30.51 T
A^{liq}	-11482.3-4.732 T
B^{liq}	-418.4-0.334 T
C^{liq}	3035.8-1.556 T
A^{Al}	-4979.6-4.732 T
B^{Al}	426.5
C^{Al}	660.6
A^{Ge}	10758.4-12.599 T
B^{Ge}	-329.3
C^{Ge}	58.9

Table 2.2. Values used for aluminum

Lattice Stabilities: $G_{liq} - G_{fcc} = 11005.028 - 11.841867.T + 7.934.10^{-20}.T^{7}$

Entropy of Melting: $\Delta S_{m} = 11.474\ J/mol$

	Liquid	f.c.c.	Diamond
Molar Volume (cm^3/mol)	11.313	9.91	13.0
Density (g/cm^3)	2.385		
∂D/∂T (mg/cm^3.K)	-0.28		
Thermal Expansion (10^{-6} K^{-1})		23.5	
Compressibility (10^{-11} Pa^{-1})	2.14	1.68	1.32

$\Delta V_{liq \to fcc} = 0.64\ cm^3/mol$

$\Delta V_{liq \to diam.} = -3\ cm^3/mol$

$\Delta V_{fcc \to diam.} = -3.09\ cm^3/mol$

Table 2.3. Values used for silicon

Lattice Stabilities: $G_{liq} - G_{diam} = 50696.36 - 30.099439.T + 2.0931.10^{-21}.T^7$

$$G_{fcc} - G_{diam} = 51000 - 21.8.T$$

Entropy of Melting: $\Delta S_m = 29.7617\ J/mol$

	Liquid	f.c.c.	Diamond
Molar Volume (cm^3/mol)	11.1873		12.00
Density (g/cm^3)	2.51		
∂D/∂T (mg/cm^3.K)	-0.32		
Thermal Expansion (10^{-6} K^{-1})			7.6
Compressibility (10^{-11} Pa^{-1})			1.0235

$\Delta V_{liq \to fcc} = 2.01\ cm^3/mol$

$\Delta V_{liq \to diam.} = -1.12\ cm^3/mol$

$\Delta V_{fcc \to diam.} = -3.14\ cm^3/mol$

Table 2.4. Comparison of our model with other models and experiments. Solubility of silicon in f.c.c. aluminum with pressure (at. %)

Pressure (kbar)	Yvon	Shynaev	Mii	Fujishiro	Degtyareva
0.001	1.60	1.59			
10	2.97	3			
25	4.93	5			
28	5.35			10	
50	8.98	9			
54	10.00		17.5		
70	12.60				>12
90	15.80				>18
100	17.90				20

Table 2.5. Values used for germanium

Lattice Stabilities: $G_{liq} - G_{diam} = 37141.49 - 30.687044\ T + 8.5663\ 10^{-21}\ T^7$

$$G_{fcc} - G_{diam} = 36000 - 23.5\ T$$

Entropy of Melting: $\Delta S_m = 30.4975\ J/mol$

	Liquid	f.c.c.	Diamond
Molar Volume (cm^3/mol)	12.96	8.737	13.63
Density (g/cm^3)	5.60		
∂D/∂T (mg/cm^3.K)	-0.625		
Thermal Expansion (10^{-6} K^{-1})			5.75
Compressibility (10^{-11} Pa^{-1})	1.83	1.68	1.32

$\Delta V_{liq \to fcc} = 3\ cm^3/mol$

$\Delta V_{liq \to diam.} = -0.6949\ cm^3/mol$

$\Delta V_{fcc \to diam.} = -4.89\ cm^3/mol$

Table 2.6. Comparison of our model with other models and experiments. Solubility of germanium in f.c.c. aluminum with pressure (at. %)

Pressure (kbar)	Yvon	Banova	Minamino	Degtyareva
0.001	2.6	2.8	2.6	
20	5.2	7.3		
22	5.6		5.7	
26	7.2		6.8	
70	19			>15
100	27			>18

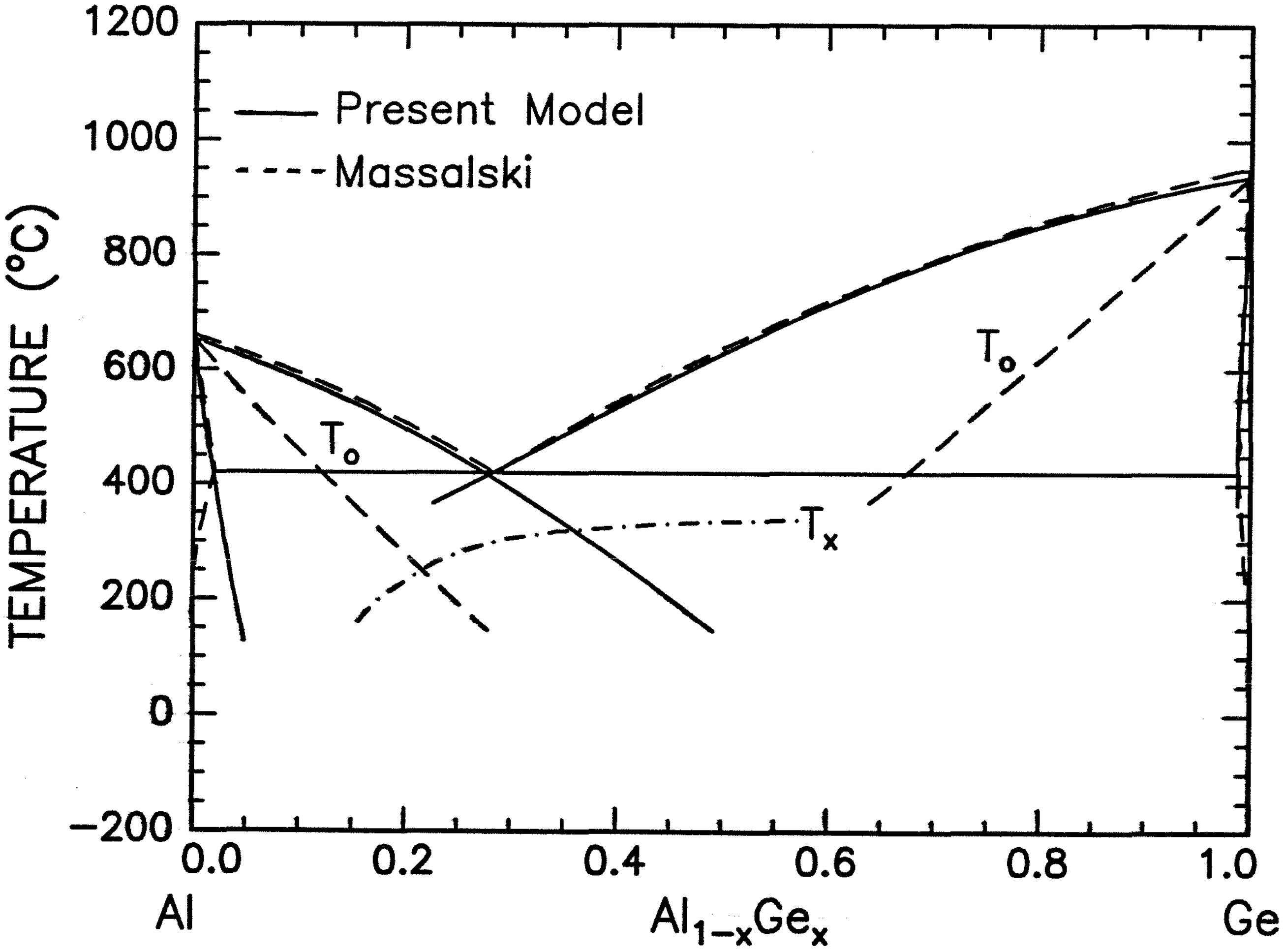

Figure 2.1 Fit of the aluminum-germanium binary phase diagram using the CALPHAD approach.

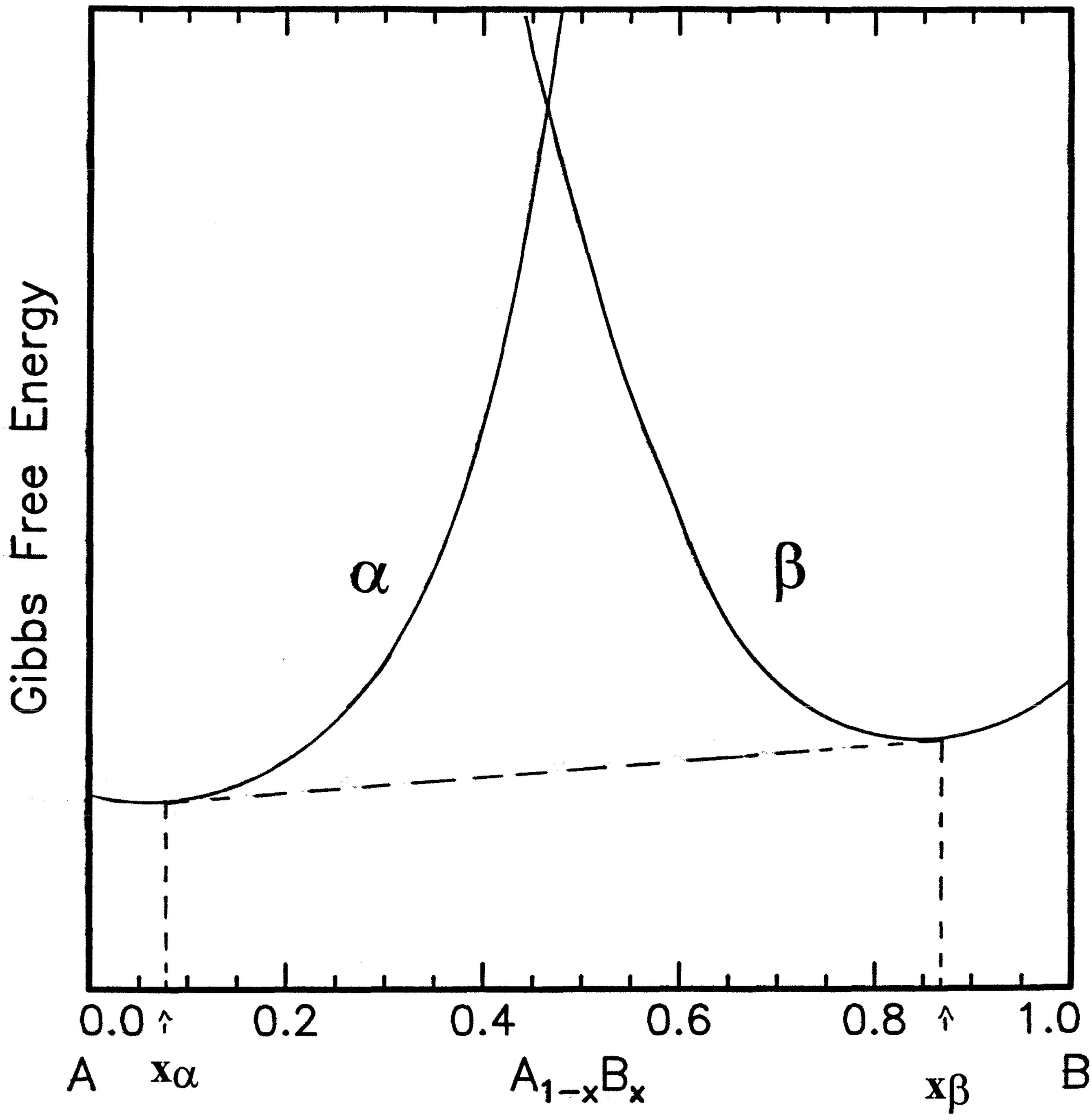

Figure 2.2 Schematic free energy-composition diagram expressing the thermodynamic equilibrium between phases α and β, at compositions x_{α} and x_{β}.

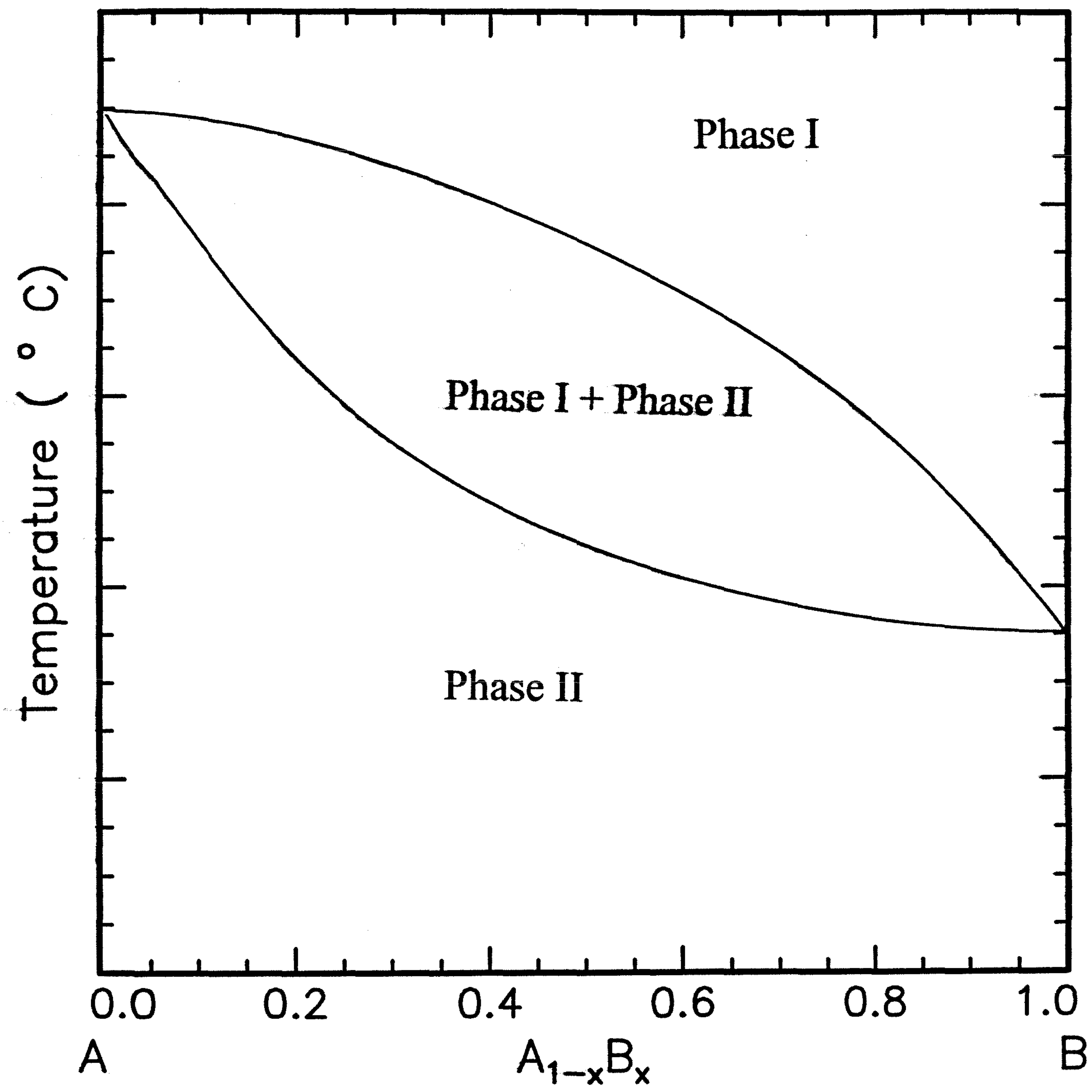

Figure 2.3 Simple two-phase equilibrium diagram.

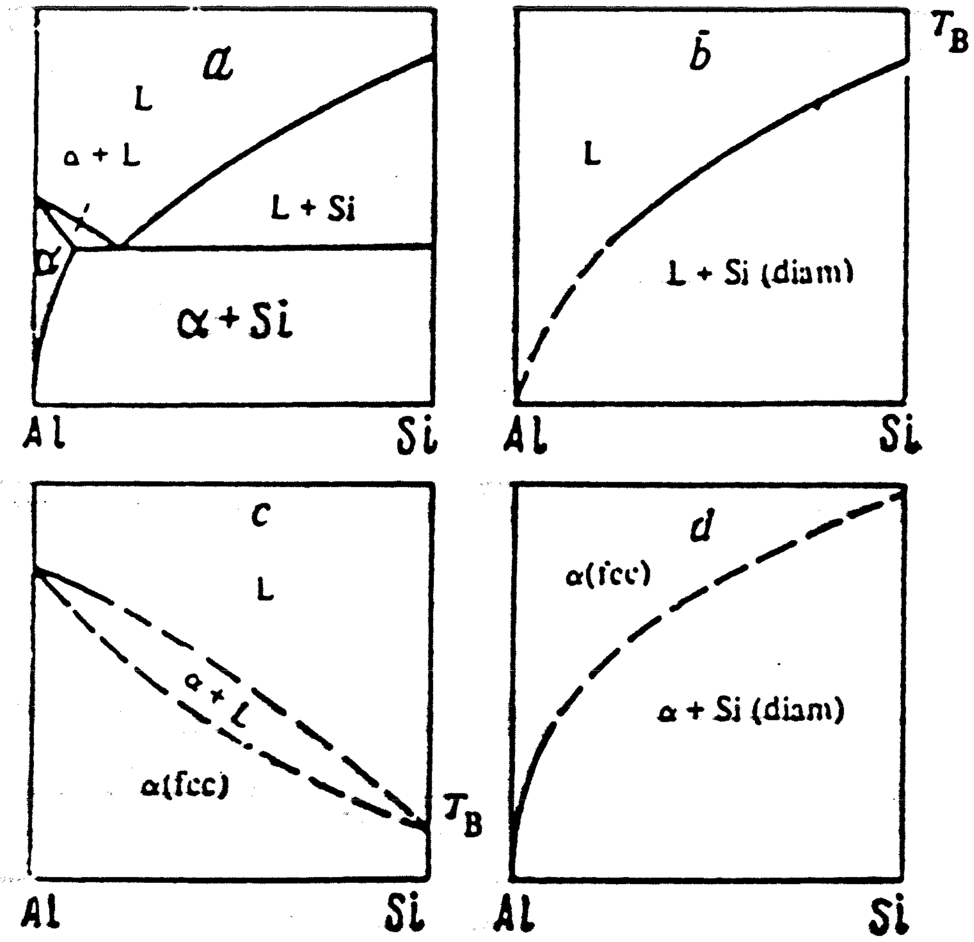

Figure 2.4 Elementary Equilibrium Diagrams used to model the aluminum-silicon binary phase diagram [5].

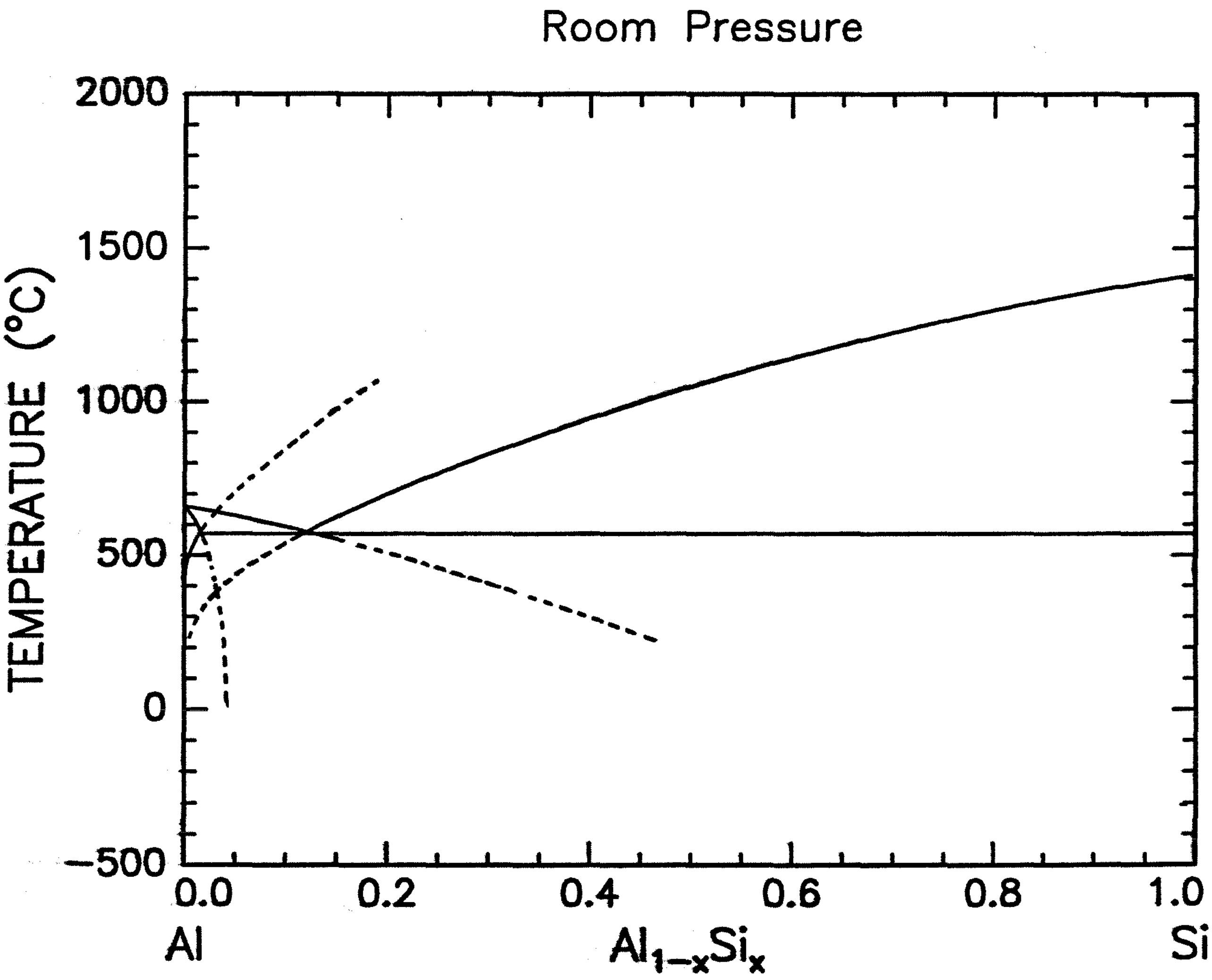

Figure 2.5 Fit of the aluminum-silicon at ambient pressure.

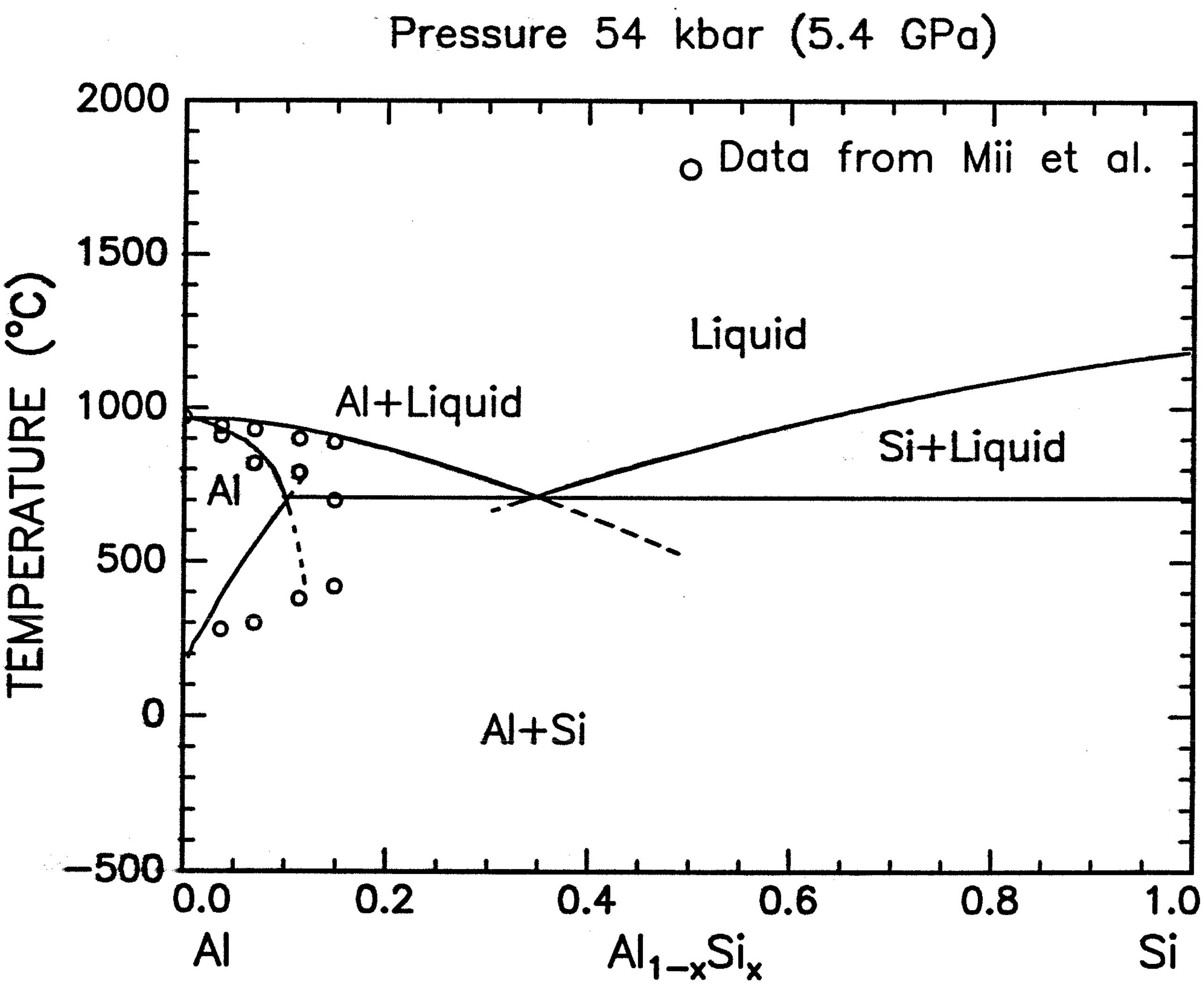

Figure 2.6 Fit of the aluminum-silicon binary phase diagram at 54 kbar.

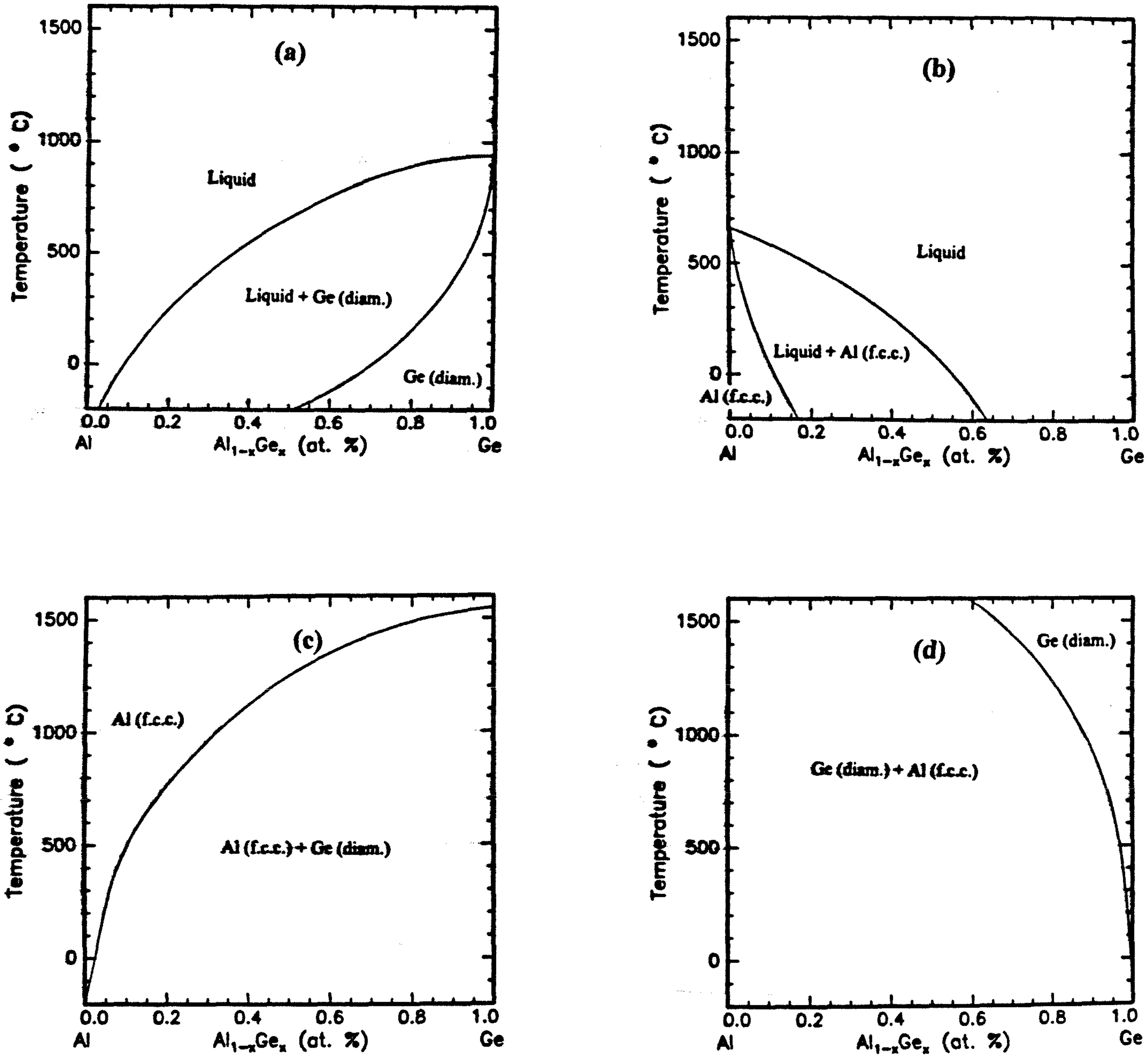

Figure 2.7 Elementary equilibrium phase diagram used to model the aluminum-germanium binary phase diagram.

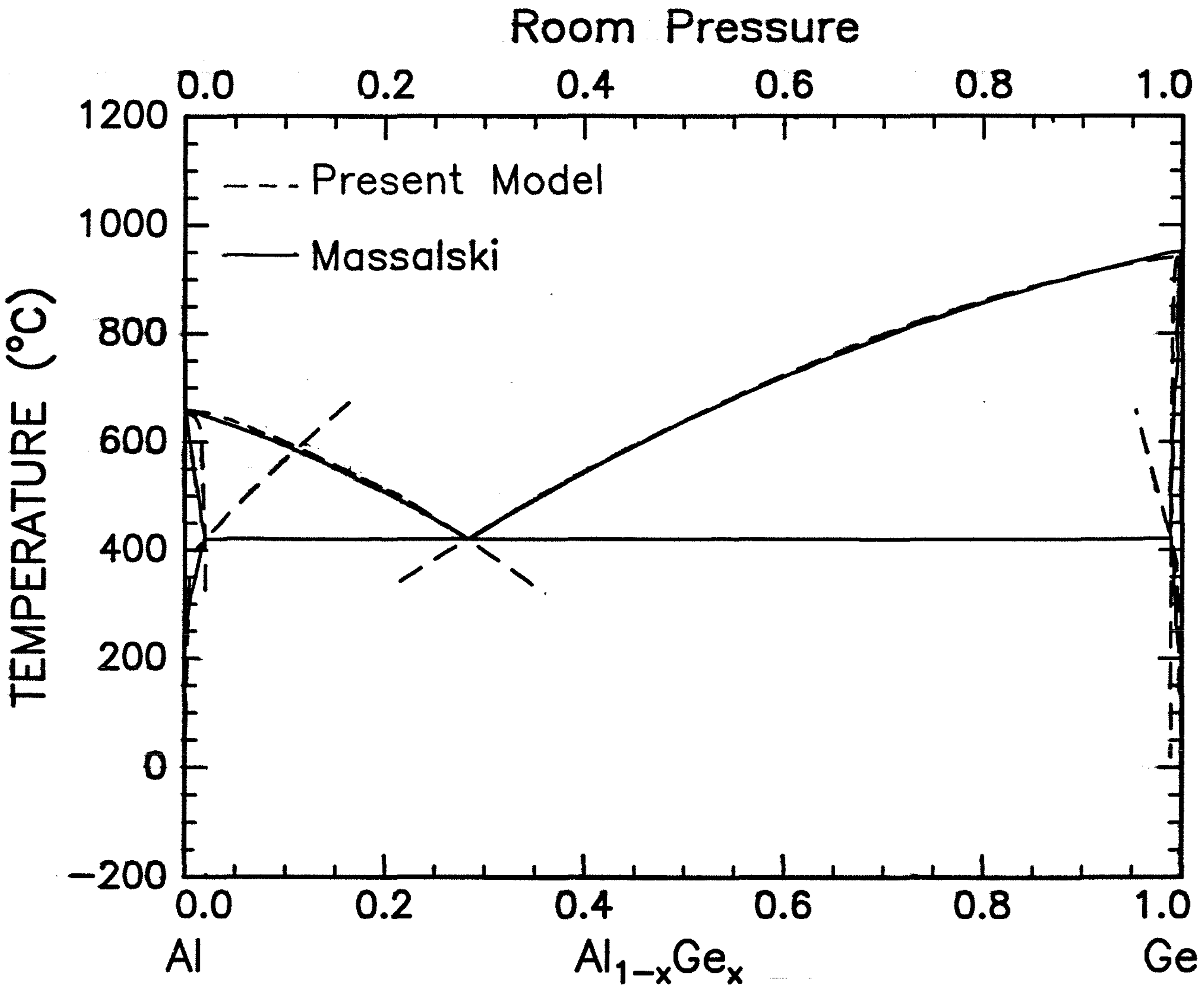

Figure 2.8 Fit of the aluminum-germanium binary phase diagram at ambient pressure.

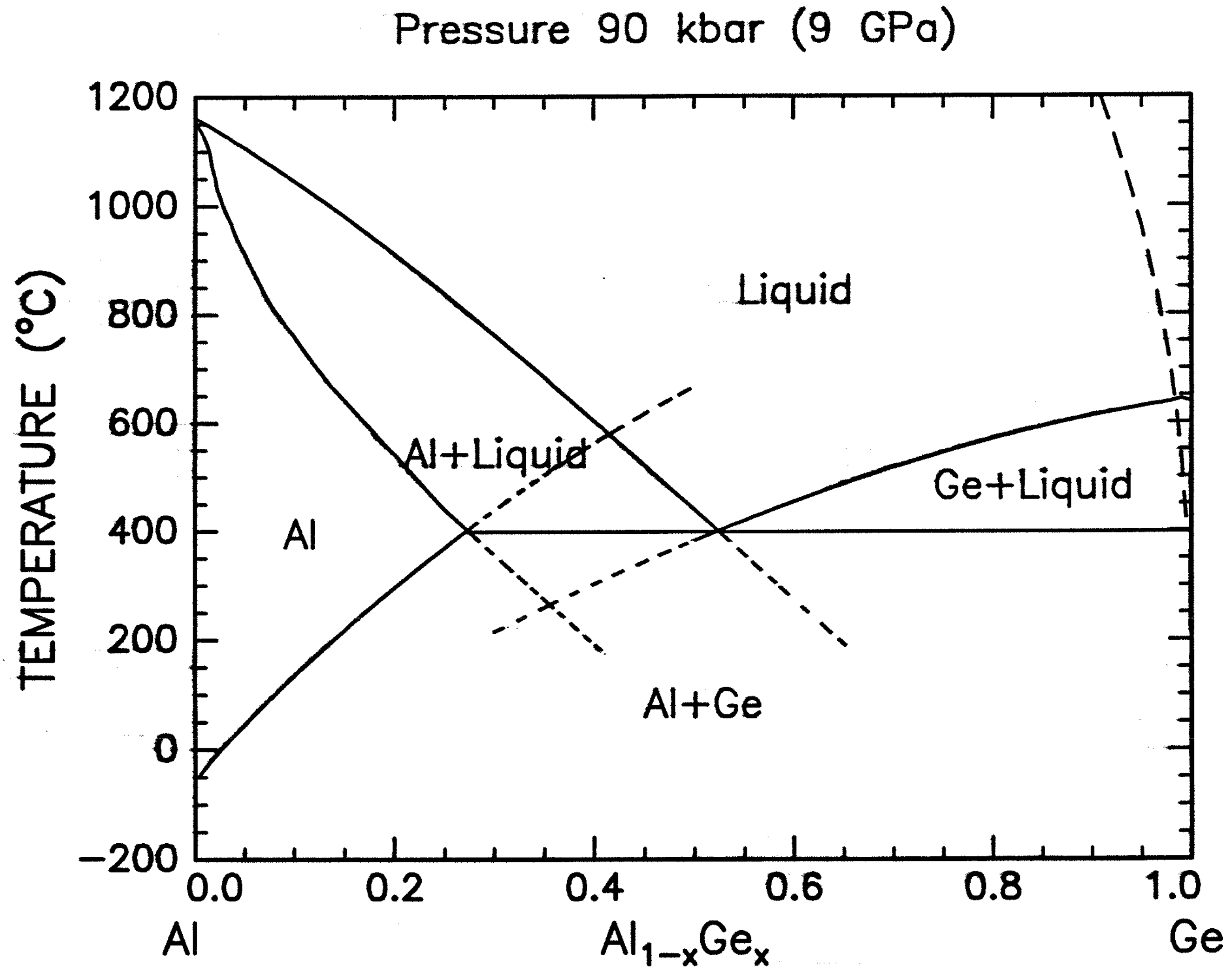

Figure 2.9 Fit of the aluminum-germanium binary phase diagram at 90 kbar.

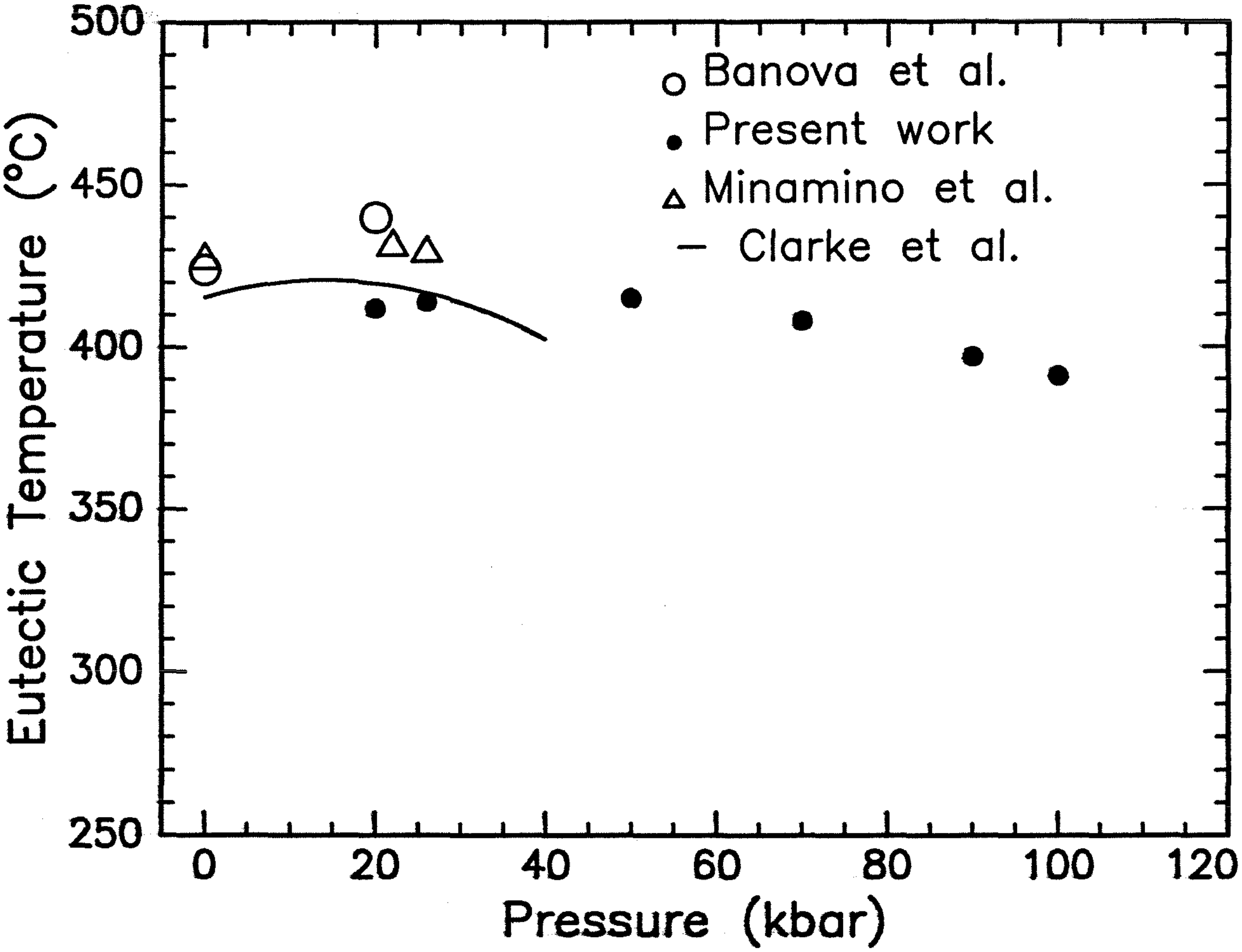

Figure 2.10 Evolution of the eutectic temperature with pressure. Comparison with other models and experiments.

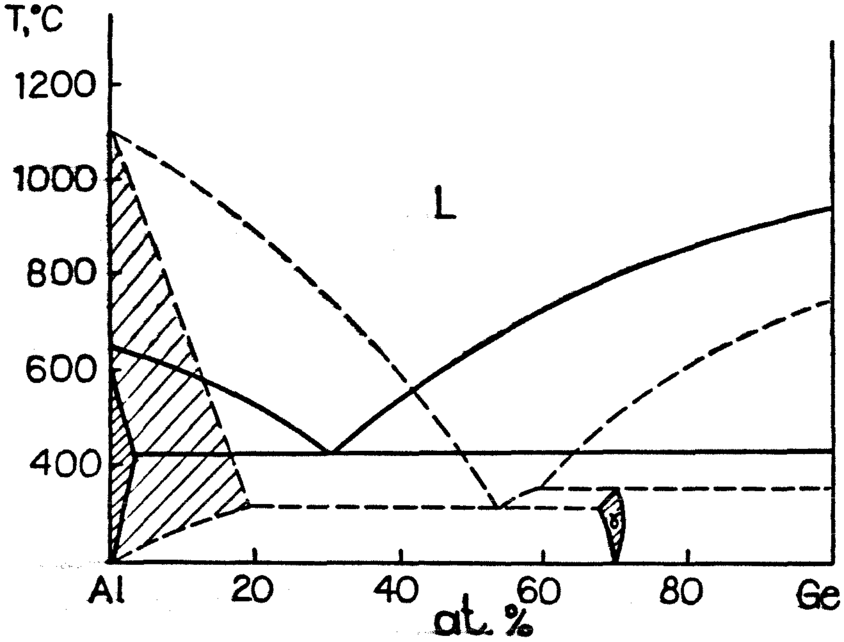

Figure 2.11 Aluminum-germanium phase at 90 kbar proposed by Ponyatovsky et al. [23].

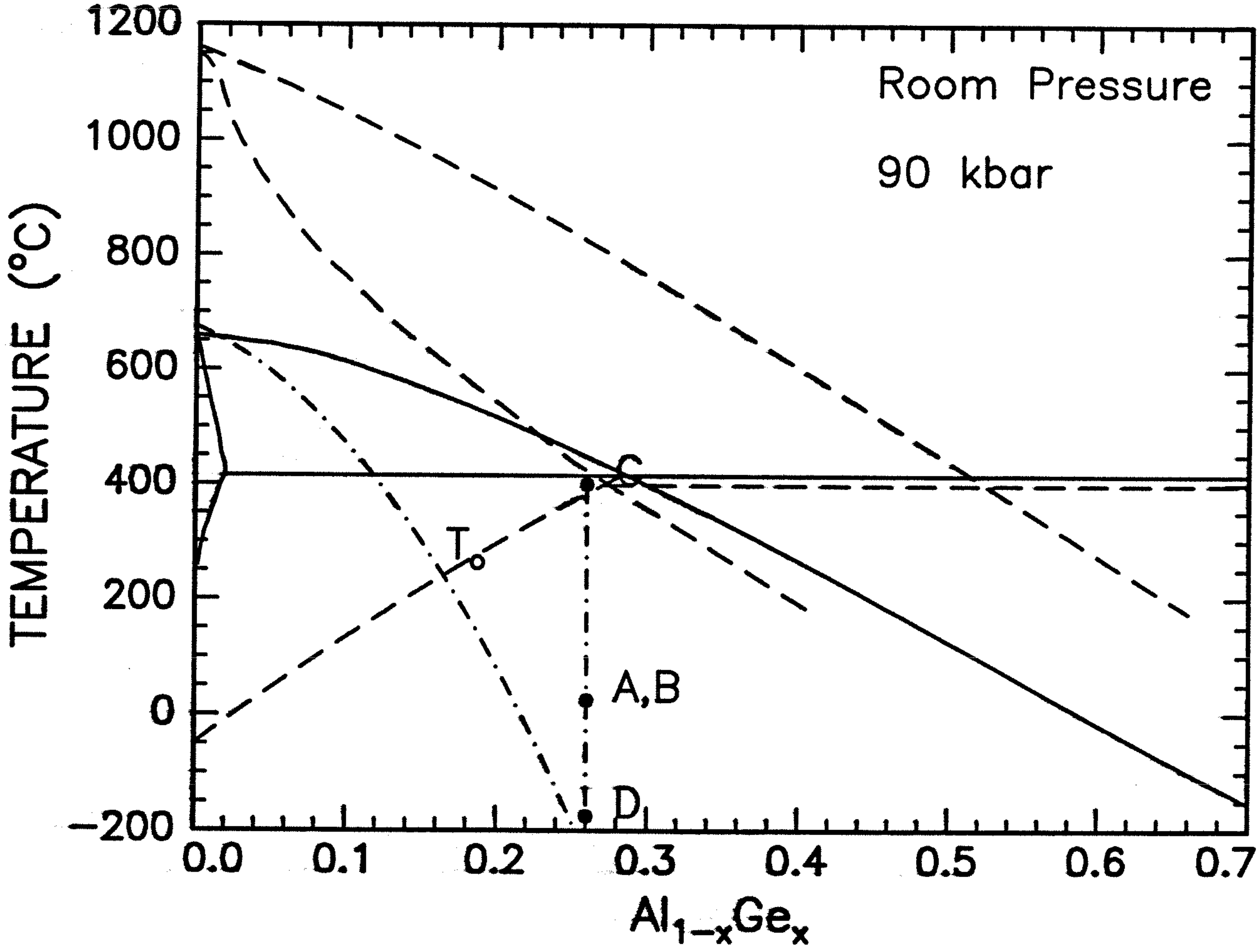

Figure 2.12 Thermobaric treatment to amorphize $Al_{1-x}Ge_x$ using an f.c.c. aluminum supersaturated solid solution as an intermediate step.

---

1. L. Kaufman and H. Bernstein, Computer Calculations of Phase Diagrams (Academic Press, New York, 1970).
2. I. Ansara, J. P. Bros, and M. Gambino, *Calphad* 3, 225 (1979).
3. A. J. McAlister and J. L. Murray, *Bull. Alloy Phase Diagrams* 5, 341 (1984).
4. K. N. Ishihara and P. H. Shingu, *Mater. Sci. Eng* 63, 251 (1984).
5. A. Ya. Shinyaev, D. B. Chernov, and G. I. Khoklova, *Russ. J. Phys. Chem* 46, 1668 (1972).
6. D. S. Kamenetskaya, *Russ. J. Phys. Chem* 38, 38 (1964).
7. B. Ya. Pines, Outline of Metal Physics (Khar'kov, USSR, 1961).
8. B. Ya. Pines, *Zh. Esp. Teor. Fiz.* 11-12, 411 (1943).
9. A. T. Dinsdale, *CALPHAD* 15, 317 (1991).
10. E. Yu. Tonkov, Phase Diagrams of Elements under Pressure (Nauk, Moscow, Russia, 1979).
11. L. D. Lucas, Physicochemical Measurements in Metals Research (R. A. Rapp editor, Interscience, New York), 243 (1970).
12. A. Schneider and G. Heymer, The Physical Chemistry of Metallic Solutions and Intermetallic Compounds (Her Majesty's Stationary Office, London, England), (1959).
13. E. S. Levin, G. D. Ayushina, and P. V. Gel'd, *Teplofiz. Vysok. Temp.* 6, 432 (1968).
14. V. M. Glazov, S. N. Chizhevskya, and N. N. Glagoleva, Liquid metals (Plenum Press, New York, 1969).
15. Smithells Metals Reference Book (Butterworths, London, England).
16. I. Fujishiro, H. Mii, M. Senoo, and M. Akao, *J. Soc. Mater. Sci. Jpn.* 20, 952 (1971).
17. H. Mii, M. Senoo, and I. Fujishiro, *Jpn. J. Appl. Phys.* 15, 777 (1976).
18. V. F. Degtyareva, G. V. Chipenko, I. T. Belash, O. I. Barkalov, and E. G. Ponyatovskii, *Phys. Stat. Sol.* 89, K127 (1985).
19. N. Nachtrieb and N. Clement, *J. Phys. Chem* 62, 747 (1958).
20. Y. Minamino, T. Yamane, H. Araki, T. Adachi, Y-S Kang, Y. Miyamoto, and T. Okamoto, *J. Mater. Sci.* 26, 5623 (1991).
21. J. B. Clark and C. W. F. T. Pistorius, *J. Less-Common Met.* 34, 233 (1974).
22. S. M. Banova, I. A. Korsunskaya, G. M. Kuznetsov, and V. A. Sergeyev, *Phys. Met. Metall.* 46, 58 (1979).
23. E. G. Ponyatovsky and O. I. Barkalov, *Mat. Sci. Rept.* 8, 147 (1992).

---

24. O. Barkalov, I. T. Belash, V. F. Degtyareva, and E. G. Ponyatovsky, *Soviet Phys. Solid State* 29, 1138 (1987).

3. EXPERIMENTAL TECHNIQUES

3. 1. Sample Preparation

Because aluminum and germanium form a simple eutectic system (section 1.5), aluminum-germanium alloys prepared by conventional casting have large grains of aluminum and germanium. Such alloys are useless in the diamond-anvil cell experiments for which only a few micrograms of alloy are employed. For these experiments we required an ultra-fine structure of aluminum and germanium. Two different techniques were used to prepare aluminum-germanium samples with ultra-fine grains: mechanical alloying (MA) and splat-quenching. The first technique produced powders, whereas the other method, splat-quenching, produced foil samples (50 to 70 μm).

3. 1. 1. Mechanical Alloying

The mechanically alloyed samples were prepared in a SPEX 8000 laboratory mill [1]. Different setups, denoted by A, B, and C, were used to ball-mill the aluminum-germanium powders. In setup A a tungsten carbide vial (SPEX model 8004) with one 7/16-in.-diam. tungsten carbide ball (SPEX model 8004A) was used. The vial and the lid were sealed with a corprene gasket. This ball-mill was located inside a glovebox filled with high-purity argon which flowed through a purifier at 1000 liters per minute. The gas composition was monitored continuously and had less than 0.1 ppm of water and oxygen. In setup B, a hardened steel vial (SPEX model 8001) with fifty 1/4-in.-diam. stainless steel balls (type H 440) was used. Approximately 5 cm^3 of hexane (C_6H_{14}) were added to prevent agglomeration of the powder, which is likely to happen with aluminum alloys. The vial and the lid were sealed with an elastomer (VITON) O-ring. Following milling, the hexane was removed by evaporation in partial vacuum. In setup C, the same balls, vial, and O-ring used in setup B were used, but no hexane was added. The ball-mill was operated in air for both setups B and C. For all methods the typical amount of powder alloyed was 5 g. Each component of the system was weighed before and after MA (resolution ± 0.01g) to obtain a crude check of contamination from hexane or from erosion of the balls. The whole system (vial, balls and powder) was also weighed before and after MA because a weight loss would have indicated a loss of hexane, whereas a weight gain would have reflected oxidation of the powder.

3. 1. 2. Splat-quenching

In a first step, chunks of aluminum and germanium in the atomic proportions 70:30 were melted together in an arc-melter (Edmund Buehler) in an argon atmosphere. The alloy ingots weighed typically 3 g and were subsequently broken into small pieces (20 to 40 mg) and put in the induction melting coil of a splat-quencher (Edmund Buehler) (see schematics of the splat-quencher in Figure 3.1). The splat-quenching process uses 2.2 MHz radio frequency (RF) power to levitate and melt a 20 to 40 mg sample in purified argon (~ . 5 atm). The RF power is turned off and the molten droplet falls. As it does so, it triggers a photo-detector sensing the thermal radiation from the sample. This in turn triggers the motion of two copper anvils together, splat-quenching the molten droplet. The cooling rate is estimated to be between 10^5 and 10^8 K s^{-1} in the resulting foil. The samples obtained were circular foils of 1 cm diameter and 50 to 70 μm thickness.

3. 2. Characterization Techniques

3. 2. 1. X-Ray Diffraction

The structure of the samples was characterized by x-ray diffraction with Cu K_α or Mo K_α radiation. A Scintag [2] diffractometer system with a germanium solid state detector was used. The system was operated at 40 kV and 31 mA. For some of the diffraction runs, a small amount of tungsten powder was added to the mechanically alloyed powder. The sharp Bragg peaks from tungsten and the use of computer deconvolution software provided an accurate determination of the d-spacings of the phases present in the samples.

The x-ray diffraction data was used to determine the strain, the crystallite size and the composition of the samples. The first two were determined using the integral breadth method [3,4,5]. Pearson VII fits were determined for each diffraction peak with the function:

$$\mathrm{I}(2\theta) = \frac{\mathrm{I_o}}{\left(1 + \frac{4}{\mathrm{FWHM}^2}(2^{\frac{1}{\mathrm{m}}} - 1)(2\theta_o - 2\theta)^2\right)^{\mathrm{m}}} \tag{3.1}$$

where m is a parameter which can vary from 0 to 10, FWHM the full width half maximum, and I_O is the maximum intensity at the position $2\theta_O$. In general m varies from peak to peak. If m is held constant at the values of 1, 1.5 or 2, the function being fitted is then called a Lorentzian, an intermediate Lorentzian, and a modified Lorentzian, respectively. For large values of m, the function used for the fit converges to a Gaussian (for m-values greater than 10, it is already very close to a Gaussian). The area A under the peak is given by:

$$A = \int_{-\infty}^{+\infty} I(2\theta)d(2\theta) \tag{3.2}$$

The measured integral breadth B_m is equal to:

$$B_m = \frac{A}{I_o} \tag{3.3}$$

Some of the peak broadening is due to the experimental setup. To correct for this experimental broadening, we used a sample of LaB_6 which was fully characterized at the

National Institute of Standards and Technology (NIST Standard N^{o} 660). A diffraction pattern was obtained from the LaB$_6$ standard, using identical experimental conditions of incoming and outgoing slits, accelerating voltage, intensity, step size, etc. to the aluminum-germanium samples, and the experimental integral B$_a$ was obtained for each Bragg peak of LaB$_6$. This data was fitted to a parabola to obtain B$_a$ as a function of 2θ, as shown in Figure 3.2. The fit to the function

$$B_A(2\theta) = a\,(2\theta)^2 + b\,2\theta + c \tag{3.4}$$

gave a = 0.50087 10^{-5}, b = -0.25943 10^{-3}, and c = 0.48503.

A parabolic correction was used to determine the true integral breadth B of the sample, where B is defined as

$$B = B_m\left(1 - \left(\frac{B_A}{B_m}\right)^2\right) \tag{3.5}$$

When using the integral breadth as a measure of the peak profile, the effect of strain and grain size can be separated by using the following equation [5]:

$$\left(\frac{B\cos\theta}{\lambda}\right)^2 = \frac{1}{D_I^2} + 16\varepsilon^2\left(\frac{\sin\theta}{\lambda}\right)^2 \tag{3.6}$$

where D_I is the grain size, ε is the strain, and λ is the wavelength of the x-rays (for Cu-K_α, $\lambda = 0.154059$ nm). To directly obtain D_I and ε, $\left(\frac{B\cos\theta}{\lambda}\right)^2$ is plotted as a function of $\left(\frac{\sin\theta}{\lambda}\right)^2$. The intercept gives $\frac{1}{D_I^2}$ and the slope gives $16\varepsilon^2$. The program used to perform these calculations is given in appendix E.

The x-ray diffraction patterns were also used to obtain a rough estimate of the alloy composition using the direct comparison method [6]. The ratio of the intensity between one peak of each phase is used to estimate the atomic fraction of each phase. The relative intensity of the peaks for each phase was compared to the theoretical intensities to determine if there was any texture in the x-ray samples. The calculation was done for several pairs of peaks to take care of possible texture effects in the powders. We verified the accuracy and the validity of this method using the x-ray patterns of standard powders of known composition. For a given pair of peaks, one of phase A and one of phase B, the following formula yields the composition:

$$\frac{\mathrm{A_A}}{\mathrm{A_B}} = \frac{\mathrm{K_A}}{\mathrm{K_B}} \frac{\mathrm{x_A}}{(1-\mathrm{x_A})} \tag{3.7}$$

where A_A and A_B are the respective intensities of the peaks of phase A and phase B (Eq. 3.2). K_A and K_B are parameters which depend on the phases studied, and the values of 2 θ, h, k, l according to the relation:

$$K = \left(\frac{1}{v^2}\right)\left[|F|^2 p \frac{(1+\cos^2(2\theta))}{\sin^2(2\theta)\cos\theta}\right] e^{-2M} \tag{3.8}$$

where v is the volume of the unit cell, F is the structure factor, p is the multiplicity factor, and e^{-2M} is the temperature factor. M is given by the following formula:

$$M = \frac{6h^2T}{mK\Theta^2}\left[\phi(x) + \frac{x}{4}\right]\left(\frac{\sin\theta}{\lambda}\right)^2 \tag{3.9}$$

where h is Planck's constant, T is the absolute temperature, m is the mass of the vibrating atom, K is Boltzmann's constant, Θ is the Debye temperature, and ϕ is the function:

$$\phi(x) = \frac{1}{x}\int_0^x \frac{\xi}{e^{\xi}-1} d\xi \tag{3.10}$$

The computer source used to perform these composition calculations is given in appendix F.

3. 2. 2. Energy Dispersive X-Rays

We used energy dispersive x-ray (EDX) fluorescence to (a) ensure that the samples prepared had the correct stoichiometry and (b) to check the mechanically alloyed powders for possible iron contamination from the milling media. The aluminum-germanium system is prone to iron contamination during MA at germanium-rich compositions [7]. The EDX machine (Kevex, model Analyst 770) was calibrated to powders of known compositions, which were prepared by thoroughly mixing high-purity aluminum, germanium, and iron powders in a ceramic mortar. To obtain K_α peaks of comparable intensities for these three elements, a rhodium primary target, operating at 12 kV and 3 MA, and a titanium secondary target were used. The spectrometer was operated in air. Calibration curves were obtained for Al-Ge and also for $(Al_{1-x}Ge_x)$-Fe for different values of x, as shown in Figure 3.3.

Figure 3.3 shows a significant fraction of iron counts (15% to 20%) in the calibration alloy powders to which no iron was added. There are two possible causes for these counts: (a) iron in the starting commercial powders and (b) iron counts intrinsic to the EDX machine. The operating conditions for the EDX machine (titanium secondary target and a 12-kV accelerating voltage) favor the detection of iron so much over the detection of germanium that even trace amounts of iron would give a relatively important number of counts. To test these possibilities, we first ran the EDX machine with no sample in the holder. We detected a small iron peak (0.8 counts/s compared with 2 counts/s in pure aluminum or pure germanium). This iron could be due to iron impurity in the titanium secondary target or to scattering from an iron impurity hit by the beam inside the EDX machine. Then we analyzed germanium and aluminum from a different source (Aesar, Ward Hill, Massachusetts) and repeated the measurements for pure aluminum, pure germanium, and a mixture of aluminum and germanium at the composition $Al_{25}Ge_{75}$; we observed, however, no noticeable change in the energy dispersive spectrometry results. This analysis proved that the relatively large number of iron counts in powders that nominally did not contain iron was due to a combination of causes (a) and (b).

3. 2. 3. Transmission Electron Microscopy (TEM)

Most of the transmission electron microscopy (TEM) was performed on a Philips CM30 (300 kV) microscope having a Kevex energy dispersive x-ray system. High resolution electron microscopy was performed on a Philips CM30ST (300 kV) microscope with a point to point resolution of 1.9 Å. Finally, as the Kevex system was out of order for most of the time we performed microscopy, we also used the JEOL 2000 FX (200 kV) at the University of New Mexico. This instrument has a 3 Å resolution and a Tracor TN 5500 energy dispersive system with a SiLi window detector. TEM was an effective tool to examine the structure and chemistry of the different phases present in samples prepared in the diamond-anvil cell, each weighing no more than a few micrograms.

3. 2. 4. Calorimetry

The apparition of metastable phases in mechanically alloyed powders was observed from x-ray diffraction patterns. To study the thermal stability of these metastable phases, differential thermal analysis (DTA) (Perkin-Elmer, model 1700) and differential scanning calorimetry (DSC) (Perkin-Elmer, model DSC 7) were used. These instruments were calibrated by using the melting point of aluminum and lead for the DTA and the DSC, respectively.

3.3. Techniques of High Pressure Research

3. 3. 1. Merrill-Bassett Diamond-Anvil Cells (DAC)

For high-pressure experiments a pair of Merrill-Bassett diamond-anvil cells (DAC) [8] (Fig. 3.4) were used. The materials used for the platens, the diamond seats, and the pressurizing bolts were changed from the original design [9] to accommodate high-temperature experiments. We used heat-treated Inconel 718 for these pieces; this material is not subject to rapid creep deformation (Inconel 718 has the highest stress rupture (585 MPa at 650°C for 1000h) of all superalloys [10]), which would cause important pressure decreases. The diamond anvils are placed on two platens pulled together by three bolts. Two steel alignment pins maintain the cell together in the absence of the bolts during the alignment procedure. They also break the symmetry of the platens, therefore providing us with a unique way to assemble the cell. The diamonds are held in seats which rest in cylindrical cavities in the backing plates. Both diamond seats are held in place by three set screws spaced 120° apart (these screws are not shown in Figure 3.4). One diamond seat has a precise fit on the platen, whereas the other seat has a loose fit; the set screws allow adjustment of the latter so that the two flat faces of the diamonds, or culets, can be perfectly aligned. The x-ray beam is perpendicular to the culets and goes through both diamonds as shown in Figure 3.5. One of the seats has a 0.75 mm diameter hole for the incoming x-ray beam; the other has a 0.75 mm x 3 mm slit to allow x-ray diffraction (XRD) cones of up to 30° to exit the cell. The slit reduces support on the outgoing side diamond and thus slightly reduces the maximum pressure that can be achieved with this diamond-anvil cell. The slit, however, is necessary to allow us to observe many diffraction rings. Type I diamonds of 1/5 to 1/4 carat made by Drukker (Amsterdam) are used. The culets have an octogonal shape with a surface area of about 0.4 mm^2. For experiments at room temperature, the diamonds are normally glued to the seats. For high-temperature experiments, glue cannot be used. We attached the diamonds to the seats with stainless steel rings and a 0.05 mm-thick sheet of copper, as shown in Figure 3.6.

For the gasket material, we used an alloy of $Mo_{90}Re_{10}$, because we require a material that would deform easily, but would not react with the sample or weld to the diamonds at high temperatures. The gasket is a 6 mm diameter disk punched out of a 0.26 mm-thick sheet of $Mo_{90}Re_{10}$. A 0.15 mm diameter hole in the metal gasket serves as the sample chamber when the gasket is placed between the two diamonds (Figure 3.7). In addition to containing the sample and the pressure media, the gasket helps achieve more uniform hydrostatic pressures. The gasket also extrudes around the diamonds and acts as a supporting ring, preventing failure of the anvils due to concentration of stresses. Pressure is applied by tightening the three heat-treated Inconel 718 bolts which pull the platens together (Figure 3.4).

Most of the assembling and loading of the DAC is done using an optical microscope. The first step is to align the diamond culets, using the three set screws. This must be done before each experiment as previous use of the DAC almost always causes a slight misalignment of the culets. The next step is to set the diamond faces parallel to each other. To check the parallelism, the two diamond faces are placed in slight contact; shining a light through the diamonds allows an interference pattern to be observed. The object is to adjust the diamonds by gently pressing the platens together with the fingers until the fringes are as wide as possible, indicating good culet parallelism. Then we attach the three pressurizing bolts to preserve the alignment and we measure the thickness of the cell at each of the three corners. The next step is to prepare and press the gasket. The cell is disassembled and the gasket is placed between the two diamonds and pressed stepwise. After each tightening of the bolts, the thickness of the cell at each corner is measured to ensure the diamonds remain parallel to each other during the process. The final gasket thickness in the area of the indentation is typically between 0.05 and 0.1 mm. The cell is disassembled once more to drill a 0.15 mm diameter hole in the gasket at the center of the indentation with a high speed-steel drill. The drilled hole must be well-centered in the indented area to achieve high pressures, because the pressure is highest in the center of the culets. Then, organic solvents are used to carefully clean the faces of the diamonds, as any impurity may add extra diffraction rings or may react with the sample. The pressed gasket is set on top of one diamond and a few chips of samarium yttrium aluminum garnet (samarium YAG) are placed in the drilled hole. The samarium YAG enables us to measure the pressure, as detailed in the next paragraph. The sample is then placed in the hole next to the samarium YAG; the other diamond is then positioned on top. The top diamond is not in contact with the gasket, as we need some space between the diamond and the gasket for the next step in the assembly. We first cool the cell with liquid nitrogen; only the bottom platen is in contact with liquid nitrogen, since we have to be careful not to load nitrogen in the sample chamber. Then the whole cell is immersed in a cup containing liquid argon. The cell is left in liquid argon for about 5 minutes to ensure that liquid argon fills all the empty space in the sample chamber, and while the cell is still immersed in liquid argon, the screws are tightened to seal the sample, samarium YAG and argon in the gasket hole. The purpose of putting argon in the sample chamber is to assist in obtaining more hydrostatic pressures. The argon also prevents the gasket hole to close; this facilitates the alignment with the laser, as we are able to shine a light through the cell. Figures 3.8 and 3.9 are optical micrographs of two cells loaded with different samples, taken through the diamonds. The first one was loaded with a piece of Al70Ge30 which was prepared by splat-quenching; the photo was taken with the sample at a pressure of 117 kbar. The second one was loaded with Al80Ge20 powder prepared by mechanical alloying. The pressure was 106 kbar. The loading procedure is now complete and the DAC is ready for experimentation.

3. 3. 2. Measurement of Pressure in the DAC

When the samarium YAG in the cell is illuminated with an argon laser, the YAG fluoresces. The shifts of the samarium YAG fluorescence lines with pressure are used to measure the pressure in the sample chamber. Historically, ruby has been used in high-pressure experiments as a calibrating material for pressure [11,12]. However, the fluorescence lines of ruby slowly fade with increasing temperature and completely disappear at 500°C. Recent investigations by Hess et al. [13,14,15] have shown that the shifts in the samarium YAG fluorescence lines are independent of temperature and the fluorescence persists to 1200° C. Blue light (wavelength 483 nm) of an argon laser was used, and the laser power was typically 100 mwatts. Some of the intensity was lost along the optical path of the laser beam and approximately 40% of the laser intensity reached the sample. The laser beam was focused on a samarium YAG chip within the cell and the fluoresced light passed through a SPEX optical spectrometer (Spex Industries, Edison, New Jersey) to a photomultiplier tube. We scanned the spectrometer between 15800 and 16400 wave numbers; in this region the spectrum exhibited three peaks, as shown in Figure 3.10. A computer program developed by Brister [16] was initially used to fit a triple Lorentzian to the spectrum. To have more flexibility with the input/output of the program, we improved the background correction of a program developed by Aziz [17] to fit a triple Lorentzian. The computer code of this program is contained in appendix G. We used the wave number-pressure calibration developed by Nancy Hess and David Schiferl [15]. For the first (W_{Y1}) and second peak (W_{Y2}), the empirical relations between pressure and wave-numbers are as follows

$$P = \frac{16187.2 - W_{Y1}}{0.8194} \tag{3.11}$$

$$P = \frac{16232.2 - W_{Y2}}{0.6584} \tag{3.12}$$

where the pressure is expressed in kbar. The accuracy of these measurements is about 2 kbar.

3. 3. 3. High Temperature Apparatus

In order to estimate the pressure fluctuations with temperature, we used a resistive heating oven, using a tungsten-rhenium coil wrapped around the cell holder, designed by Dave Schiferl [18]. There were two heat shields, one around the cell, and the other around the resistive coil as shown in figure 3.11. The assembly was placed in a vacuum-tight, water-cooled container. Quartz windows are positioned so as to allow the laser light in and out of the diamond-anvil cell. This apparatus allowed us to measure pressure from room temperature to 500°C. The plot of the pressure as a function of temperature (Fig. 3.12) is typical of the results we obtained: the pressure relaxes as the temperature increases. Note however that the pressure measured at the highest temperature is retained during cooling down. The amount of relaxation varied from a few kbar to 60 kbar, depending on the sample, and also on the number of iterations.

3. 3. 4. X-Ray Diffraction Apparatus

We used x-ray diffraction to determine the structural changes in the $Al_{1-x}Ge_x$ alloys as a function of pressure and temperature. We used molybdenum K_α for the following two reasons: (1) we needed a short wavelength to get as many diffraction rings as possible within the diffraction window of 30° and (2) we needed a radiation that would go through 5 mm of diamonds (which is the total thickness of the two diamond anvils). Using mass absorption coefficients [19], we determined molybdenum K_α radiation to be a good candidate. The tube was powered by a Picker power supply, and the working conditions were typically 44 kV and 20 mA. When necessary, we used a 0.1 mm-thick zirconium filter, which decreased the $\frac{K_\beta}{K_\alpha}$ intensity ratio from $\frac{1}{9}$ to $\frac{1}{400}$. In addition, the filter decreased the bremstrahlung intensity. With the filter, the K_α transmitted beam had only 40% of its original intensity. In some instances a direct beam (no filter) was used to shorten the exposure times to 2 to 3 hours. A 210 micron collimator reduced the size of the outgoing x-ray beam (see Fig. 3.13). The whole x-ray assembly was mounted on X, Y and Z translators that facilitated the positioning of the diamond-anvil cell in the x-ray beam path.

We built two temperature-controlled cell holders to get x-ray diffraction data under different thermal conditions. The first holder allowed us to get XRD patterns from 20 K to room temperature. We used a displex (Air Products, model DE202) as a cold source. As shown in Figure 3.14, the cell is bolted to a copper holder. There are three $Au_{99.93}Fe_{0.07}$/chromel thermocouples located close to the cell as shown in Figure 3.15. The cell holder thermally attached to the cold tip of the displex by a thermal link consisting of a flexible wire of oxygen-free copper. We used a flexible wire so that the vibrations of the cold tip would not be transmitted to the cell and affect the XRD pattern. A primary copper heat shield is attached to the cell holder. A secondary copper heat shield is screwed onto the displex. Finally, a vacuum-tight stainless steel heat shield is attached to the displex. MYLAR films provide vacuum-tight windows for the x-ray beam to enter and exit the apparatus. Each of the heat shields has four holes on the x-ray incoming side; one allows the x-ray beam to reach the cell, and the other three, aligned with the pressure-adjusting bolts on the cell, allow us to modify the pressure in situ (Figure 3.16). On the outgoing side, the heat shields have 25mm x 5mm slits to allow the diffracted beam to exit the cryostat.

The second cell holder allowed us to get XRD patterns from room temperature to 400 ^{o}C. Again the cell was bolted on a copper holder. The holder is heated by a 1/4-in diameter cartridge heater (Fast Heat, Elmhurst, Illinois, model H12-3) placed in a hole in the copper block. The temperature was controlled electronically (Omega Engineering, Stamford, Connecticut, model CN310KC), and the temperature-controlling thermocouple (type K) was placed in a hole near the heater. A second thermocouple (type K) was held by a bolt and washer on top of the cell. An aluminum heat shield was placed on top of this assembly. Both the high and low temperature thermally controlled cell holders were designed to fit a rotating table which enabled us to place the sample perfectly perpendicular to the beam.

We used a scintillation detector to help us align the x-ray beam with the sample. The detector was positioned on a track on the rotating table mentioned above. We moved the x-ray assembly laterally (X direction from Fig. 3.13) and vertically (Z direction from Fig. 3.13) to perform this alignment. We alternatively moved the beam in the X and the Z direction until we measured a maximum intensity with the detector. Since the gasket material was essentially molybdenum, it was fairly transparent to the x-ray beam. This helped us to get an approximate alignment, since we would get a high number of counts as soon as the beam would go through the gasket. On the other hand, it was difficult to ensure that the x-ray beam was hitting the sample, as there was not a clearly defined maximum in most cases. Thus, to refine the alignment, we used a germanium solid state detector coupled with a single channel analyzer (SCA). We calibrated the SCA by using the fluorescence of the K_α lines of copper, molybdenum and silver. We then set the SCA energy window to detect only the fluorescence of the K_α line of germanium. We moved the x-ray assembly in the X and Z directions in order to maximize the number of counts. This method gave us evidence that the x-ray beam and the sample were accurately aligned.

To record the XRD pattern from the sample, we designed a double film x-ray camera [20] which is attached to the same rotating table. The two cassettes holding strips of x-ray sensitive films are made of brass. They have beryllium windows which makes them light-tight, but transparent to x-rays. The two cassettes are spring-loaded inside parallel grooves to ensure perfect positioning, as the distance between the two films is a crucial factor in determining accurate lattice parameters. We used Kodak direct exposure films (DEF 392), Kodak GBX developer (4 min), and Kodak GBX fixer (5 min). The rings which appear on the films correspond to the peaks one usually obtains with a diffractometer (see Fig. 3.17).

The two-film technique was used because the distance of the sample to the films is not known with great accuracy. On the other hand, the distance between the two cassettes is well defined (50 mm). It is important to measure the angles as accurately as possible, since we are working with Mo K_α, which has a short wavelength (λ=0.07093 nm); since the d-spacings are proportional to the λ^{-1}, a small error in the measure of the angle is amplified and leads to larger errors in the d-spacings. Using the notations of Fig. 3.18, we see that:

$$x = \frac{d\, d_1}{d_2 - d_1} \tag{3.13}$$

therefore:

$$2\theta = Arc\tan\left(\frac{d_1}{x}\right) \tag{3.14}$$

An optical microdensitometer (Blake Industries, Scotch Plains, New Jersey, model KD-540) was used to analyze the films. It was very helpful in detecting faint rings, and in giving us accurate positions of the peaks. A digitizing program was also used to store the position of the rings in a computer file. We wrote a computer code (appendix H) to determine the radii of the rings from the digitized positions using a least square fit method. This program used the data from both films to determine the distance to the sample, then the d-spacings.

3. 4. Preparation of TEM Samples

Diamond-anvil cells were used to prepare TEM samples; a copper TEM grid (Ted Pella, Redding, California) was placed on top of the bottom diamond. A chip of samarium YAG was placed in the center of this grid, as well as a small amount of mechanically alloyed aluminum-germanium powder. The cell was then assembled, and pressure was applied by tightening the bolts of the DAC. The pressure would be measured by recording the shifts of the fluorescence peaks of samarium YAG. The pressure measured was the pressure at the center of the cell. The pressure in this case was not as hydrostatic as the pressure obtained with the molybdenum gasket. Each sample was kept under pressure for 45 minutes, before the pressure was released at room temperature.

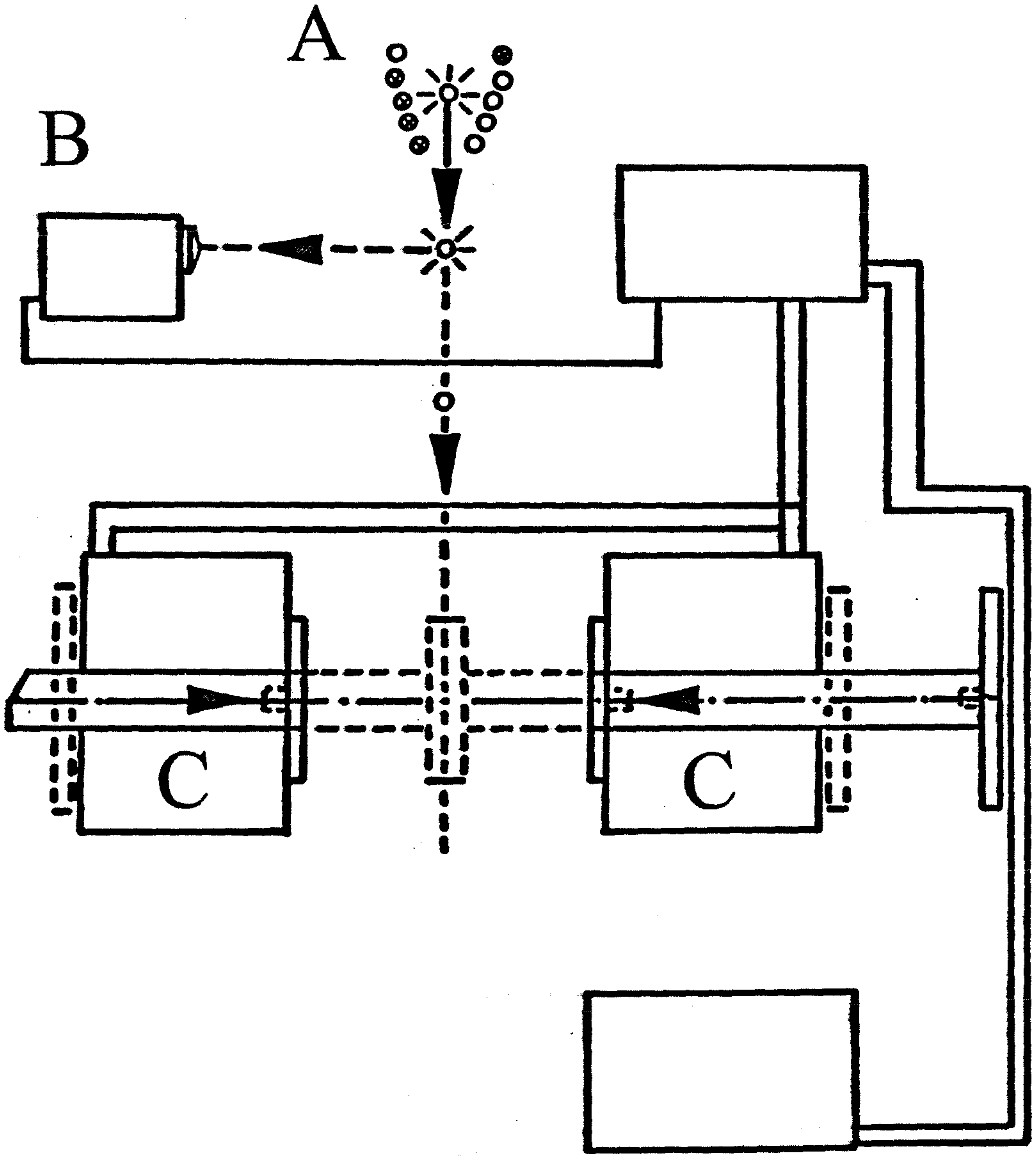

Figure 3.1 Schematics of a splat-quencher. (A) represents the coil, (B) the sensor, and (C) are the two copper anvils.

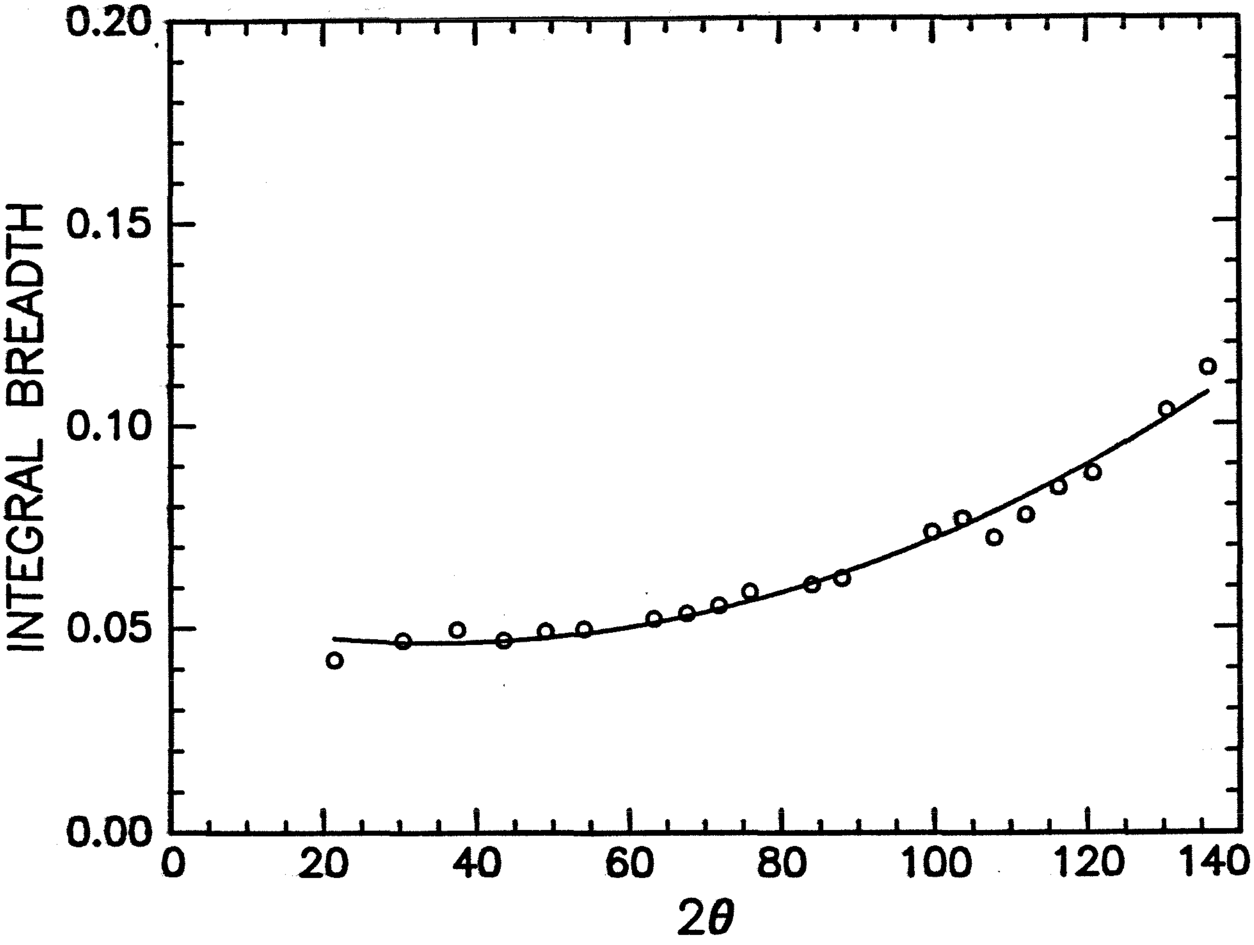

Figure 3.2 Calibration curve to correct the instrumental integral breadth.

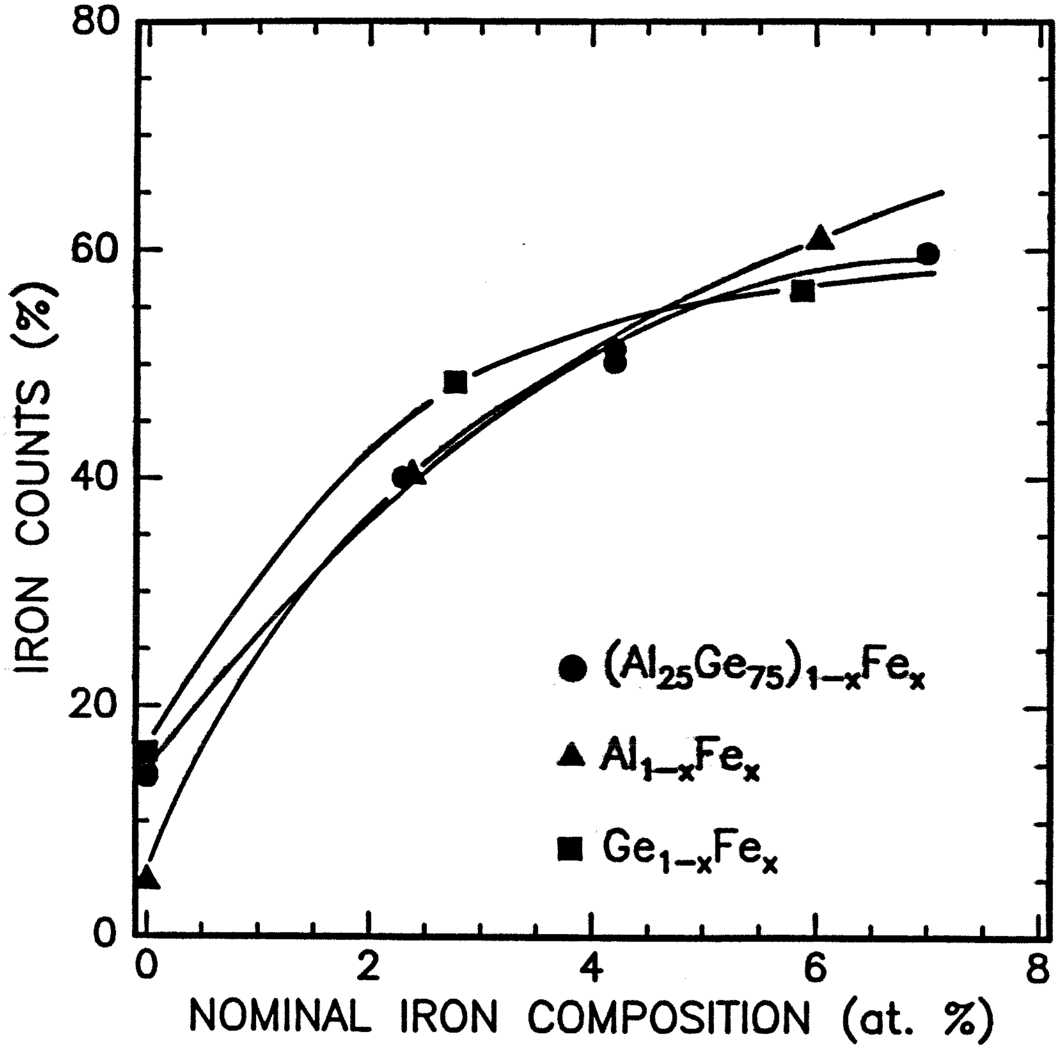

Figure 3.3 Calibration curves to determine the iron contamination.

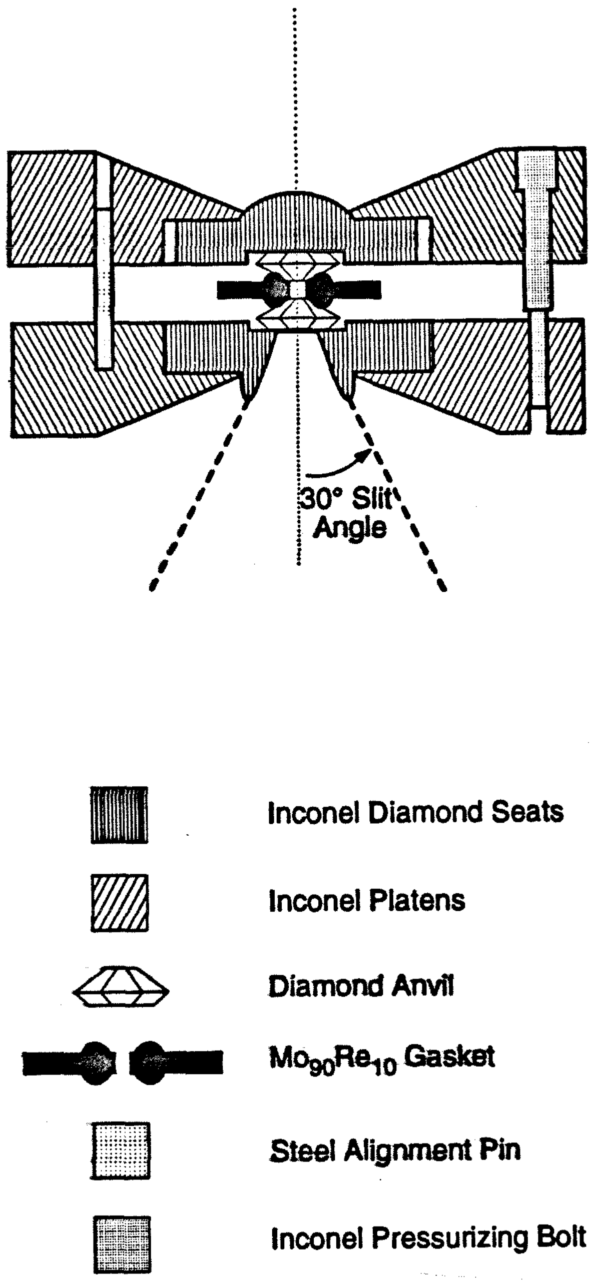

Figure 3.4 Schematics of the modified Merrill-Bassettt diamond-anvil cell.

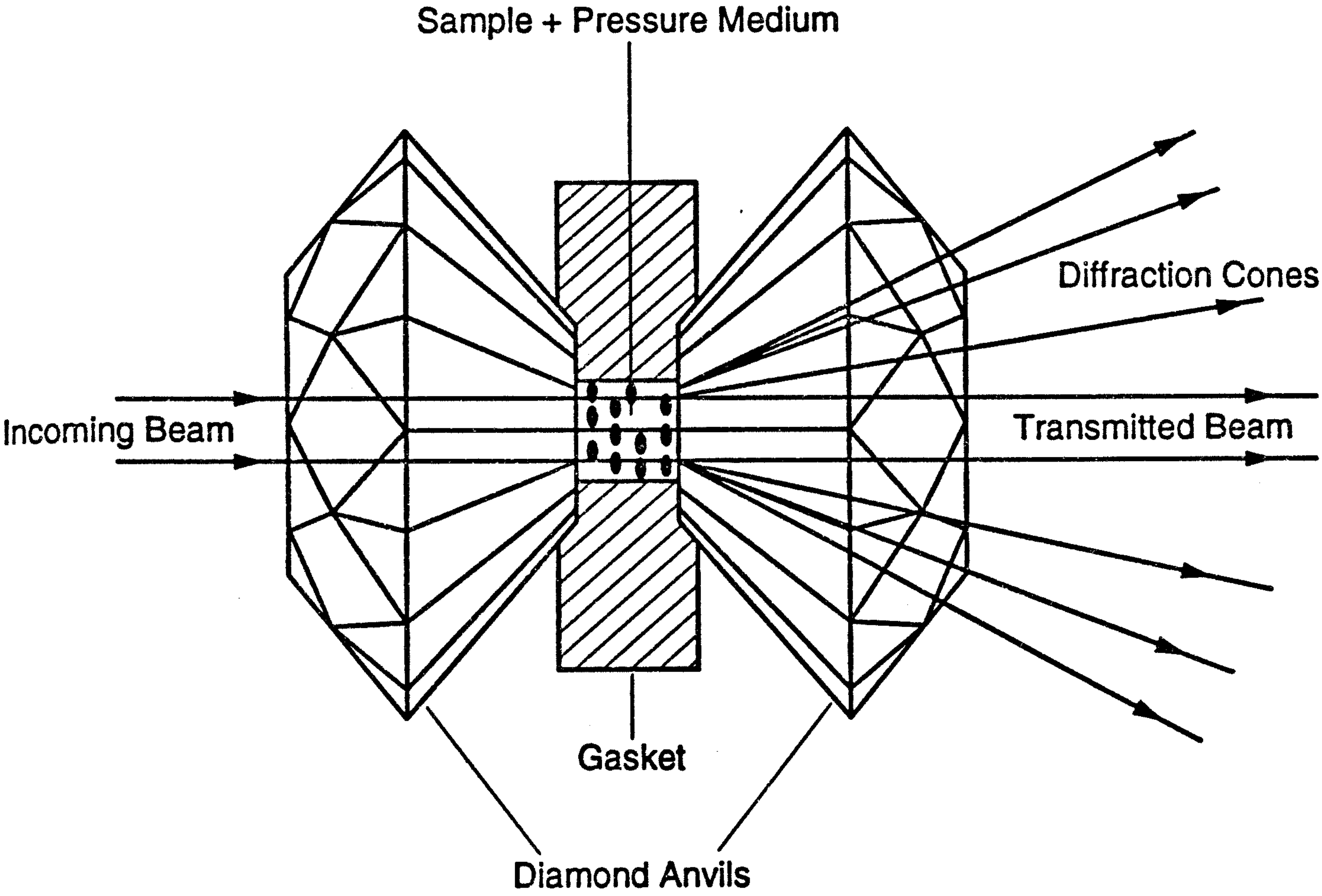

Figure 3.5 Detail of diamonds and sample chamber in a diamond-anvil cell.

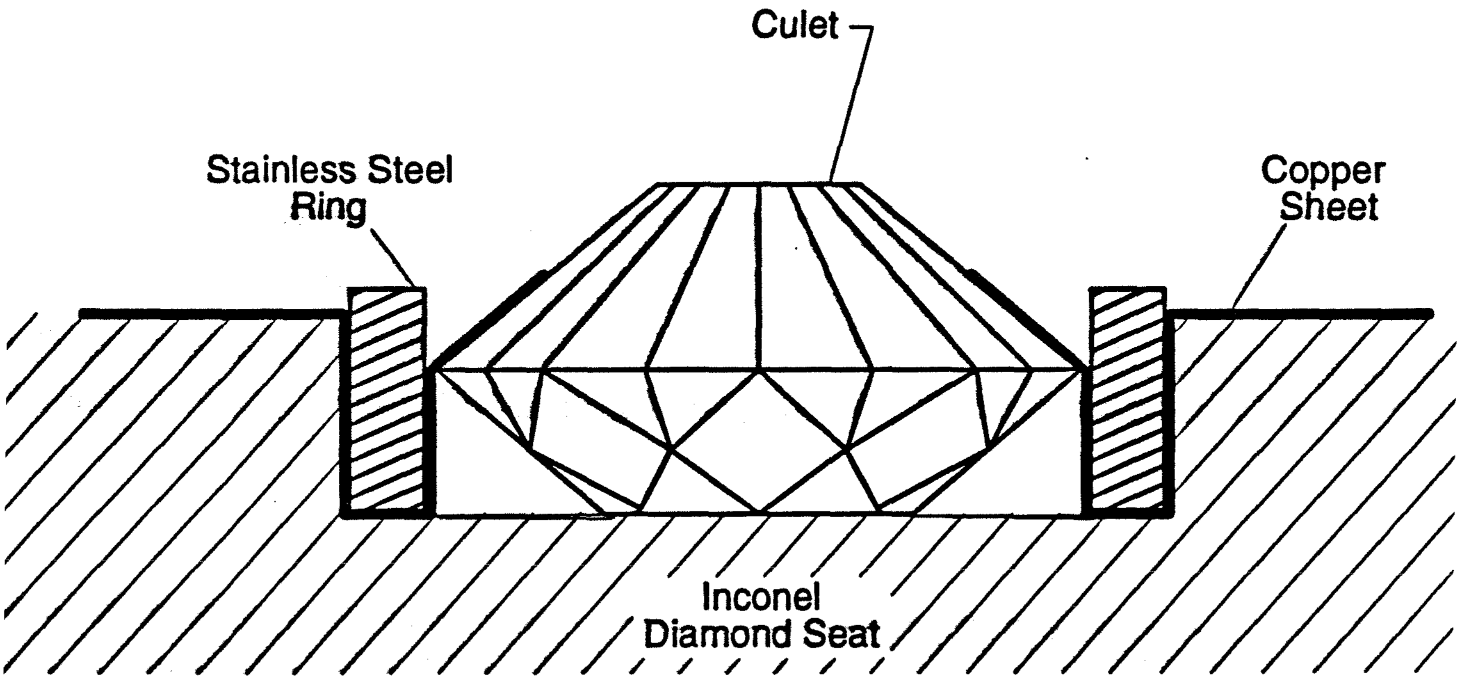

Figure 3.6 Attachment of the diamonds.

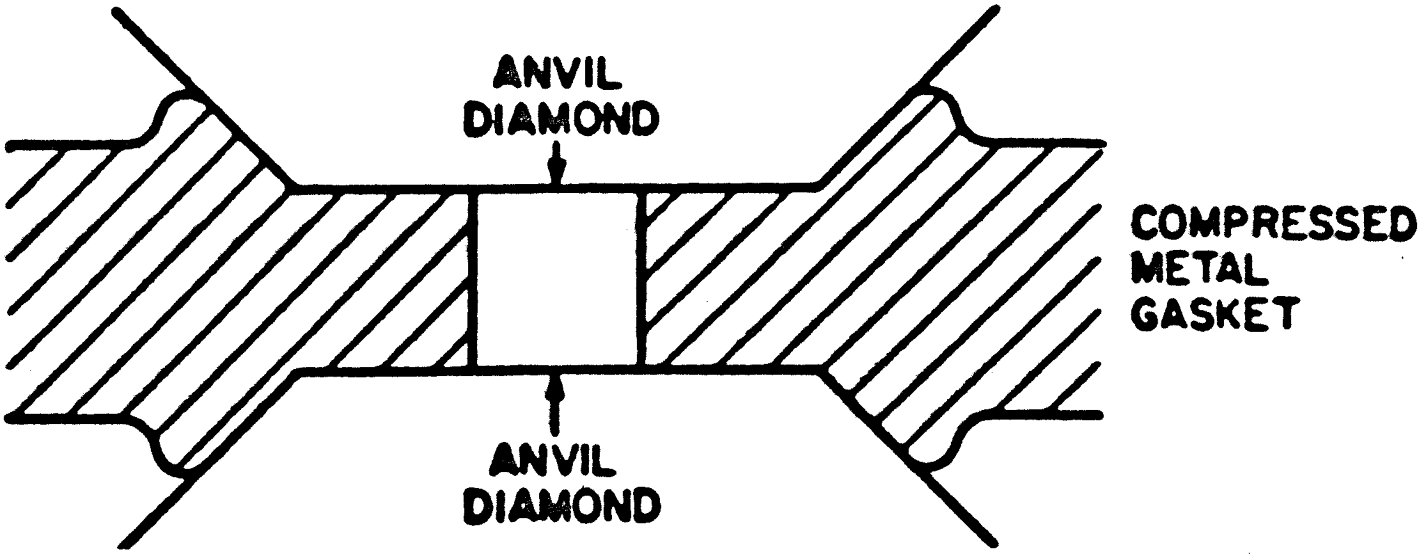

Figure 3.7 The shape of a compressed gasket (between two anvil diamonds) supporting the diamond edges (from [8]).

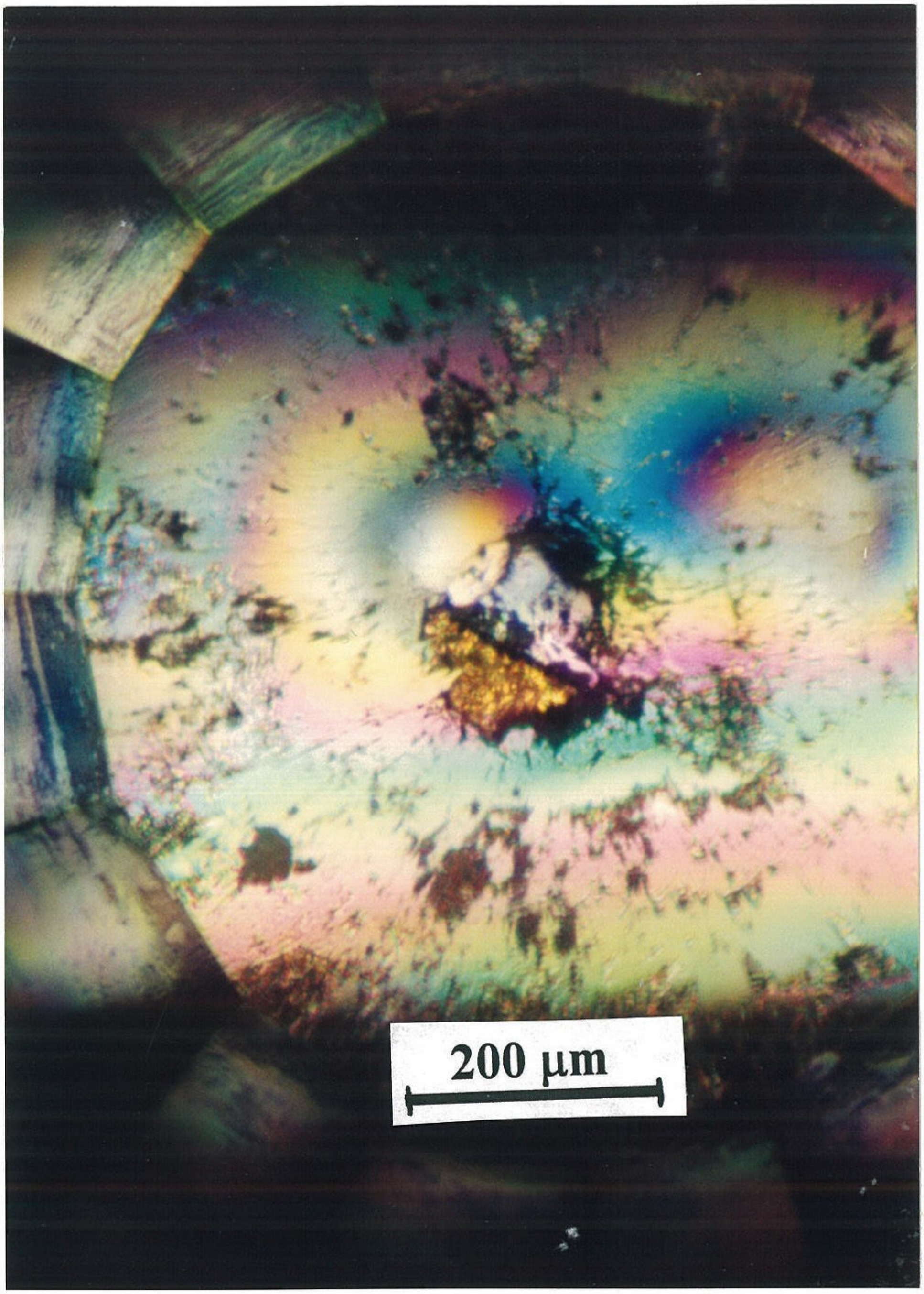

Figure 3.8 Optical micrograph of a $Al_{70}Ge_{30}$ sample prepared by splat-quenching at 117 kbar.

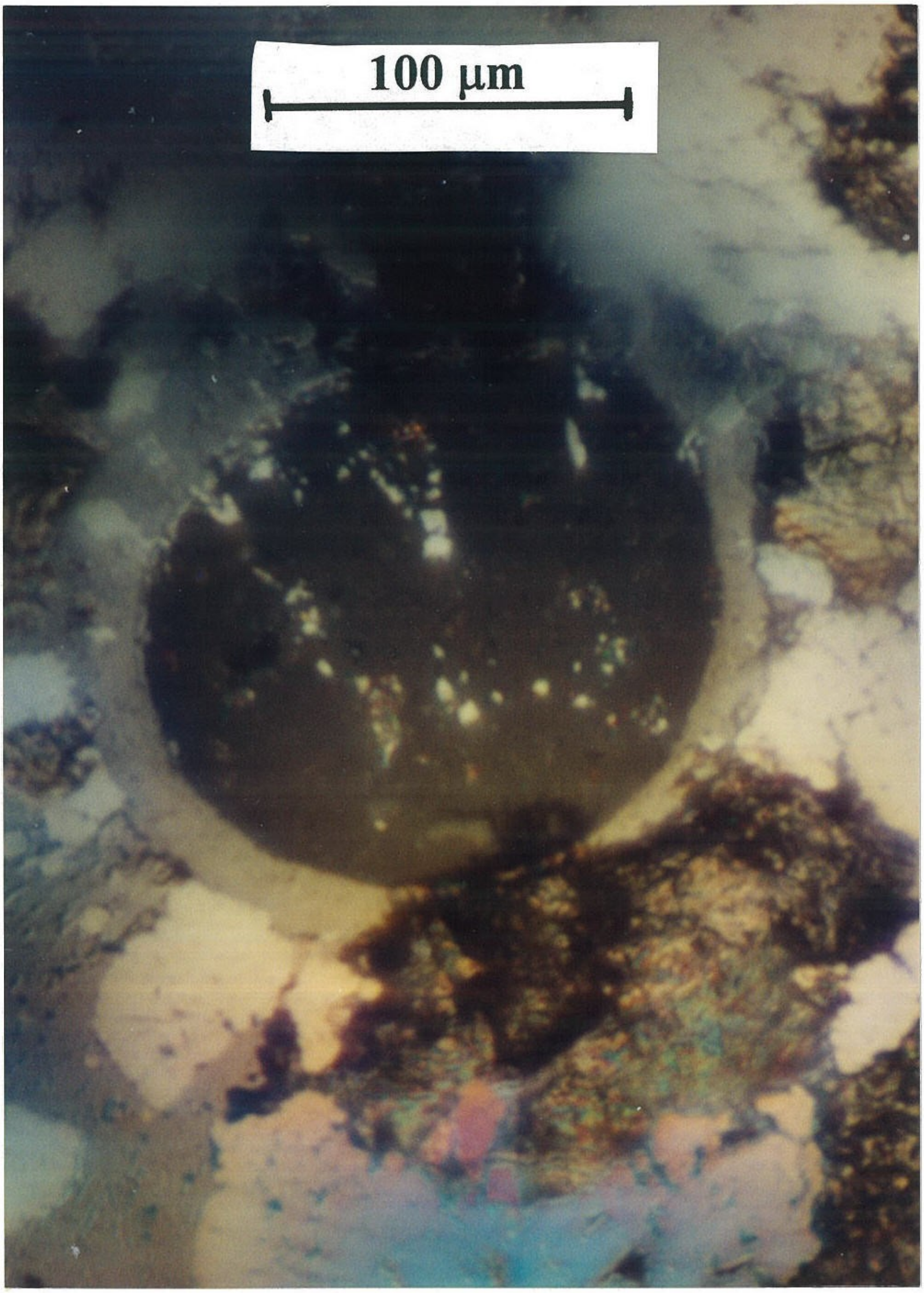

Figure 3.9 Optical micrograph of a $Al_{80}Ge_{20}$ sample prepared by mechanical alloying at 106 kbar.

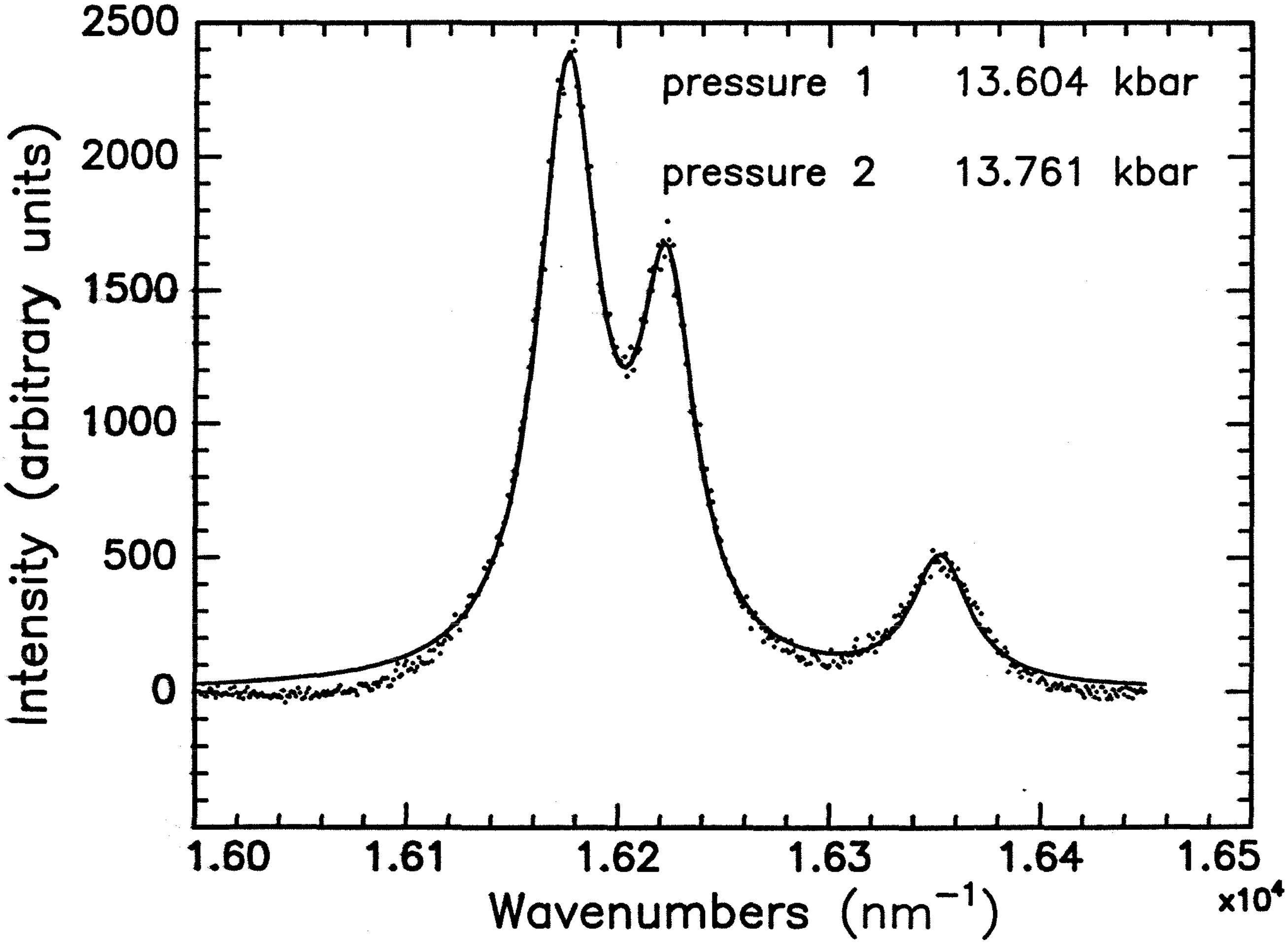

Figure 3.10 Samarium YAG fluorescence lines.

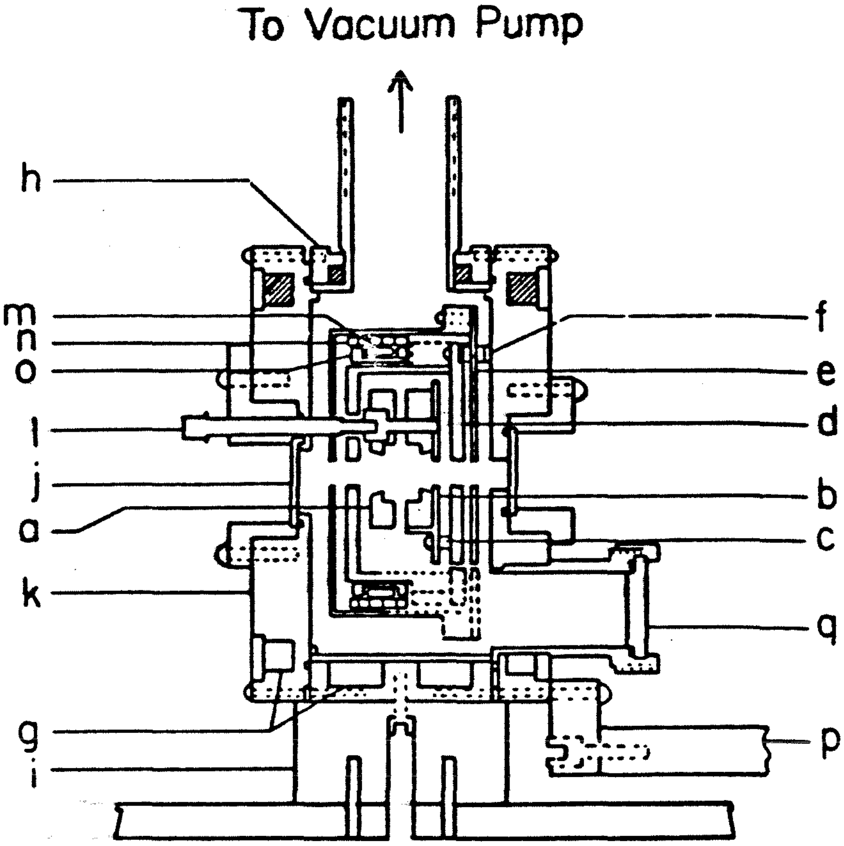

Figure 3.11 Vacuum oven consisting of: (a) high-temperature diamond-anvil cell; (b) cell mount; (c) ceramic standoff; (d) externally heated container for cell; (e) thermal radiation shield; (f) standoff; (g) water channels; (h) oven body; (i) oven mount; (j) quartz window; (k) cover plate; (l) feed-through for pressure adjustment; (m) heater coil; (n) outer insulator for heater; (o) inner insulator for heater; (p) mount for heater and thermocouple hardware; (q) heater and thermocouple feed-through port.

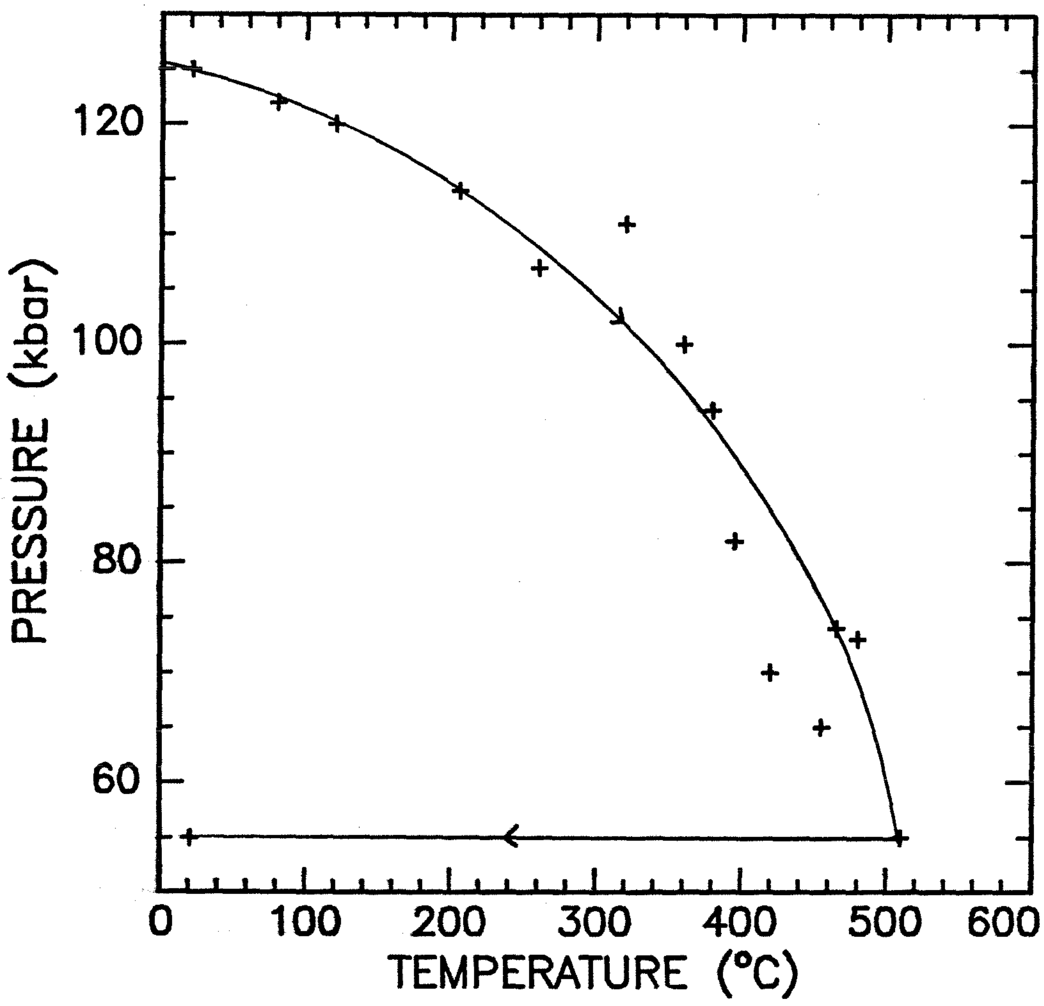

Figure 3.12 Temperature-pressure curve in a heated diamond-anvil cell.

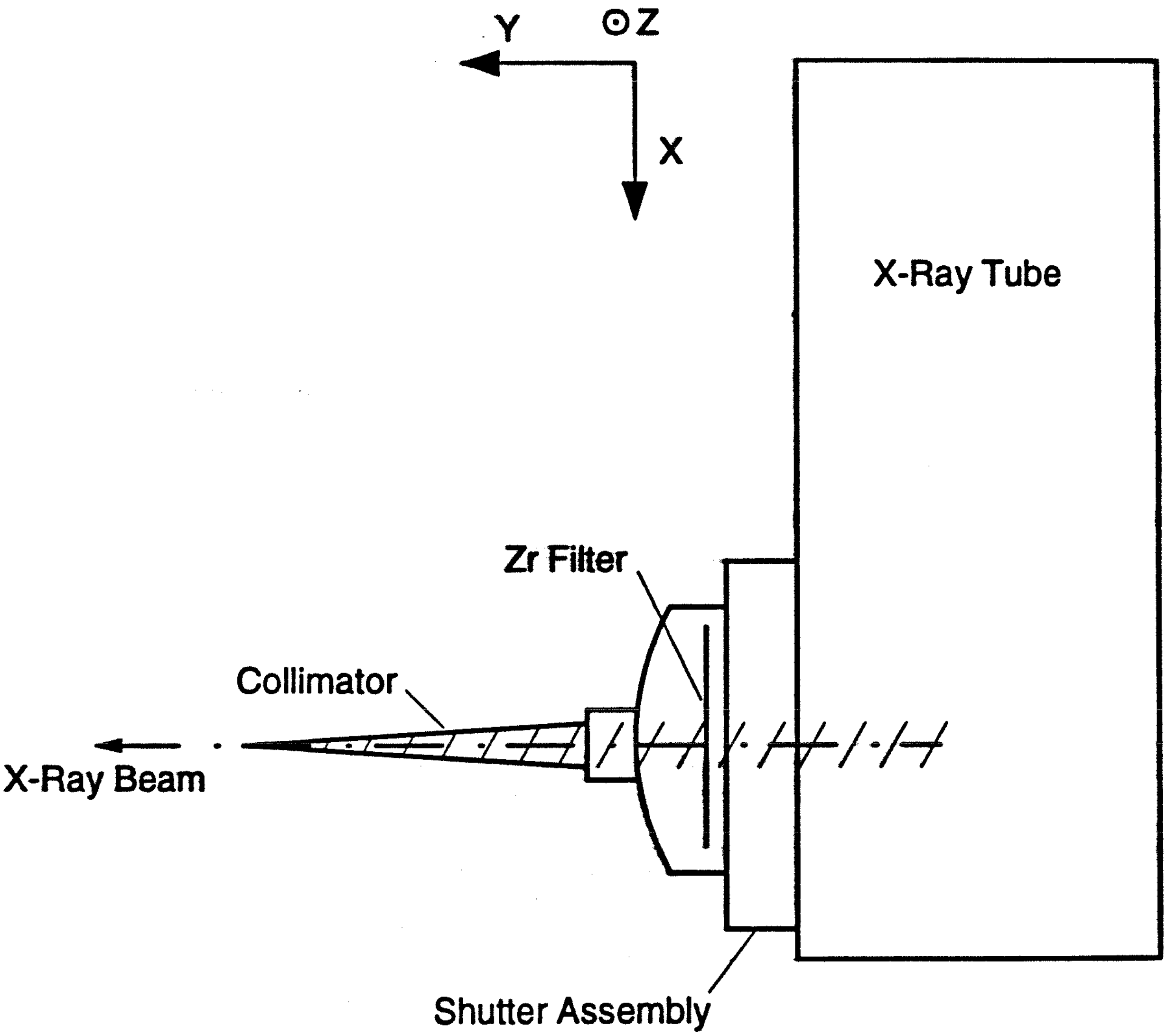

Figure 3.13 X-ray tube assembly.

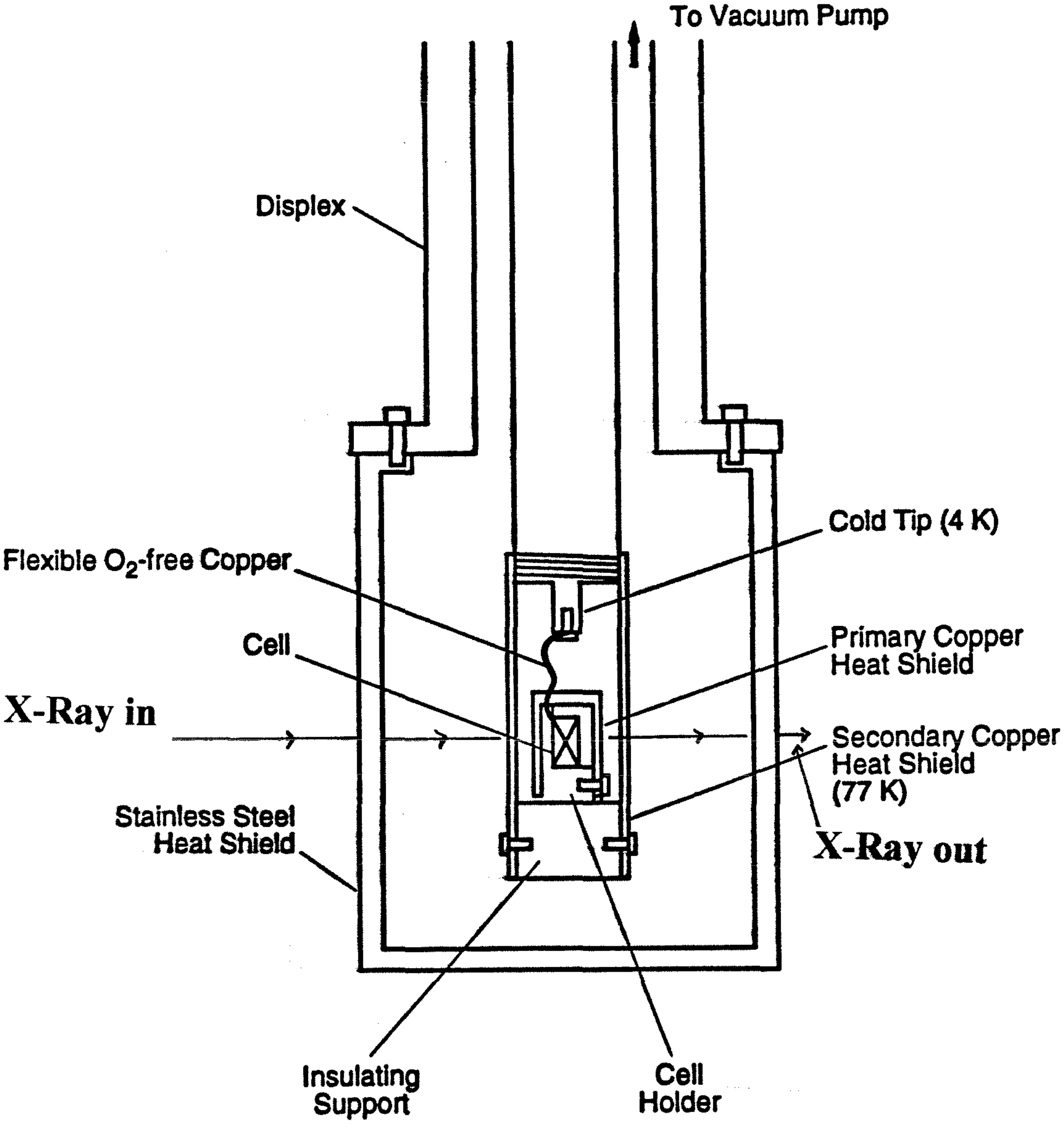

Figure 3.14 Schematics of the cryogenic cell holder.

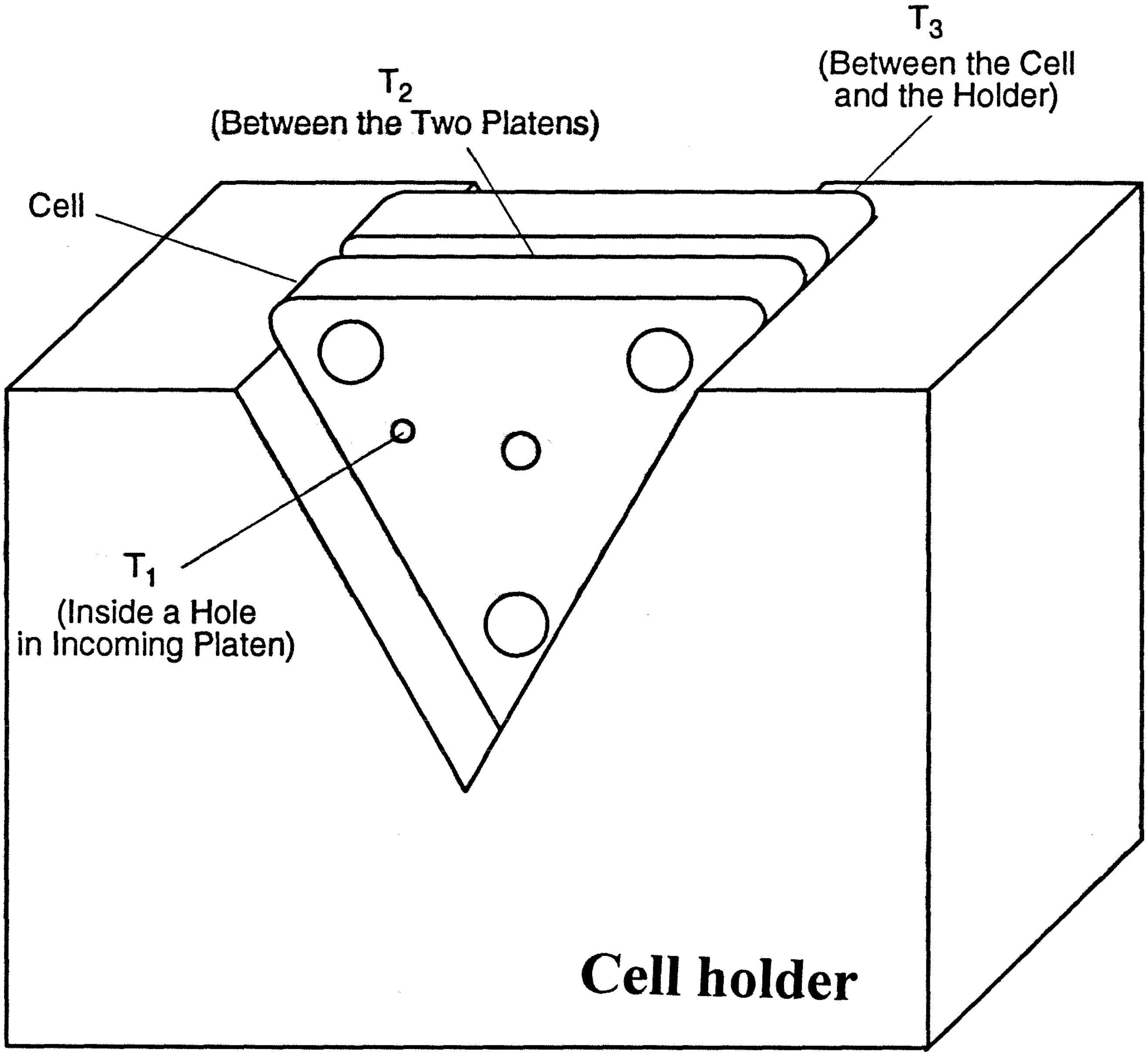

Figure 3.15 Location of the thermocouples in the cryogenic cell holder.

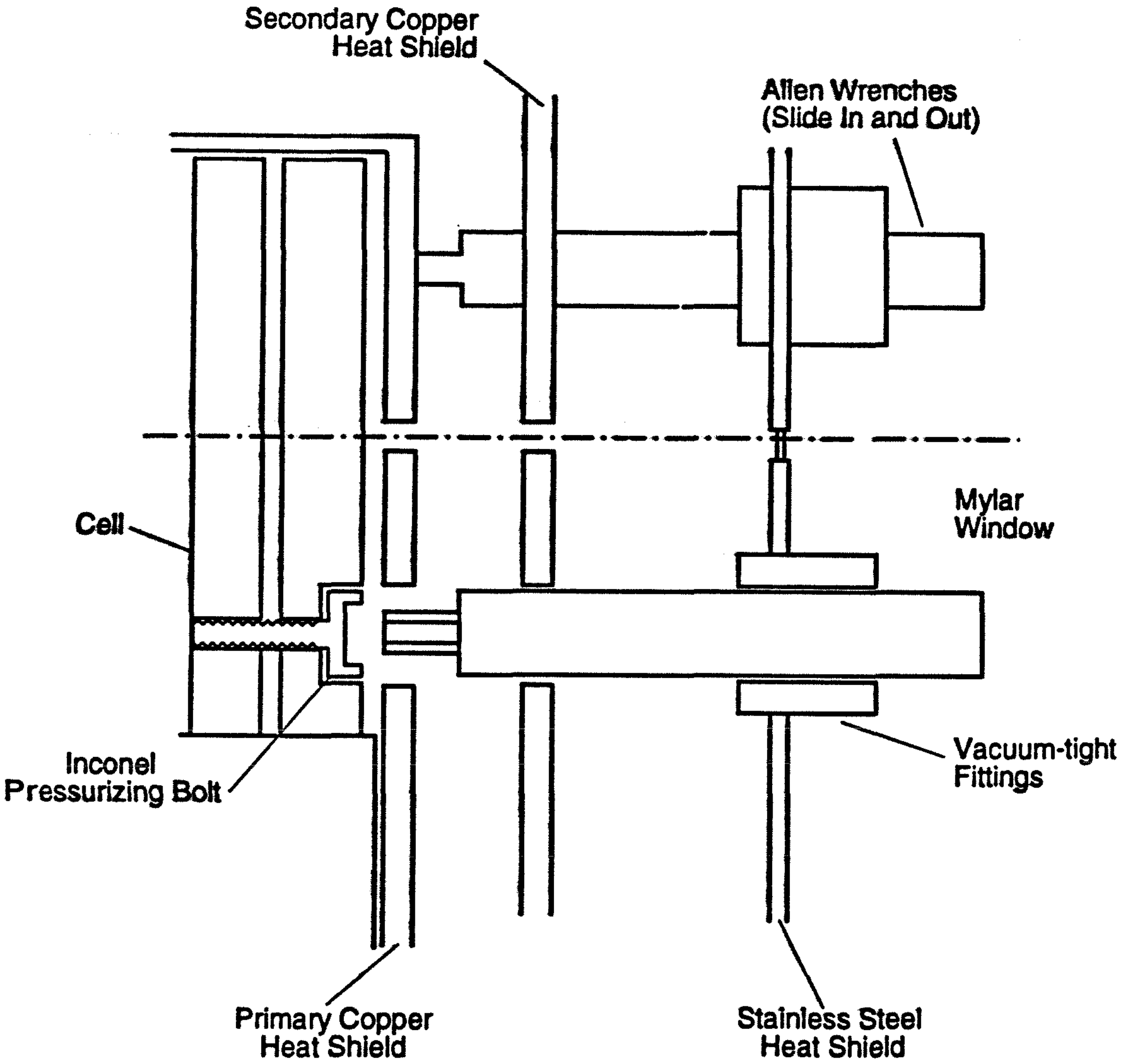

Figure 3.16 Detail of the cryogenic cell holder.

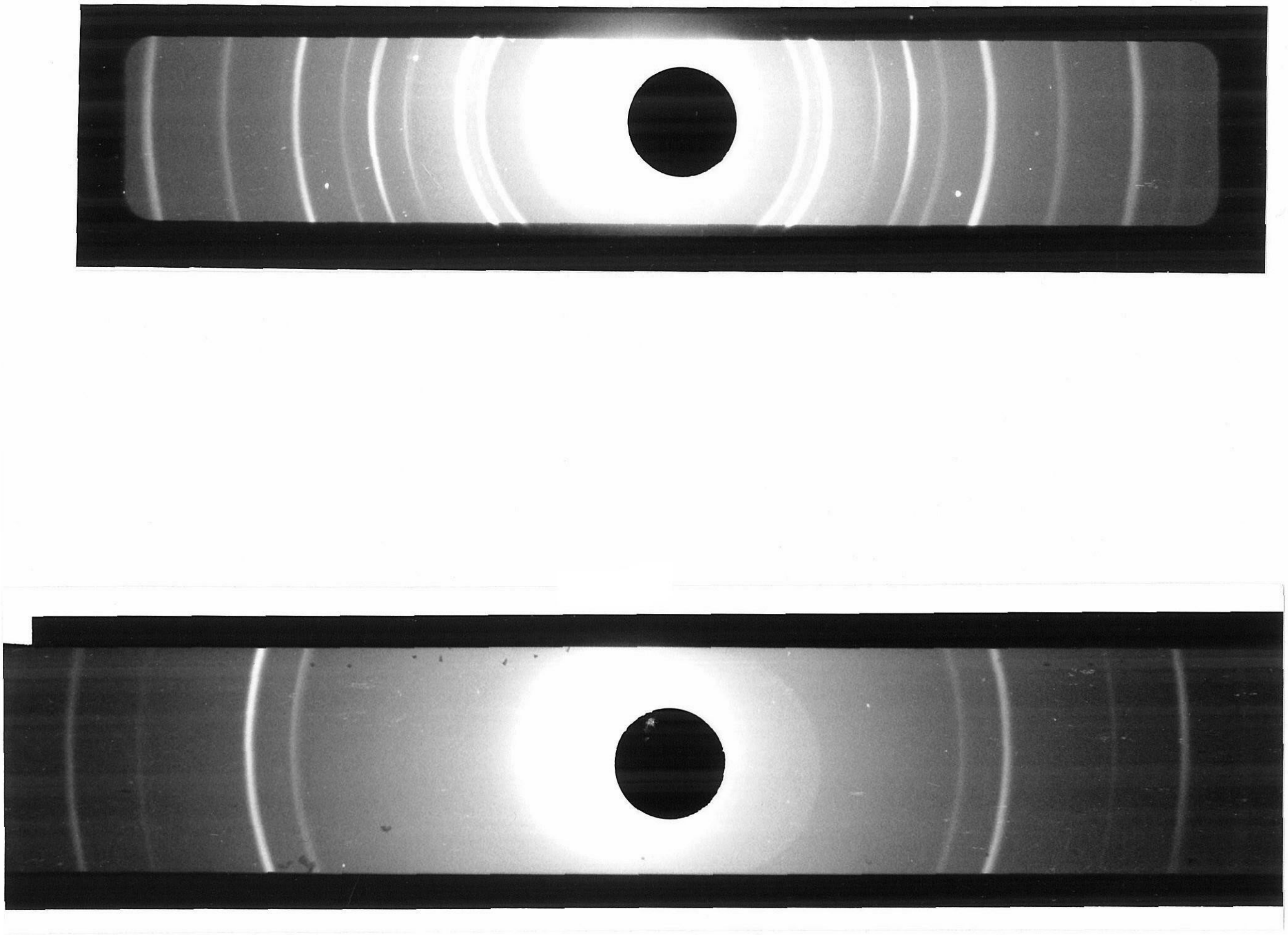

Figure 3.17 X-ray films from the front (top) and back (bottom) cameras.

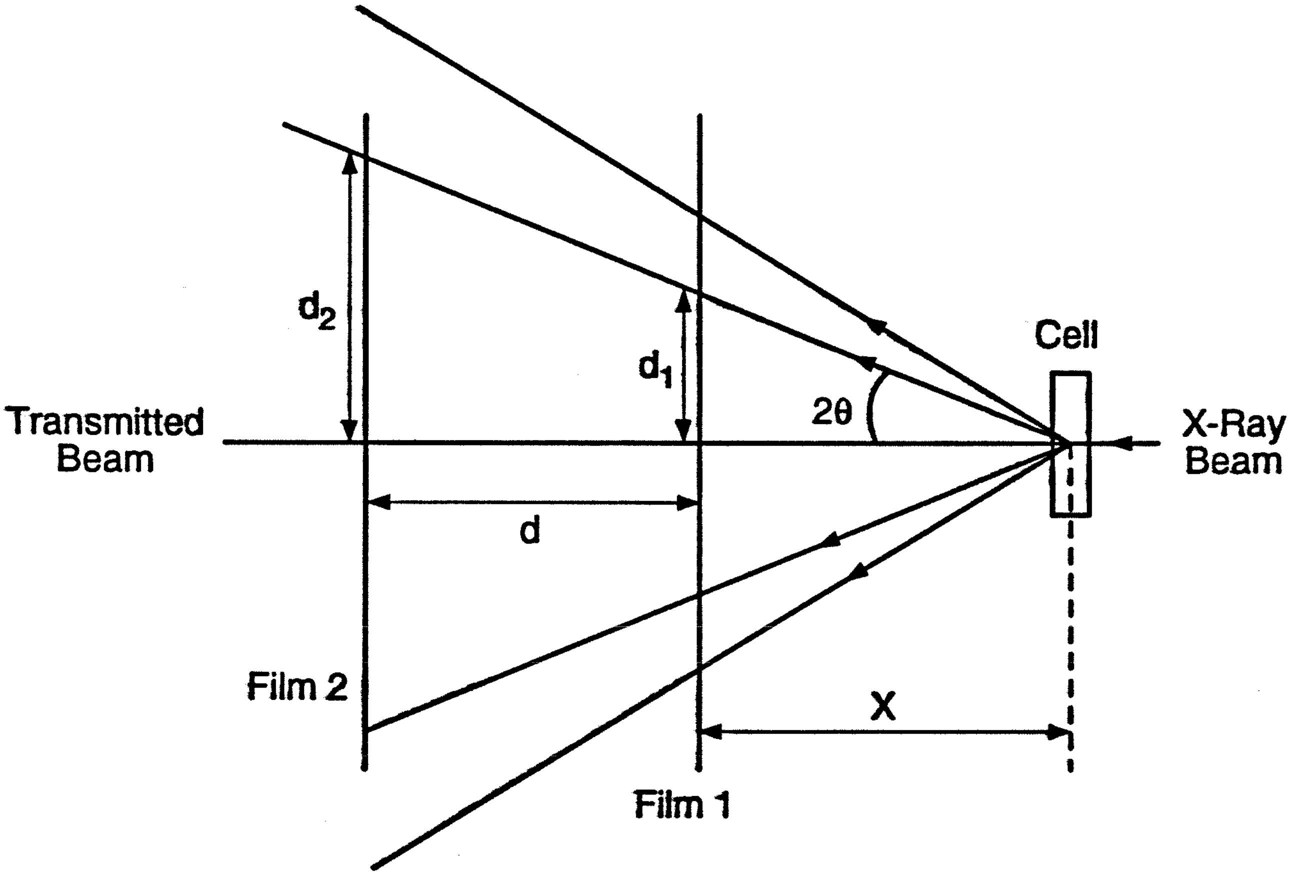

Figure 3.18 Geometry of the two-film cassette.

---

1. Spex Industries, Edison, New Jersey.
2. Scintag, Sunnyvale, California.
3. A. J. C. Wilson, Mathematical Theory of X-Ray Powder Diffractometry, Eindhoven:Philipps (1963).
4. E. N. Aqua, *Acta Crystall.* 20, 560 (1966).
5. H. P. Klug and L. Alexander, X-Ray Diffraction Procedures for Polycrystalline and Amorphous Materials (John Wiley and sons, New York, 1974), chapter 9.
6. B. D. Cullity, Elements of X-Ray Diffraction (Addison-Wesley, Reading, Massachusetts), 411 (1978).
7. P. J. Yvon and R. B. Schwarz, *J. Mater. Res.* 8, 239 (1993).
8. Leo Merrill and William A. Bassett, *Rev. Sci. Instrum.* 45, 290 (1974).
9. D. Schiferl, *Rev. Sci. Instrum.* 58, 1316 (1987).
10. American Society for Metals Handbook 3, 222.
11. R.A. Forman, G. J. Piermarini, J. D. Barnett, and S. Block, *Science* 176, 284 (1972).
12. J. D. Barnett, S. Block, and G. J. Piermarini, *Rev. Sci. Instrum.* 44, 1 (1973).
13. N. J. Hess and G. J. Exarhos, *High Press. Res.* 2, 57 (1989).
14. N. J. Hess and D. Schiferl, *J. Appl. Phys.* 68, 1953 (1990).
15. N. J. Hess and D. Schiferl, *J. Appl. Phys.* 71, 1082 (1992).
16. Keith Brister, Cornell University, private communication.
17. Michael Aziz, Harvard University, private communication.
18. A. S. Zinn, D. Schiferl, and M. F. Nicol, *J. Chem. Phys.* 87, 1267 (1987).
19. C. H. Macgillavry and G. D. Rieck, International Tables for X-ray Crystallography III, 157 (The Kynoch Press, Birmingham, England, 1962).
20. A. K. Singh, *Rev. Sci. Instrum.* 43, 1311 (1972).
21. S. W. Johnson, Ph. D. Thesis, UCLA (1991).

4. EXPERIMENTAL RESULTS

From this point on, we are going to denote f.c.c. aluminum by α-aluminum and diamond-structured germanium by β-germanium in order to simplify the notations.

4.1 Structure and Thermal Stability of Al-Ge Alloys Prepared by Rapid Solidification

The structure of the splat-quenched samples prepared at Caltech was characterized by x-ray diffraction (Figure 4.1). The samples were found to be a mixture of α -aluminum, and two metastable phases described in chapter 1: the rhombohedral γ_1 and the monoclinic γ_2 phases. The x-ray results are summarized in Table 4.1. We used the integral breadth method described in section 3.2.1 to deduce the crystallite size of these three phases. The results were 50 nm for aluminum, 83 nm for γ_1, 63 nm for γ_2. The samples were too small to be analyzed by DSC, but we know from previous work [1,2], including our own [3], that the two metastable phases decompose between 240 and 260°C. These splat-quenched samples were used first in the diamond anvil cell, but the x-ray diffraction patterns obtained were too weak. For subsequent experiments we used mechanically alloyed powders as starting alloy material, as the facilities to produce them were located at Los Alamos, whereas the splat-quencher was located at Caltech.

4.2. Structure and Thermal Stability of Al-Ge Alloys Prepared by Mechanical Alloying

4.2.1 Effects of Iron Contamination During Ball Milling

The experimental setup used to prepare the mechanically alloyed powders was described in section 3.1.1. In this section we discuss results obtained in $Al_{1-x}Ge_x$ alloys with $x > 0.7$. These alloy powders have been prepared by three techniques: a tungsten carbide vial (setup A), a hardened steel vial with hexane (setup B), and a steel vial without hexane (setup C).

For $Al_{25}Ge_{75}$ powders mechanically alloyed in tungsten carbide media and for milling times up to 90 h, the DTA and DSC traces show only the endothermic peak corresponding to the crossing of the eutectic line (Figure 4.2). However, for the first heating (curve a), the eutectic temperature and the melting enthalpy were approximately 9°C and 27 J/g lower than the values measured on a subsequent heating (curve b). For the second heating the eutectic melting peak occurs at its accepted value of 420°C. Similar shifts were observed previously in mechanically alloyed Ge-Sn alloys [4] and Pb-Ge alloys [5] and were explained by Turnbull et al. [6] as resulting from the thin-layer morphology taken by the soft element (Sn or Pb) in the mechanically alloyed powders. However, some recent experimental results [7] have not been supporting this theory, and Leonard and Koch [8] also expressed doubts. A simpler and more plausible explanation for this melting temperature depression and decrease in melting enthalpy is that the lattice and point defects produced during mechanical alloying raise the free energy of the crystalline α-aluminum and β-germanium phases and that this causes the free energies of the crystal and the liquid phases to cross at a lower temperature, as illustrated in Figure 1.3. The results in Figure 4.2 are typical of all powders prepared with the tungsten carbide media and for all MA times, the only differences being the size of the melting temperature and the melting enthalpy shifts.

For $Al_{25}Ge_{75}$ powders mechanically alloyed in steel media using hexane as dispersant (setup B), with increasing milling time, we observed that the endothermic eutectic peak at 420°C starts to disappear and another endothermic peak at 515°C appears (Figure 4.3). For a MA time of 15 h or less, the two endothermic peaks coexist on the first heating. However, on a subsequent heating of the same powder, we observed that the eutectic peak grew at the expense of the second peak (Figure 4.4). For the powders that were ball-milled more than 15 h, we did not see any peaks in the range $25 < T < 700^{o}C$ in any of the DTA runs, even after melting the alloys. We did, however, observe the melting of the alloy at its expected value of $820^{o}C$. These results were very puzzling at first because our weight measurements showed that the powders had little or no hexane contamination and because we suspected very little iron contamination.

For the powders ball-milled in steel media but with no hexane (setup C), we observed the same differential calorimetry results as those for the powders from setup B. This observation indicates that the presence of hexane during milling had no significant influence on the structure nor on the composition of the mechanically alloyed powders.

The x-ray diffraction patterns for powders alloyed in steel media (setups B and C) for 15 h or less show only β-germanium Bragg peaks. For milling times greater than 15 h, one or two other phases appeared on the x-ray diffraction patterns, which were found to be ternary phases of aluminum, germanium, and iron. The ternary phase diagram of Al-Fe-Ge has not been investigated, and the only section of it that has been determined is the iron-rich corner [9]. The crystalline phases that form on the iron-poor part of the ternary diagram are not known. We can, however, make educated guesses of the composition and structure of these phases from the Al-Fe-Si ternary phase diagram, which is known [10]. In this system, increasing amounts of iron on the silicon-rich side lead first to the formation of a τ_6 phase, and then to the formation of a τ_4 phase (see Figure 4.5). The structure of τ_4 is tetragonal, and its composition is about Al_4FeSi_2. The structure of τ_6 has been reported either as tetragonal or monoclinic (with lattice parameters $a \approx b$, and $\beta \approx 90^{o}$), and its composition is $Al_9Fe_2Si_2$. The ternary phase diagram for the Al-Fe-Ge system should be quite similar to that of Al-Fe-Si, and thus we expect the formation of ternary tetragonal phases of approximate composition Al_4FeGe_2 and $Al_9Fe_2Ge_2$. An attempt was made to identify these phases in our mechanically alloyed products by adding on purpose a given amount of iron before mechanical alloying

[11]. Another method was to prepare Al-Fe-Ge alloys by melting together the elements in a flux. Although the task of indexing these phases has not been completed, we are certain that the appearance of extra peaks in the DTA traces of Figures 4.3 and 4.4 are due to iron contamination introduced during MA when using steel media.

We use energy dispersive x-ray (EDX) analysis to investigate the iron contamination for the range of compositions $0.1 < x < 1$, but we performed a more extensive study on the composition $Al_{25}Ge_{75}$. Table 4.2 summarizes the EDX results. The first set of entries in the table (above the solid line) is for the calibration powders, whereas the second set of entries includes the powders mechanically alloyed using setup B. These data are plotted in Figures 4.6 and 3.3. Figure 4.6 shows the EDX measurements for the calibration $Al_{1-x}Ge_x$ powders. Here, the x-ray counts are normalized to the sum of aluminum and germanium counts. As for most binary alloys [12], the relationship between composition and the ratio of the number of counts is not linear. This non-linearity prevents us from using a matrix formalism to calculate the composition of the powders, given the number of counts. In Figure 3.3 we plotted the iron counts for the calibration $Al_{1-x}Fe_x$ and $Ge_{1-x}Fe_x$ powder mixtures. The x-ray counts for iron are normalized to the total number of counts. Because the curves do not coincide, we calibrated the EDX machine with $(Al_{25}Ge_{75})_{1-x}Fe_x$ alloys to study the iron contamination in our powders. Figure 3.3 also illustrates the calibration curves for these alloys.

The solid circles in Figure 4.7 show the EDX iron counts found in $(Al_{25}Ge_{75})_{1-x}Fe_x$ powders mechanically alloyed for various times between 15 min and 60 h. Using Figures 3.3 and 4.7, we are able to determine the precise amounts of iron in each of these powders. Figure 4.8 shows that the iron contamination in $Al_{25}Ge_{75}$ powder mechanically alloyed in steel media (setup B) increases linearly with MA time. The measured levels of iron contamination are higher than those we deduced from simply weighing the milling balls before and after MA. Apparently, iron eroded from the balls is partially replaced by aluminum-germanium powder that adheres to the balls.

The amount of iron in the mechanically alloyed powders was an increasing function of the atomic fraction of germanium in the powders. Figure 4.9 shows the iron contamination after 15 hours of ball milling for different compositions. An increase in contamination with increasing germanium concentration is to be expected, since germanium is the harder of the two components and therefore more likely to erode the balls and the vial.

Powders produced with setup A have no noticeable iron contamination; the single data point (solid triangle) in Figure 4.7 is for $Al_{25}Ge_{75}$ mechanically alloyed for 90 h and has the same number of iron counts as that for the initial mixture of elemental powders. Here, we also checked for tungsten and cobalt contamination, but we did not detect any traces of these two elements. Cobalt would be present if there were erosion of the tungsten carbide ball or vial, since it is used as a binding element for tungsten carbide parts.

From these studies, we deduced that the cleanest way to produce aluminum-germanium alloy powders is to use a tungsten carbide vial. However, for compositions richer in aluminum ($x < 0.5$), aluminum agglomerates on the ball and the vial. Because we wanted to have comparable starting powders for the diamond-anvil cell experiments, we used a steel media with hexane as dispersant to prepare powders at all compositions. Using Figures 4.8 and 4.9, we determined that a suitable length of time for MA would be 3 h for which the contamination is less than 0.5 at.% iron, and the crystallite size is in the nanometer range as discussed in section 4.3.

4.2.2. Formation of Metastable Phases by Mechanical Alloying

Rapid quenching of $Al_{1-x}Ge_x$ produces metastable phases, as discussed in section 1.5. MA is also known to produce metastable phases (e.g., amorphous alloy phases). We wanted to investigate the formation of non-equilibrium phases in the aluminum-germanium system, and we took x-ray diffraction patterns of the $Al_{70}Ge_{30}$ powder after different lengths of mechanical alloying in steel media using hexane as dispersant. We noticed the appearance of a metastable phase after approximately 5 h of ball-milling. Figure 4.10 shows x-ray diffraction patterns for 5 and 120 h of MA. Both patterns show Bragg peaks of α-aluminum, β-germanium, and a rhombohedral aluminum-germanium phase, the latter at the same positions as reported by Köster [13] (table 4.1). For $25^o < 2\theta < 30^o$, several of the Bragg peaks of the metastable γ_1 phase overlap with the (111) peak of pure β-germanium. Figure 4.11 shows a deconvolution of the x-ray signal in terms of three γ_1 peaks and the (111) peak of β-germanium. A similar deconvolution was done for other regions of 2θ. All the Bragg peaks found by this procedure belong to either β-germanium, α-aluminum, or the γ_1 phase (table 4.1).

The volume fraction of the γ_1 phase increases with MA time and approaches a saturation limit for a MA time of 120 h as shown in Figure 4.12 for $Al_{70}Ge_{30}$. We also observed the formation of this metastable phase in mechanically alloyed $Al_{80}Ge_{20}$, $Al_{75}Ge_{25}$, $Al_{60}Ge_{40}$, and $Al_{50}Ge_{50}$, but not for compositions outside the range 20-50 at. % germanium. The γ_1 phase becomes unstable at about 260°C; the x-ray diffraction patterns of mechanically alloyed powder that was annealed above this temperature shows only the Bragg peaks of α-aluminum and β-germanium.

We used DSC and DTA to study the decomposition of the γ_1. An exothermic peak was observed around 260°C for powders containing between 20 and 50 at.% germanium. This peak is due essentially to the decomposition of the γ_1 phase to α

-aluminum and β-germanium. Figure 4.13 shows two consecutive DSC heating curves on an $Al_{70}Ge_{30}$ sample. There is already an exothermic reaction starting around 125°C. This indicates that the temperature reached by the powder during mechanical alloying was at about 125°C, as there is no differences between the two DSC traces below this temperature. Annealing the powder in the DSC at various temperatures below 260°C and subsequent x-ray studies showed that the difference between the two DSC traces for $T < 260^{o}C$ was due to release of strain energy, to grain growth, and to a partial decomposition of the γ_1 phase. Most of the decomposition of the γ_1 phase occurs near 260°C, giving rise to the exothermic peak. The peak is very broad as a result of large grain size distribution. Presumably, the smaller grains decompose at a lower temperature than the larger grains, due to a greater surface energy and more nucleation sites. The enthalpy of decomposition of the γ_1 phase is shown in Figure 4.14 for $Al_{70}Ge_{30}$ for different milling times. This curve has the same shape as Figure 4.12.

The exothermic peak near 260°C was also observed in the DTA traces of $Al_{80}Ge_{20}$, $Al_{25}Ge_{75}$, $Al_{60}Ge_{40}$, and $Al_{50}Ge_{50}$. Figure 4.15 shows the enthalpy of transformation of $Al_{1-x}Ge_x$ mechanically alloyed for 15 h as a function of composition. This fitted curve is broad and shows a maximum for the equilibrium eutectic composition. This suggests that the γ_1 phase has a wide homogeneity range and that this compound is most stable near the composition $Al_{70}Ge_{30}$. A much less likely explanation for the shape of the curve in Figure 4.15 is that the efficiency for the formation of the γ_1 alloy by MA is largest at the composition $Al_{70}Ge_{30}$.

For $Al_{1-x}Ge_x$ alloys with $x < 0.5$, the iron counts did not change significantly with ball-milling time, and remained within the impurity level of the starting materials, below 0.5 at.% iron. This implies that the metastable γ_1 phase obtained by MA is intrinsic to the aluminum-germanium alloy system and to the processing MA technique, and is unrelated to iron contamination. In agreement with this, the DTA traces for the as-mechanically alloyed powder did not show the exothermic peaks near 520°C that we detected previously in iron-contaminated aluminum-germanium alloys [14]. Furthermore, on reheating these powders, the DTA traces showed only the expected endothermic peak at 420^{o}C corresponding to the crossing of the equilibrium eutectic melting temperature.

The severe plastic deformation of the powder particles during MA introduces lattice and point defects in the α-aluminum and β-germanium phases. This is largely an athermal, mechanically driven process. Some of these defects, however, recombine and annihilate during the MA. This thermally-activated process limits the net density of defects that is retained in the elements. During MA at an average temperature T, the defect density N stored in the pure elements changes at the rate [3]:

$$\frac{dN}{dt} = R_1(W) - R_2(T/T_m, W)N^{\alpha} \tag{4.1}$$

where R_1 describes the rate of defect generation which is a function of the attrition energy W; R_2 describes the rate of defect recombination at a constant value of the defect density. R_2 should increase with increasing values of T/T_m , where T_m is the melting temperature. R_2 is also a function of W because the attrition energy determines the maximum instantaneous temperature reached by the powder particles trapped between colliding balls. The exponent α describes the kinetics of defect recombination. For isolated defects recombining in pairs, we expect $\alpha \approx 2$. For $\alpha = 2$, integrating equation 4.1 yields:

$$N = \sqrt{\frac{R_1}{R_2}}.\tanh(\sqrt{R_1 R_2}\,t) \tag{4.2}$$

With increasing milling time the defect density approaches the saturation value $[R_1 / R_2]^{1/2}$. Because this value increases with decreasing T/T_m, under similar MA conditions, the defect density stored for long MA times will increase monotonically with the melting temperature. Such a dependence has been observed in mechanically alloyed f.c.c. metals [15] where the atomic-level strains (measured by x-ray diffraction) increase monotonically with T_m. We thus expect that germanium will store a larger defect density than aluminum. Based on these considerations, Figure 4.16 shows qualitatively the Gibbs free energies of α-aluminum and β-germanium before and after extensive MA. The figure also shows the free energy of the metastable γ_1 phase. Because aluminum has a lower melting temperature than germanium, we expect that after prolonged MA time the free energy of aluminum will saturate at a much lower value than germanium. The figure shows that there is a driving force for the strained α-aluminum and β-germanium to react and form the rhombohedral γ_1 phase. As the milling time increases, a bigger volume fraction of the metastable phase forms. However, there is little difference in the x-ray diffraction patterns of the powders mechanically alloyed for 60 and 120 hours. This is probably explained by the fact that as soon as the rhombohedral phase is formed, it gets strained and its Gibbs free energy raises as explained above for the pure α-aluminum and β-germanium phases. Thus, when a critical volume fraction of γ_1 is formed, a dynamic equilibrium is reached where the γ_1 phase dissociates into α-aluminum and β-germanium as fast as it forms.

The present results suggest that the composition of the metastable γ_1 phase is close to $Al_{70}Ge_{30}$, as this is the composition for which the largest volume fraction of this metastable is produced.

The Al-Ge foils prepared by rapid solidification showed two metastable phases: the γ_1 phase already discussed and also the monoclinic γ_2 phase (section 4.1.1). We searched carefully for the Bragg peaks of the γ_2 phase in the x-ray diffraction patterns of the mechanically alloyed powders, but we were unable to detect them. Previous studies on rapidly quenched Al-Ge alloys [13,16,17] report the composition of the γ_2 phase to be close to $Al_{50}Ge_{50}$ and, thus, we expected to produce it by MA over a wide composition range centered around the equimolar composition. That this phase was not produced by MA is probably due to its free energy lying above the common tangent to the free energies of the strained α-aluminum and β-germanium phases.

4.2.3. Evolution of the Crystallite Size and Residual Strain During Ball Milling

The crystallite size and the residual strain in the mechanically alloyed powders were studied using the broadening of the x-ray diffraction peaks. The grain size obtained by ball milling was approximately 60 nm, and the strain, 0.25% for aluminum and 30 nm and 0.8% for germanium. Figures 4.17 and 4.18 show typical integral breadth analyses of the β-germanium and α-aluminum peaks for $Al_{70}Ge_{30}$ powders. The integral breadths for three powders are plotted: a reference powder prepared by grinding in a mortar aluminum and germanium powders, a mechanically alloyed powder, and a mechanically alloyed powder after an anneal at 300°C. A smaller grain size and a larger strain were obtained for germanium, which is to be expected, as germanium has a higher melting temperature than aluminum and does not recover as well at the milling temperature (estimated to be between 100 and 150°C [18,19]). This also was observed by Eckert et al. for different f.c.c. metals [15]. The grain size and strain did not vary much with the composition of the mechanically alloyed powders, so we focused this study on the alloy composition $Al_{70}Ge_{30}$. We studied the evolution of the grain size and the strain with increasing ball milling time. Figures 4.19 and 4.20 show the crystallite size and strain for different milling times. We observe that with increasing MA time the crystallite size reaches a minimum value for both aluminum (about 23 nm) and germanium (about 14 nm). The strain increases and reaches a maximum value of about 0.25% and 1% for aluminum and germanium, respectively. We also studied the influence of the ball milling temperature on these two parameters. After milling $Al_{70}Ge_{30}$ for 5 hours in hexane, we removed the hexane, and ball milled further this powder. The mechanical alloying was performed in 5-minute intervals, cooling the vial in between in liquid nitrogen for 10 minutes. This ensured that the milling temperature did not raise above room temperature. The strain obtained was greater and the grain size smaller as shown in Figures 4.19 and 4.20, where an open star represents germanium, and the filled star represents aluminum. Ball milling at a lower temperature causes the rate of defect recombination R_2 (from Eq. 4.1) to decrease, therefore increasing the maximum defect density stored, as it goes as $R_2^{-\frac{1}{2}}$. The speed at which the defects forms also increases as easily deduced from equation 4.1. This explains why mechanical alloying at low temperatures causes the crystallite size to decrease at a higher rate to a lower value, whereas the strain increases at a higher rate to a higher value.

.4.2.4. Optimal Conditions for the Preparation of the Starting Materials for Pressure Experiments

Now that we have learned about the effects of MA on the aluminum-germanium alloy system, we can choose the adequate experimental conditions to prepare the starting materials for the high pressure experiments. The starting materials for the high pressure experiments were prepared in the following manner. First they were ball milled for 3 hours to ensure small grain size and store energy in the form of lattice and point defects. The powders used for the diamond anvil cell samples were mechanically alloyed for a short time to prevent the formation of metastable phases and to limit the contamination from the milling media. These powders were also annealed at 300° C to ensure that the starting materials would be a mixture of α-aluminum and β-germanium. The typical grain size was 65 nm, and the typical strain was 0.2% for aluminum and 35 nm and 0.6% for germanium. The x-ray diffraction pattern of a typical starting powder is shown in Figure 4.21. The anneal, aside from allowing the decomposition of the γ_1 phase, increases slightly the grain size, but does not affect much the strain in the starting materials.

4.3. In situ X-Ray Studies of Pressure-Driven Transformations in Al-Ge

In situ x-ray diffraction patterns were difficult to obtain and to analyze for a variety of reasons. The first problem was one of resolution: to obtain an *in situ* diffraction pattern, the x-ray beam had to traverse both diamonds. The loss of intensity prevented us from using a monochromator, as this would have increased excessively the exposure times to about one to two weeks. The x-ray diffraction pictures obtained were never totally clean, and even with the use of a zirconium filter, the characteristic K_β line of the molybdenum radiation and the bremstrahlung were always present. The second problem was that the gasket ($Mo_{90}Re_{10}$) was transparent to the x-ray beam and thus it contributed to the diffraction pattern. A third problem was that the sample thickness was typically between 50 and 100 μm. Therefore, the thickness of the aluminum phase was less than 50 μm, which is way too thin for ideal diffracting conditions: the mass-absorption coefficient for molybdenum K_α radiation is $\mu/\rho = 5.043\ cm^2\ gm^{-1}$ and the density of aluminum is $\rho = 2.70\ gm\ cm^{-3}$ [20]. This yields $\mu = 13.62\ cm^{-1}$, and thus the optimum thickness of the aluminum should be close to $\mu^{-1} \approx 700\ \mu m$. Similarly, for germanium and molybdenum μ^{-1} are 31 μm and 53 μm, respectively. Therefore, the thickness for germanium and the molybdenum gasket were close to the optimum values for diffraction. This explains why the α-aluminum diffraction rings were so hard to observe. The fourth problem in these studies was that the weak amorphous diffraction halos could not be distinguished from the superimposed bremstrahlung. We could infer on the formation of an amorphous phase by default through the absence of any crystalline diffraction rings, except of course for those of the Mo-Re gasket. It was not possible to obtain the positions of the amorphous diffraction halos.

According to previous works, the phases we expected to observe in our diffraction patterns were (beside α-aluminum and β-germanium) six high-pressure phases of germanium [21] and two high-pressure phases of composition $Al_{30}Ge_{70}$ [22]. The summary of these phases can be found in Table 1.2. Another crystalline phase that could have been present in the diffraction pattern was samarium YAG. The composition of this phase is $Al_5Y_3O_{12}$ doped with 4 at.% samarium. Its structure is b.c.c. with a lattice parameter of 1.20089 nm [23]. The strongest x-ray diffraction peaks are listed in Table 4.3. Because we used such minute quantities of YAG, we did not expect it to contribute significantly to the diffraction pattern.

4.3.1. Experiments at High Pressures and Temperatures

Figure 4.22 summarizes the composition, pressure, and temperature for the experiments done in the diamond cell at high temperatures. For these experiments we chose alloy compositions on the aluminum-rich side of the binary phase diagram, since our initial goal was to first produce a single-phase f.c.c. solid solution of aluminum and germanium, and then follow a thermobaric path similar to that shown in Figure 2.12. We did not study pressure-induced structural changes at room temperature, since the main focus was to use pressure and temperature to produce a supersaturated solution of germanium in α-aluminum.

Typically, the samples were first loaded in the diamond cell, and the pressure increased until a value above 120 kbar was reached. The pressure was obtained from the shifts of the fluorescence peaks of samarium YAG with pressure. We then brought the samples to temperatures typically in the 300-400^{o}C range. We know from previous studies (see Figure 3.12) that the pressure in the cell drops when the sample is heated. Our objective was to apply a pressure higher than 80 kbar (8 GPa) at high temperatures, in order to be inside the solid solution phase-field (illustrated by point C in Figure 2.12). We subsequently cooled the diamond anvil cell to 50 K (point D in Figure 2.12) and obtained a x-ray diffraction pattern under pressure before releasing the pressure and taking another x-ray diffraction pattern at ambient pressure. We did not notice any differences if we cooled the cell to only room temperature and released the pressure. The thermobaric treatment illustrated in Figure 2.12 was performed for most samples with point D being at room temperature.

We first experimented with a piece of splat-quenched $Al_{70}Ge_{30}$. This sample was brought to 90 kbar (9 GPa) and 500°C. No x-ray diffraction patterns were obtained *in situ* because of severe intensity problems with the x-ray diffraction apparatus. However, a diffraction pattern was taken after opening the cell, on the sample stuck to one of the two diamonds. This pattern showed only diffraction rings of an f.c.c. structure with a lattice parameter a = 0.4035 nm. Because the β-germanium rings were absent, we concluded that the f.c.c. structure was a solid solution of aluminum and germanium. However, according to Eq. 1.8, the lattice parameter for a 30 at.% Ge solid solution should be 0.410 nm. The difference in lattice parameters suggests that this solid solution coexists with an amorphous phase richer in germanium which we could not detect by x-rays.

The following experiments were done on mechanically alloyed and annealed aluminum-germanium powders. A typical x-ray diffraction pattern of these powders is shown in Figure 4.21. Two results were obtained in these samples depending on the pressure. For pressures lower than 80 kbar (8 GPa), we observed a mixture of α -aluminum and β-germanium when the sample was brought to temperature (between 300 and 400°C), and was retained after cooling down to room temperature. For pressures higher than 80 kbar (8 GPa), we only observed faint rings of a f.c.c. structure. These rings were very faint on the diffraction patterns taken at temperatures, and no lattice parameter measurement was possible. On cooling the diamond anvil cell to room temperature, we were able to measure the *a*-lattice parameter under pressure with an uncertainty of 0.003 nm and found it to be between 0.390 and 0.395 nm. We could not establish any correlation between pressures, composition and lattice parameters, as the measurement error was too big. After measuring the lattice parameter under pressure, we released the pressure and took an x-ray diffraction pattern at ambient pressure. After releasing the pressure at room temperature on these samples, we only observed diffraction rings of an f.c.c. structure with lattice parameters ranging between 0.407 and 0.411 nm, and still very faint. We heated these samples in increments of 50^{o}C and did not observe any noticeable changes. The α-aluminum diffraction rings appeared to get a little fainter and broader, but there was no clear evidence of amorphization. Above 300^{o}C, the structure changed to the equilibrium mixture of α-aluminum and β-germanium, with *a*-lattice parameters of 0.404 (± 0.001) nm and 0.565 (± 0.001) nm, respectively.

The x-ray generator met an untimely demise in the middle of the experiments (blown transformer) and the entire x-ray diffraction apparatus had to be transferred to a Philips generator. We had to design and build new adapters between the tube and the setup, and we did not have the same accuracy in the alignment of the beam, and the diffraction patterns became weaker due to this problem.

In conclusion, the *in situ* experiments at high pressures and temperatures were inconclusive and did not confirm or infirm the possibility of amorphization through the first mechanism described in section 2 and Figure 2.12. However, some interesting results were recorded when the pressure was increased at ambient temperature, and we decided to study them more in detail.

4.3.2. Experiments at ambient T as a function of P

We decided to study the evolution of the x-ray diffraction patterns as the pressure was increased slowly at room temperature. After turning the three bolts of the diamond anvil cell 1/16th of a turn at a time, we measured the pressure and took a nx-ray diffraction pattern. Typically, this increased the pressure by 10 to 15 kbar (1 to 1.5 GPa).

For pressures lower than 25 kbar (2.5 GPa), the diffraction patterns remained unchanged from the initial patterns of the powders at atmospheric pressure, except for a reduction of the lattice parameters. For pressures above 25 kbar (2.5 GPa), a new phase started to appear in coexistence with α-aluminum and β-germanium. This phase was easy to detect because instead of having the uniform and smooth rings of α-aluminum and β-germanium, it had spotty rings. With increasing pressure, the α-aluminum and β -germanium rings gradually vanished, and the diffraction spots of the new phase became more abundant and formed uniform rings. The strong reflections of this new phase were between 0.260 and 0.270 nm for the strongest one and between 0.240 and 0.250 nm for the second one, depending on the pressure. A weaker reflection was observed around 0.180 nm. The d-spacings of the new phase were independent of the composition of the starting material, but decreased as pressure increased. This high-pressure phase seemed to be in agreement with the hexagonal γ phase reported by Barkalov and coworkers [22], as the three reflections obtained matched the first three reflections they reported.

Figure 4.23 shows the pressure in the diamond anvil cell as a function of the number of times we tightened the bolts. The pressure increased almost linearly with the turning of the bolts, until the pressure reached 75 kbar. At around 75 kbar we noticed that the pressure remained constant as the bolts were tightened several times. After three tightenings, the pressure started to increase again. X-ray patterns taken at pressures above the pressure plateau did not show any diffraction peaks, except for the Bragg peaks of the gasket. This was our first clear observation of pressure-induced amorphization in the Al-Ge system. These measurements also show that the amorphization reaction is accompanied by a large volume decrease. We will further show in section 5.3 that this amorphous phase is a high density metallic phase.

Because we could infer on the formation of the amorphous Al-Ge phase only through the absence of crystalline diffraction (except those of the gasket), we investigated carefully whether the lack of diffraction rings was an experimental artifact. We first suspected that the cell became misaligned and that the x-ray beam was missing the sample. However, after repeatedly realigning the cell and taking new x-ray diffraction patterns several times, the only diffraction rings we obtained were those of the gasket. This prompted us to find a way to ensure that the x-ray beam was going through the sample. We designed an x-ray energy dispersive attachment to the x-ray diffraction apparatus, which enabled us to detect the fluorescence peak of germanium. With this detector we were sure the x-ray beam was traversing the sample. X-ray diffraction patterns taken with the cell aligned in this fashion still did not show any Bragg peaks except those of the gasket. We concluded that a phase transition associated with the volume decrease at around 75 kbar (7.5 GPa) (Figure 4.23) made the sample fully amorphous.

We did not notice any differences in the x-ray diffraction patterns after releasing the pressure which indicated that the amorphous phase formed at pressure was either metastable at ambient pressure or had transformed to another amorphous phase. We observed this behavior first in $Al_{80}Ge_{20}$, and subsequently in $Al_{75}Ge_{25}$, $Al_{70}Ge_{30}$, and $Al_{50}Ge_{50}$.

We observed that the amorphous Al-Ge samples transformed back to a mixture of α-aluminum and β-germanium when heated above $300^{o}C$, either under pressure or after releasing the pressure.

These results prompted us to design a different experiment to be able to investigate further the effects of a pressure increase at room temperature. The fact that an amorphous phase was retained after release of the pressure led us to make samples we could observe by TEM.

4.4. Ex situ TEM Studies of Pressure-Driven Transformations in Al-Ge

Figure 4.24 shows the pressure-composition map of the TEM samples prepared and the way they were stored after preparation. Amorphous metallic alloys are metastable and crystallize when heated above T_x. We observed crystallization both under pressure and at ambient pressure between 250 and $300^{o}C$. Because we did not know if any structural changes would occur at room temperature, we separated the samples into three groups: one group was kept in liquid nitrogen at all times, another was kept at room temperature for a week, and then placed in liquid nitrogen, and the third group was kept at room temperature at all times. The samples were prepared directly on TEM copper grids as explained in section 3.4. More samples would have been made, but this method proved to be expensive (diamond-destructive), as the copper sample holder did not provide enough support to the edges of the diamonds, and three diamonds were broken in the process, leaving us unable to prepare any more samples. The samples obtained through this method were thin enough to be observed directly by transmission electron microscopy with no additional preparation.

In the TEM micrographs we saw various crystalline and amorphous phases. Energy dispersive x-ray (EDX) spectroscopy is the easiest method to identify these phases. However, for most of the tests conducted in the fall of 1992, the EDX detector in the TEM of the Center for Materials Science was broken. We learned, however, to recognize the phases by their diffraction pattern. The copper grid could be easily recognized by its typical f.c.c. diffraction pattern with a small lattice parameter. The samarium YAG could be easily recognized because it has a large lattice parameter of 1.2 nm, much larger than that of any of the other phases. A typical bright field micrograph of Sm YAG is shown in Figure 4.25, and the corresponding pattern (zone axis 001) is shown in Figure 4.26.

Because for these samples we did not use gaskets, the pressure was not constant and decreased rapidly away from the sample center, as shown in Figure 4.27. The pressure to which we will refer in the next sections is the maximum pressure near the center of the samples which we measured by the laser fluorescence method (section 3.2.2). We studied by TEM the structure of over 20 samples near the center and away from it. We can rattionalize these observations as described in the next sections.

4.4.1 Pressures Less Than 60 kbar

For $P < 60$ kbar (6 GPa) and for all compositions, the samples did not show any amorphous phases. In every area we examined the structure was fully crystalline. Beside the copper and the samarium YAG, the only other phases present were α-aluminum and β -germanium, these two always present together. Figure 4.28 is a TEM bright field picture from a mixture of α-aluminum and β-germanium for the composition $Al_{75}Ge_{25}$ after mechanically alloying for 3 hours and pressing at 40 kbar (4 GPa). From this micrograph we estimate that the crystallites (aluminum and germanium) have sizes below 50 nm. This number agrees with the crystallite sizes we determined by x-ray diffraction (section 4.2.3). The selected area diffraction (SAD) pattern for these bright field pictures is shown in Figure 4.29. The strong two sets of diffraction spots can be located onto rings corresponding to the diffraction rings of α-aluminum with a lattice parameter of 0.410 nm and β-germanium with a lattice parameter of 0.581 nm. The few weak diffraction spots in the pattern belong to samarium YAG.

4.4.2 Pressures Between 60 and 80 kbar

In this pressure range, and for compositions between 20 and 50 at.% germanium, we found near the center of the sample areas where a crystalline structure was imbedded in an amorphous matrix. We denote this phase amorphous phase I. We found the same structure away from the center in samples that were taken to higher pressures, up to 200 kbar (20 GPa). Figures 4.30 and 4.31 show typical TEM micrographs of these areas for $Al_{70}Ge_{30}$ pressed to 200 kbar. In the lower magnification micrograph of Figure 4.30, the dark spots are crystalline material which happen to be in a diffracting condition. Some of the crystallites appear as thick double or triple bands. These bands are the so-called 'bend contours' and tell us that the crystallites are heavily strained. In the higher magnification TEM micrograph of Figure 4.31, we see many Moiré fringes caused by double diffraction. Towards the bottom of the figure we see clearly a 'bent contour'. Figure 4.32 shows a typical diffraction pattern. Although Figures 4.30 to 4.32 are for samples pressed to a maximum pressure of 200 kbar, these areas are typical of the 60-80 kbar pressure range.

In Figure 4.32, we see the diffuse halos of an amorphous phase, and sharp rings. The halos for the amorphous phase I were found to be independent of the composition of the starting material and were located at $k = 19.57\ \mathrm{nm}^{-1}$ and $k = 32.72\ \mathrm{nm}^{-1}$. The diffraction rings matched a f.c.c. structure with a lattice parameter of 0.405 nm, and we concluded that they corresponded to crystalline α-aluminum. These phases are similar to those obtained in aluminum-germanium alloys prepared by rapid solidification for compositions on the aluminum-rich side of the diagram [24,25].

Figure 4.33 shows the positions of the first two diffraction halos of the amorphous phase I obtained in the 60-80 kbar pressure range. We notice that in the cases where the amorphous phase I is in equilibrium with α-aluminum, the nearest neighbor distance (proportional to k^{-1}) is independent of the germanium content, whereas k^{-1} increases with increasing germanium content when a single phase amorphous alloy is produced. These observations suggest that the alloy stability is determined by a free energy diagram as in Figure 4.34 for the free energies of α-aluminum and the amorphous phase as a function of composition. For compositions between 20 and 50 at.% Ge, α-aluminum is in thermodynamic equilibrium with the amorphous phase. That the amorphous phase has a constant composition accounts for the fact that the position of the amorphous halos is invariant. On the other hand, for germanium concentrations higher than 60 at.%, the amorphous alloy is single phase, and its composition varies, causing the diffraction halos to vary. Figure 4.33 predicts that the composition range of the amorphous phase I is between 60 and 100 at.% germanium, and that the amorphous phase which is in equilibrium with α-aluminum contains 60 at.% Ge.

Figures 4.35 and 4.36 are from a $Al_{40}Ge_{60}$ sample pressed to 180 kbar which became single-phase amorphous. The first two diffraction halos are at $k = 19.57$ nm^{-1} and $k = 32.72$ nm^{-1}.

4.4.3 Pressures Greater than 80 kbar

For pressures above 80 kbar we observed the same mixtures of amorphous Al-Ge and α-aluminum observed at lower pressures. The amorphous phase I coexisted with α -aluminum for all compositions except for $Al_{40}Ge_{60}$, where we observed a single phase amorphous alloy; but we also observed a second amorphous phase, called amorphous phase II, clearly different from the first one. For $80 < P < 140$ kbar, the amorphous phase II formed only near the center of the TEM specimens whereas for $P > 140$ kbar, the amorphous phase II was detected in a large portion of the samples. The first two diffraction halos of this phase were located around $k = 29.92$ nm^{-1} and $k = 55.12$ nm^{-1} and thus the amorphous phase II is much denser than the amorphous phase I. The amorphous phase II was present at all compositions, and the locations of the halos were independent from the composition of the starting material. Figures 4.37 and 4.38 show bright field pictures of this amorphous phase for $Al_{40}Ge_{60}$ at 180 kbar (18 GPa) and $Al_{60}Ge_{40}$ pressed to 140 kbar (14 GPa), repectively. Amorphous phase II always appeared to have a smoother morphology than amorphous phase I (more homogeneous in thickness and smoother edges). Figure 4.39 shows the diffraction pattern that corresponds to the bright field image in Figure 4.38. The diffuse diffraction halos of phase II were always very faint suggesting that the halos are wider than those in phase I. Wider halos are indicative of an amorphous structure with a low degree of short-range order and/or atomic level strains (lack of relaxation).

To investigate the composition of these two amorphous phases, we performed EDX on selected samples ($Al_{70}Ge_{30}$, $Al_{60}Ge_{40}$, and $Al_{30}Ge_{70}$). For any given sample we measured the same composition at every region we analyzed, meaning that there was no aluminum or germanium solute segregation within the sample. This analysis also showed than the samples were free of iron contamination as shown in Figure 4.40 for an EDX pattern obtained at the TEM facilities of the University of New Mexico in Albuquerque. The samples examined on the EDX system at CMS showed iron and cobalt peaks that concerned us. But these peaks also showed up on the EDX analysis of the copper grid alone; we found out that these two peaks were intrinsic to the system, as the EDX detector window has been intentionally pushed far back to prevent another accidental breaking of the window. The first such occurrence deprived CMS from an EDX system for over eight months.

4.4.4. Polymorphic Pressure-Composition Phase Diagram

The results obtained are summarized in Figure 4.41. Figure 4.41 shows the compositions and pressures for which we detected the presence of an amorphous phase I with diffraction halos around $k = 19.57$ nm^{-1} and $k = 32.72$ nm^{-1}. This phase was found in equilibrium with α-aluminum crystallites in all samples, except for the $Al_{40}Ge_{60}$ samples where a single amorphous phase I alloy was produced. This figure also shows the pressures and compositions for which we detected, in addition to the amorphous phase I, the presence of the amorphous phase II with diffraction halos located at $k = 29.92$ nm^{-1} and $k = 55.12$ nm^{-1}.

Table 4.1. Summary of the x-ray diffraction peaks. The values for the rhombohedral γ_1 phase (a=0.767 nm and α=96.55°) and the monoclinic γ_2 phase (a=0.6734 nm, b=0.5818 nm, c=0.4282 nm, and β=88.98°) are from reference 13.

Aluminum	Germanium	γ_1	γ_2	d-spacing (calculated)	as MA (measured)	after anneal (measured)	splat (measured)
		1 0 -1		5.726			5.692
		1 1 0		5.031			
			-1 1 0	4.402			4.379
		2 0 0		3.779			
			1 0 1	3.643			3.626
			-1 0 1	3.584			
		2 0 -1		3.569			3.569
			0 1 1	3.448			3.436
			2 0 0	3.367			3.330
		2 -1 -1		3.306	3.293		2.292
	1 1 1			3.262	3.258	3.257	
		2 1 0		3.219	3.211		3.206
		2 1 -1		3.154	3.146		3.142
			-1 1 1	3.051			3.043
			-2 0 1	2.914			2.904
			0 2 2	2.909			2.904
		2 0 -2		2.863			2.852
		2 1 1		2.800	2.792		2.790
		2 1 -2		2.677	2.670		2.665
			-1 2 0	2.670			2.665
		2 2 0		2.516	2.507		2.507
		3 0 -1		2.488			2.480
			-2 1 1	2.391			2.371
1 1 1				2.332	2.334	2.342	2.335
		3 1 -1		2.306	2.300		2.299
		3 1 0		2.303	2.300		2.299
		2 2 -2		2.282			2.280
		3 0 -2		2.233			2.233
		3 -1 -2		2.164	2.160		2.159
2 0 0				2.020	2.021	2.027	2.023
	2 2 0	3 2 0		1.998	1.997	2.000	1.997
			-2 2 -1	1.967			1.968
			-2 2 1	1.948			1.941
		3 0 -3		1.909	1.905		1.904
		4 0 0		1.890	1.886		1.886
		4 -1 -1		1.874			1.874
			-3 2 0	1.777			1.776
		4 -1 -2		1.761			1.757
	3 1 1			1.704	1.704	1.703	

			1 2 2	1.676			1.673
		4 -2 -2		1.653	1.649		1.657
			-3 2 -1	1.650			1.649
		4 2 0		1.609	1.607		1.606
		4 2 -2		1.577	1.572		1.574
			2 3 -1	1.559			1.561
		4 2 1		1.524	1.518		1.517
		2 0 5		1.470	1.467		1.467
		2 3 3		1.444	1.445		1.444
2 2 0				1.428	1.430	1.431	1.430

Table 4.2. Energy Dispersive Results

sample	germanium counts	aluminum counts	iron counts
$Al_{25}Ge_{75}$	74.19	11.91	13.90
$Al_{25}Ge_{75}$	74.11	11.58	14.31
$Al_{24.3}Ge_{73.3}Fe_{2.3}$	48.59	11.31	40.10
$Al_{24.3}Ge_{73.3}Fe_{2.3}$	49.92	9.98	40.10
$Al_{23.9}Ge_{71.9}Fe_{4.2}$	42.74	7.02	50.24
$Al_{23.9}Ge_{71.9}Fe_{4.2}$	41.57	7.03	51.40
$Al_{23.4}Ge_{69.6}Fe_{7.0}$	36.53	3.70	59.77
Al	0.13	95.07	4.80
$Al_{97.6}Fe_{2.4}$	0.26	59.47	40.27
$Al_{94.0}Fe_{6.0}$	0.24	38.88	60.88
Ge	83.34	0.52	16.03
$Ge_{97.2}Fe_{2.8}$	49.60	0.92	48.48
$Ge_{94.1}Fe_{5.9}$	42.99	0.50	56.51
$Al_{25}Ge_{75}$ MA 15 min	75.48	4.83	19.69
$Al_{25}Ge_{75}$ MA 7.5 hrs	66.70	4.81	28.49
$Al_{25}Ge_{75}$ MA 15 hrs	57.68	4.20	38.12
$Al_{25}Ge_{75}$ MA 42 hrs	34.27	2.26	63.47
$Al_{25}Ge_{75}$ MA 60 hrs	30.76	2.73	66.51

Table 4.3. Strongest X-Ray Diffraction Peaks of Samarium YAG. The structure is b.c.c. with a = 1.20089 nm.

d (nm)	Intensity	hkl	d (nm)	Intensity	hkl
0.4905	27	211	0.17730	17	444
0.3210	19	321	0.16652	31	640
0.3002	27	321	0.16338	9	721
0.2687	100	400	0.16046	28	642
0.2452	20	422	0.15006	10	800
0.2192	23	521	0.13102	31	640
0.19474	26	532	0.11151	14	1040

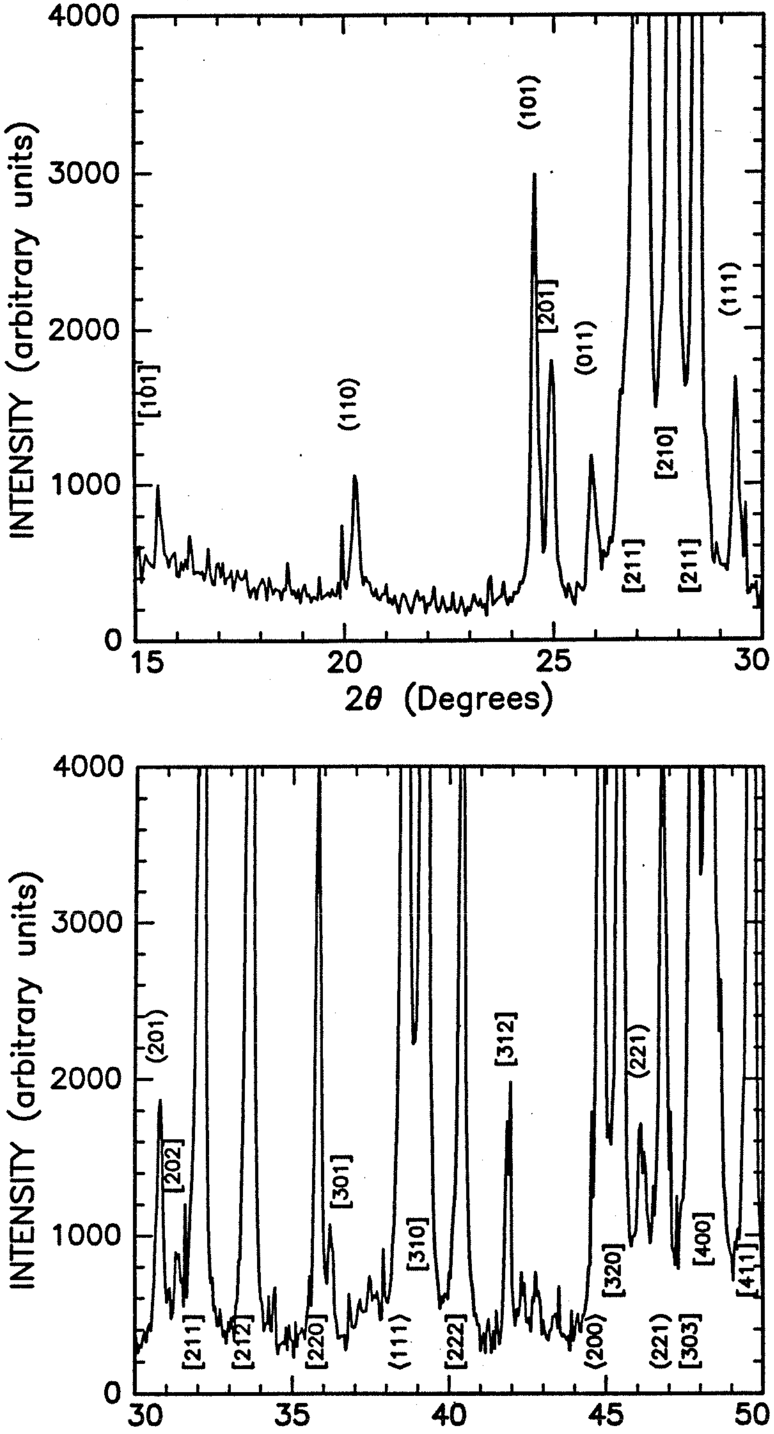

Figure 4.1 X-ray diffraction pattern of splat-quenched aluminum-germanium alloy. [] represents the γ_1 peaks, () represents the γ_2, and <> represents the α -aluminum peaks.

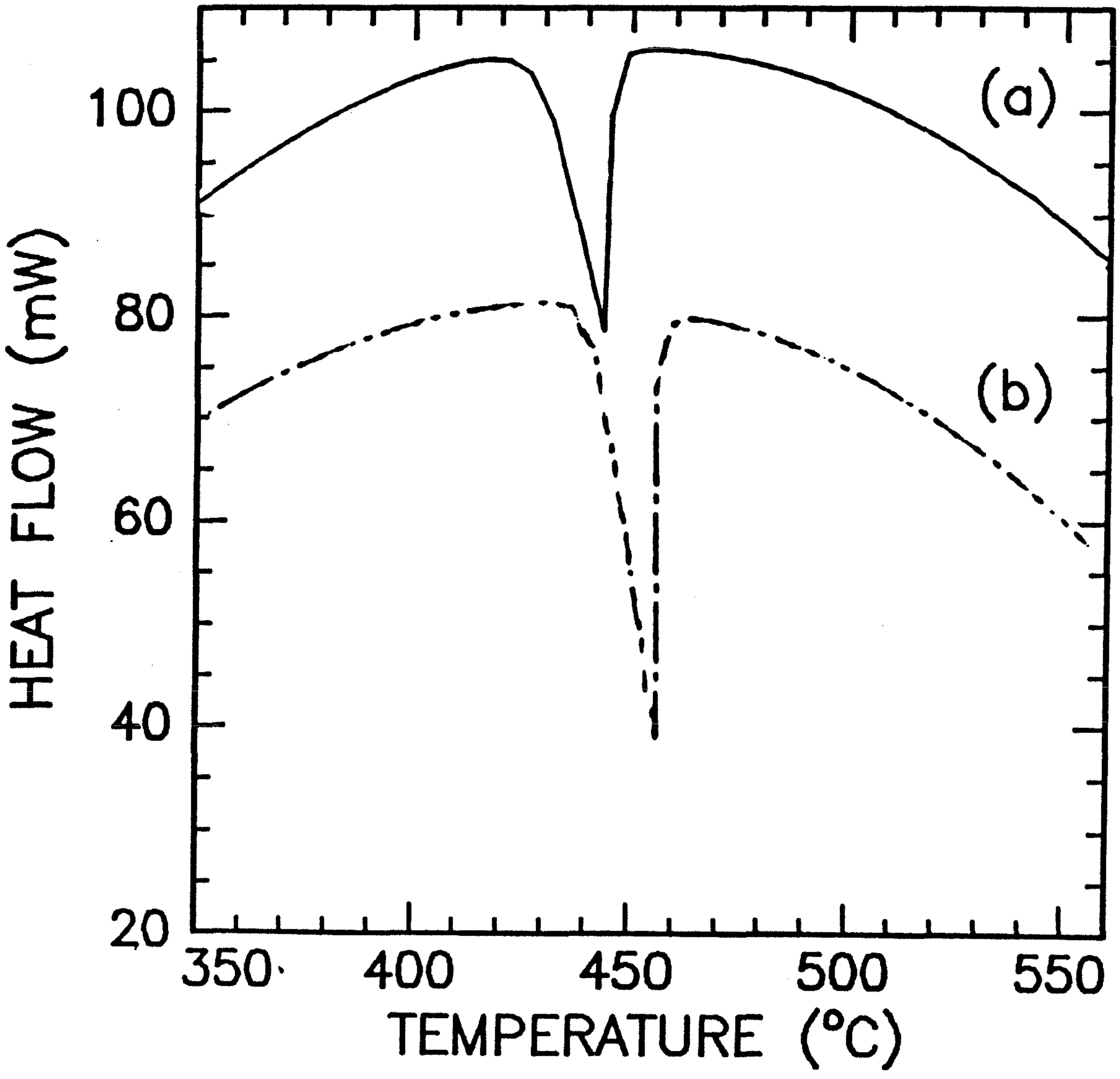

Figure 4.2 DSC trace of $Al_{25}Ge_{75}$ ball-milled in tungsten carbide.

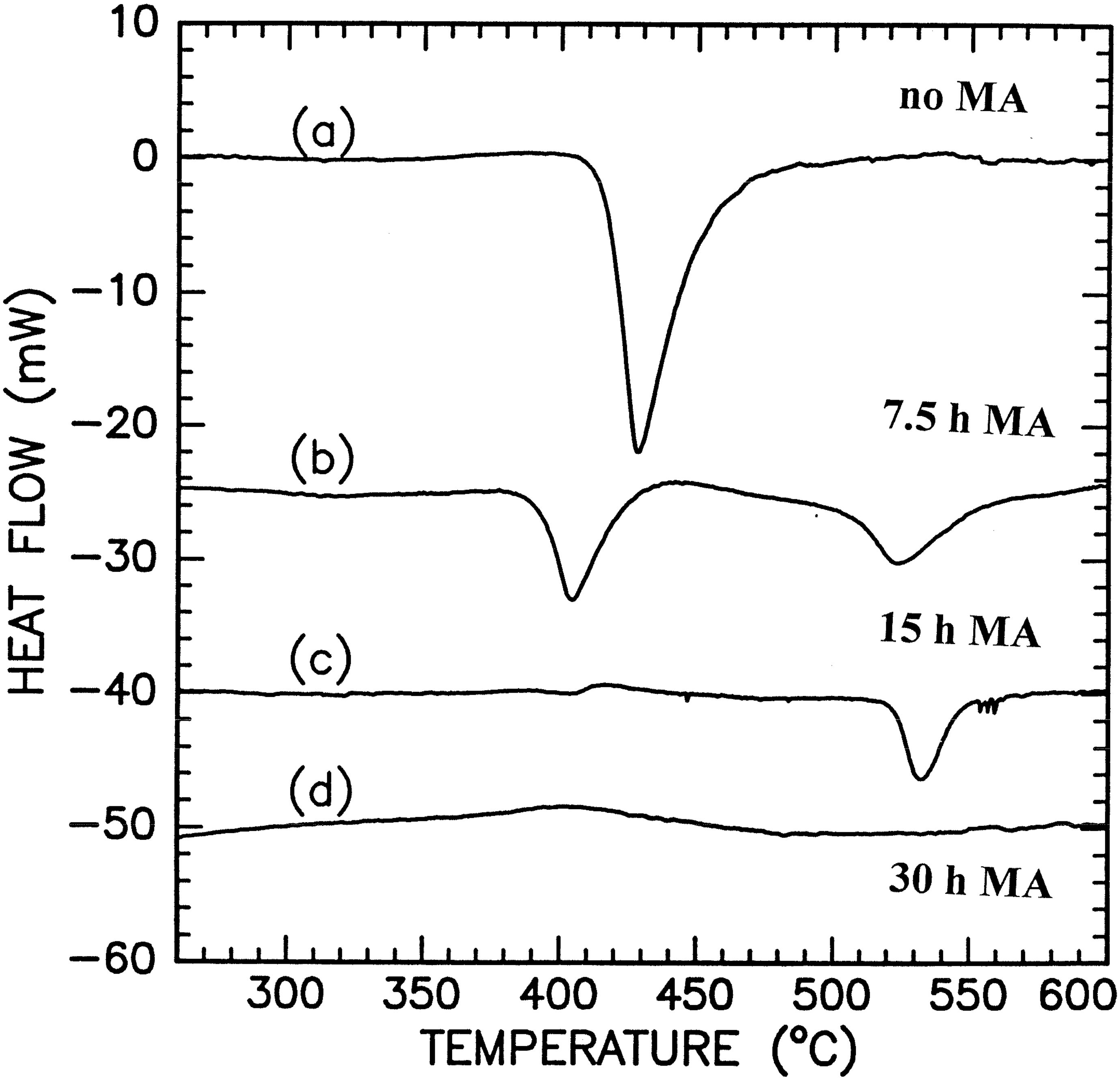

Figure 4.3 DTA traces of $Al_{25}Ge_{75}$ for different ball-milling times.

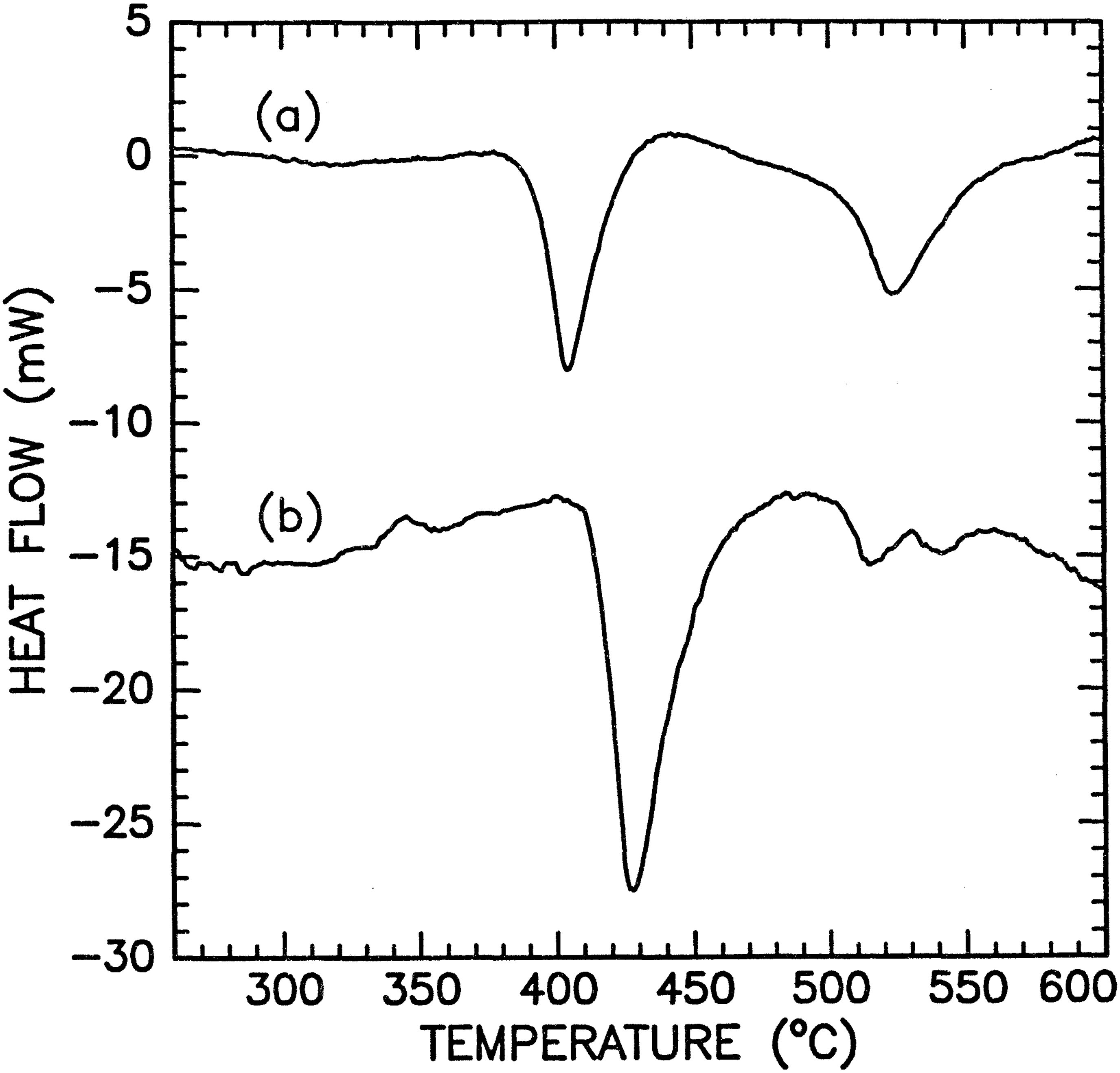

Figure 4.4 DTA traces for two consecutive heating of $Al_{25}Ge_{75}$ ball-milled in steel media.

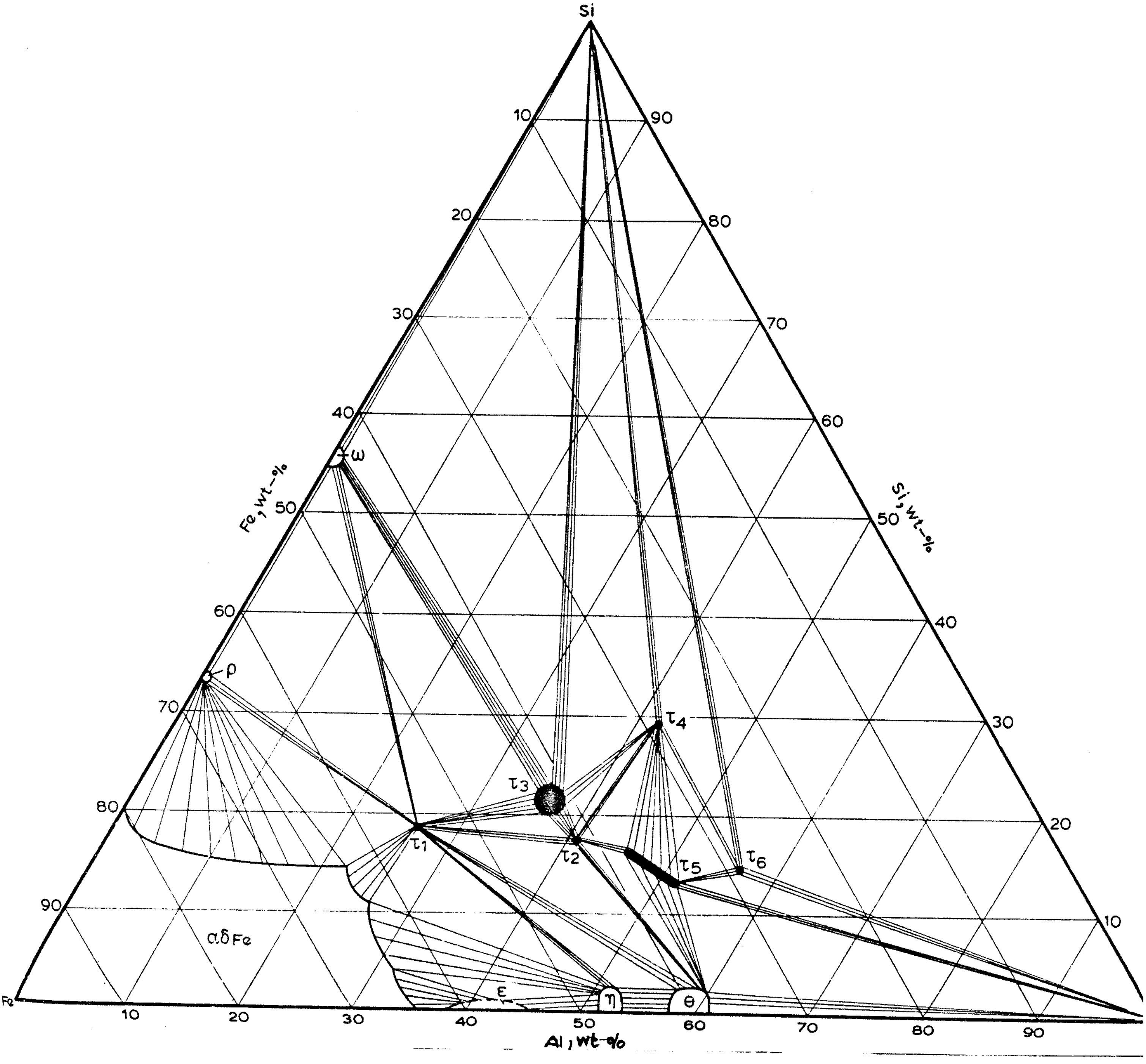

Figure 4.5 Aluminum-iron-silicon ternary phase diagram.

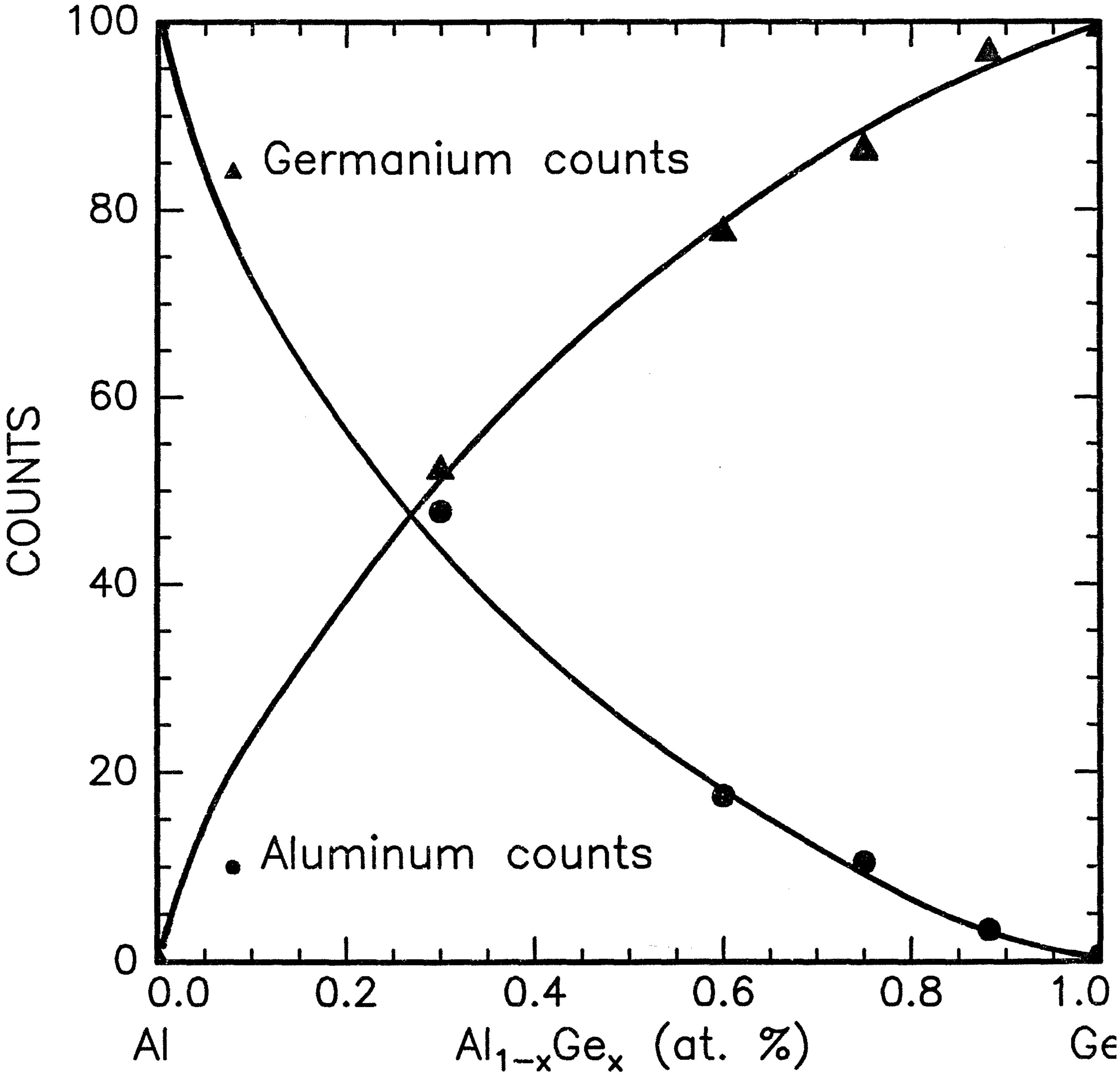

Figure 4.6 Aluminum-germanium counts for different compositions.

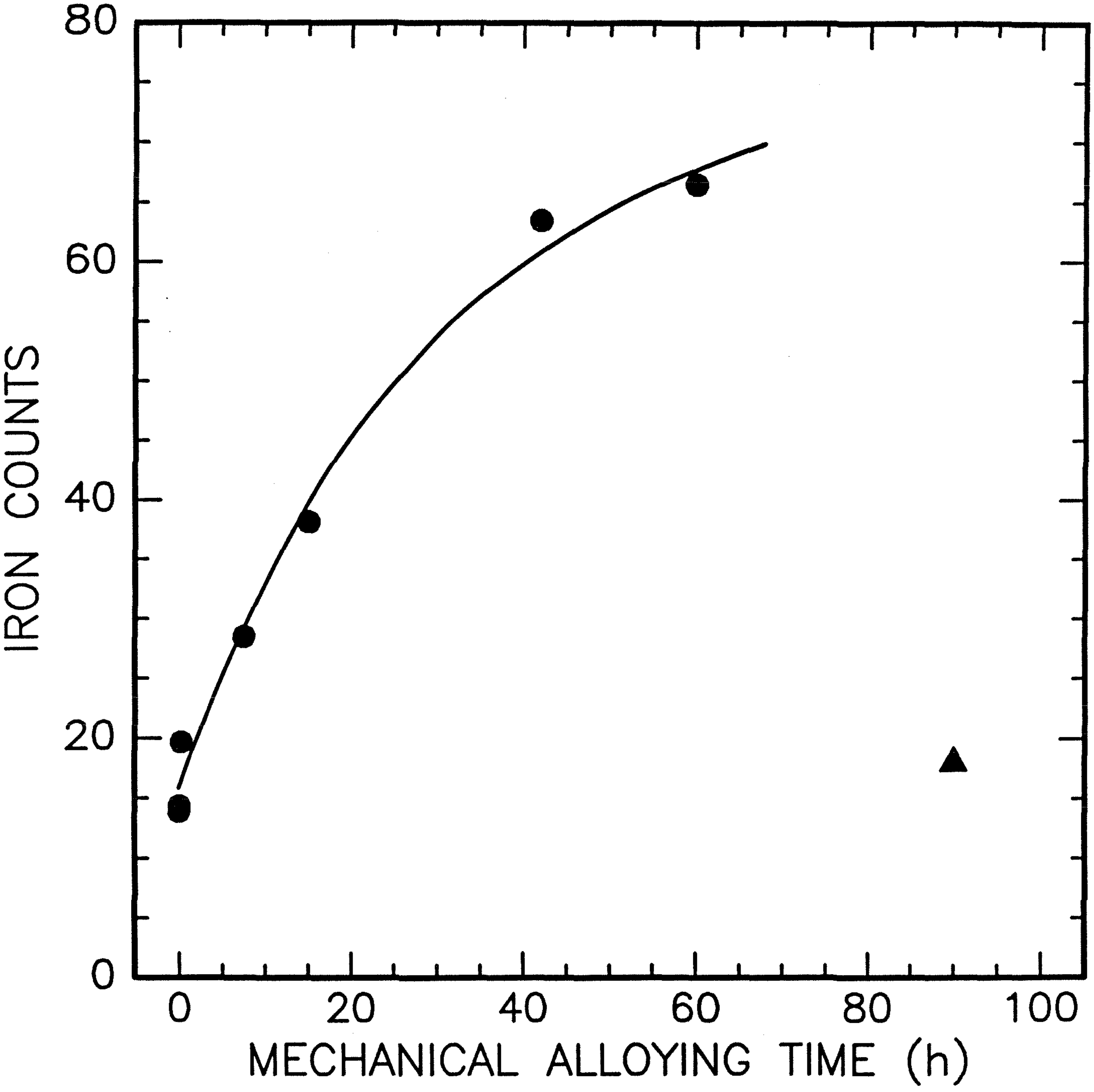

Figure 4.7 Iron counts as a function of mechanical alloying time.

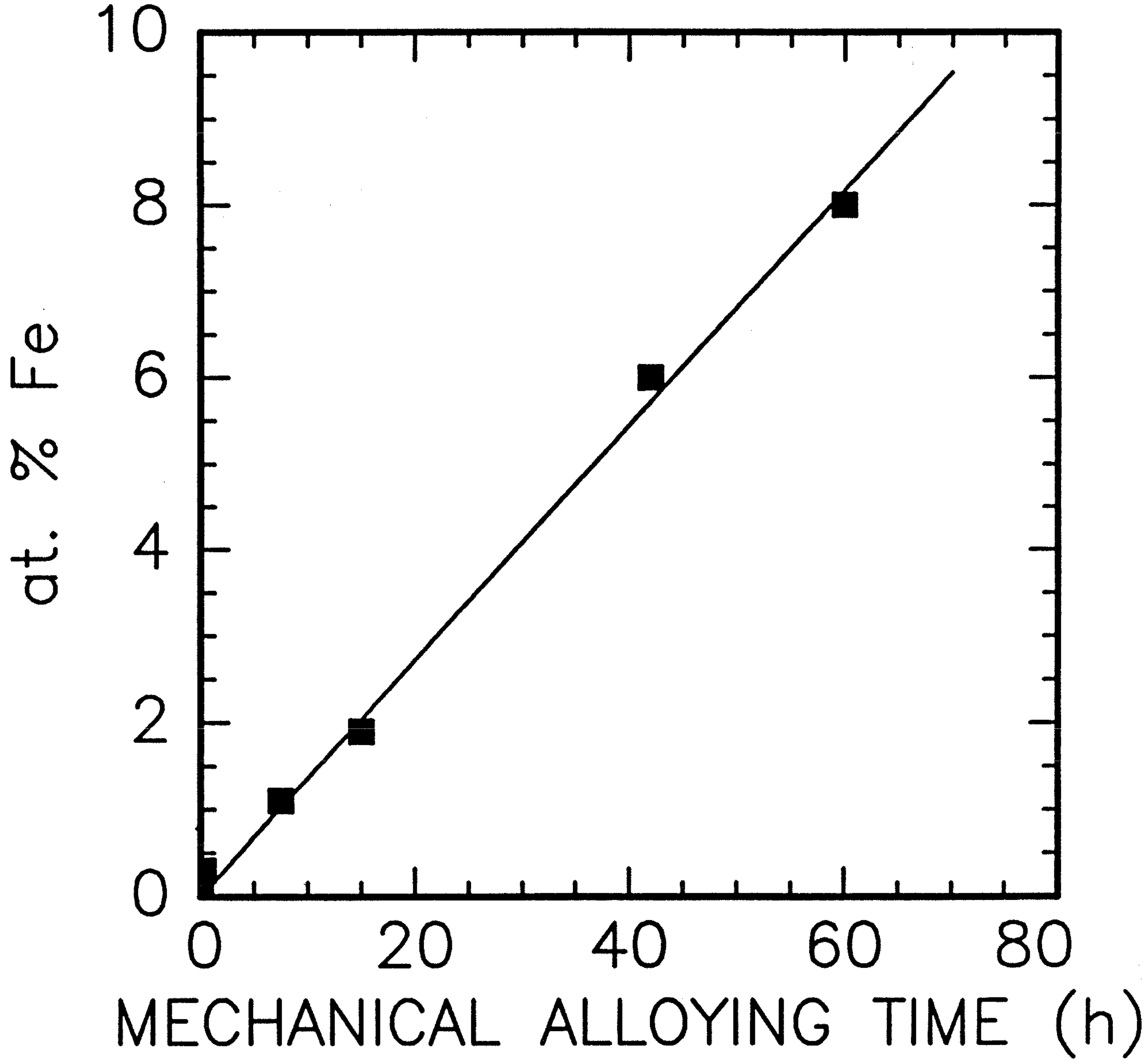

Figure 4.8 Atomic iron contamination as a function of mechanical alloying time.

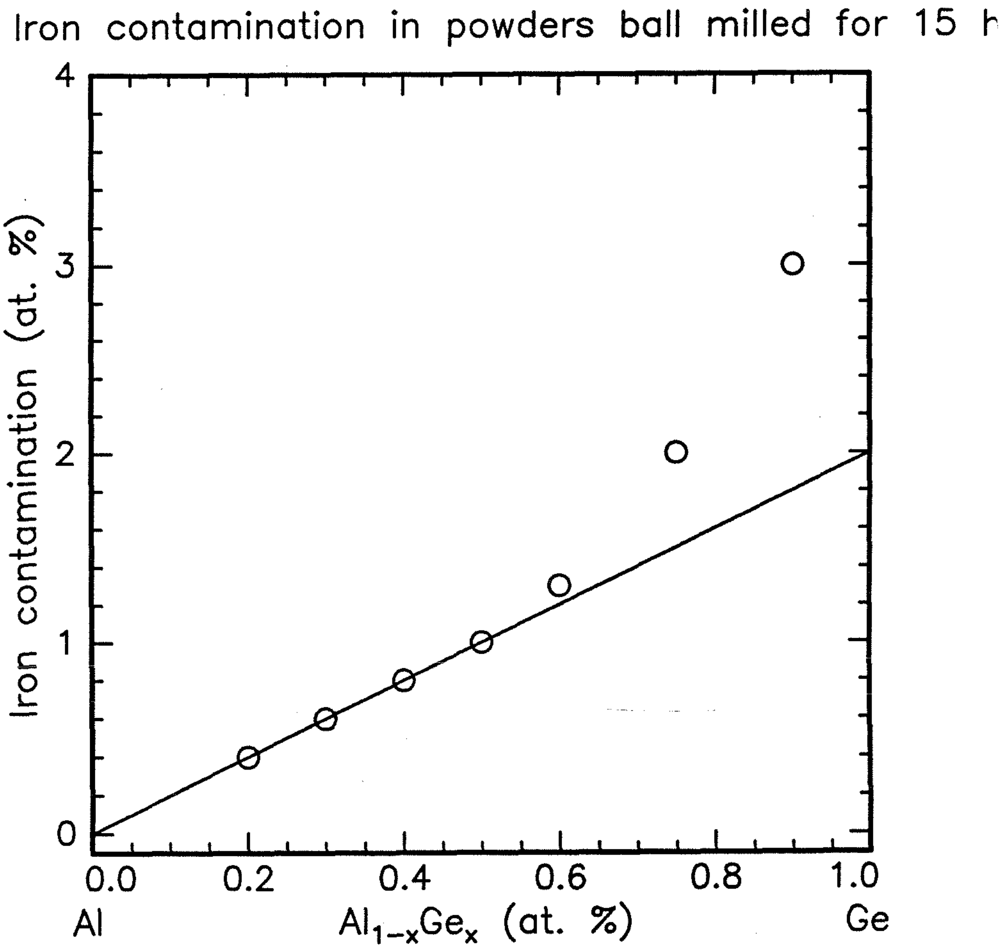

Figure 4.9 Iron contamination as a function of composition.

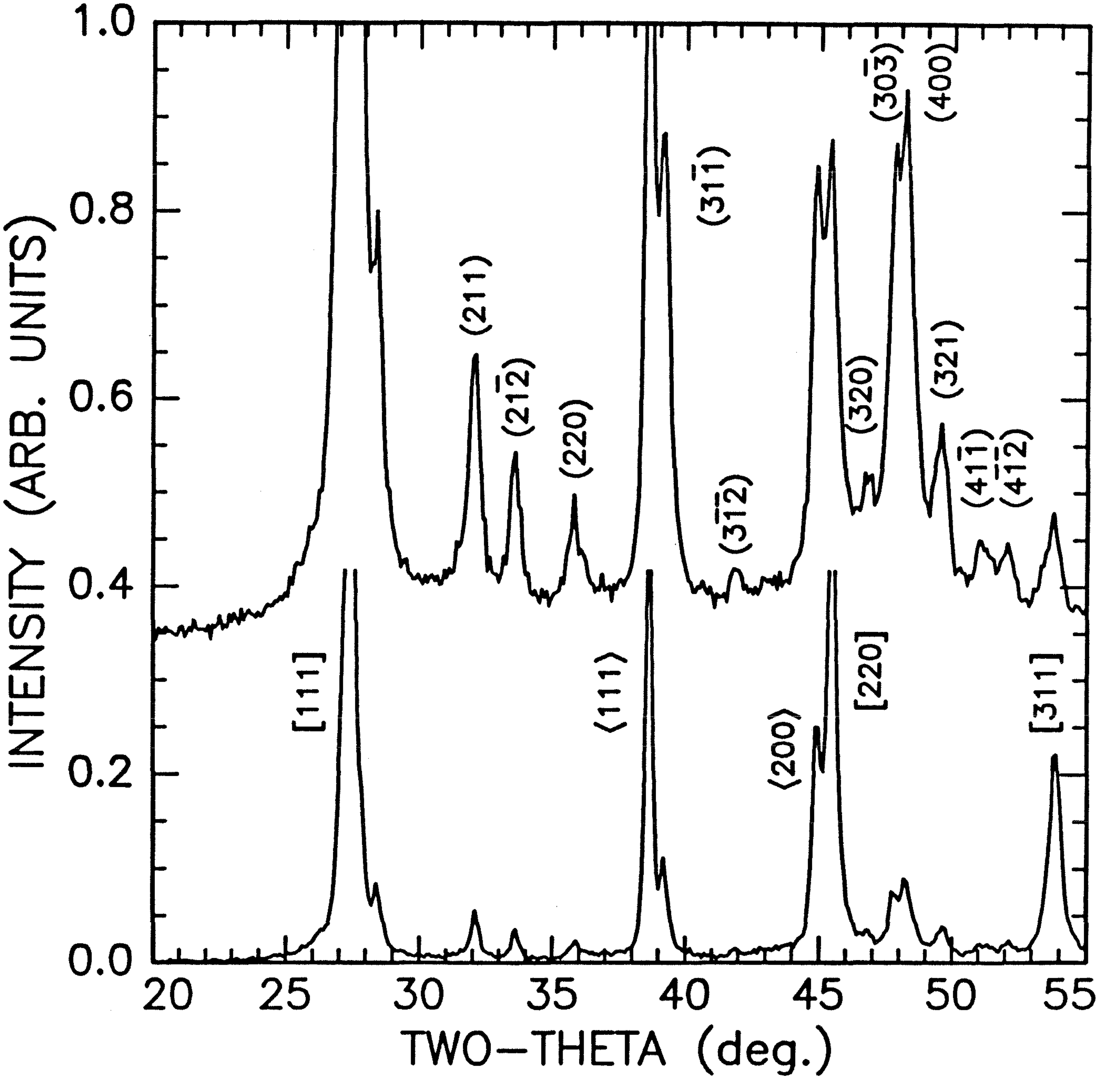

Figure 4.10 X-ray diffraction pattern of mechanically alloyed $Al_{70}Ge_{30}$.

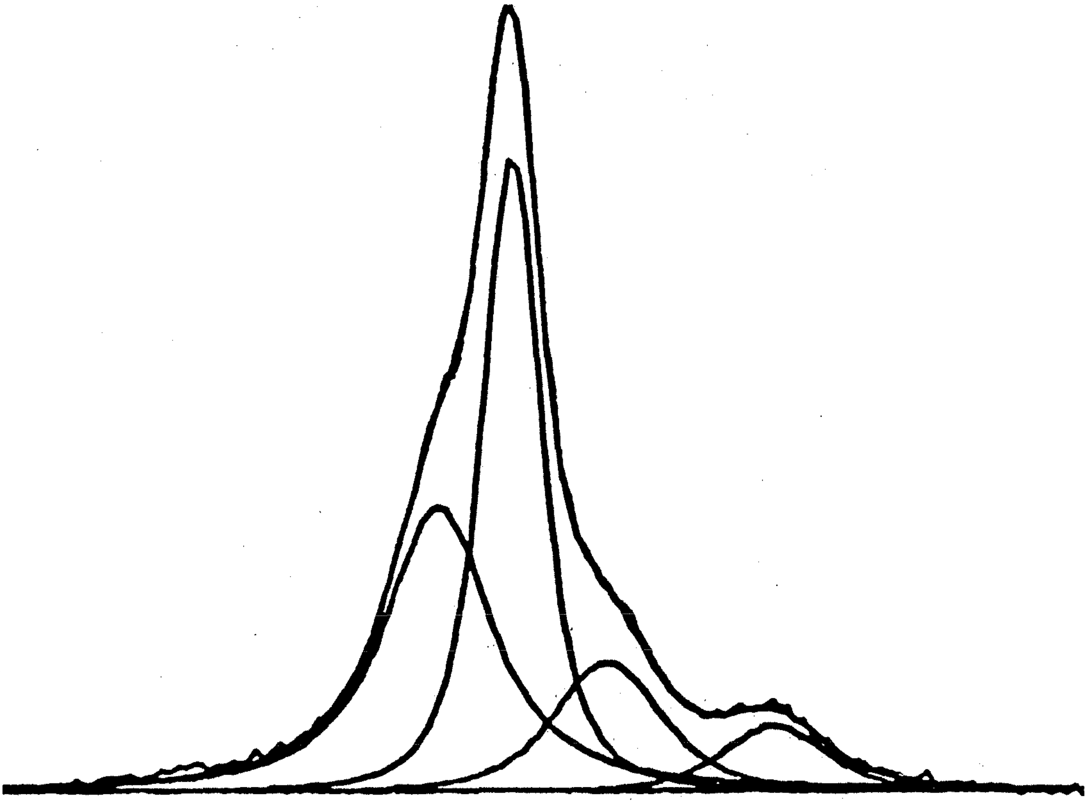

Figure 4.11 Detail of diffraction pattern around Ge(111). The peaks are in increasing 2θ, γ_1 (2,-1,-1), Ge (1,1,1), γ_1 (2,1,0), and γ_1 (2,1,-1).

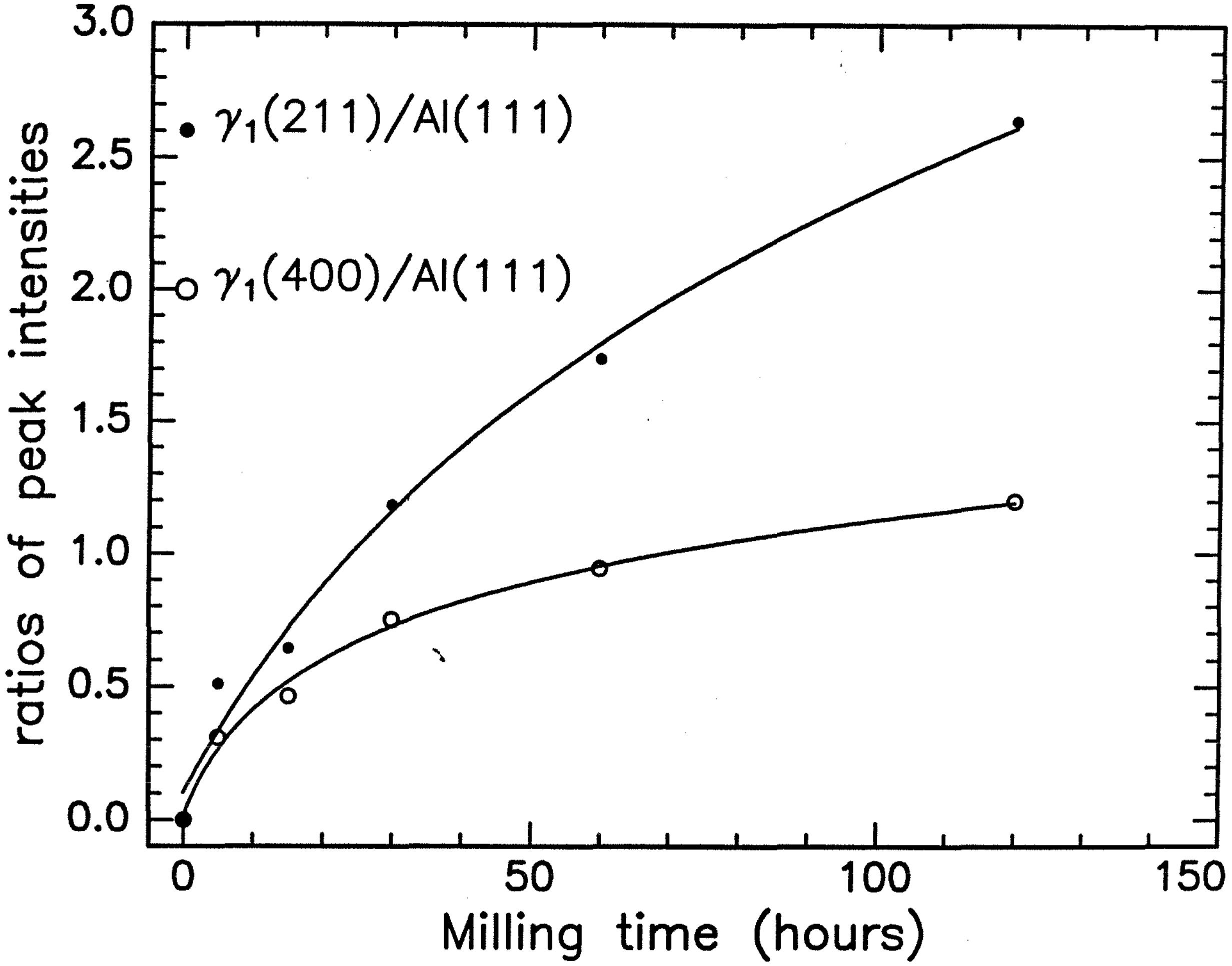

Figure 4.12 Intensities of γ_1 diffraction peaks as function of MA time.

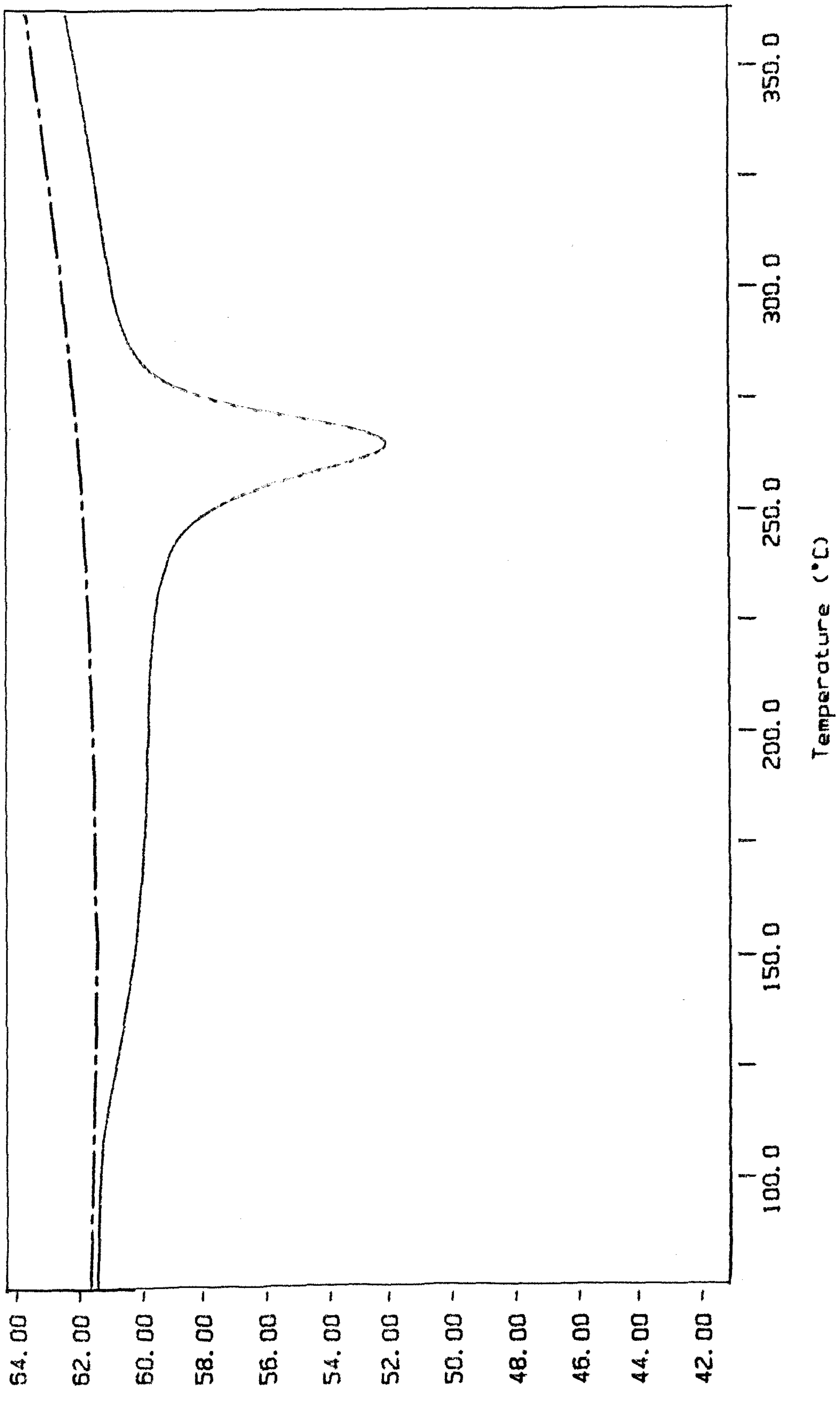

Figure 4.13 DSC traces for two consecutive heatings of $Al_{70}Ge_{30}$.

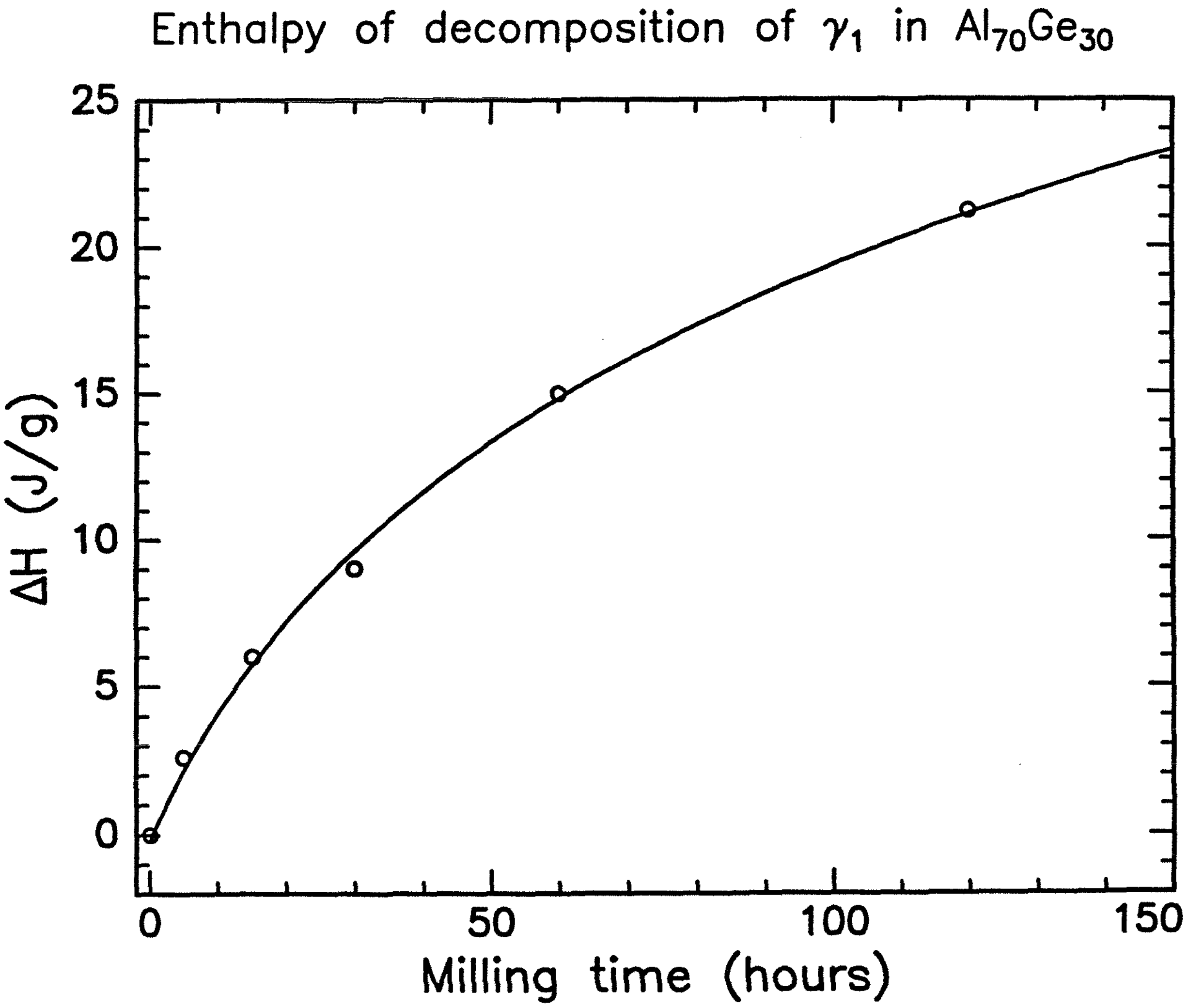

Figure 4.14 Enthalpy of decomposition of the γ_1 phase as a function of MA time.

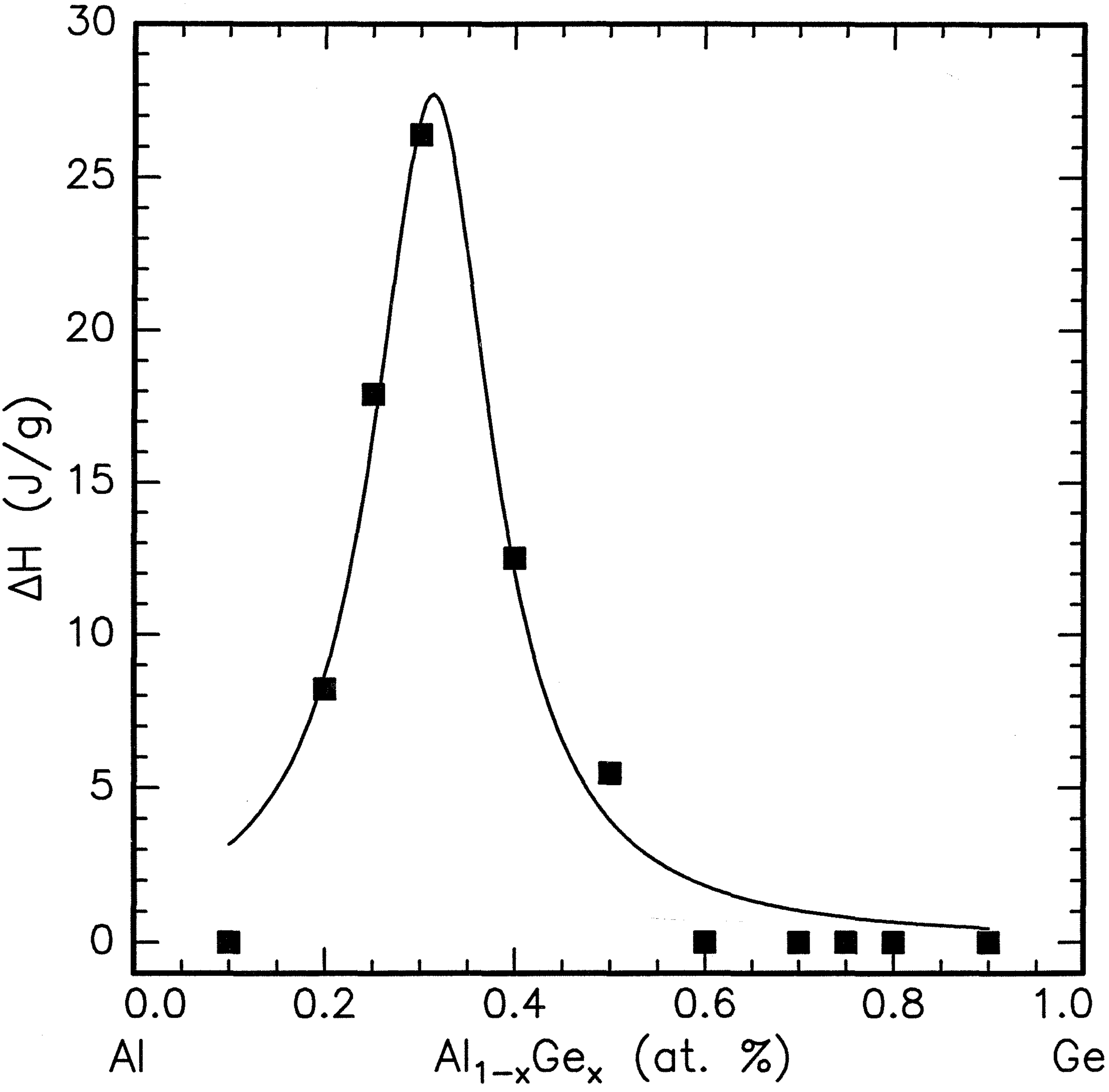

Figure 4.15 Enthalpy of decomposition of the γ_1 phase as a function of composition.

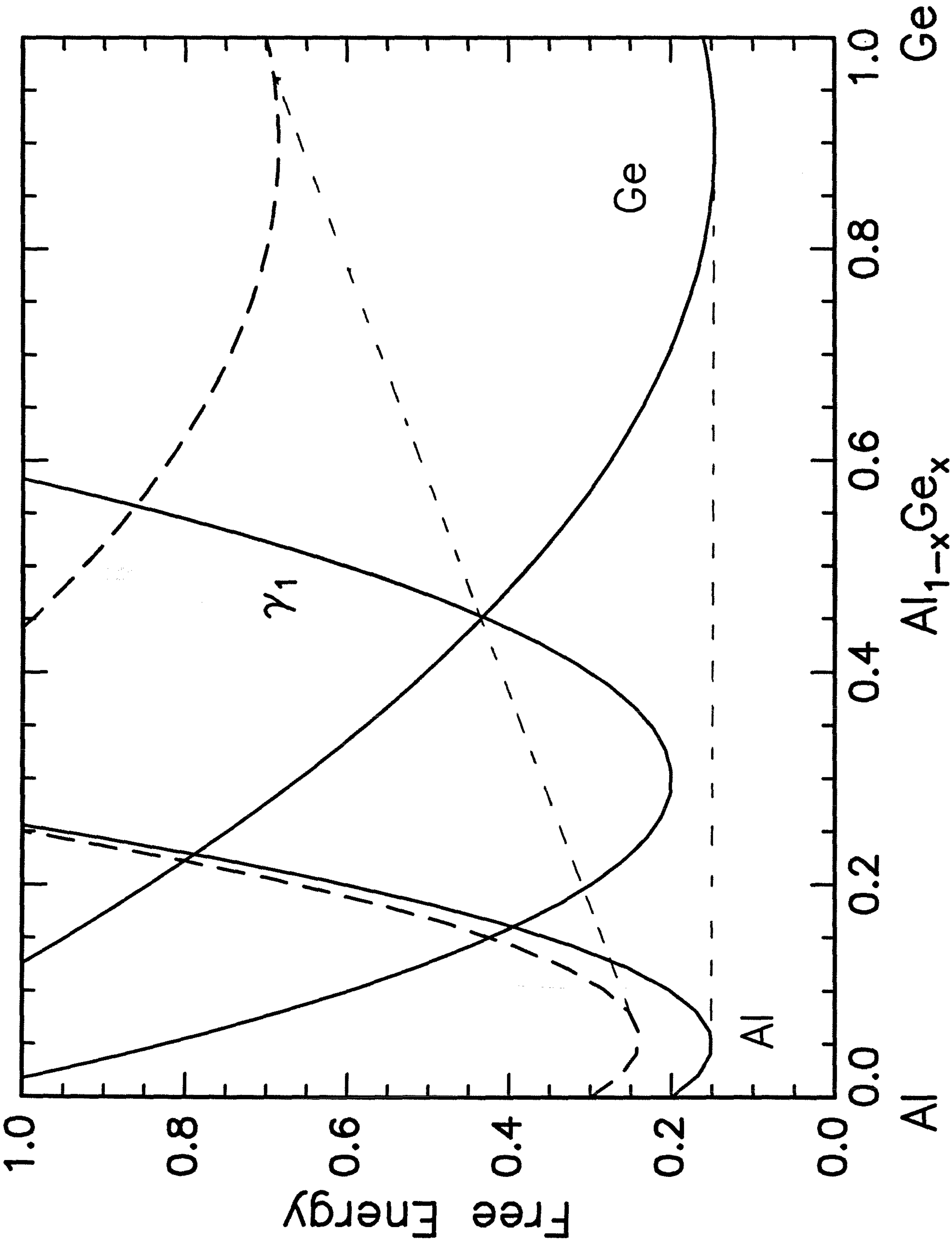

Figure 4.16 Schematic free energy diagram of aluminum-germanium.

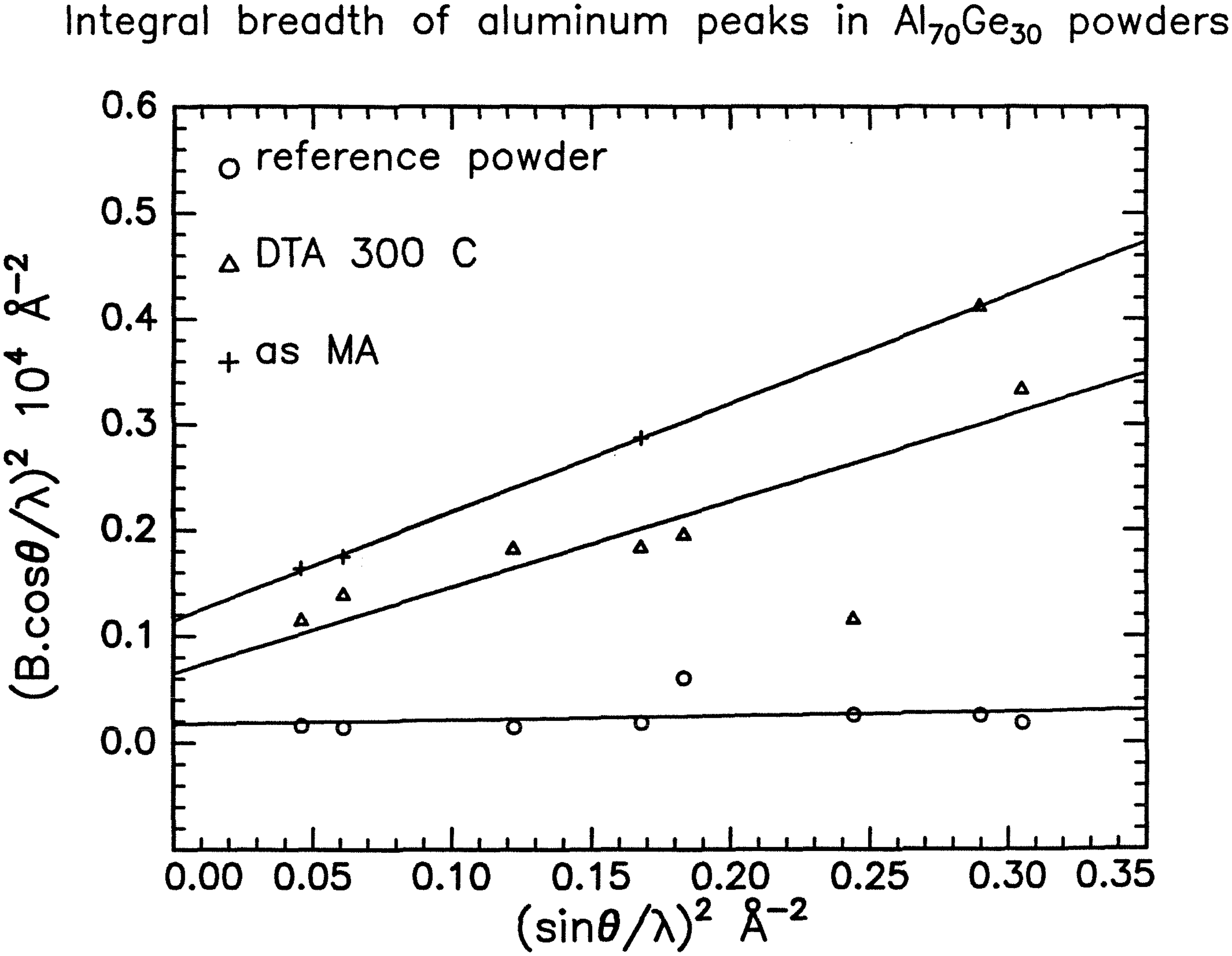

Figure 4.17 Typical integral breadth results for aluminum.

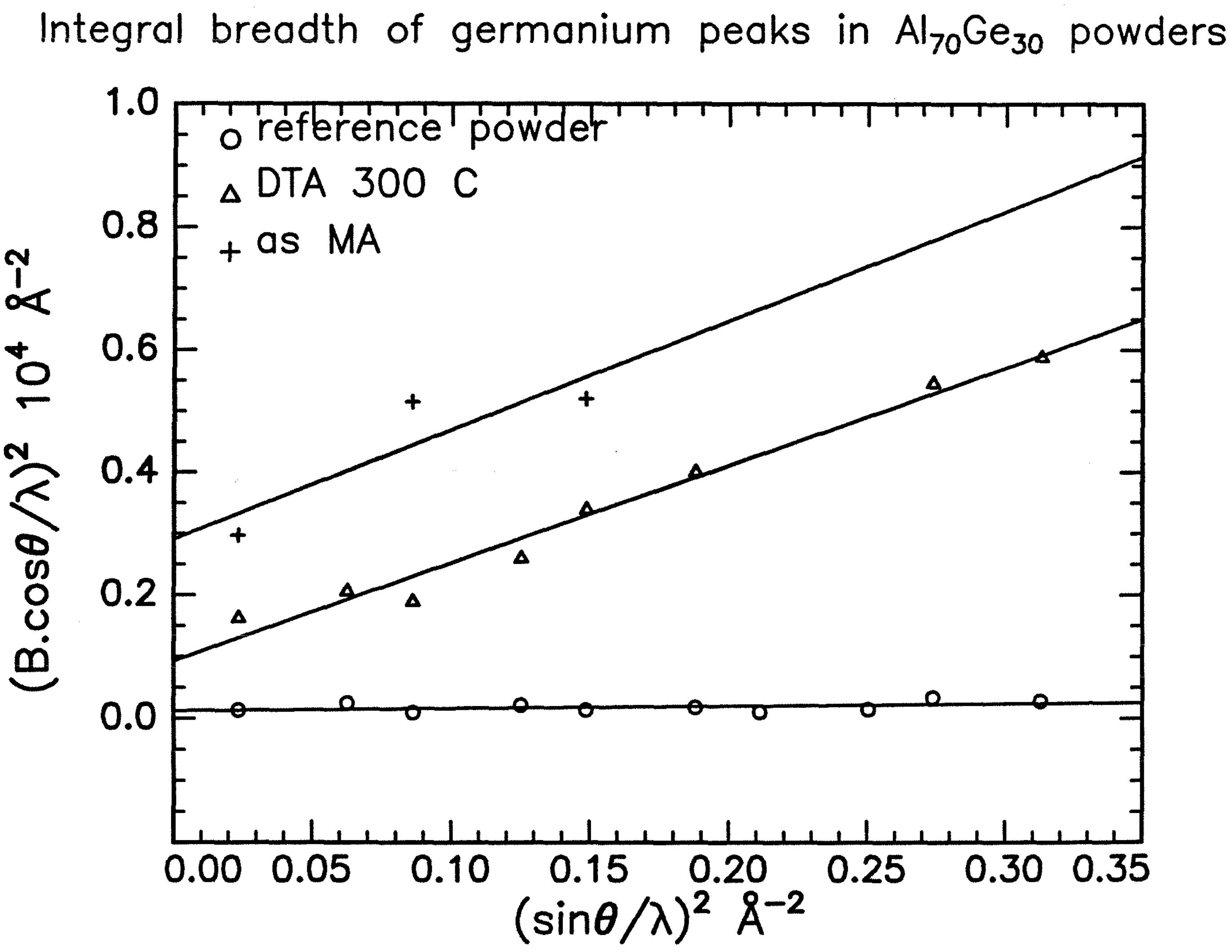

Figure 4.18 Typical integral breadth results for germanium.

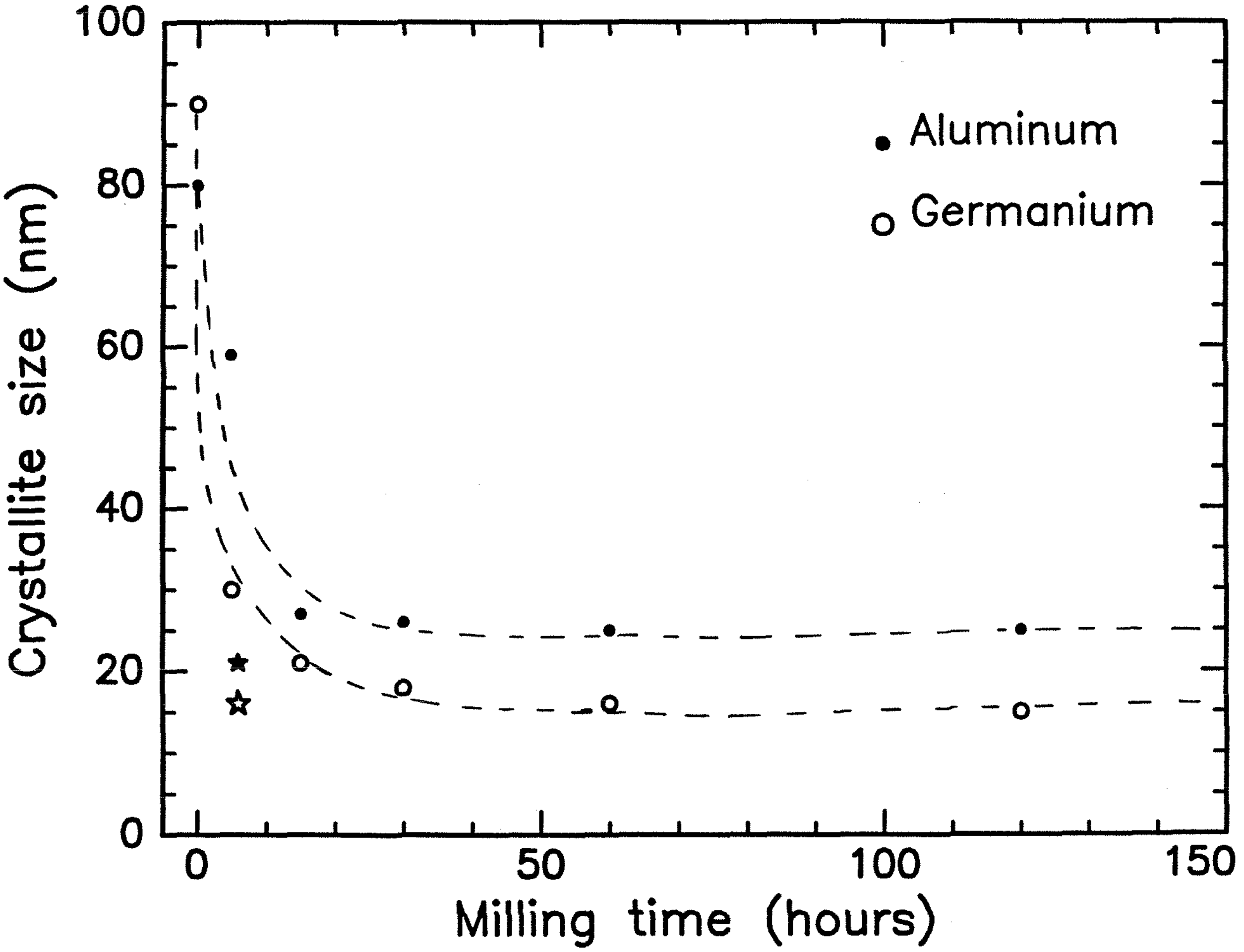

Figure 4.19 Crystallite size as a function of MA time for aluminum and germanium.

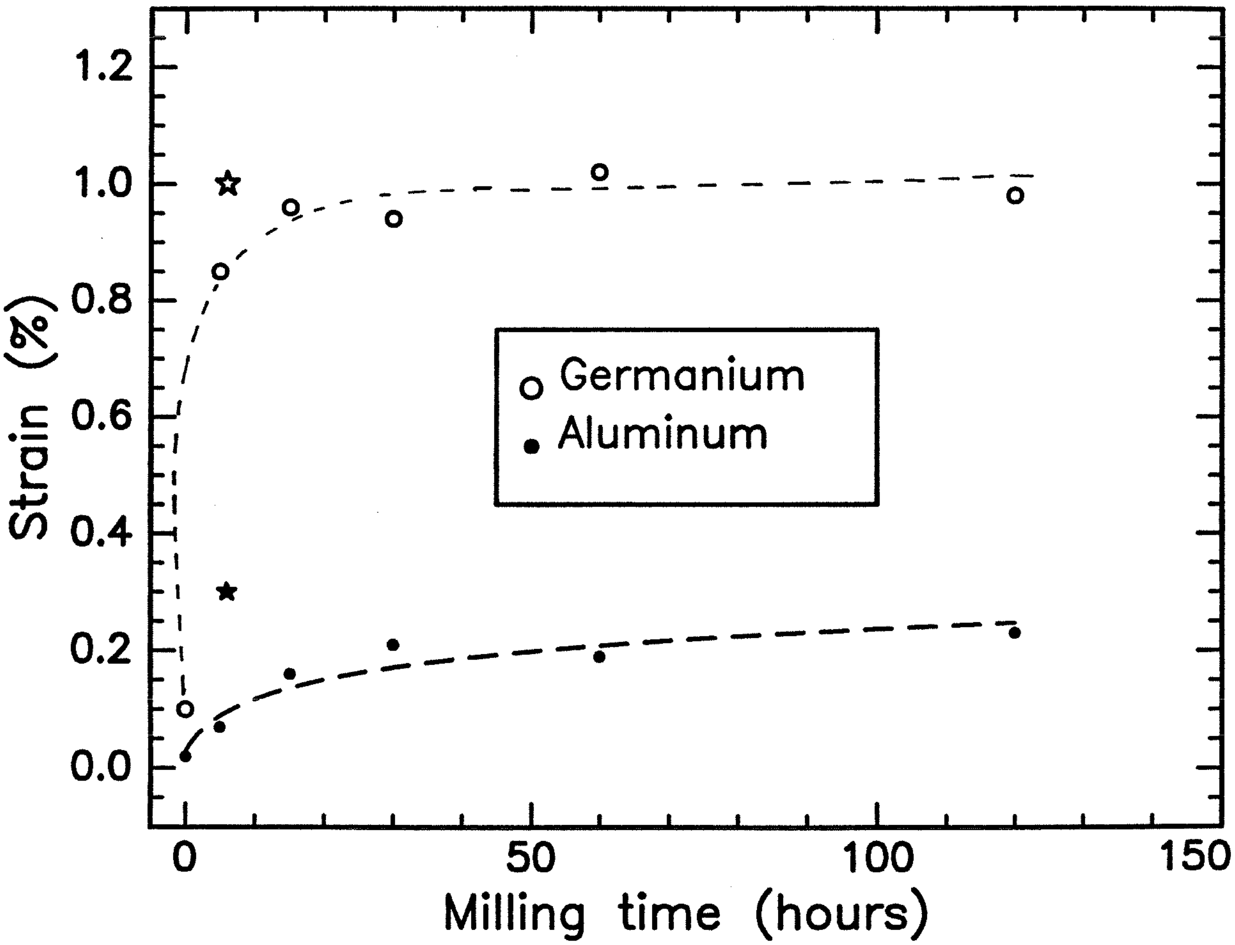

Figure 4.20 Strain as a function of MA time for aluminum and germanium.

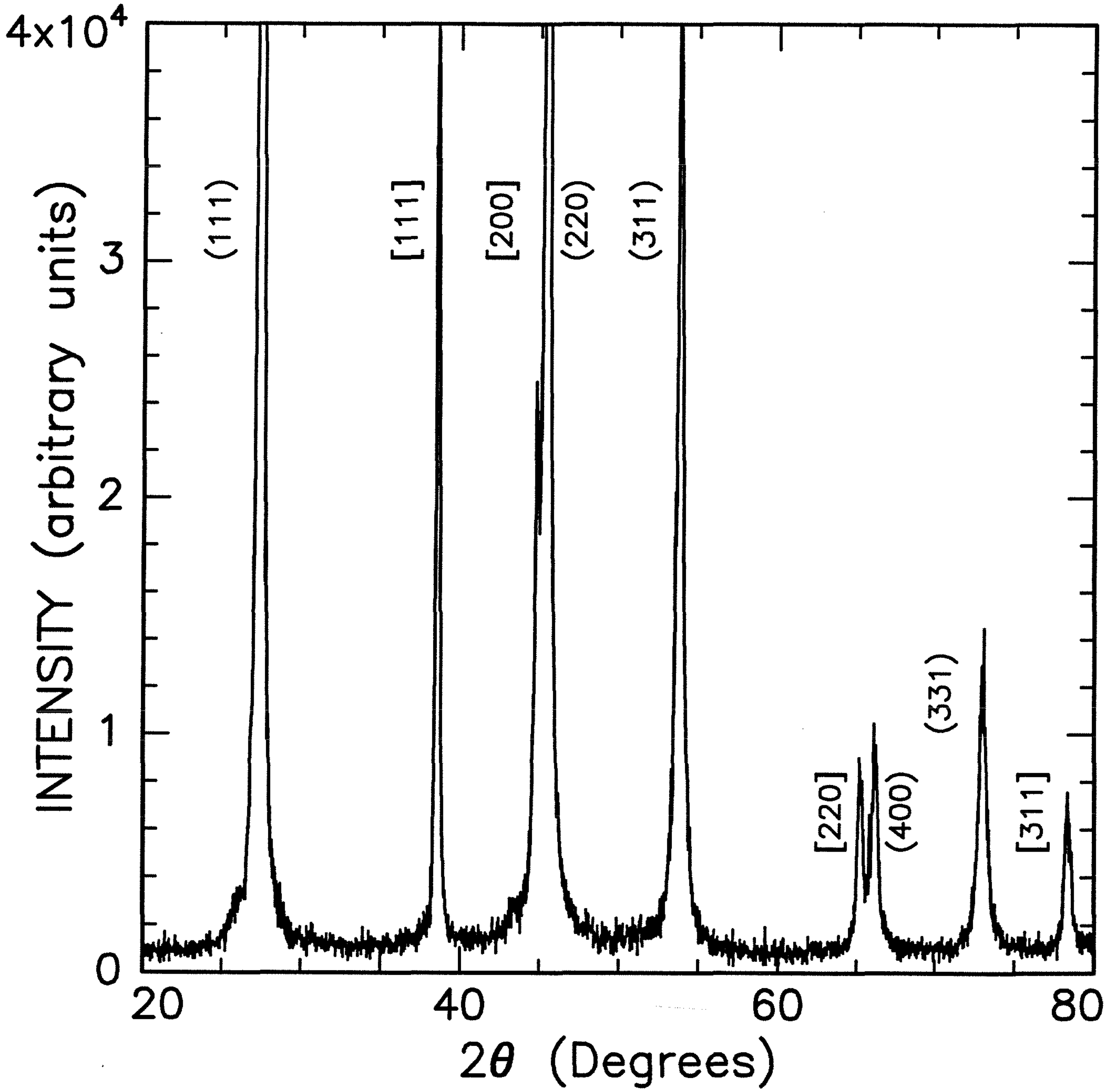

Figure 4.21 Typical x-ray diffraction pattern of a mechanically alloyed powder after annealing. () represents the germanium peaks and [] represents the aluminum peaks.

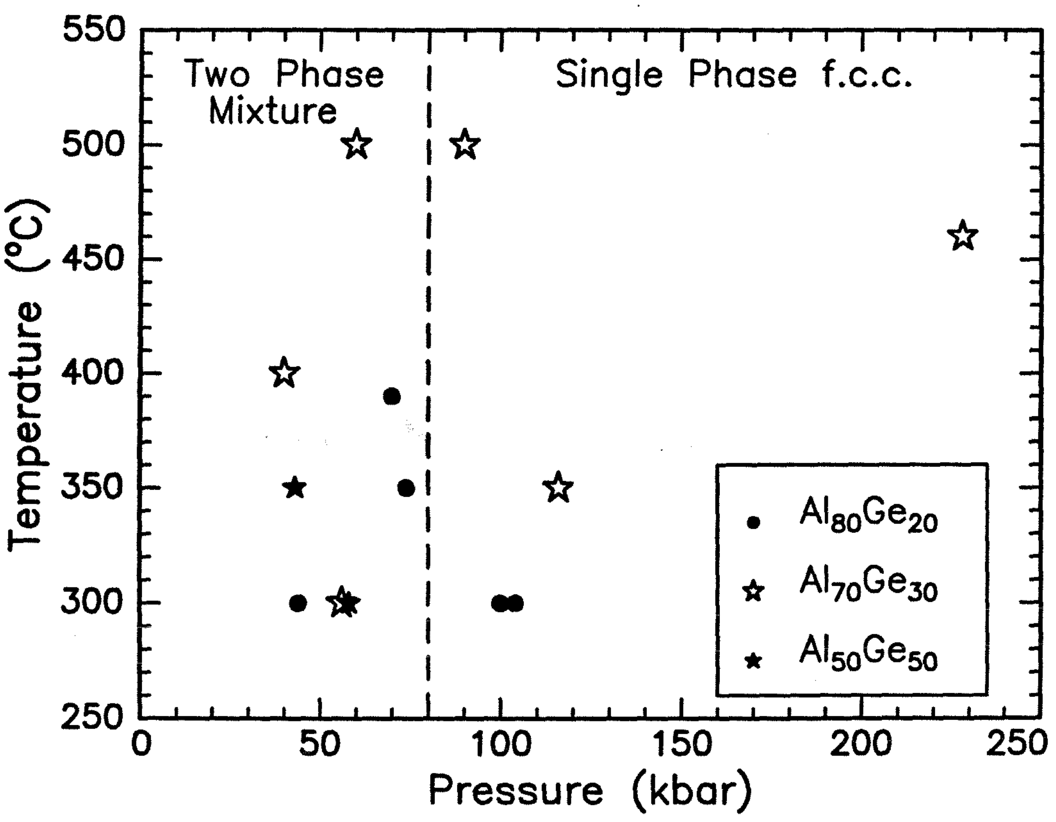

Figure 4.22 Pressure-temperature-composition map of *in situ* experiments.

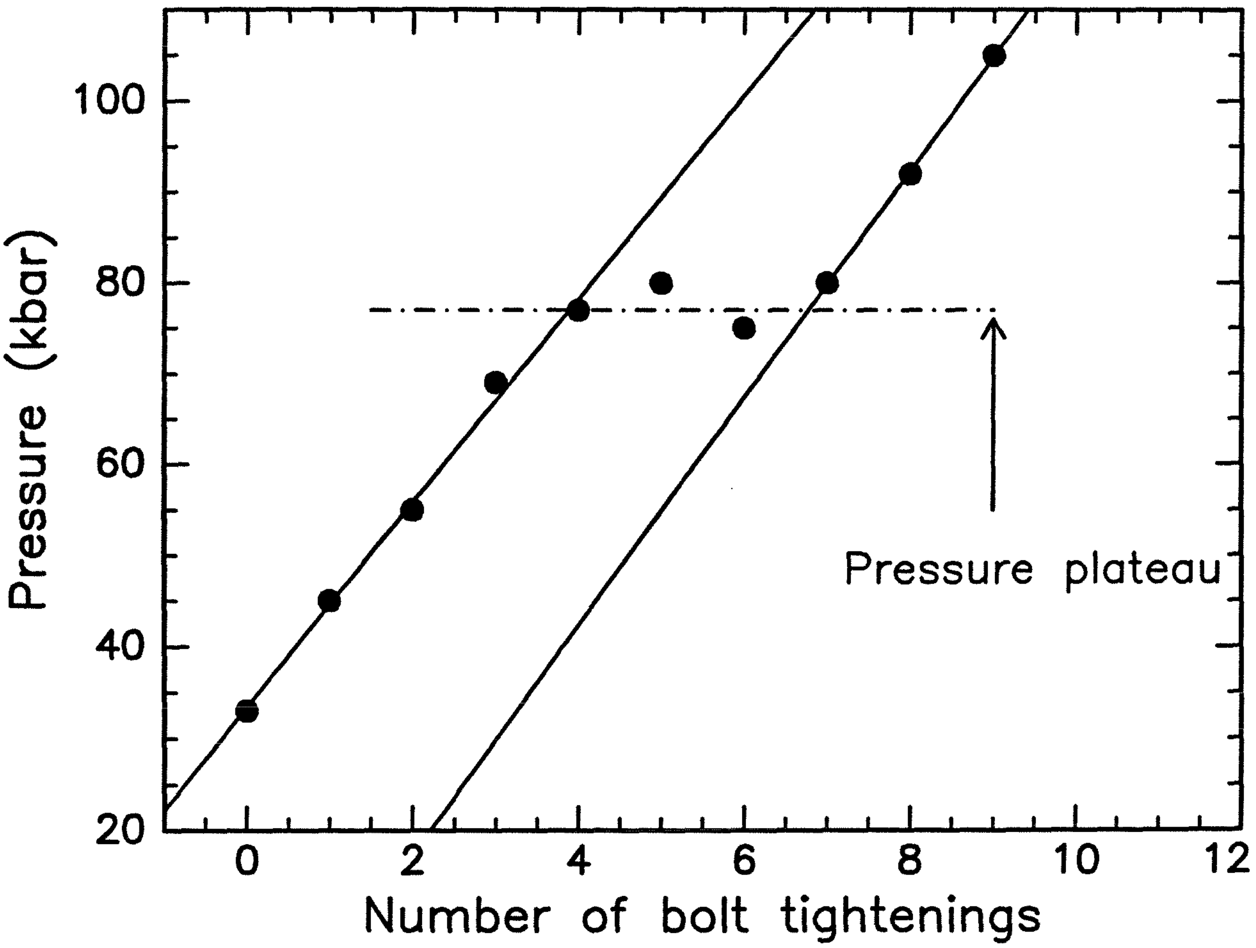

Figure 4.23 Pressure as a function of the number of 1/16th turns the bolts were tightened.

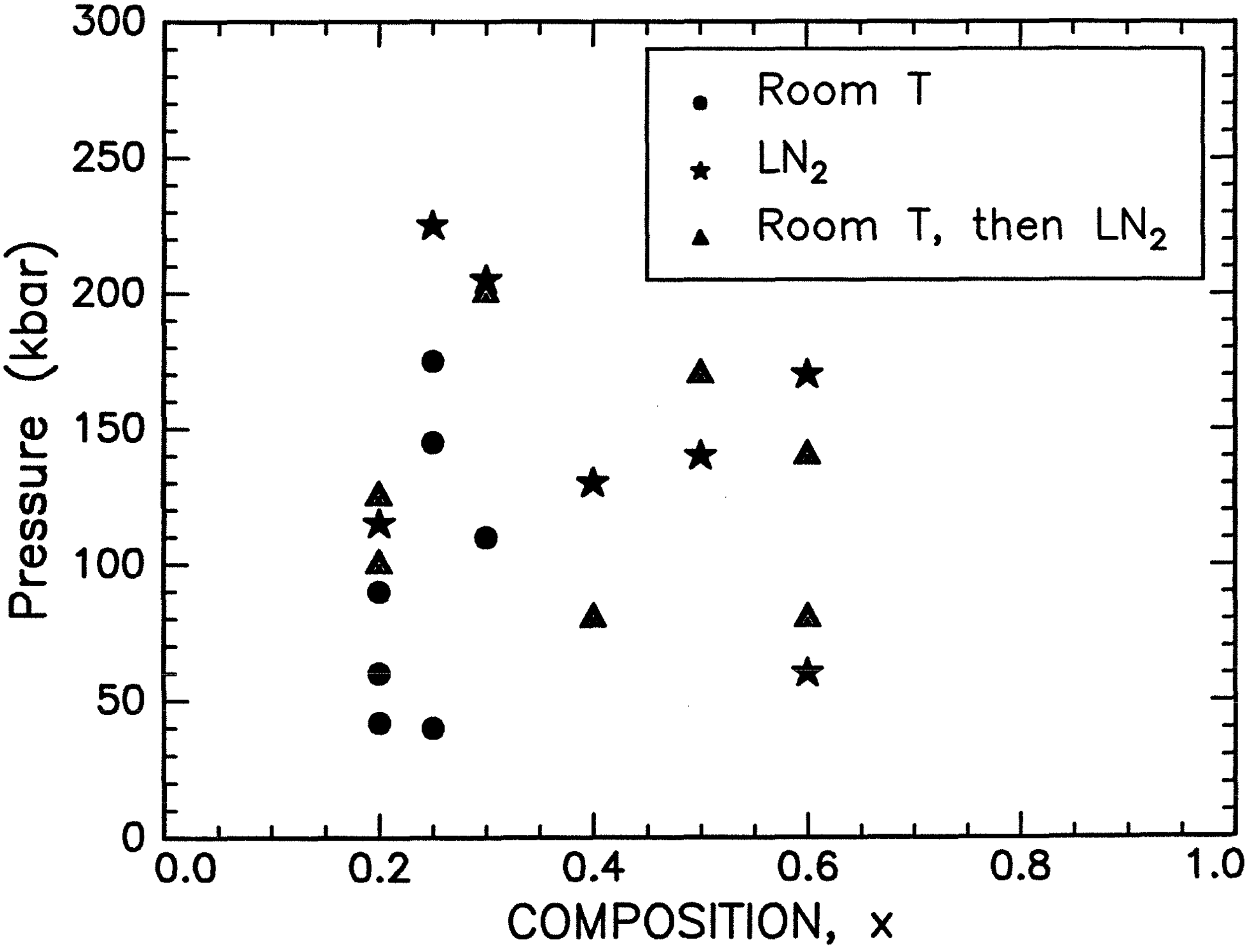

Figure 4.24 Pressure-composition map of TEM samples. The different symbols indicate the mode of storage.

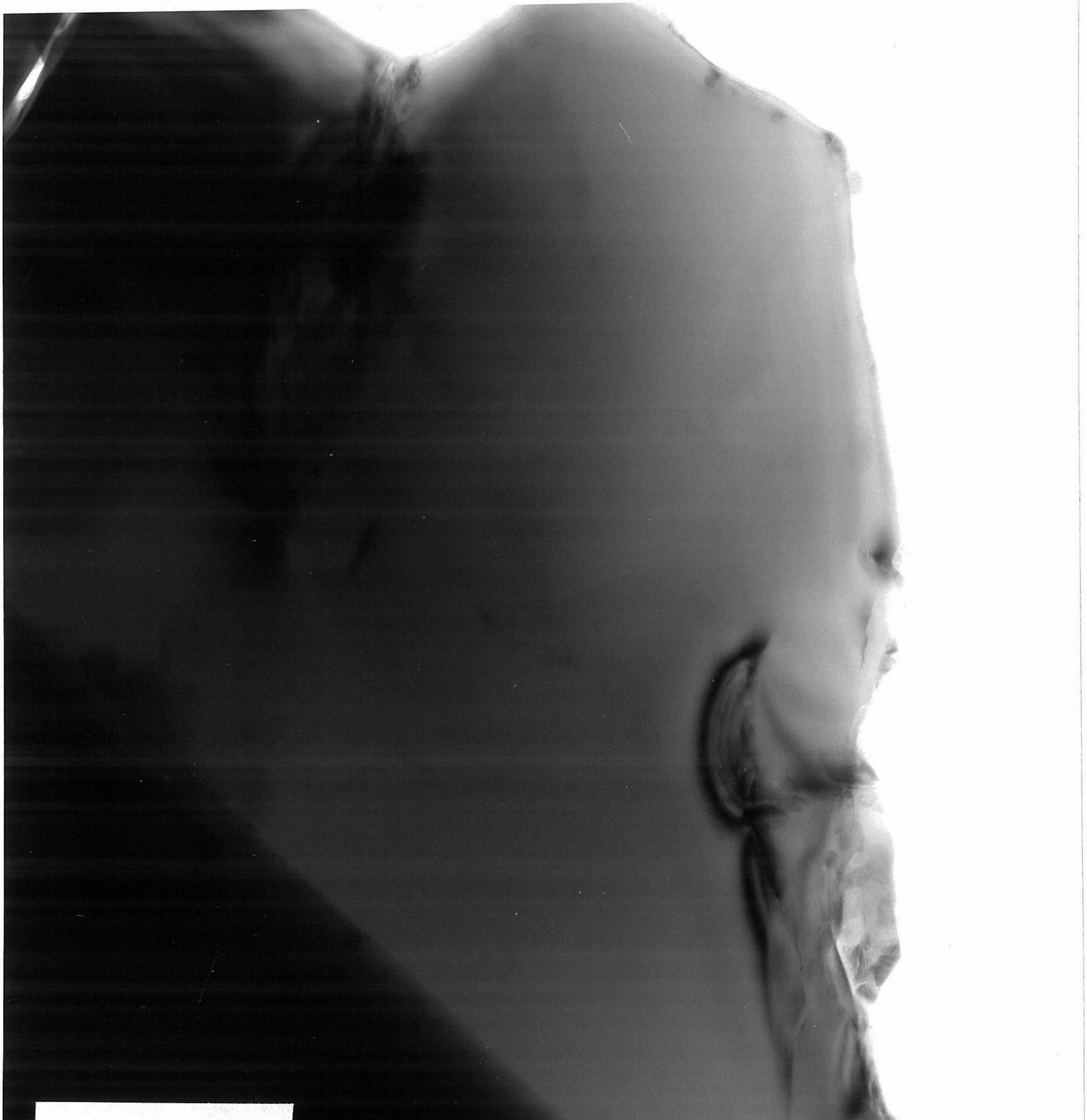

Figure 4.25 Bright field TEM photograph of samarium YAG.

Figure 4.26 Selected area diffraction pattern of samarium YAG (zone axis 001).

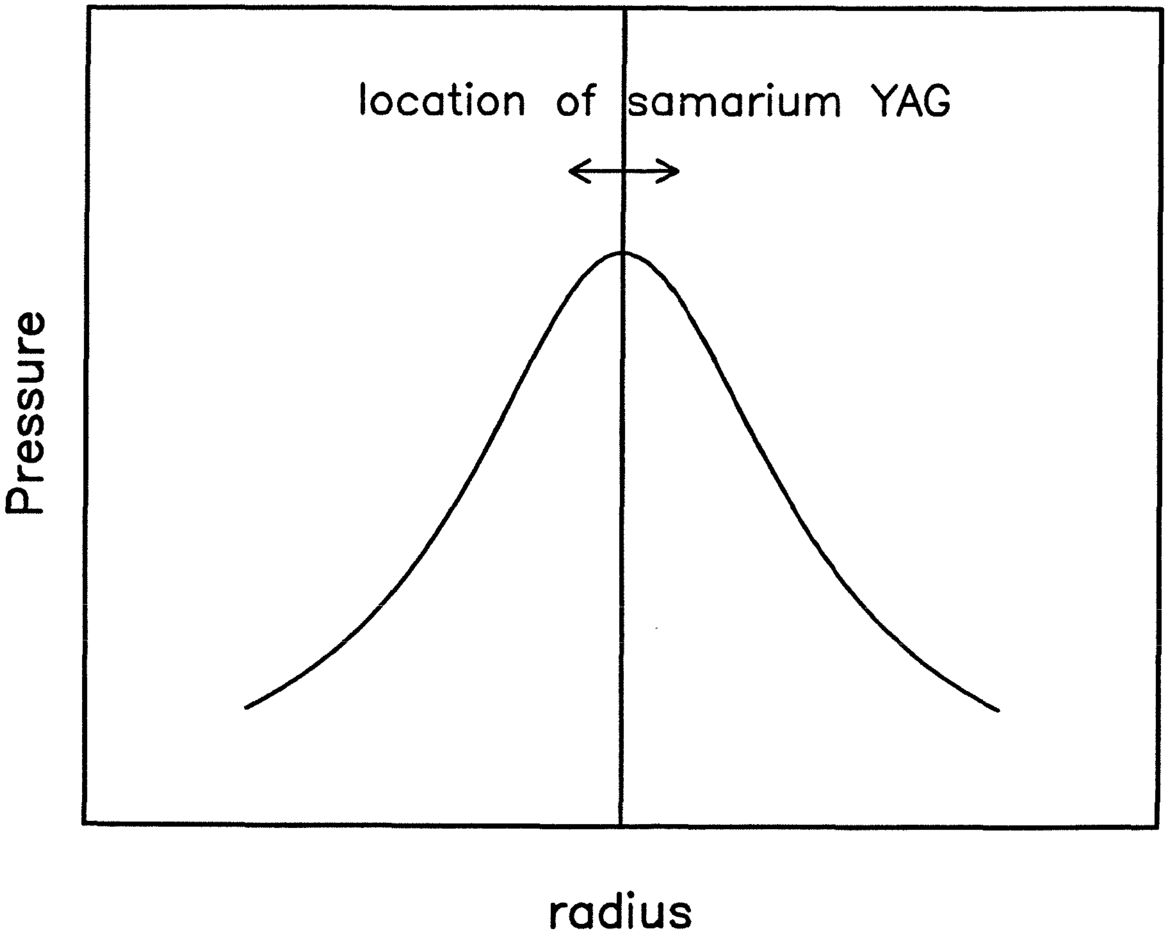

Figure 4.27 Schematic radial pressure gradient in the diamond-anvil cell when not using a gasket.

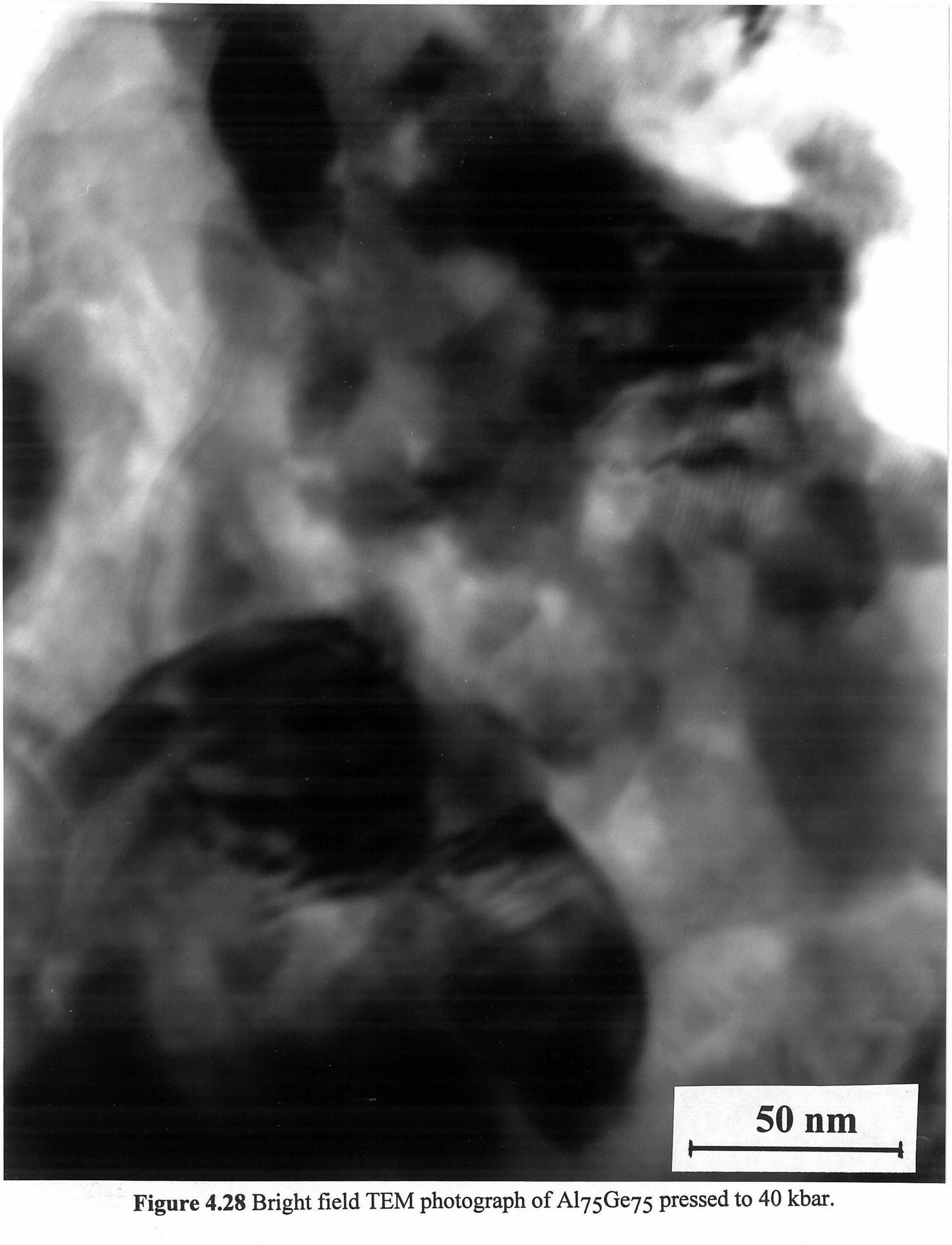

Figure 4.28 Bright field TEM photograph of $Al_{75}Ge_{75}$ pressed to 40 kbar.

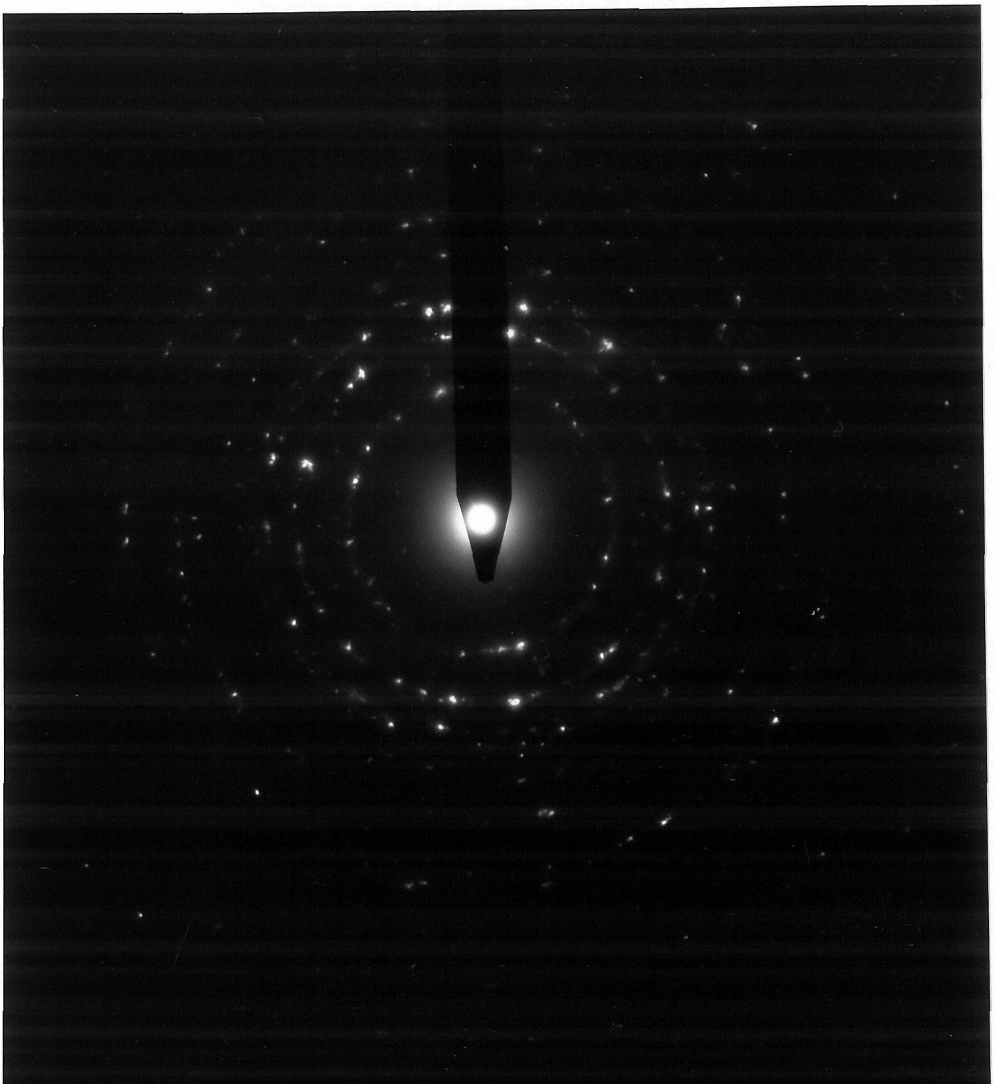

Figure 4.29 Selected area diffraction pattern of $Al_{75}Ge_{25}$ pressed to 40 kbar.

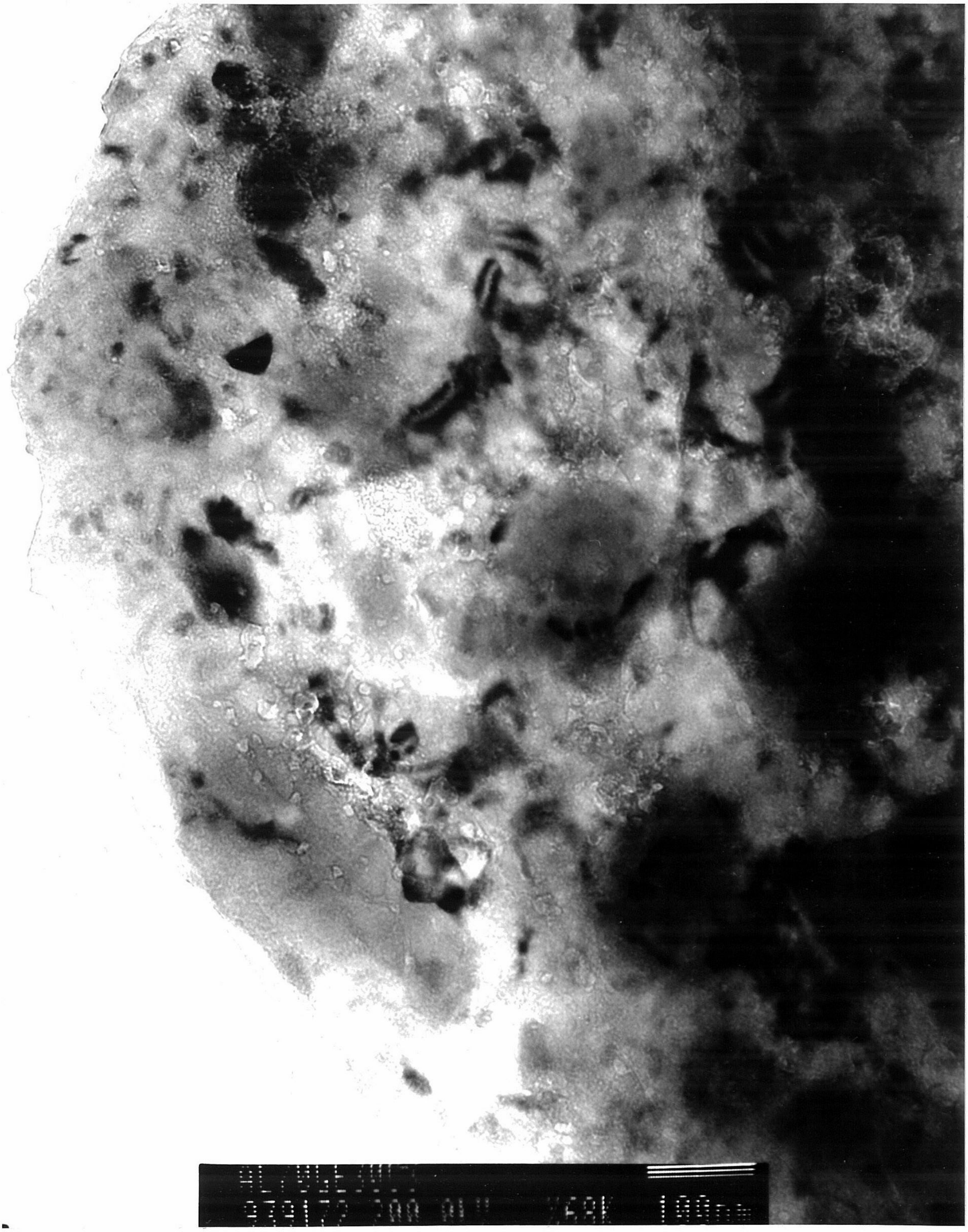

Figure 4.30 Bright field TEM Photograph of $Al_{70}Ge_{30}$ pressed to 200 kbar.

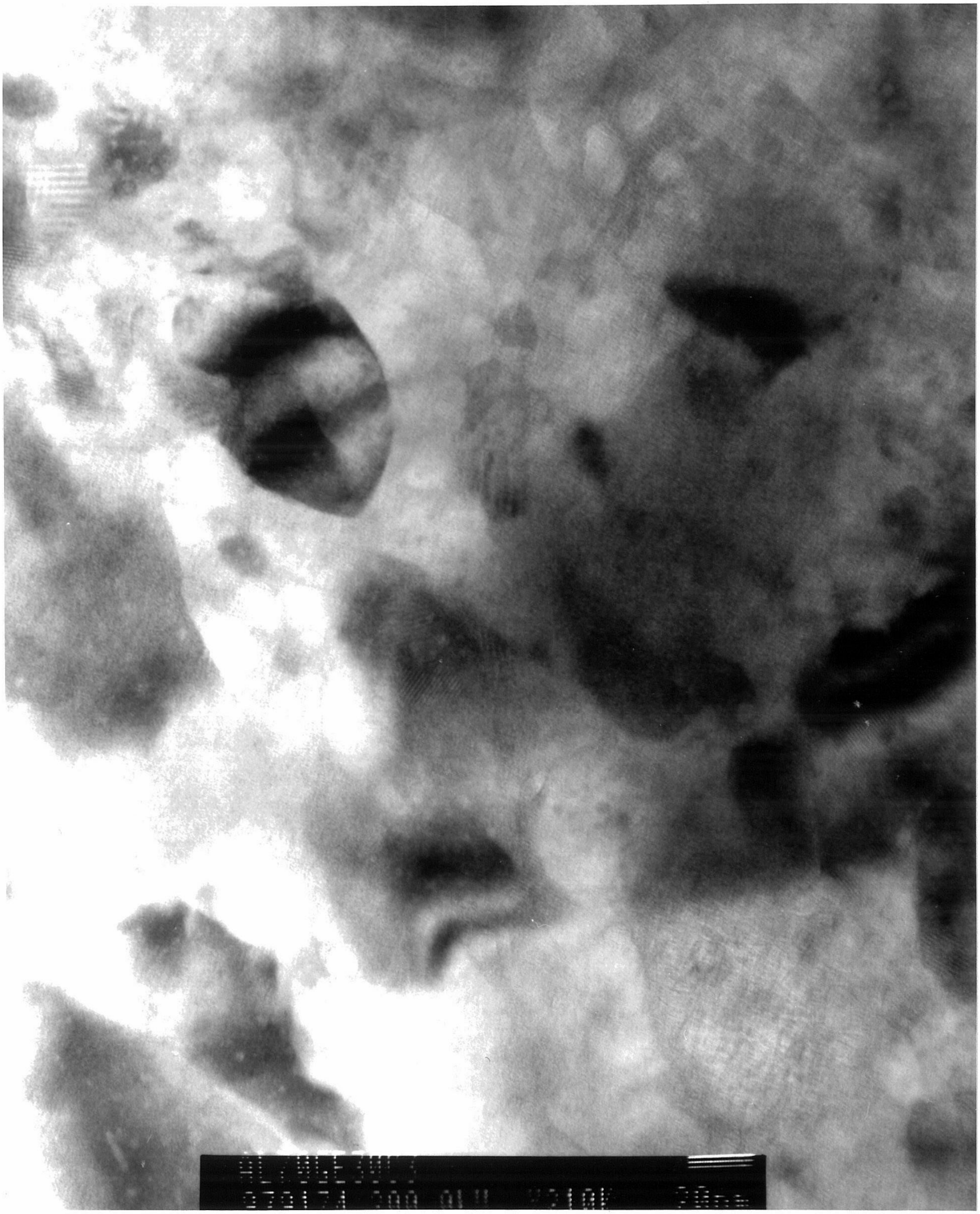

Figure 4.31 Bright field TEM Photograph of $Al_{70}Ge_{30}$ pressed to 200 kbar.

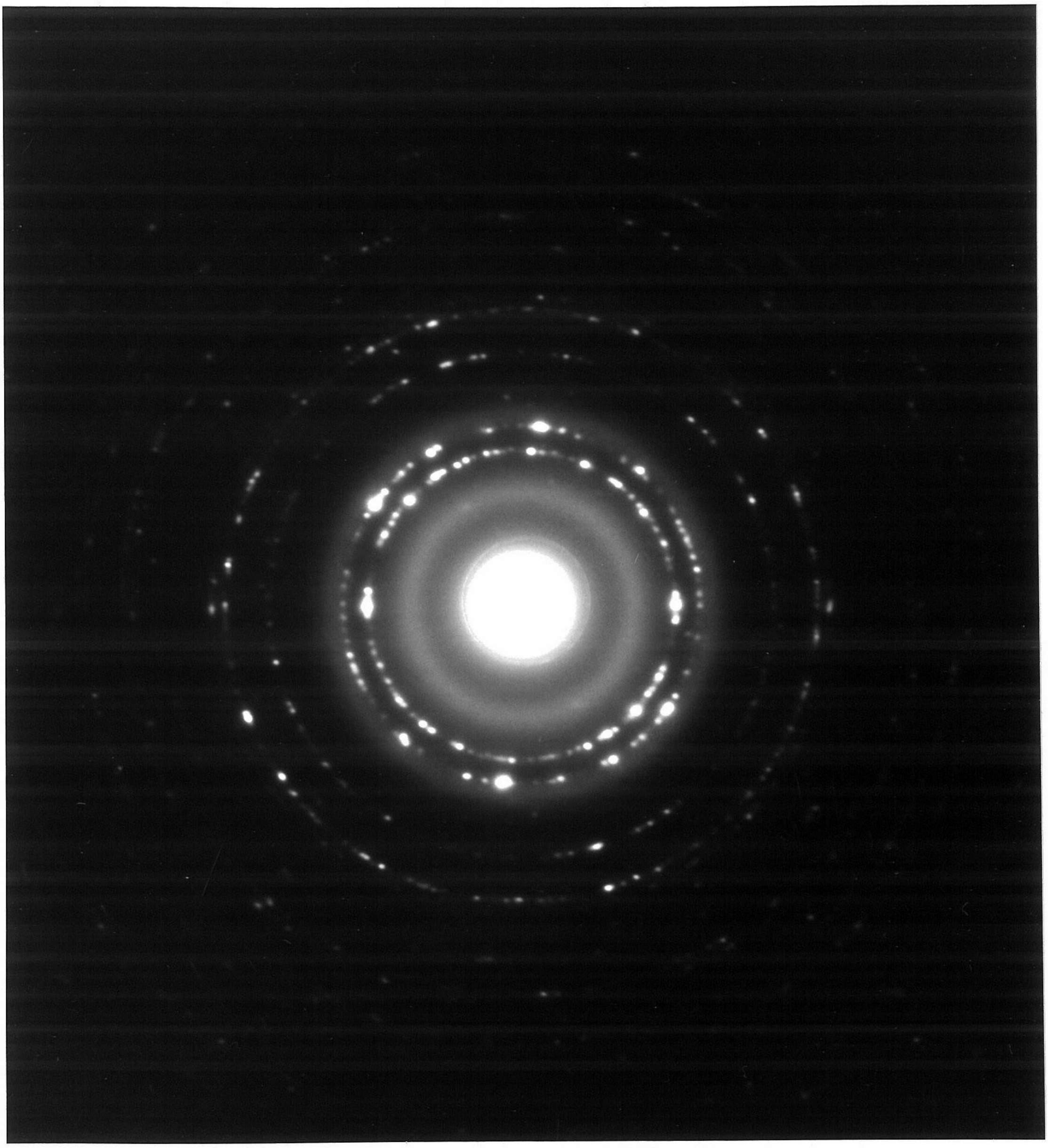

Figure 4.32 Selected area diffraction pattern of $Al_{70}Ge_{30}$ pressed to 200 kbar.

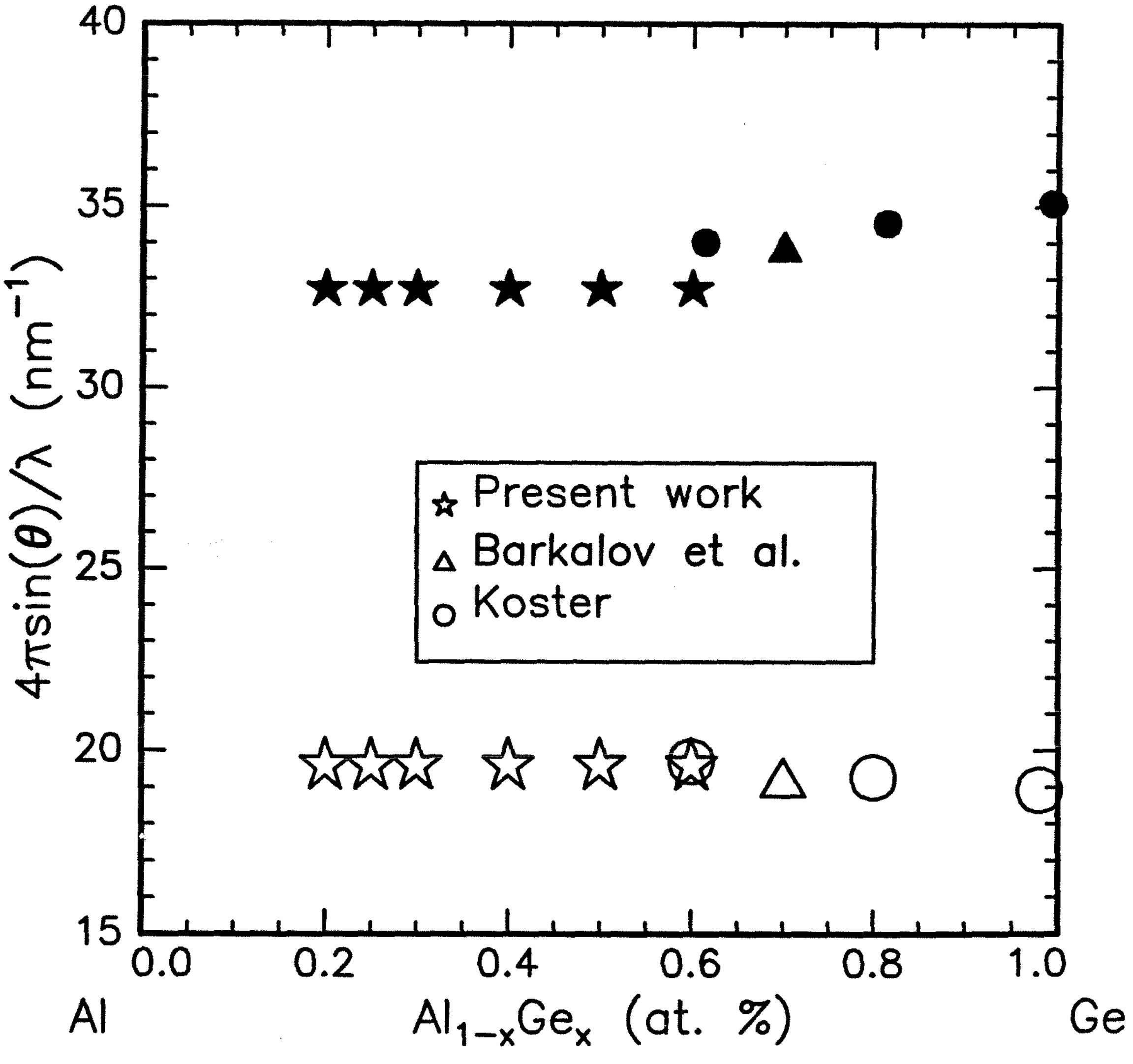

Figure 4.33 Position of amorphous halos as function of composition for the amorphous phase I. The open symbols represent the first halo and the filled symbols represent the second halo.

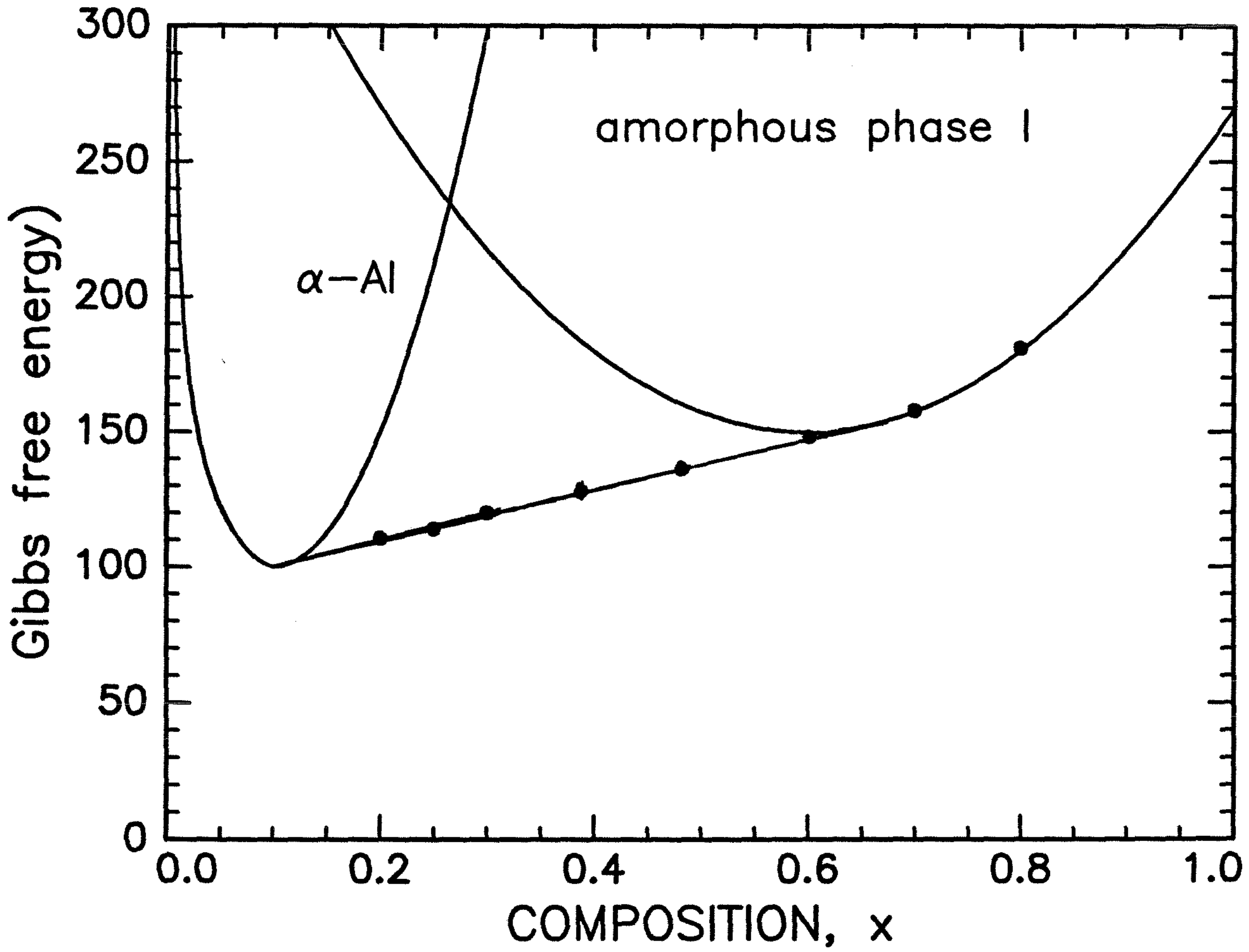

Figure 4.34 Schematic free energy-composition diagram.

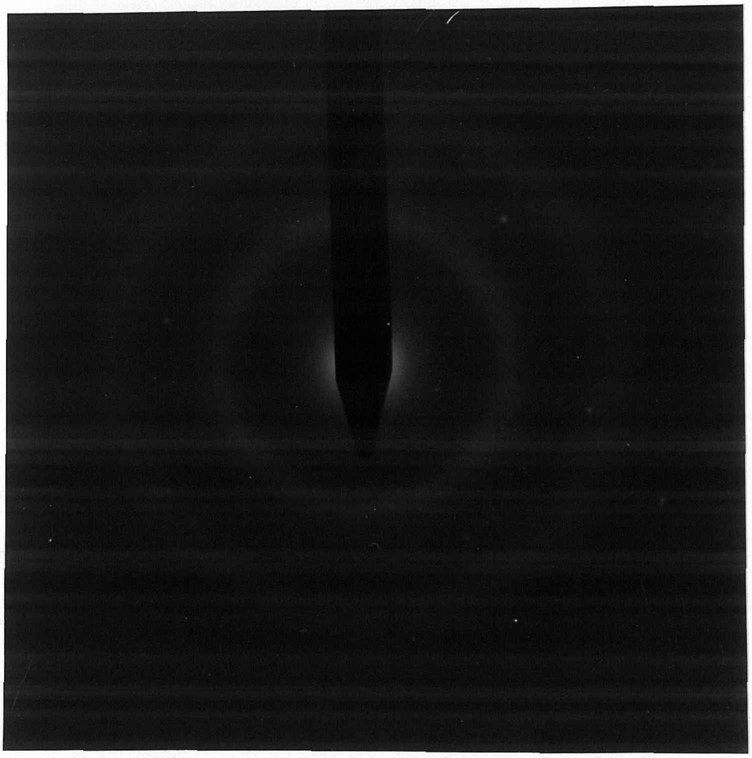

Figure 4.35 Selected area diffraction pattern of $Al_{40}Ge_{60}$ pressed to 180 kbar.

Figure 4.36 Bright field TEM Photograph of single phase amorphous phase I in $Al_{60}Ge_{40}$ pressed to 180 kbar.

Figure 4.37 Bright field TEM photograph of amorphous phase II in $Al_{40}Ge_{60}$ after 180 kbar.

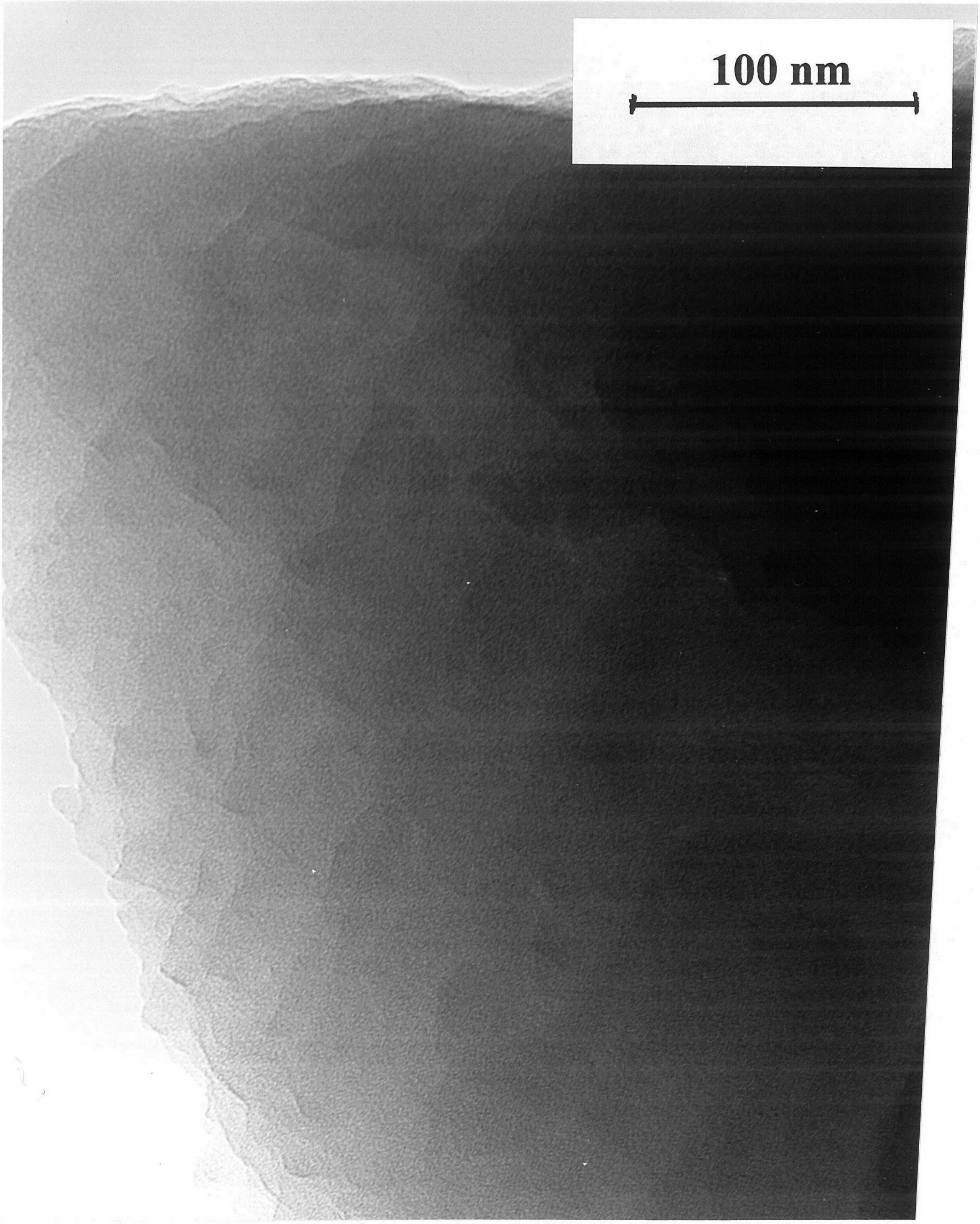

Figure 4.38 Bright field TEM photograph of amorphous phase II in $Al_{60}Ge_{40}$ after 140 kbar.

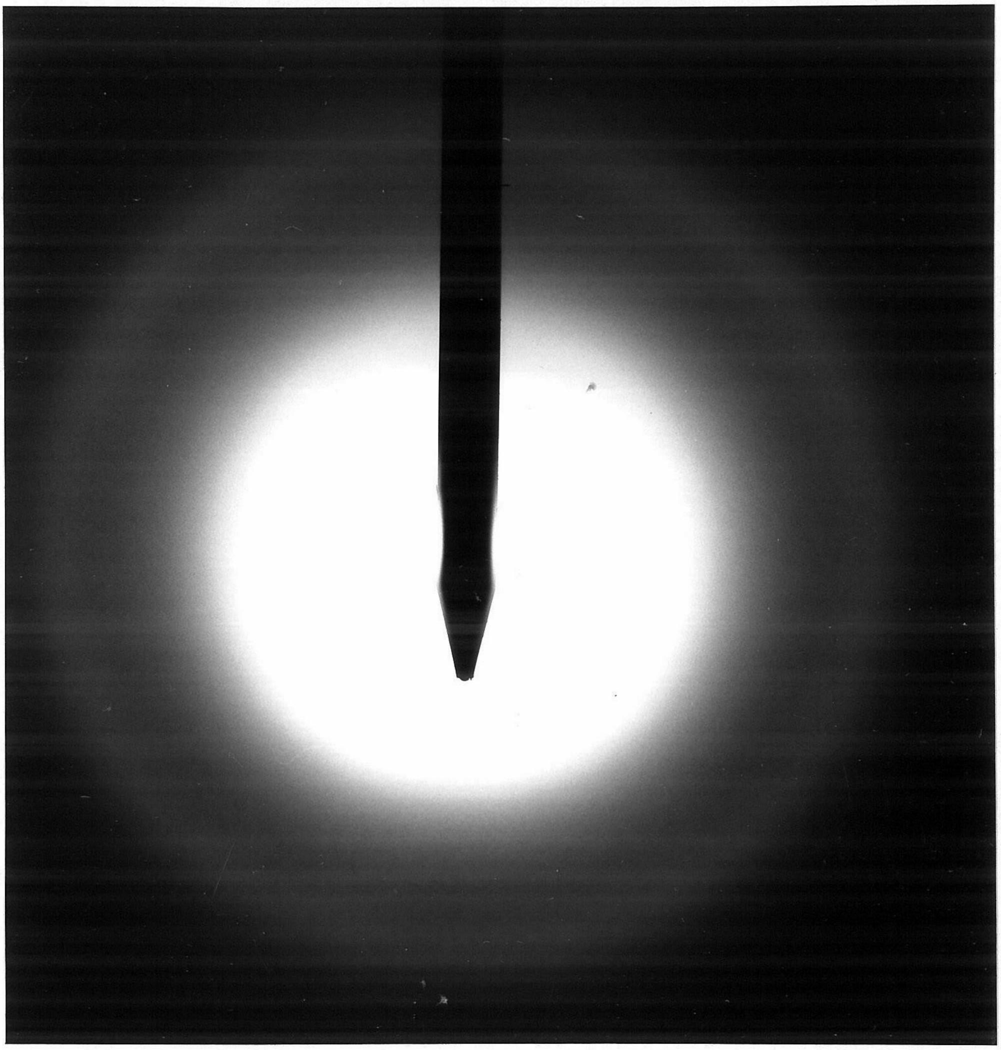

Figure 4.39 Selected area diffraction pattern of amorphous phase II in $Al_{60}Ge_{40}$ after 140 kbar.

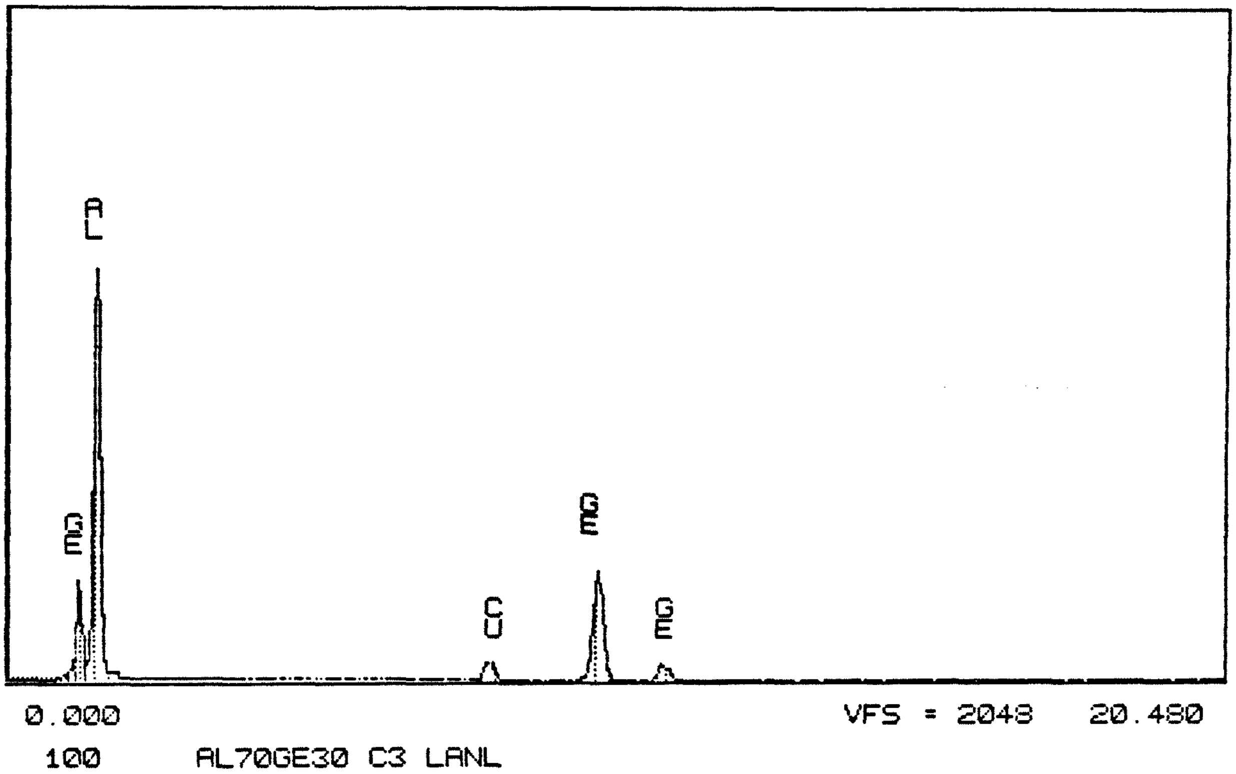

Figure 4.40 EDX spectrum of $Al_{70}Ge_{30}$ after 200 kbar.

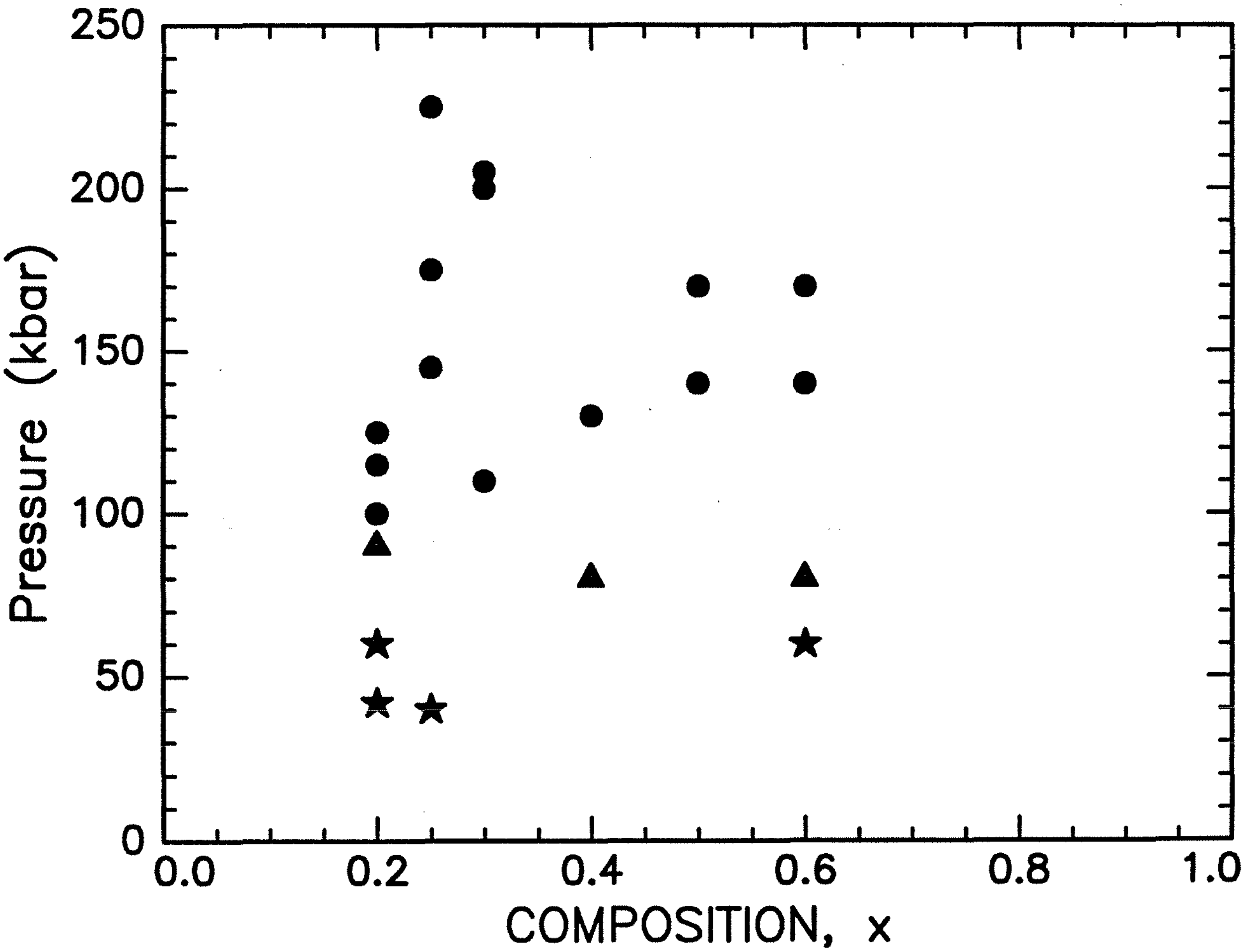

Figure 4.41 Summary of results in TEM samples. Stars indicate samples in which no amorphous phase was observed. Triangles indicate samples in which the amorphous phase I was observed. Circles indicate samples in which both amorphous phases were observed.

---

1. P. Ramachandrarao, M. Laridjani, and R. W. Cahn, *Z. Metallk.* 63, 43 (1972).
2. M. Laridjani and R. W. Cahn, *Mat. Sci. Eng.* 23, 125 (1976).
3. P. J. Yvon and R. B. Schwarz, *Proc. 2nd Int. Conf. Structural Applications of Mechanical Alloying*, (Vancouver, Canada, 1993).
4. C. C. Koch, J. S. C. Jang, and S. S. Gross, *J. Mater. Res.* **4**, 557 (1989).
5. J. S. C. Jang and C. C. Koch, *J. Mater. Res.* **5**, 325 (1990).
6. D. Turnbull, J. S. C. Jang, and C. C. Koch, *J. Mater. Res.* **5**, 1731 (1990).
7. P. J. Yvon and R. B. Schwarz, unpublished results, Los Alamos National Laboratory (1993).
8. R. T. Leonard and C. C. Koch, *NanoStructured Mater.* 1, 471 (1992).
9. R. Schmid-Fetzer, Ternary Alloys (G. Petzow and G. Effenberg editors, VCH, Stuttgart, Germany), Vol. 5, 222 (1991).
10. V. G. Rivlin and G. V. Raynor, *Int. Met. Rev.* 26, 133 (1981).
11. P. J. Yvon and R. B. Schwarz, unpublished results, Los Alamos National Laboratory (1993).
12. Eugene P. Bertin, Principles and Practice of X-ray Spectrometric Analysis (Plenum, New York, 1975).
13. U. Köster, *Z. Metallk.* 63, 472 (1972).
14. P. J. Yvon and R. B. Schwarz, *J. Mater. Res.* 8, 239 (1993).
15. J. Eckert, J. C. Holzer, C. E. Krill, III, and W. L. Johnson, *J. Mater. Res.* **7**, 1751 (1992).
16. C. Suryanarayana and T. Anantharaman, *J. Mater. Sci.* 5, 992 (1990).
17. S. N. Ohja, K. Chattopadhyay, and S. Ranganathan, *Mater. Sci. Eng.* A 123, 177 (1985).
18. R. B. Schwarz and C. C. Koch, *Appl. Phys. Lett.* 49, 146 (1986).
19. R. B. Schwarz, R. R. Petrich, and C. K. Saw, *J. Non-Cryst. Solids* 76, 281 (1985).
20. B. D. Cullity, Elements of X-ray diffraction (Addison Wesley, Reading, Massachusetts, 1978), 523.
21. J. F. Cannon, *J. Phys. Chem Ref. Data* 3, 781 (1974).
22. O. I. Barkalov, I. T. Belash, V. F. Degtyareva, and E. G. Ponyatovsky, *Soviet Phys. Solid State* 29, 1138 (1987).
23. *Nat. Bur. Stand. (U. S.) Monogr 25.* 19, 11 (1982).
24. F. Catalina, C. N. Afonso, E. Rollan, and C. Ortiz, *J. Less-common Met.* 145, 209 (1988).
25. F. Catalina, C. N. Afonso, and C. Ortiz, *Thin Solids Films* 167, 57 (1988).

5. DISCUSSION

5.1 Plurality of Amorphization Process

Most of the results presented in chapter 4 were not those we had expected to obtain. The amorphization process described in section 2.4 and illustrated in Figure 2.12 is likely to occur, but it was not possible to prove it with the experimental tools we used. We did obtain a supersaturated solid solution (step A to B to C in Figure 2.12), but it was difficult to observe structural changes in this phase when the pressure was released or upon increasing the temperature. More powerful structure determination techniques are needed to investigate the possible crystal-to-glass transformation of an aluminum solid solution supersaturated in germanium.

The second amorphization process proposed, i.e., the crossing of the polymorphous melting curve at a temperature below the glass-transition temperature described in Figure 2.14, is responsible for the formation of the high-density amorphous phase II. The phase transition did not occur exactly as predicted, since the mixture of α -aluminum and β-germanium did not transform directly to a glass. We first observed the formation of an intermediate high-pressure hexagonal γ phase which did transform to a glass under further increase in pressure.

We obtained some puzzling results, as the γ phase formed at relatively low pressures (25 kbar), but would transform back to the initial equilibrium mixture of aluminum and germanium upon annealing under pressure. On a subsequent pressure increase, the hexagonal γ phase would reappear. This was explained by (a) the fact that the pressure dropped when the temperature was raised, which took the sample back below the phase transition pressure and (b) the free energy of the starting material was raised by the defects introduced during mechanical alloying, which caused the phase transition to occur at lower pressures.

We could not construct a polymorphous melting curve for the γ phase for a variety of reasons. First, this structure has not been entirely determined and only the structure and the lattice parameters are known. The second problem is that the structure of the liquid phase of aluminum-germanium is not known. Molten aluminum, like most liquid metals, has an atomic coordination number equal to 12. Liquid germanium has a different structure with only 6 to 8 neighbors [1,2]. The structure of the molten Al-Ge is believed [3] to have strong chemical short range order and to consist of a two-phase mixture of Al_2Ge aggregates in equilibrium with an otherwise random melt. There is very little thermodynamic data available on liquid Al-Ge, so we will have to look at the amorphous phases to have access to density values. As discussed in the next section, the amorphous phase II is much denser than the hexagonal γ phase, which probably means that the liquid phase is also denser than the hexagonal γ phase. We believe this is the reason why the slope of the melting curve of the γ phase in the P-T phase diagram is negative. Therefore, we are able to melt $Al_{70}Ge_{30}$ by applying pressure at room temperature.

5.2 Density of the Amorphous Phases

In this section we will to use the Å as the unit of length. For an amorphous material having the structure of a liquid metal, the nearest-neighbor distance, d_{nn} can be deduced from the position of the first amorphous halo. The Debye formula [4] is:

$$d_{nn} = \frac{1.230\,\lambda}{\sin\theta} \tag{5.1}$$

This formula can be rewritten in terms of k as

$$d_{nn} = \frac{7.6953}{k} \tag{5.2}$$

(7.6953 is equal to $2\pi\sqrt{\frac{3}{2}}$). If we apply this formula to the amorphous phase I, the d_{nn} value obtained does not make any sense, as it yields an interatomic distance around 4 Å, which we know to be incorrect. The problem is that the amorphous phase I is not liquid-like, but is better described as a continuous random network (CRN), with an atomic coordination number close to 4. For this phase, a more appropriate formula would be:

$$d_{nn} = \frac{4.7124}{k} \tag{5.3}$$

(here 4.7124 is equal to $0.75\,(2\pi)$). We derived Eq. 5.3 by calculating the ratio of d_{nn} and d_{111} in a diamond structure. With the measured k-value for the amorphous phase I, we obtain an interatomic distance around 2.4 Å, which is consistent with the nearest-neighbor distances in both crystalline and amorphous germanium.

Using the known molar volumes of α-aluminum, β-germanium, and amorphous germanium, we can deduce approximate molar volumes for the two-phase mixture of α -aluminum and amorphous $Al_{40}Ge_{60}$ (amorphous phase I) for $x < 0.6$, and for the single -phase amorphous phase I for $x > 0.6$. The goal of this exercise is to show that the density of the amorphous Al-Ge phase I is lower than that of the mixture of the starting crystalline materials. This means that the phase I could not have formed in the diamond-anvil cell during a pressure increase.

The atomic volumes for the α-aluminum and β-germanium are 16.61 $Å^3$ and 22.64 $Å^3$, respectively. The average atomic volume for an $Al_{1-x}Ge_x$ aggregate is given by:

$$V(x) = 16.61 + 6.03\,x \tag{5.4}$$

The atomic volume of covalent amorphous germanium is 25.17 $Å^3$. Figure 4.33 shows that the k-number increases slightly with increasing aluminum concentration and reaches a maximum for 40 at.% Al. We fitted the data in the range $0.6 < x < 1$ to a straight line. This gives:

$$k(x) = 2.0535 - 0.165\,x \tag{5.5}$$

Because $k \propto d_{nn}^{-1}$ and $V \propto d_{nn}^{3}$, it follows that for any structure we should expect $V \propto k^{-3}$. The proportionality constant will certainly depend on the structure and coordination number. Using the atomic volume of pure amorphous germanium [5], we deduce an empirical formula that expresses the relation between k and the atomic volume in a tetrahedrally-bond continuous random network:

$$V = \frac{171}{k^3}. \tag{5.6}$$

For $0.6 < x < 1$, replacing k from Eqs. 5.5, we obtain:

$$V(x) = \frac{171}{(2.0535 - 0.165\,x)^3}. \tag{5.7}$$

For $0 < x < 0.6$, we have a mixture of aluminum and an amorphous germanium phase with an atomic volume of 22.849 Å^3. This gives:

$$V(x) = 16.61 + 10.398\,x \tag{5.8}$$

Therefore, whether x is lower or higher than 0.6, the covalent amorphous phase I is not as dense as the starting mixture of α-aluminum and β-germanium. This suggests that the covalent amorphous phase I does not form under pressurization since, as we showed in 4.3.1, the amorphization is accompanied by a large volume *decrease*.

In the following paragraph we perform a similar volumetric analysis of the γ phase. The high-pressure γ phase has an average atomic volume of 18.19 Å^3 [6] and a composition of $Al_{30}Ge_{70}$. In first approximation, the average molar volume of a mixture of α-aluminum and γ $Al_{30}Ge_{70}$ phase should be:

$$V = 16.61 + 2.257\,x \tag{5.9}$$

where x is the germanium content in the $Al_{1-x}Ge_x$ alloy. This mixture is denser than the starting mixture of aluminum and germanium (this is clear from Eqs. (5.4) and (5.9)).

The formation of this phase under pressure makes sense, but the volume decrease for this transformation is probably small and that is the reason why no plateau was observed during the phase transition on increasing the pressure.

The other amorphous phase obtained, phase II, has amorphous diffraction halos located at $k = 2.99$ Å^{-1} and $k = 5.51$ Å^{-1}. This phase is reported here for the first time. This phase is much denser than the covalent germanium-rich amorphous phase I, and if we assume that it has a metallic liquid-like structure, using Eq. 5.2 we can estimate the average nearest neighbor distance to be 2.57 Å. The ratio of the first two diffraction halos is equal to 1.84 which is also typical of metallic liquid like structures [7]. This phase exists over a wide range of compositions ($0.2 < x < 0.6$) and the germanium concentration does not affect noticeably the position of the diffraction halos. From the values of nearest-neighbor distances of various metallic amorphous alloys quoted by Cargill [7] and Bergmann [8], we estimate the atomic volume of amorphous phase II to be around 11.2 Å^3. This phase is much denser than the starting mixture of f.c.c. aluminum and diamond germanium. It is also much denser than the hexagonal γ phase. A phase transformation to the amorphous phase II is accompanied by a large volume decrease of about 30%. This is the reason why it was observed so dramatically in the diamond anvil cell (Figure 4.24).

From the previous discussion we conclude that the amorphous phase II forms under pressure between 70 and 80 kbar and is retained after the pressure is released. We also conclude that the amorphous phase I cannot possibly be formed under pressure, but is formed upon the release of the pressure. This is in agreement with the work of Barkalov and coworkers [9], who reported that the hexagonal γ phase is retained upon the release of the pressure at -150°C and transforms to a β-white tin structure at -30°C, before becoming amorphous at 20°C. The amorphous phase they obtained had broad amorphous diffraction peaks near $k = 1.92$ Å^{-1} and $k = 3.38$ Å^{-1}, which are comparable to the k-values we measured for the amorphous phase I.

We are somewhat puzzled that we did not see the γ phase in any of our TEM studies. We interpret this as further indication that at ambient pressure and temperature, the γ phase is not stable and transforms into the amorphous phase I. To retain the γ phase, we must first cool the cell under pressure and release the pressure at temperatures below -30^{o}C [8].

5.3 Characteristics of the Crystal-to-Glass Transformation

The observation of a pressure plateau (Figure 4.24) for the formation of amorphous phase II suggests that the amorphization reaction is a transition of the first order as is ordinary melting. The question then arises: the sample volume being so small and being in contact with massive diamonds of high thermal conductivity, what prevents the transformation from becoming catastrophic? Because it involves a large volume decrease, the transformation causes a drop in the applied pressure and therefore it stops before completion. To resume the transformation we need to manually increase the pressure in the cell. This is done in small increments (see section 4.3.2). The mechanism of this structural transformation is explained with the help of Figure 5.1. This is a schematic Volume-Pressure diagram which helps determining the operating pressure and volume in the system. The dashed curves represent the response of the diamond anvil cell for different spacings between the two platens Zi, where $Z_1 > Z_2 > Z_3 > Z_4$. These curves represent the (extrinsic) elastic response of the cell. The solid lines represent the (intrinsic) elastic response of the sample and give the volume as a function of pressure for the initial phase (rightmost line) and the final phase (leftmost line). The slope of these lines represent the compressibility of the material. For a given sample and a given spacing of the platens, the intersection of the cell response curve and the sample compressibility curve represents the operating conditions, i.e., the pressure and volume of the sample for this given spacing. P_1 represents the pressure at which the transformation starts, and P_2, the pressure at which the transformation will stop after it has already started. $\Delta P = P_1 - P_2$ represents the internal friction of the reaction. We start with the sample at A in its initial structure, and we decrease the spacing between the platens from Z_1 to Z_2. The pressure in the cell will move along the compressibility curve AB of the sample until it reaches P_1 (Point B). At this point, the amorphization phase transition starts and the sample volume decreases along the diamond cell response curve, BC for Z_2 constant. The pressure decreases until it reaches P_2 (Point C) where the transformation stops and the system is again stable. To resume the transformation we must increase the pressure, going from C to D. As we tighten the bolts to go from Z_2 to Z_3, the pressure increases, until P1 is reached again (point D). Similarly, the pressure and volume in the cell will move from Point D to Point E to Point F to Point G, where the transformation is complete. So, although the transformation may be catastrophic on a microscopic scale, the transformation is rather smooth on a macroscopic scale because of the combined effects of the elastic response of the system and internal friction. The melting character of this pressure-induced phase transformation is also apparent in our TEM observations as we observed the amorphous phase II to be very smooth, as if it formed by a liquid-like flow.

5.4. Discussion of Ponyatovsky's Model

Ponyatovsky et al. [6] proposed a thermobaric treatment to obtain pressure-driven crystal-to-glass transformations in specific systems, including the aluminum-germanium system. This thermobaric treatment is described in detail in section 1.4.4. One of their claims was that amorphization occurred while crossing the metastable extension of the melting curve when heating up the sample after the pressure was released (see Figure 1.12). We have problems understanding this model. The first problem with this approach is that the hexagonal γ phase does not transform to a glass, but to another crystalline phase (with a β white-tin structure), which in turns transforms to an amorphous phase. The location of this phase is not shown in their P-T phase diagram. The second problem is that the amorphous phase they reported has a tetrahedrally-bonded continuous random structure, which is very different from the structure of liquid germanium (coordination 6 to 8) and liquid aluminum (coordination 12). By crossing the melting line, one would expect to obtain an amorphous phase with a density closer to that of the melt. It thus seems doubtful that the mechanism of the pressure-driven amorphization process they describe corresponds to the P-T phase diagram they propose.

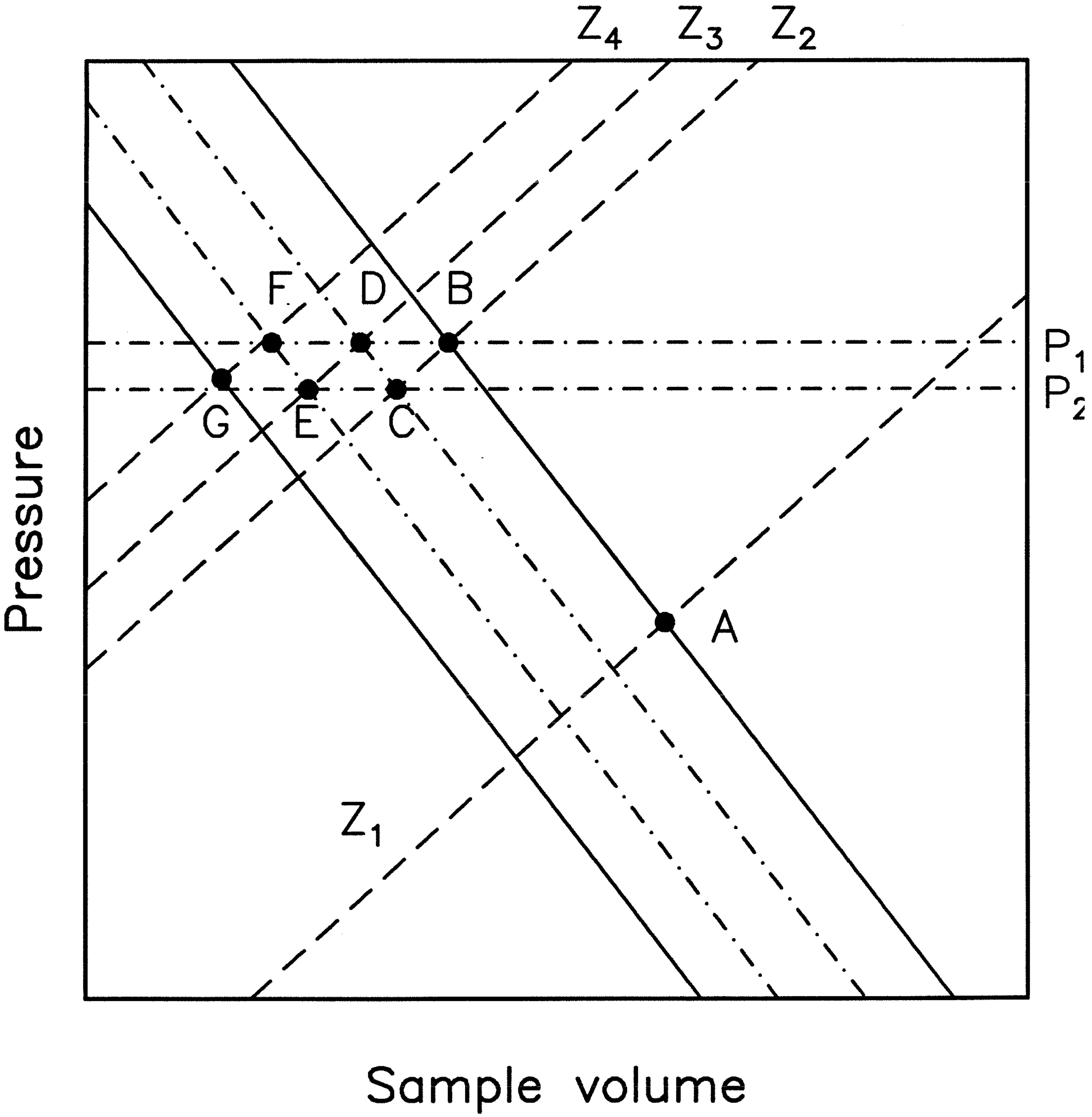

Figure 5.1 Schematic volume-pressure phase diagram to determine the operating pressure and volume in the sample.

---

1. H. Hendus, *Z. Naturforsch.* 2a, 505 (1947).
2. H. Krebs, V. B. Lazarev, and L. Winkler, *Z. Anal. Allg. Chem.* 353, 277 (1967).
3. N. Kh. Abrikosov, N. N. Glaloleva, and S. N. Chizhevskaya, *Izv. Akad. Nauk SSSR Neorg. Mater.* 5, 2055 (1968).
4. A. Guinier, X-Ray Diffraction (W. H. Freeman, San Francisco, California), 72 (1963).
5. H. Richter and O. Fürst, *Z. Naturforsch.* 6, 38 (1951).
6. E. G. Ponyatovsky and V. F. Degtyareva, *High Press. Res.* 1, 163 (1989).
7. G. S. Cargill III, *Solid State Phys.* 30, 227 (1975).
8. G. Bergmann, *Phys. Rept.* 27, 159 (1976).
9. O. I. Barkalov, I. T. Belash, V. F. Degtyareva, and E. G. Ponyatovsky, *Soviet Phys. Solid State* 29, 1138 (1987).

6. CONCLUSION AND FUTURE WORK

We report in this dissertation the pressure-induced formation of two distinct amorphous phases in the aluminum-germanium system labeled phase I and phase II. These phases have been characterized indirectly by x-ray diffraction and directly by transmission electron microscopy.

Amorphous phase I had already been obtained in rapidly solidified aluminum-germanium alloys, and had also been produced by a thermobaric treatment. This phase has a tetrahedrally-bonded continuous random network structure, and can be formed as single phase between 60 and 100 at.% germanium. This phase has approximately 90% of the density of the starting mixture of α-aluminum and β -germanium. It does not form under pressure, but results instead from the decomposition of a high-pressure γ phase which forms between 25 and 65 kbar. The thermobaric treatment we used to form the amorphous phase I is simpler than that of Barkalov and coworkers.

Amorphous phase II has a liquid-like structure and we believe it is metallic. We formed a single-phase amorphous II alloy for all $Al_{1-x}Ge_x$ compositions studied $(0.2 < x < 0.6)$. This is the first time that this metallic amorphous phase is reported in the aluminum-germanium system. This phase forms at a pressure of about 80 kbar, and is metastable (for at least a week) at room temperature following the pressure release.

This study is far from being complete, as it would be interesting to observe all the structural changes *in situ* and know accurately the phase transition pressures. It would also be interesting to produce bigger quantities of the amorphous phase II to be able to study its thermal stability and transport properties. This amorphous phase may also possess interesting superconducting properties, since some of the metastable phases produced by rapid solidification are superconducting.

In collaboration with Ricardo Schwarz (CMS) and Robert Von Dreele (Los Alamos Neutron Scattering Facility (LANSCE)), neutron diffraction studies will be carried in the summer of 1993. For these studies we will use a tungsten carbide high-pressure cell able to reach pressures up to 100 kbar which should be sufficient to produce the metallic amorphous phase II. The sample volume in these tests, about 0.1 cm^3, will be sufficient for differential calorimetry measurements.

During the course of this work, we also became interested in the synthesis of superconducting $YBa_2Cu_3O_7$ alloys by mechanical alloying. We investigated the oxygen isotope effect on $YBa_2Cu_3O_7$. This work, which was published in five papers and reviews, is not included in this thesis. However, it is worth mentioning that the techniques we learned (mechanical alloying, EDX analysis, differential scanning calorimetry, etc.) were later used in the course of this thesis work.

Curvature of the melting curve in the P-T phase diagram

In this appendix, the curvarture of the melting curve in the P-T phase diagram is discussed. This discussion will be as general as possible, with an emphasis on the case when the initial slope is negative. The polymorphous Clapeyron equation is:

$$\left(\frac{dP}{dT}\right)_m = \frac{\Delta S}{\Delta V} \qquad (1)$$

To study the curvature of the melting curve, we have to determine the sign of the second derivative of P with respect to T.

$$\frac{d(\Delta S)}{dT} = \left(\frac{\partial(\Delta S)}{\partial T}\right)_P + \left(\frac{dP}{dT}\right)\left(\frac{\partial(\Delta S)}{\partial P}\right)_T \qquad (2)$$

$$\frac{d(\Delta V)}{dT} = \left(\frac{\partial(\Delta V)}{\partial T}\right)_P + \left(\frac{dP}{dT}\right)\left(\frac{\partial(\Delta V)}{\partial P}\right)_T \qquad (3)$$

Setting $X = \left(\frac{dP}{dT}\right)$ and using (2) and (3) we get:

$$(\Delta V)^2\left(\frac{d^2P}{dT^2}\right) = \Delta V\left(\left(\frac{\partial(\Delta S)}{\partial T}\right)_P + X\left(\frac{\partial(\Delta S)}{\partial P}\right)_T - X\left(\frac{\partial(\Delta V)}{\partial T}\right)_P - X^2\left(\frac{\partial(\Delta V)}{\partial P}\right)_T\right) \qquad (4)$$

Using a Maxwell relation, we get: $\left(\frac{\partial S}{\partial P}\right)_T = -\left(\frac{\partial V}{\partial T}\right)_P$ (5)

we can rewrite (4) as:

$$(\Delta V)^2\left(\frac{d^2P}{dT^2}\right) = -\Delta V\left(X^2\left(\frac{\partial(\Delta V)}{\partial P}\right)_T + 2X\left(\frac{\partial(\Delta V)}{\partial T}\right)_P - \left(\frac{\partial(\Delta S)}{\partial T}\right)_P\right) \qquad (6)$$

$$C_P = T\left(\frac{\partial S}{\partial T}\right)_P \qquad (7)$$

$$\alpha = \left(\frac{1}{V}\right)\left(\frac{\partial V}{\partial T}\right)_P \qquad (8)$$

$$K_T = -\left(\frac{1}{V}\right)\left(\frac{\partial V}{\partial P}\right)_T \tag{9}$$

we can rewrite (6) as:

$$(\Delta V)^2\left(\frac{d^2P}{dT^2}\right) = \Delta V\left(X^2\,\Delta(V\,K_T) - 2X\,\Delta(\alpha\,V) + \Delta\left(\frac{C_P}{T}\right)\right) \tag{10}$$

We are interested in the sign of $\frac{d^2P}{dT^2}$. To simplify (10) let us write :

$$A = \Delta(V\,K_T) = V_l\,K_{Tl} - V_x\,K_{Tx} \tag{11}$$

$$B = \Delta(V\,\alpha) = V_l\,\alpha_l - V_x\,\alpha_x \tag{12}$$

$$C = \frac{\Delta(C_P)}{T} = \frac{C_{Pl} - C_{Px}}{T} \tag{13}$$

$$(\Delta V)^2\left(\frac{d^2P}{dT^2}\right) = \Delta V\left(A\,X^2 - 2B\,X + C\right) \tag{14}$$

ΔV and X have the same sign, we have to study the sign of (14). First let us look at the sign of F defined as:

$$F(X) = A\,X^2 - 2B\,X + C \tag{15}$$

To study how the sign of F varies we have to look at the signs of A, B, and C. The coefficients of compressiblity are not well known around the melting point, but a typical value for a liquid is in the 10^{-9} $m^2 \cdot N^{-1}$ [1]· For solids, we have access to bulk moduli [2], which are the reciprocal of K_T. A typical value for a bulk modulus is in the 10 GPa range, which yields a compressibility one or two orders of magnitude lower than that of the liquid. V_l and V_x are in the same order of magnitude, therefore A is a positive quantity. A typical thermal expansion coefficient for a solid is around 10^{-5} K^{-1}, where it is around 10^{-4} K^{-1} for a liquid, therefore B is also a positive quantity. We can start discussing the sign of F, before getting into discussing the sign of C, which is harder to determine. This second degree equation has two roots which we will note X_1 and X_2.

$$X_1 = \frac{B + \sqrt{B^2 - AC}}{A} \tag{16}$$

$$X_2 = \frac{B - \sqrt{B^2 - AC}}{A} \tag{17}$$

If $X_2 < X < X_1$, then F(X) is negative (opposite sign from A), and F(X) is positive otherwise. X_1 is always positive, and X_2 is also positive if C is positive. If C is negative, X_1 and X_2 are of opposite signs. This already yields the following result: if the initial slope is negative, and lower than X_2, then (15) is negative to start with, which ensures that X decreases, and therefore (15) is always negative.

Let us discuss how C varies along the melting curve. This difference can be positive (e. g. aluminum) or negative (e. g. germanium) at the melting temperature at room pressure [3

$$\delta Q = C_P \, dT + k_T \, dP \tag{18}$$

Thus, $dH = C_P \, dT + (k_T + V) \, dP$ (19)

where k_T is the isothermal expansion coefficient. Thus

$$\left(\frac{\partial C_P}{\partial P}\right)_T = \left(\frac{\partial (k_T + V)}{\partial T}\right)_P \tag{20}$$

$$d(C_{Pl} - C_{Px}) = d(\Delta C_P) = \left(\frac{\partial(\Delta C_P)}{\partial T}\right)_P dT + \left(\frac{\partial(\Delta C_P)}{\partial P}\right)_T dP \tag{21}$$

$$\left(\frac{\partial(\Delta C_P)}{\partial T}\right)_P = \beta_l - \beta_x \tag{22}$$

$$\left(\frac{\partial(\Delta C_P)}{\partial P}\right)_T = \left(\frac{\partial(k_{Tl} - k_{Tx})}{\partial T}\right)_P + \alpha_l.V_l - \alpha_x.V_x \tag{23}$$

$$K = k_{Tl} - k_{Tx} \tag{24}$$

(21) can be rewritten:

$$d(C_{Pl} - C_{Px}) = (\beta_l - \beta_x) \, dT + \left[\left(\frac{\partial(K)}{\partial T}\right)_P + B\right] dP \tag{25}$$

$$(\Delta C_P)_P - (\Delta C_P)_{P_{atm}} = (\beta_l - \beta_x) \, \Delta T_m + \left[\left(\frac{\partial K}{\partial T}\right)_P + B\right]\left[\frac{dP}{dT}\right] \Delta T_m \tag{26}$$

To study how this evolves becomes impossible to do without considering specific materials. For a given material, one can obtain values or estimates for the coefficients, and use them to obtain the slope of the melting curve. In the aluminum-germanium case, on the germanium-rich side, the initial slope is negative ($\Delta T/\Delta P \approx -4$ K kbar^{-1}), where an estimate of X_2 gives a number an order of a magnitude lower at worst, which means that the melting curve is concave downward for the germanium-rich part of the phase diagram.

---

1. Handbook of Chemistry and Physics (CRC Press, Boca Raton, Florida, 1986).
2. Smithells Metals Reference Book (Butterworths, London, England).
3. A. T. Dinsdale, *CALPHAD* 15, 317 (1991).

```
'Author :Pascal Yvon, January 1991
DECLARE SUB gibbsk (phase$, T!, x!, G!)
' ====== Calculate the liquidus, solidus, and T0 curve for Al(1-x)Ge(x) =====
' ====== Thermodynamic model of Kaufman, CALPHAD Vol.
   OPEN "a:T0-AlGe.dat" FOR OUTPUT AS #6
   OPEN "a:T0-AlGe.Glq" FOR OUTPUT AS #7
   OPEN "a:T0-AlGe.Gfc" FOR OUTPUT AS #8
   DIM TT(200), solidus(200), x00(200), liquidus(200)
   i = 1
' ====== Melting temperatures:
   TMAl = 660.37 + 273: TMSi = 9000
'
' ====== Calculate G(liq) and G(fcc) for given tempartures
L0:
   INPUT "calculate G(liq)..(Y/N) "; ans$
   IF ans$ <> "Y" AND ans$ <> "y" THEN GOTO L1
   INPUT "Input temperature in K "; TT
   TT$ = STR$(TT)
   PRINT #7, "G(liq) for T=" + TT$
   FOR x = 0 TO .9 STEP .02
       CALL gibbsk("liq", TT, x, Gliq)
       PRINT #7, x, Gliq
   NEXT x
L1:
   INPUT "calculate G(fcc)..(Y/N) "; ans$
   IF ans$ <> "Y" AND ans$ <> "y" THEN GOTO L2
   INPUT "Input temperature in K "; TT
   TT$ = STR$(TT)
   PRINT #8, "G(fcc) for T=" + TT$
   FOR x = 0 TO .9 STEP .02
       CALL gibbsk("fcc", TT, x, Gfcc)
       PRINT #8, x, Gfcc
   NEXT x
L2:
   INPUT "Another temperature ... "; ans$
   IF ans$ = "Y" OR ans$ = "y" THEN GOTO L0
   CLOSE #7: CLOSE #8

   LPRINT "          T          solidus        x0          liquidus"
' ====== Start temperature loop
   FOR T = 920 TO 100 STEP -20
' ====== Find the composition at T0 point
     x = 0: dx = .02
1 :  x = x + dx
     PRINT "T="; T; "   x="; x
     CALL gibbsk("liq", T, x, Gliq)
     CALL gibbsk("fcc", T, x, Gfcc)
     IF Gfcc > Gliq THEN
        x = x - dx: dx = dx / 3: x0 = x
        IF dx < .00001 THEN GOTO 2
     END IF
     GOTO 1
' ========= Find the compositions of the equil. liquid and fcc phases ======
' ========= y=compos. of liquid:   z=compos. of fcc
2 :   dx = .005: y = x0 + dx: z = x0 - dx
      CALL gibbsk("liq", T, y, Gliq)
      CALL gibbsk("fcc", T, z, Gfcc)
      oslope = (Gliq - Gfcc) / (y - z)
5 :   y = y + dx
      CALL gibbsk("liq", T, y, Gliq)
```

```
      CALL gibbsk("fcc", T, z, Gfcc)
      nslope = (Gliq - Gfcc) / (y - z)
      IF nslope < oslope THEN
         oslope = nslope
         GOTO 5
         ELSE
         y = y - dx
         GOTO 6
      END IF
6 :   z = z - dx
      CALL gibbsk("fcc", T, z, Gfcc)
      CALL gibbsk("liq", T, y, Gliq)
      nslope = (Gliq - Gfcc) / (y - z)
      IF nslope > oslope THEN
         oslope = nslope
         GOTO 6
        ELSE
         z = z + dx
         dx = dx / 3
         GOTO 8
      END IF
8 :   IF dx > .00001 THEN GOTO 5 ELSE GOTO 9
9 :   LPRINT USING " T= ####.## K"; T;
      LPRINT USING "      #.####"; z; x0; y
      TT(i) = T: solidus(i) = z: x00(i) = x0: liquidus(i) = y
      i = i + 1
      NEXT T
      FOR j = 1 TO i
        PRINT #6, USING " #.####^^^^   "; TT(j), solidus(j), x00(j), liquidus(j)
      NEXT j
      CLOSE #6
3 : END


SUB gibbsk (phase$, T, x, G)
' Thermody. modelling of Al-rich fcc and liq phases according to Kaufman
' For phase zzz, free energy in CALPHAD description has the form:
'        Gzzz = (1-x)*GA + x*GB + R*T*[x*ln(x)+(1-x)*ln(1-x)] + Gex
'        Gex  = x*(1-x)*[A + B*(1-2x) + C*(1-6x+6x*x)]
'parameters from Murray after correcting usual typos
   IF phase$ <> "fcc" THEN GOTO 20
   GA = -10797! + 11.56 * T
   GB = 5021 + 8.368 * T
   A = -4979.6 - .208 * T
   B = 426.5
   C = 660.6
   GOTO 21
20 : IF phase$ <> "liq" THEN PRINT "phase does not exist"
   GA = 0
   GB = 0
   A = -11463.5 - 4.765 * T
   B = -316.1 - .305 * T
   C = 3218.3 - 1.441 * T
   GOTO 21
21 : R = 8.314
     Gex = x * (1 - x) * (A + B * (1 - 2 * x) + C * (1 - 6 * x + 6 * x * x))
     IF x <= 0 THEN x = .000001
     IF x >= 1 THEN x = .999999
     Entr = R * T * (x * LOG(x) + (1 - x) * LOG(1 - x))

      G = (1 - x) * GA + x * GB + Entr + Gex
   END SUB
```

```
' Author: Pascal Yvon, September 1992
' This program calculates phase diagram for Aluminum-Silicon
'It uses a regular solution model
  Te = 850            'eutectic temperature
  Ta = 933            'Al melting temperature
  tb = 1687           'Si melting temperature
  Sa = 11.4744        'Al entropy of melting
  Sb = 29.7617        'Si entropy ofmelting
  xae = .0159         'concentation of Si in fcc Al at eutectic T
  xe = .121           'concentration of Si at eutetic composition
  Vla = .64           'change of volume upon melting in fcc Al
  Vls = -1.25         'change of volume upon melting in diamond Si
  R = 8.314           'universal gas constant
  Vda = 2            'change of volume upon melting in fcc Si
  Vll = -3.14           'change of volume upon fcc to diamond in Si
  El = (-R * Te * LOG(xe) + Sb * (Te - tb)) / (1 - xe) ^ 2
  EAl = (El * xe ^ 2 + Sa * (Ta - Te) + R * Te * LOG((1 - xe) / (1 - xae))) / xa
  tbl = (-R * Te * LOG(xe / xae) + Sa * Te - El * (1 - xe) ^ 2 + EAl * (1 - xae)
  Tb2 = 2340          'from lattice stabilities (Dinsdale)
  'tb2 : fcc to diamond transition temperature
  Sc = (-R * Te * LOG(xae) - EAl * (1 - xae) ^ 2) / (Tb2 - Te)
  INPUT "what pressure do you want? (in kbar)", p
  INPUT "filename 1", an1$
  INPUT "filename2", an2$
  OPEN "a:an1$" FOR OUTPUT AS #1
  OPEN "a:an2$" FOR OUTPUT AS #2
  p = p * 100
  x = 0
  ym = .0000001
  FOR i = 1 TO 50
  adel = 10000
  x = i * .01
  y = ym
1 : t1 = (El * x ^ 2 - EAl * y ^ 2 + Sa * Ta + p * Vla) / (Sa - R * LOG((1 - x)
  t2 = (El * (1 - x) ^ 2 - EAl * (1 - y) ^ 2 + Sa * tbl + p * Vda) / (Sa - R * L
  del = ABS(t1 - t2)
  IF del > .5 THEN
  IF del < adel THEN
  adel = del
  ym = y
  END IF
  y = y + .0001
  IF y >= x THEN GOTO 2
  IF y >= .8 THEN GOTO 2
  GOTO 1
  ELSE
  ym = y
  END IF
2 : t1 = (El * x ^ 2 - EAl * ym ^ 2 + Sa * Ta + p * Vla) / (Sa - R * LOG((1 - x)
  t2 = (El * (1 - x) ^ 2 - EAl * (1 - ym) ^ 2 + Sa * tbl + p * Vda) / (Sa - R *
  PRINT #1, x, ym, t1, t2
  NEXT i
  FOR i = 1 TO 199
  x = i * .005
  y = i * .001
  t3 = (El * (1 - x) ^ 2 + tb * Sb + p * Vls) / (Sb - R * LOG(x))
  t4 = (EAl * (1 - y) ^ 2 + Tb2 * Sc + p * Vll) / (Sc - R * LOG(y))
  PRINT #2, x, y, t3, t4
  NEXT i
  CLOSE #1
```

```
' Program calculates phase diagram for eutectic phase diagram
' It uses regular solution model
  te = 693          'eutectic temperature
  ta = 933          'Al melting temperature
  tb = 1211.3       'Ge melting temperature
  sa = 11.474       'Al entropy of melting
  sb = 30.4975      'Ge entropy ofmelting
  xae = .02         'concentation of Ge in fcc Al at eutectic T
  xe = .283         'concentration of Ge at eutetic composition
  xbe = .989        'concentration of Ge in diamond Ge at eutectic T
  Vla = .64         'change of volume upon melting in fcc Al
  Vlg = -.6949      'change of volume upon melting in diamond Ge
  Vla1 = 3          'change of volume of fcc Ge upon melting
  Vlg1 = -3         'change of volume of diamond Al upon melting
  Vla2 = -3.09      'change of volume of fcc to diamond for Al
  vlg2 = -.489      'change of volume from diamond to fcc for GE
  R = 8.314         'universal gas constant
  tb2 = 20          'From Dinsdale dg=141.49 -5.3870 *T
  Tb3 = 1614.35     'From Dinsdale dg =36000-23.5*T
  a1 = te * (sa - R * LOG((1 - xae) / (1 - xbe))) - ta * sa
  a2 = te * (sa - R * LOG(xae / xbe)) - tb2 * sa
  DET = (xae * (1 - xbe)) ^ 2 - (xbe * (1 - xae)) ^ 2
  EAl = (-xae ^ 2 * a2 + a1 * (1 - xae) ^ 2) / DET
  El = (a1 * (1 - xbe) ^ 2 - a2 * xbe ^ 2) / DET
  'This all comes fron aluminum-liquid equilibrium
  Ege = (te * (sb - R * LOG((1 - xae) / (1 - xbe))) - tb * sb - El * xae ^ 2) /
  ta1 = (te * (sb - R * LOG(xae / xbe)) - El * (1 - xae) ^ 2 + Ege * (1 - xbe) ^
  'This come sfrom germanium-liquid equilibrium
  'WE obtain the last two parameters from figure c and d
  Sc = (-(1 - xae) ^ 2 * EAl - R * te * LOG(xae)) / (Tb3 - te)
  Ta4 = (te * Sc - R * te * LOG(1 - xbe) - xbe ^ 2 * Ege) / Sc
  'Now all the parameters are known at P=0
  'I'll take Vm =0 as in the Shinaev paper
   INPUT "which pressure do you want (kbar)", p
   p = p * 100
   OPEN "a:pt1.dat" FOR OUTPUT AS #1
   OPEN "a:pt2.dat" FOR OUTPUT AS #2
   OPEN "a:pt3.dat" FOR OUTPUT AS #3
   OPEN "a:pt4.dat" FOR OUTPUT AS #4
   x = 0
   ym = .0001
   FOR i = 1 TO 99
   adel = 10000
   x = i * .01
   y = ym
1 : t1 = (El * x ^ 2 - EAl * y ^ 2 + sa * ta + p * Vla) / (sa - R * LOG((1 - x)
   t2 = (El * (1 - x) ^ 2 - EAl * (1 - y) ^ 2 + sa * tb2 + p * Vla1) / (sa - R *
   del = ABS(t1 - t2)
   IF del > .5 THEN
   IF del < adel THEN
   adel = del
   ym = y
   END IF
   y = y + .0001
   IF y >= x THEN GOTO 2
   IF y >= .4 THEN GOTO 2
   GOTO 1
   ELSE
   ym = y
   END IF
```

```
2 : t1 = (El * x ^ 2 - EAl * ym ^ 2 + sa * ta + p * Vla) / (sa - R * LOG((1 - x)
   LPRINT t1, , x, ym
   PRINT #1, x, ym, t1
   NEXT i
   ym = .999
   FOR i = 1 TO 99
   adel = 10000
   x = 1 - i * .01
   y = ym
3 : t1 = (El * x ^ 2 - Ege * y ^ 2 + sb * ta1 + p * Vlg1) / (sb - R * LOG((1 - x
   t2 = (El * (1 - x) ^ 2 - Ege * (1 - y) ^ 2 + sb * tb + p * Vlg) / (sb - R * L
   del = ABS(t1 - t2)
   IF del > .5 THEN
   IF del < adel THEN
   adel = del
   ym = y
   END IF
   y = y - .0001
   IF y <= x THEN GOTO 4
   IF y <= .6 THEN GOTO 4
   GOTO 3
   ELSE
   ym = y
   END IF
4 : t1 = (El * (1 - x) ^ 2 - Ege * (1 - ym) ^ 2 + sb * tb + p * Vlg1) / (sb - R
   LPRINT t1, x, ym
   PRINT #2, x, ym, t1
   NEXT i
   FOR i = 1 TO 199
   x = i * .005
   t3 = (EAl * (1 - x) ^ 2 + Tb3 * Sc + p * vlg2) / (Sc - R * LOG(x))
   t4 = (Ege * x ^ 2 + Ta4 * Sc + p * Vla2) / (Sc - R * LOG(1 - x))
   PRINT #3, x, t3
   PRINT #4, x, t4
   NEXT i
   PRINT #1, 1, 1, tb2
   PRINT #2, 1, 1, tb
   PRINT #3, 1, Tb3
   PRINT #4, 1, 273
   CLOSE #1
   CLOSE #2
   CLOSE #3
   CLOSE #4
 END
```

```
' Author :  Pascal Yvon, February 1993
' This program calculates the GRAIN SIZE and the STRAIN from x-ray
' diffraction data.  The input data is the variance of the diffraction peaks
' which have been fitted with a Pearson type VII function.
' The datafile should have:
'              two lines with comments (inside double quotes)
'              np,  the number of peaks in the file
' for each peak:
'              TT, PEAK, FWHM, EXP, AREA
' Where:
'       TT    = two-theta value for the peak from the PVII fit
'       PEAK  = peak height from the PVII fit
'       FWHM  = full-width Half-maximum from the PVII fit
'       EXP   = exponent value from the PVII fit
'       AREA  = area under the fitted peak (intensity)
'       RANGE = range that the variance is calculated
'       IB    = calculated integral half breadth (AREA/PEAK)
'
' The integral breadth must be corrected by the instrumental breadth which is
' determined by taking a diffraction pattern from a NIST standard (such as
' LaB6 powder).
' The integral breadth has to be in RADIANS.
' VARIANCE is the variance of the peak
' This program is based on the following references:
'       X-Ray Diffraction by Warren
'       X-Ray Diffraction Procedures by Klug and Alexander, chapter 9
'       E. Aqua, Acta Cryst. vol 20, p 560 (1966)
'       P. Yvon, Ph. D. Thesis, CALTECH, 1993.
'
' Parameters for the instrumental breadth correction
' The following data (aaa, bbb, and ccc) are for a specific setup.
' slits: 1, 2, .5, .3 (going along with the x-rays)
' These parameters must be recalculated if we change slits or
' if we realign the diffractometer.  To do this, run this program setting the
' values of aaa, bbb, and ccc to zero (comment these three lines).
aaa = .0000050087#
bbb = -.00025943#
ccc = .048503

CLS
pi = 4 * ATN(1)
Wavelength = 1.54059
COLOR 10
PRINT "======================== GRAIN SIZE AND STRAIN ==========================
COLOR 7: PRINT
'
'=========================for manual input of peak parameters
INPUT "Manual data input (Y or N) ? ", an$
IF an$ = "y" OR an$ = "Y" THEN
    INPUT "Input 2-THETA value ", tt
    INPUT "Input PEAK value ", peak
    peak = peak * 60: 'convert CPS to CPM
    INPUT "Input Full-width half-maximum ", fwhm
    INPUT "Input EXPONENT ", m
    INPUT "Input AREA ", area
    INPUT "How many times FWHM should the range be? ", X
    range = fwhm * X
    PRINT "How many divisions do you wish the peak"
    INPUT "to be divided into for the variance calculation", DIVISION
    TOTAREA = peak * range / (2 * DIVISION)
```

```
    TOTVAR = 0
    rd = range / (2 * DIVISION)
    FOR inc = (tt + rd * 2) TO (tt + range / 2) STEP (range / DIVISION)
           i = peak * (1 + (((inc - tt) / fwhm) ^ 2) * 4 * (2 ^ (1 / m) - 1)) ^
           PRINT i
           DIF = (tt - inc) ^ 2
           PRINT DIF
           TOTAREA = TOTAREA + i * (range / DIVISION)
           TOTVAR = TOTVAR + i * DIF * (range / DIVISION)
   NEXT inc
   TOTAREA = TOTAREA * 2
   TOTVAR = TOTVAR * 2
   variance = TOTVAR / TOTAREA
   PRINT area, TOTAREA, TOTVAR, var
   ib = TOTAREA / peak
   ib = ib * pi / 180
   PRINT "For these parameters:"
   PRINT "Integral Breadth = "; ib
   PRINT "Variance = "; variance
   PRINT "Calculated area = "; TOTAREA

' =end of manual input section.  Next section is for data from a file =====

ELSE
DIM tt(20), peak(20), m(20), fwhm(20), area(20), dsp(20), ib(20), ibx(20), iby(2
PRINT "   Input the file name for the x-ray data"
INPUT datain$
OPEN datain$ FOR INPUT AS #1
PRINT "   Input the file name for results"
INPUT dataout$
OPEN dataout$ FOR OUTPUT AS #2
'INPUT #1, comm1$, comm2$
INPUT #1, np
FOR i = 1 TO np
        INPUT #1, tt(i), peak(i), fwhm(i), m(i), area(i)
NEXT i
FOR i = 1 TO np
        tt = tt(i): ttr = pi * tt / 180
        PRINT tt, ttr
        peak(i) = peak(i) * 60                   'convert to counts per second
        dsp(i) = Wavelength / (2 * SIN(ttr / 2))        ' calculate d-spacing
        range = 30 * fwhm(i) / m(i)                    ' range of integration
        DIVISION = 1500 / m(i)                ' number of steps in integration
        rd = range / (2 * DIVISION)           ' increment
        TOTAREA = peak(i) * rd
          TOTVAR = 0
        FOR inc = (tt + 2 * rd) TO (tt + range / 2) STEP (range / DIVISION)
          ii = peak(i) / (1 + (((inc - tt) / fwhm(i)) ^ 2) * 4 * (2 ^ (1 / m(i))
          DIF = ((pi / 180) * (tt - inc)) ^ 2
          TOTAREA = TOTAREA + ii * (range / DIVISION)
          TOTVAR = TOTVAR + ii * DIF * (range / DIVISION)
    NEXT inc
          TOTAREA = 2 * TOTAREA          ' becasue integration was on half only
          TOTVAR = 2 * TOTVAR
          variance = TOTVAR / TOTAREA
          ib(i) = TOTAREA / peak(i)              'data integral breath
          ba = ccc + bbb * tt + aaa * (tt ^ 2)   'instrumental integral breath
          IF ba < b(i) THEN                      'then correct
            ib(i) = ib(i) * SQR((1 - (ba / ib(i)) ^ 2))
       ELSE
```

```
          ib(i) = ib(i)                              'dont touch it
       END IF
          ib(i) = ib(i) * pi / 180
          PRINT dsp(i), range, DIVISION, variance, TOTAREA, ib(i), fwhm(i)
          range = range * pi / 180
          vx(i) = 4 * SIN(ttr / 2) * TAN(ttr / 2) / (Wavelength * range)
          vy(i) = variance * COS(ttr / 2) / (range * Wavelength)
          'create variables for direct analysis and store for genplot
          ibx(i) = (SIN(ttr / 2) / Wavelength) ^ 2
          iby(i) = (ib(i) * COS(ttr / 2) / Wavelength) ^ 2
          'plot:                            x      y
          PRINT #2, dsp(i), vx(i), vy(i), ibx(i), iby(i)
          '   y-intercept = 1/(grain size)^2
          '        slope  = 16 * strain^2
NEXT i
CLOSE #1
CLOSE #2
       END IF
END
```

```
'Author: Pascal Yvon February 1993
'this program calculates the temperature factor for the intensity,
'then calculates the intensity for 2 peaks, one of each phase, and
'using the measured ratio of the intensities of these two peaks
' then calculates the volume and atomic fractions of the two elements
DIM sc1(13), sc2(14), u1(10), u2(10), v1(10), v2(10), w1(10), w2(10)
pi = 4 * ATN(1)
la = 1.54059
temp = 298
PRINT "symbol and intensity of the first peak"
INPUT s1$, int1
INPUT "h,k,l,2 theta"; h1, k1, l1, tt1
PRINT "symbol and intensity of the second peak"
INPUT s2$, int2
INPUT "h,k,l,2 theta"; h2, k2, l2, tt2
'
'read data
'
2 READ sym$, name1$
IF sym$ = s1$ THEN 1
READ buf, bif, bof, bef, byf
FOR i = 0 TO 11
READ baf
NEXT i
GOTO 2
1 READ deb1, at1, st1, a1, den1
   FOR i = 0 TO 11
   READ sc1(i)
   NEXT i
 RESTORE
4 READ sym$, name2$
IF sym$ = s2$ THEN 3
READ buf, bif, bof, bef, byf
FOR i = 0 TO 11
READ baf
NEXT i
GOTO 4
3 READ deb2, at2, st2, a2, den2
   FOR i = 0 TO 11
   READ sc2(i)
   NEXT i
tt1 = tt1 * pi / 180
tt2 = tt2 * pi / 180
'
'determination of structure
'
u1(1) = 0
v1(1) = 0
w1(1) = 0
u1(2) = 0
v1(2) = .5
w1(2) = .5
u1(3) = .5
v1(3) = .5
w1(3) = 0
u1(4) = .5
v1(4) = 0
w1(4) = .5
IF st1 = 1 THEN na1 = 4
IF st1 = 2 THEN
```

```
na1 = 8
u1(5) = .25
v1(5) = .25
w1(5) = .25
u1(6) = .25
u1(7) = .75
u1(8) = .75
v1(6) = .75
v1(7) = .25
v1(8) = .75
w1(6) = .75
w1(7) = .75
w1(8) = .25
END IF
u2(1) = 0
v2(1) = 0
u2(2) = 0
v2(2) = .5
w2(2) = .5
u2(3) = .5
v2(3) = .5
w2(3) = 0
u2(4) = .5
v2(4) = 0
w2(4) = .5
w2(1) = 0
IF st2 = 1 THEN na2 = 4
IF st2 = 2 THEN
na2 = 8
u2(5) = .25
v2(5) = .25
w2(5) = .25
u2(6) = .25
u2(7) = .75
u2(8) = .75
v2(6) = .75
v2(7) = .25
v2(8) = .75
w2(6) = .75
w2(7) = .75
w2(8) = .25
END IF
'
'calculation of structure factor
'
sum1 = 0
sum2 = 0
var = SIN(tt1 / 2) / la
ilow = INT(var * 10)
ihigh = ilow + 1
ffn = sc1(ilow) + (var * 10 - ilow) * (sc1(ihigh) - sc1(ilow))
FOR i = 1 TO na1
sum1 = sum1 + ffn * SIN(2 * pi * (h1 * u1(i) + k1 * v1(i) + l1 * w1(i)))
sum2 = sum2 + ffn * COS(2 * pi * (h1 * u1(i) + k1 * v1(i) + l1 * w1(i)))
NEXT i
ffact1 = sum1 * sum1 + sum2 * sum2
PRINT "ffact1", ffact1
sum1 = 0
sum2 = 0
var = SIN(tt2 / 2) / la
```

```
ilow = INT(var * 10)
ihigh = ilow + 1
ffn = sc2(ilow) + (var * 10 - ilow) * (sc2(ihigh) - sc2(ilow))
FOR i = 1 TO na2
sum1 = sum1 + ffn * SIN(2 * pi * (h2 * u2(i) + k2 * v2(i) + l2 * w2(i)))
sum2 = sum2 + ffn * COS(2 * pi * (h2 * u2(i) + k2 * v2(i) + l2 * w2(i)))
NEXT i
ffact2 = sum1 * sum1 + sum2 * sum2
PRINT "ffact2", ffact2
'
'Calculation of multiplicity factor
'
p1 = 48
p2 = 48
IF (h1 = k1 OR h1 = l1 OR k1 = l1) THEN p1 = 24
IF (h1 * k1 * l1 = 0) THEN p1 = 24
IF (h1 * k1 * l1 = 0 AND (h1 = k1 OR h1 = l1 OR k1 = l1)) THEN p1 = 12
IF (h1 = k1 AND h1 = l1) THEN p1 = 8
IF (h1 * k1 = 0 AND h1 * l1 = 0 AND k1 * l1 = 0) THEN p1 = 6
IF (h2 = k2 OR h2 = l2 OR k2 = l2) THEN p2 = 24
IF (h2 * k2 * l2 = 0) THEN p2 = 24
IF (h2 * k2 * l2 = 0 AND (h2 = k2 OR h2 = l2 OR k2 = l2)) THEN p2 = 12
IF (h2 = k2 AND h2 = l2) THEN p2 = 8
IF (h2 * k2 = 0 AND h2 * l2 = 0 AND k2 * l2 = 0) THEN p2 = 6
PRINT "p1,p2", p1, p2
'
'Calculation of temperature factor
'
m1 = 1.15 * temp * 10000 / (at1 * deb1 * deb1)
s1 = SIN(tt1 / 2) * SIN(tt1 / 2) / (la * la)
x1 = deb1 / temp
'calculation of Phi(x1)
xint = 1000 * x1
nint = INT(xint)
inter = x1 / nint
phi1 = 0
FOR i = 1 TO nint
xi = i * inter
phi1 = phi1 + inter * xi / (EXP(xi) - 1)
NEXT i
phi1 = phi1 / x1
PRINT "x1, phi1", x1, phi1
m1 = m1 * s1 * (phi1 + (x1 / 4))
'
'Calculation of temperature factor
'
m2 = 1.15 * temp * 10000 / (at2 * deb2 * deb2)
s2 = SIN(tt2 / 2) * SIN(tt2 / 2) / (la * la)
x2 = deb2 / temp
'calculation of Phi(x2)
xint = 1000 * x2
nint = INT(xint)
inter = x2 / nint
phi2 = 0
FOR i = 1 TO nint
xi = i * inter
phi2 = phi2 + inter * xi / (EXP(xi) - 1)
NEXT i
phi2 = phi2 / x2
PRINT "x2,phi2", x2, phi2
```

```
m2 = m2 * s2 * (phi2 + (x2 / 4))
'
'calculation of Lorenz-polarisation factor
'
lp1 = (1 + COS(tt1) * COS(tt1)) / (SIN(tt1 / 2) * SIN(tt1 / 2) * COS(tt1 / 2))
lp2 = (1 + COS(tt2) * COS(tt2)) / (SIN(tt2 / 2) * SIN(tt2 / 2) * COS(tt2 / 2))
PRINT "lp1,lp2", lp1, lp2
'
'calcul of volume of unit cell
'
v1 = a1 * a1 * a1
v2 = a2 * a2 * a2
PRINT "v1,v2", v1, v2
'
'calcul of r
'
r1 = ffact1 * p1 * lp1 * EXP(-2 * m1) / (v1 * v1)
r2 = ffact2 * p2 * lp2 * EXP(-2 * m2) / (v2 * v2)
aa = r1 * int2 / (int1 * r2)
c1 = 1 / (1 + aa)
PRINT "volume fraction of ", name1$, c1
arc1 = (c1 / den1) / ((c1 / den1) + ((1 - c1) / den2))
PRINT "atomic fraction of", name1$, arc1
DATA "Al","Aluminum",390,26.98154,1,4.0459,9.9932,13,11,8.95,7.75,6.6,5.5,4.5,3.
DATA "Ge","Germanium",374,72.59,2,5.65,13.6447,32,28.8,24.1,20,17.1,15,13.2,11.6
```

```
/* file TL3PAS.MAC
/* first corrects tha background, then fits data to 3 Lorentzians .
/* This program is invoked by typing 'call tl3pas' after your data've
/* been culled to remove the regions that you don't want to fit.
/* (see HELP CULL in the GENPLOT on-line help file.)
/* the SETVAR commands give it first guesses for peak heights, FWHM's,
/* and locations of the Lorentzians.
/* They are all keyed to the first guess for the variable w2,
/* which I have set up to be a good guess when the data file format is:
/*        wavelength (nm)      intensity (arbitrary units)
/* If you insist on fitting to files where the x-coordinate is
/* channel number or wavenumber, you'll have to modify the first guess
/* for w2.  The rest of the first guesses should follow automatically.
/* This program was written by Mike Aziz.
/* this program HAS been modified by Pascal YVON (7/92) to accomodate
/* wavenumbers and the new values from Hess et al (J. Appl Phys, March 1st,92)
/* this program has been improved to take better care of the background
/* substraction.  The background is fitted to a polynomial of order 3, and
/* substracted from the data.
:start
linewidth 3
label bottom 'Wavenumbers (nm)'
label left 'Intensity (arbitrary units)'
read &query -prompt 'file to be analyzed:'
let x = -x
archive c1
pl -sym 0 -ltype 0
setvar be=@min(x)
setvar en=@max(x)
setvar bp1 = &query -prompt 'beginning of peaks 1 and 2:'
setvar ep1 = &query -prompt 'end of peaks 1 and 2:'
setvar bp2 = &query -prompt 'beginning of peak 3:'
setvar ep2 = &query -prompt 'end of peak 3:'
/* this determines the regions for which we have only background
cull_data delete xrange bp1 ep1
cull_data delete xrange bp2 ep2
fit poly 3 -xrange be en /* fits background
ltype 1
overlay -fit
retrieve c1
let y = c1:y-fit(x) /* substract background
pl -sym 0 -ltype 0
setvar omega01 = 16187.2
setvar omega02 = 16232.2
setvar I1=@max(y) /* guess#1 for ht. of 1st Lorentzian = highest # cnts
setvar w1=x($I)   /*   "      " loc'n "   "   " = channel w/highest # cnts
setvar I2=I1*0.6  /*   "      " ht. of 2d Lor. = RT fraction of I1
setvar w2=w1+44    /* "loc'n 2d Lor.= RT dist from 1st Lor IN WAVENUMBERS
setvar fwh1=.7*abs(w1-w2) /* guess#1 for FWHM of Lor. #1 = RT value
setvar w3=w1+3.45*(w2-w1) /* guess#1 for loc'n of 3d Lor = RT value
setvar fwh2=fwh1  /* guess#1 for FWHM of Lor. #2 = FWHM of Lor. #1
setvar fwh3=fwh1
setvar I3=I1*0.23 /*   "      " ht. of 3d Lor. = RT fraction of I1
setvar c1w2=-0.658415 /* pressure dependence of Sm:YAG line,
setvar c1w1=-0.8194   /* from Nancy Hess 3/92 (cm**-1/kbar)
define lorent(x,ii,wi,fwhi)=ii*(fwhi^2/(4*(x-wi)^2+fwhi^2)) /* Lorentzian
defin f(x)=lorent(x,i1,w1,fwh1)+lorent(x,i3,w3,fwh3)+lorent(x,i2,w2,fwh2)
fit nlsfit                                /* Nonlinear Least-Squares Fit
reset                                      /* forget about previous fits
function f                                 /* fit this function - 3 Lor's
```

```
vary I1 / vary w1 / vary fwh1 /           /* vary these parameters
vary i2 / vary w2 / vary fwh2 /
vary i3 / vary w3 / vary fwh3 /                      /* ...'vary FWH3 /'
fit                                       /* do it NOW
return                                    /* return to plotting routine
evaluate (w1-omega01)/c1w1              /* PRESSURE IN KILOBARS (main peak)
evaluate (w2-omega02)/c1w2        /* pressure in kbars (secondary peak)
ltype 1                                  /* use a solid line
overlay -fit                             /* overlay the fit on the data
allocate pre1 real
allocate pre2 real
let pre1=(w1-omega01)/c1w1
let pre2=(w2-omega02)/c1w2
declare str1 = &encode (F8.3) pre1
declare str2 = &encode (F8.3) pre2
annote size 0.18
label 16220 2235 'pressure 1 %str1% kbar'  /* prints pressure from main peak
label 16220 1900 'pressure 2 %str2% kbar' /* prints pressure from secondary peak
return
```

```
' Author :Pascal Yvon June 1990
' Program to interpret double X-Ray camera  pictures.  Given a polycrystalline d
' pattern (coordinates of points on rings digitized), calculate the
' coordinates of the center and the radii.We do this fot two films and then
' determine d-spacings.
' Data must be in the form :
'           Comment (A$)
'           x(1), y(1), w(1)..          coordinates of a point on first circle
'           x(2), y(2), w(2)...             "           another "    "    "
'           >400, >400             x or y values over 400
'           repeat for second circle, etc
'           end with -1, -1  (last entry)
'           the w's are level of confidence ( between 0 and 1)
DIM x(30, 35), y(30, 35), r(2, 35), npoint(35), aa(30, 35), bb(30, 35), xca(30,
' ========= Read Data ==============================================
     CLS
     FOR ij = 1 TO 2
     INPUT "Input filename with data : ", filein$
     OPEN filein$ FOR INPUT AS #1
     INPUT #1, label1$
     j = 0: '  j is index for radii
lb1: j = j + 1: i = 0
lb2: i = i + 1
     INPUT #1, xx, yy, ww
     IF xx > 400 OR yy > 400 THEN GOTO lb1
     IF xx < 0 OR yy < 0 THEN GOTO lb3
     x(i, j) = xx: y(i, j) = yy: ww(i, j) = ww
     npoint(j) = i: GOTO lb2
lb3: ' data has been read
     CLOSE #1
     imax = jmax
     jmax = j
  LPRINT " There are "; jmax; " rings "
  LPRINT
  FOR k = 1 TO jmax: LPRINT " Ring "; k; " has "; npoint(k); " points": NEXT k
  LPRINT
' ========= Calculate the bisecting lines joining two points ==============
'  LPRINT "       J         I        x         y         Xc         Yc         m
  sa = 0: sb = 0: saa = 0: sbb = 0: sab = 0
  FOR j = 1 TO jmax
  FOR i = 1 TO npoint(j)
     IF i = npoint(j) THEN
       xc = (x(i, j) + x(1, j)) / 2!
       yc = (y(i, j) + y(1, j)) / 2!
       dd = y(1, j) - y(i, j)
       IF ABS(dd) < 1E-20 THEN dd = 1E-20
       m1 = -(x(1, j) - x(i, j)) / dd
       ELSE
       xc = (x(i, j) + x(i + 1, j)) / 2!: xca(i, j) = xc
       yc = (y(i, j) + y(i + 1, j)) / 2!: yca(i, j) = yc
       dd = y(i + 1, j) - y(i, j)
       IF ABS(dd) < 1E-20 THEN dd = 1E-20
       m1 = -(x(i + 1, j) - x(i, j)) / dd: m(i, j) = m1
       END IF
' ========= Calculate the normalization parameters for ax+by+1=0 ==========
  a = m1 / (yc - m1 * xc): aa(i, j) = a
  b = 1! / (m1 * xc - yc): bb(i, j) = b
' ========= calculate the sums for least squared fit =====================
  denom = (a * a + b * b)
```

```
  sa = sa + a * ww(i, j) / denom: sb = sb + b * ww(i, j) / denom
  saa = saa + a * a * ww(i, j) / denom: sbb = sbb + b * b * ww(i, j) / denom
  sab = sab + a * b * ww(i, j) / denom
NEXT i: NEXT j
' ========= Calculate the coordinates of the center: (xo, yo) ==============
  denom2 = saa * sbb - sab * sab
  xo = -(sa * sbb - sb * sab) / denom2: yo = -(saa * sb - sab * sa) / denom2
  FOR j = 1 TO jmax
  FOR i = 1 TO npoint(j)
  dist = (1 + xo * aa(i, j) + yo * bb(i, j)) / (SQR(aa(i, j) ^ 2 + bb(i, j) ^ 2)
 ' LPRINT USING "######.###"; j, i, x(i, j), y(i, j), xca(i, j), yca(i, j), m(i,
  NEXT i: NEXT j
'PRINT "denom2="; denom2
'PRINT "coordinates of center (xo,yo) "; xo, yo
' ====== Calculate the Radius for each circle ==============================
  FOR j = 1 TO jmax
     sumr = 0
  FOR i = 1 TO npoint(j)
     sumr = sumr + SQR((x(i, j) - xo) ^ 2 + (y(i, j) - yo) ^ 2)
  NEXT i
  r(ij, j) = sumr / npoint(j)
PRINT USING " film number =###"; ij;
PRINT USING " J=###"; j;
PRINT USING " R=###.###"; r(ij, j)
NEXT j
' ========= print results ================================================
  LPRINT
  LPRINT "    j    i    Radius   % error"
  FOR j = 1 TO jmax
  FOR i = 1 TO npoint(j)
  LPRINT USING "#####"; j, i;
  xerror = (SQR((y(i, j) - yo) ^ 2 + (x(i, j) - xo) ^ 2) - r(ij, j)) * 100 / r(i
  LPRINT USING "######.###"; r(ij, j), xerror
  NEXT i: NEXT j
  NEXT ij
    PRINT : INPUT "What is the ring # for which we have a real measure ?"; o
    PRINT : INPUT "What is the radius of this ring( in mm) ?"; rr
    alpha = rr / r(1, o)
    FOR j = 1 TO imax
    ratio(j) = alpha * r(1, j)
    LPRINT " ring # "; j; "  radius "; r(1, j); " real value "; ratio(j)
  NEXT j
  FOR j = 1 TO jmax
  PRINT : INPUT "enter ring # on 1st film corresponding to this ring"; irr
  dd(j) = 50 * r(1, irr) / (r(2, j) - r(1, irr))
  LPRINT USING "###.###"; dd(j)
  NEXT j
  dd = 0
  FOR j = 1 TO jmax
  dd = dd + dd(j)
  NEXT j
  dd = dd / jmax
  LPRINT "         Two theta       d-spacing       Intensity "
  LPRINT "                         Mo Kalpha  "
  FOR i = 1 TO imax
  twotheta = ATN(ratio(i) / dd)
  dsp = .7093 / (2 * SIN(twotheta / 2))
  twothet = twotheta * 180 / 3.1415926535#
 LPRINT USING "#########.#####"; twothet, dsp
  NEXT i
```